UNIVERSITY OF Southampton

Faculty of Environmental and Life Sciences

Ocean and Earth Science

Deglacial and palaeoenvironmental history of Anvers-Hugo Trough, western Antarctic Peninsula

By

Zoë Amelia Roseby

ORCID ID: 0000-0003-1151-0172

Thesis for the degree of Doctor of Philosophy

August 2019

University of Southampton
Abstract

Faculty of Environmental and Life Sciences
Ocean and Earth Science

Thesis for the degree of Doctor of Philosophy

Deglacial and palaeoenvironmental history of Anvers-Hugo Trough, western Antarctic Peninsula

By

Zoë Amelia Roseby

The Antarctic Peninsula Ice Sheet (APIS) is currently experiencing significant mass loss, contributing to global sea level rise. Increasing mass loss is primarily a response to reductions in the thickness and extent of ice shelves, triggering retreat, acceleration and drawdown of marine terminating glaciers. These changes have occurred in tandem with atmospheric and oceanic warming, which have had additional impacts on sea ice, the properties of water masses and marine productivity. A full assessment of these recent changes, together with the relative importance of key drivers for initiating grounding line and ice shelf retreat, is limited by the timescales over which we have recorded contemporaneous measurements of ice sheet change(s) and climate observations. Consequently, there remains a need to understand the behaviour of the APIS over a range of timescales so that we can fully understand future ice sheet change. This study utilises marine geological and geophysical data from Anvers-Hugo Trough (AHT), to improve our understanding of the glacial and environmental history of the western Antarctic Peninsula following the Last Glacial Maximum (25-19 kyr BP).

Detailed multi-proxy analysis of sediment cores allows identification of sedimentary units deposited over the last deglaciation of AHT. Particular focus is paid investigating the variability in sediments deposited in the transitional (grounding line proximal to distal) environment in order to identify key depositional processes active in this setting and infer grounding line behaviour over deglaciation. Transitional sedimentary units are found to be deposited systematically; varying with marine processes, grounding line retreat rate, the presence/absence of an ice shelf, bathymetric position and across trough position. Quantitative assessment of absolute diatom abundance and species assemblages, aid reconstruction of the palaeoenvironmental conditions in AHT during and after deglaciation and allow the link between deglaciation and primary productivity to be assessed. These data indicate that the AHT experienced a period of enhanced diatom productivity following the last deglaciation of the trough, associated with meltwater discharge and nutrient input from sea and glacial ice melt. This led to deposition of laminated diatomaceous oozes, with their spatial distribution and accumulation influenced by seafloor bathymetry. This indicates that the distribution of laminated oozes does not necessarily reflect the spatial extent of surface productivity. The timing of deglaciation and post-glacial environmental change is inferred from 27 new radiocarbon dates. The grounding line had retreated from the mid-shelf as early as 15.84 cal. kyr BP, reaching Palmer Deep on the inner shelf shortly before ~12.85 cal. kyr BP. Peak, post-glacial primary productivity on the mid to inner shelf followed grounding line retreat by ~4.6 kyr, indicating that deglaciation alone did not create this highly productive environment within AHT. Additional drivers of glacial and/or sea-ice melt, including high atmospheric and sea surface temperatures, were required to trigger this period of peak diatom productivity.

Contents

List of figures

List of tables

Research thesis: Declaration of authorship

Print name:	Zoë Amelia Roseby

Title of thesis:	Deglacial and palaeoenvironmental history of Anvers-Hugo Trough, western Antarctic Peninsula

I declare that this thesis and the work presented in it are my own and has been generated by me as the result of my own original research.

I confirm that:

1. This work was done wholly or mainly while in candidature for a research degree at this University;
2. Where any part of this thesis has previously been submitted for a degree or any other qualification at this University or any other institution, this has been clearly stated;
3. Where I have consulted the published work of others, this is always clearly attributed;
4. Where I have quoted from the work of others, the source is always given. With the exception of such quotations, this thesis is entirely my own work;
5. I have acknowledged all main sources of help;
6. Where the thesis is based on work done by myself jointly with others, I have made clear exactly what was done by others and what I have contributed myself;
7. None of this work has been published before submission.

Signature:		Date:	09/08/2019

Acknowledgements

I would first like to thank my supervisors Matthieu Cartigny, James Smith and Claus-Dieter Hillenbrand for their guidance and advice throughout my PhD. You have all been patient and generous with your time and I am incredibly grateful. I would also like to thank Esther Sumner, Peter Talling, Claire Allen, Robert Larter and Kelly Hogan, for their support and scientific guidance; I have thoroughly enjoyed getting to know you and collaborating with you all. Special thanks goes to Claire Allen for stepping in as a PhD mentor and for getting me into diatoms! I am grateful to Kelly and Claire for supporting my involvement in our South Orkney Island research cruise, it was a fantastic experience and I will treasure my memories of that beautiful place.

I have had amazing opportunities visiting international institutes, Colgate University, University of South Florida, Alfred Wegener Institute and Woods Hole Oceanographic Institution. I would like to thank my hosts Amy Leventer, Brad Rosenheim, Gerhard Kuhn and Ann McNichol, as well as students and laboratory technicians at these institutes; Isabel Dove, Natalie Kozlowski, Dylan Peck, Christina Subt, Ryan Venturelli, Lexie Freeman, Rita Fröhlking-Teichert and Susanne Wiebe. You have all been incredibly kind, welcoming and generous with your support. It has been a pleasure to work with you all; thank you for the wonderful experiences and for your scientific insight and advice. Additional thanks goes to the NERC, Trans-Antarctic Association, British Sedimentological Research Group, Quaternary Research Association and International Association of Sedimentologists, for providing funding that facilitated these research visits and associated data collection. Furthermore, I am grateful to everyone that assisted with my data collection, including Werner Ehrmann at University of Leipzig and the BOSCORF team. I would especially like to thank Mike Edwards for his core-splitting assistance and friendship.

I would like to thank my friends for their support, especially Bonita Barrett, Emma Bagnall and Jessica Casey who have been great listeners and provided fun (and dancing!) over the last four years. I am lucky to have you all and look forward to our future adventures. I have had the pleasure of working at NOC, BAS and Durham University and have met amazing people during my time at these institutes. I would particularly like to thank Sophie Hage, Juliet Sefton and Mateja Ogrič for the coffee and pub trips, advice, friendship and encouragement.

My parents and sister, Eloise, deserve the biggest thank you for their patience, love and understanding. You have been the best support system throughout my PhD- I could not have

done it without you. Above all, I would like to thank Matt; there are no words to describe how grateful I am to you.

Abbreviations

AASW	Antarctic Surface Water
ACC	Antarctic Circumpolar Current
ACR	Antarctic Cold Reversal
ADA	Absolute Diatom Abundance
AHIS	Anvers-Hugo Ice Stream
AHT	Anvers-Hugo Trough
AIO	Acid Insoluble Organic fraction
AIS	Antarctic Ice Sheet
AMS	Accelerator Mass Spectrometry
AP	Antarctic Peninsula
APCC	Antarctic Peninsula Coastal Current
APIS	Antarctic Peninsula Ice Sheet
BAS	British Antarctic Survey
BC	Box Core
BOSCORF	British Ocean Sediment Core Research Facility
BP	Before Present
CDW	Circumpolar Deep Water
Chs	*Chaetoceros subg. Hyalochaete*
***Chs*-RS**	*Chaetoceros subg. Hyalochaete* Resting Spore
***Chs*-veg**	*Chaetoceros subg. Hyalochaete* vegetative cells
EAIS	East Antarctic Ice Sheet
EAP	Eastern Antarctic Peninsula
ENSO	El Niño/Southern Oscillation (ENSO)
GC	Gravity Core
GZW	Grounding Zone Wedge

IRD	Ice Rafted Debris
JRI	James Ross Island
LGM	Last Glacial Maximum
LCDW	Lower Circumpolar Deep Water
LCO	Local Contamination Offset
mbsl	Metres Below Sea Level
M-CDW	Modified Circumpolar Deep Water
MHH	Mid-Holocene Hypsithermal
MISI	Marine Ice Sheet Instability
MS	Magnetic Susceptibility
MRE	Marine Reservoir Effect
MSCL	Multi Sensor Core Logger
MSGL	Mega-Scale Glacial Lineations
mvpg	Million Valves Per Gram
MWP	Meltwater Pulse
ODP	Ocean Drilling Program
RS	Resting Spore
SAM	Southern Annular Mode
SEM	Scanning Electron Microscope
SHWW	Southern Hemisphere Westerly Winds
SST	Sea-Surface Temperature
TC	Total Carbon
TOC	Total Organic Carbon
UCDW	Upper Circumpolar Deep Water
WAIS	West Antarctic Ice Sheet
WAP	Western Antarctic Peninsula

XRF	X-ray Fluorescence

Abbreviations

Chapter 1

1. Introduction and research objectives

1.1. Introduction

The Antarctic Peninsula Ice Sheet (APIS) (Fig. 1.1) is currently experiencing significant mass loss (Paolo et al., 2015; Cook et al., 2016; The IMBIE team, 2018). Between 1992 and 2017 the rate of mass loss increased from 7±13 billion to 33±16 billion tonnes per year (The IMBIE team, 2018), raising global sea level by ~2.5 mm per year (Rignot et al., 2019). Increasing mass loss is primarily a response to reductions in the thickness and extent of ice shelves, which have triggered retreat, acceleration and drawdown of marine terminating glaciers (Pritchard et al., 2012; The IMBIE team, 2018). Notable examples of ice shelves that have disintegrated in part, or entirely, include Larsen B (Scambos et al., 2004; Rignot et al., 2004), Prince Gustav Channel (Cooper, 1997), Larsen A (Skvarca, 1993), Wordie (Doake and Vaughan, 1991) and Wilkins (Humbert and Braun, 2008). The retreat and collapse of Antarctic Peninsula (AP) ice shelves has occurred in tandem with atmospheric warming, which peaked in the late 1990s but has since slowed (Turner et al., 2016). Several AP ice shelves also thinned in the decades leading up to collapse, primarily through ocean-driven melting at their bases (Paolo et al., 2015).

The impact of recent atmospheric and oceanic forcing is also reflected in changes to sea ice extent and duration (Stammerjohn et al., 2012; Henley et al., 2019), the properties of water masses adjacent to melting ice (Meredith and King, 2005; Meredith et al., 2017) and marine productivity and ecosystems (Meredith et al., 2018). A time series of sea ice concentration between 1979 and 2011, shows that the sea ice season within the AP and Bellingshausen Sea regions has decreased in duration by 3.3 months over this time period; with sea ice advancing in the austral autumn 2 months later and retreating in the austral spring 1.3 months earlier (Stammerjohn et al., 2012). A reduced winter sea ice extent, concurrent with oceanic warming, has increased salinity of offshore AP surface waters in the spring (Meredith and King, 2005; Stammerjohn et al., 2012). Closer to the western AP (WAP) coast, increased meltwater runoff from glaciers decreases the salinity of surface waters, producing a stratified water column and promoting enhanced phytoplankton biomass (Schloss et al., 2012). Increases in glacial meltwater associated with enhanced melting is in turn leading to the release of additional nutrients which can modify phytoplankton biomass and the dependant food chain in the modern Southern Ocean (Schloss et al., 2002; Montes-Hugo et al., 2009; Saba et al., 2014; Schmidtko et al., 2014; Kim et al., 2018) and influence carbon sequestration (Peck et al., 2015;

Hendry et al., 2018). Moreover, recent modelling work indicates that increased glacial discharge acts to warm the sub-surface ocean around Antarctica, which could lead to further ice sheet and ice shelf melting through a positive feedback mechanism (Bronselaer et al., 2018; Golledge et al., 2019).

A full assessment of these recent changes, together with the relative importance of key drivers (atmospheric and/or oceanic warming) for initiating ice sheet grounding line and ice shelf retreat is limited by the timescales over which we have recorded contemporaneous measurements of ice sheet change(s) and climate observations. This additionally includes our understanding of the potential global and regional impacts of these environmental changes on marine ecosystems. Discontinuous satellite data and aerial photographs are available from the 1970s and 1940s respectively, whilst continuous satellite observations are only available since 1992. However, Antarctic climatic change and the associated ice sheet response can be driven by a number of forcing mechanisms acting over a range of timescales (Bentley et al., 2009). Therefore, observations collated over the satellite era can fail to capture long-term ice sheet behaviour and the link between contemporary change and perturbations instigated prior to the start of ice sheet observations (e.g. Stone et al., 2003; Smith et al., 2017). Consequently, there remains a need to understand the behaviour of the APIS over a range of timescales so that we can fully understand future ice sheet change, the processes that drive ice sheet retreat, as well as the response of the marine ecosystem to increases in glacial meltwater.

1.2. Research objectives

The overarching aim of this study is to expand our understanding of the glacial and environmental history of the Anvers-Hugo Trough (AHT), WAP, following the Last Glacial Maximum (LGM; 25-19 kyr BP). It exploits newly collected marine geological and geophysical data from AHT (Fig. 1.1b) during cruise JR284 (January 2014), on RRS *James Clark Ross*. The geophysical data set recovered during this cruise makes the AHT of one the best-surveyed Antarctic palaeo-ice stream troughs (Larter et al., 2019) and this extensive geophysical data set has allowed focussed sediment coring within a known geomorphic context. The next chapter will introduce the AHT study area and will outline our existing understanding of the palaeoenvironmental history of the WAP and AHT. Chapter 2 will conclude with the key research questions that will be investigated in this thesis.

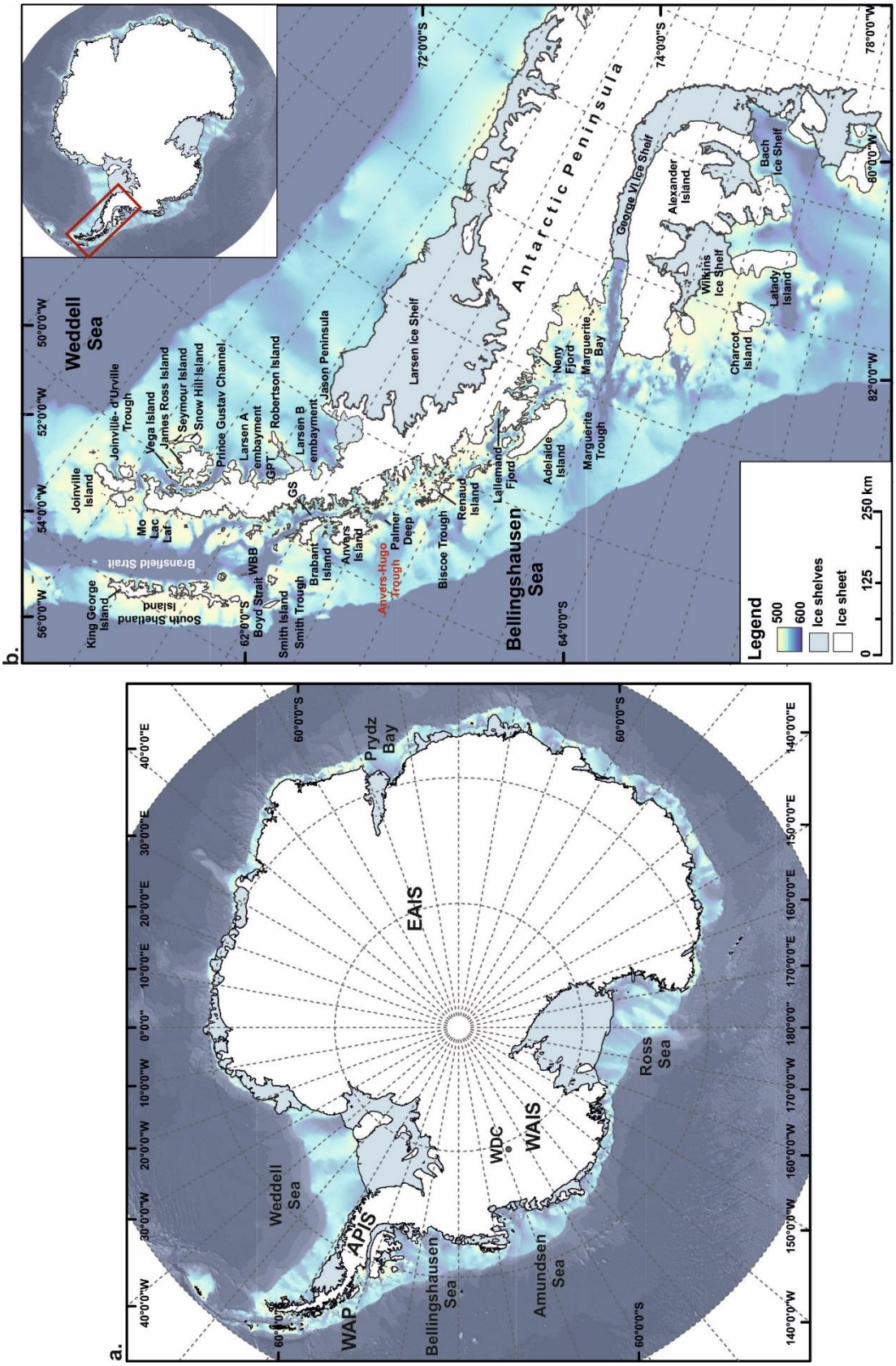

Figure 1.1: (a) Map of Antarctica showing regional bathymetry (Arndt et al., 2013) (Antarctic Peninsula Ice Sheet (APIS), western Antarctic Peninsula (WAP), West Antarctic Ice Sheet (WAIS), location of WAIS Divide ice core (WDC) and East Antarctic Ice Sheet (EAIS)). (b) Map of the Antarctic Peninsula showing regional bathymetry (Arndt et al., 2013) (Mott Snowfield Trough (Mo), Laclavere Trough (Lac), Lafond Trough (Laf), Western Bransfield Basin (WBB), Gerlache Strait (GS), Greenpeace Trough (GPT)).

Chapter 2

2. Background and study area

2.1. Introduction

This chapter will introduce the AHT study area and will outline our existing understanding of the palaeoenvironmental history of the WAP and AHT. In doing so, it summarises the broad physiographic setting of AHT and its modern climate and oceanography. It also reviews our existing understanding of the glacial and environmental history of AHT (and AP region more generally) and timing of ice retreat following the LGM based on available geophysical and geological data. This highlights current limitations in our knowledge of grounding line proximal sedimentation, the link between ice sheet retreat and impacts on marine productivity as well as the ongoing challenges of dating Antarctic shelf sediments.

2.2. Antarctic Peninsula and Anvers-Hugo Trough

2.2.1. Geographic and geological setting

The AP consists of a central spine of mountains, with a plateau 1800-2000 m above sea level, covered by the 500 m-thick APIS. The APIS is drained by a series of marine-terminating glaciers, some of which are buttressed by floating ice shelves (Domack et al., 2001). Deep bathymetric troughs, once occupied by ice streams, were eroded into the continental shelf during previous glaciations and were last occupied during the LGM. These include the AHT, Smith Trough, Biscoe Trough and Marguerite Trough (Fig. 1.1b) that can be observed as elongate low points within bathymetric data in the modern day. The AHT is a north to south oriented trough and extends from the WAP coast to the edge of the continental shelf (Fig. 1.1b and Fig. 2.1). It is approximately 144 km long and 24-40 km wide. Water depth within the AHT generally increases landwards, with a water depth of 400-430 m at the shelf edge, deepening southwards to a depth of 800 m on the mid shelf (Pudsey et al., 1994; Livingstone et al., 2012). The inner-shelf has a water depth of 500-1400 m and features streamlined bedrock and meltwater channels (Larter et al., 2019). The reverse slope morphology of the AHT is typical of the West Antarctic shelf and is thought to be an important driver of ice stream retreat (e.g., marine-ice sheet instability (MISI); Schoof, (2007)). On the mid-shelf, the AHT coalesces with a tributary trough that extends from Dallmann Bay (Fig. 2.1 and 2.2) (Lavoie et al., 2015). The inner AHT has a bathymetric low point, Palmer Deep; a glacially scoured basin located at the convergence between the Anvers Island, Bruce Plateau and Graham Coast accumulation centres (Fig. 2.1) (Domack et al., 2006). The local geology of

AHT includes middle Jurassic to lower Cretaceous volcanic rocks and late Cretaceous to early Palaeogene plutonic intrusions (including granodiorite, gabbro, diorite and tonalite) exposed on the Bruce Plateau and Graham Coast (Fig. 2.1) (British Antarctic Survey, 1981a; British Antarctic Survey, 1981b; Burton-Johnson and Riley, 2015). Cenozoic intrusions of granite and tonalite are exposed on the southern edge of Anvers Island AHT (Fig. 2.1) (British Antarctic Survey, 1981b).

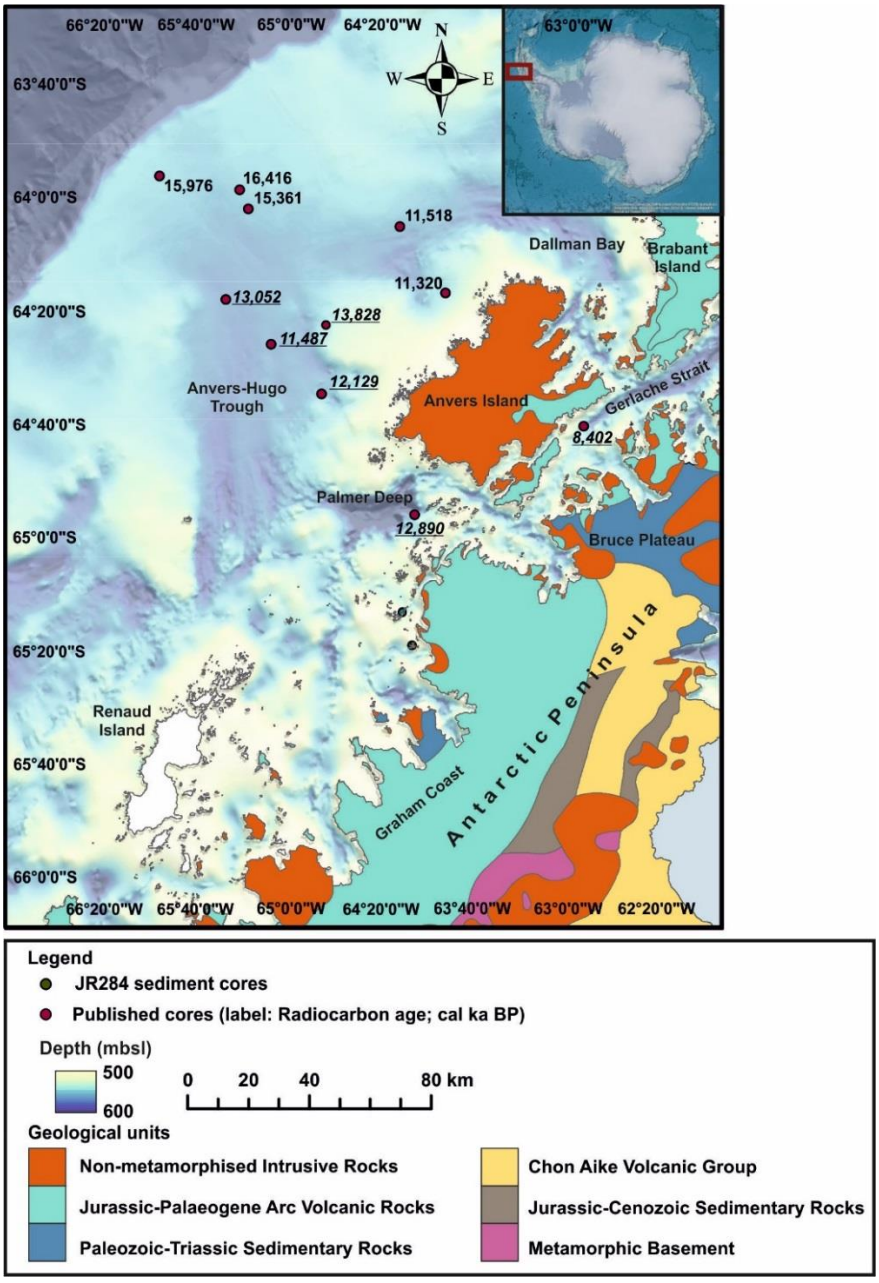

Figure 2.1 Geological map of the Antarctic Peninsula adjacent to the Anvers-Hugo Trough (British Antarctic Survey, 1981a; British Antarctic Survey, 1981b; Burton-Johnson and Riley, 2015). Published deglacial ages (red; cal. yrs BP) are from the acid-insoluble fraction of organic matter (italicised and underlined) and calcareous foraminifera (normal font) (Harden et al., 1992; Pudsey et al., 1994; Domack et al., 2001; Yoon et al., 2002; Heroy and Anderson, 2005, 2007; Nishimura et al., 1999; Ó Cofaigh et al., 2014).

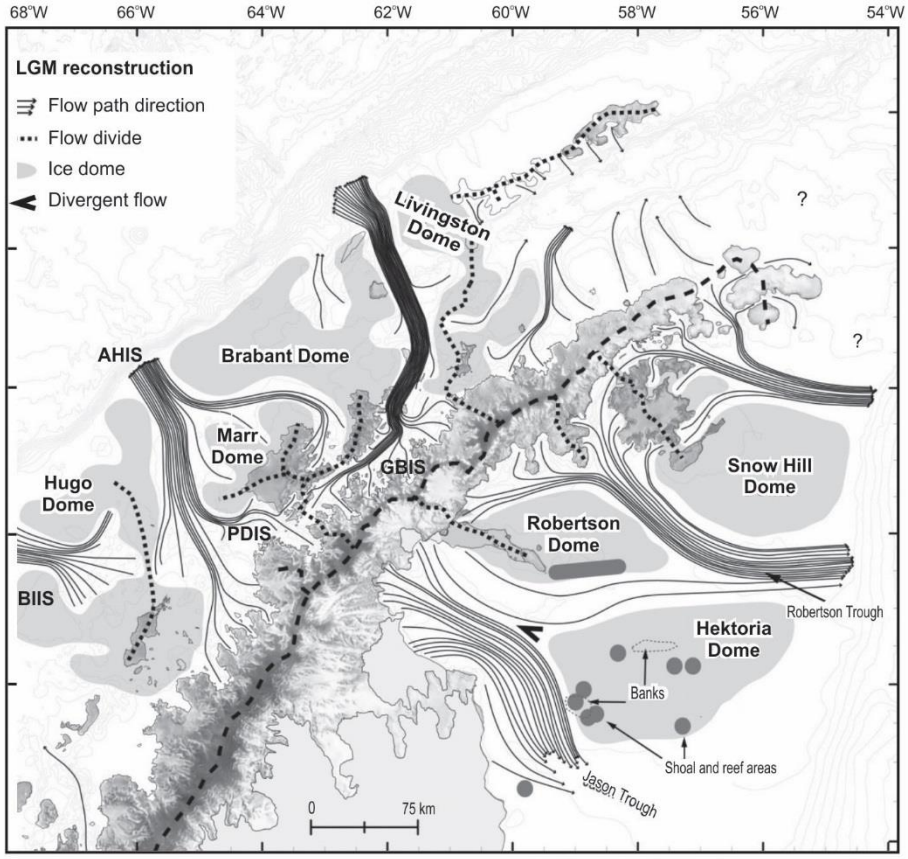

Figure 2.2 LGM ice sheet reconstruction for the northwestern and northeastern Antarctic Peninsula, showing inferred palaeo-ice flow directions and location of ice domes (Anvers-Hugo Ice Stream (AHIS), Biscoe Island Ice Stream (BIIS), Palmer Deep Ice Stream (PDIS) and Gerlache and Boyd Strait Ice Stream (GBIS)) (after Lavoie et al., 2015).

2.2.2. Modern climate and oceanography

The AP extends to 66°22'S, north of the Antarctic Circle, and has a relatively warm climate compared to the rest of continental Antarctica, with air temperatures exceeding 0°C at sea level over the summer (Vaughan et al., 2003). The WAP and eastern AP (EAP) experience different climatic conditions. The WAP has a maritime climate, making it relatively warmer (~7°C) than locations at an equivalent latitude on the EAP, which experiences a continental climate (Martin and Peel, 1978; Vaughan et al., 2003). The WAP experiences high snow accumulation rates, with a high rate of snow accumulation delivered by prevailing westerlies and associated cyclonic systems, and precipitation derived from the Bellingshausen Sea (Turner et al., 1995; Domack et al., 2003; Vaughan et al., 2003). The high snow accumulation rates on the WAP produce a relatively low altitude equilibrium (snow) line, compared to the EAP, where snow accumulation rates are lower (Domack et al., 2003). The El Niño/Southern Oscillation (ENSO), the Southern Annular Mode (SAM) and the Amundsen Sea Low influence the AP climate, including precipitation, temperature and atmospheric circulation

patterns, on interannual scales (Turner, 2004; Raphael et al., 2016; Turner et al., 2017; Paolo et al., 2018).

Antarctic station records indicate that major atmospheric warming of the AP took place between 1951 and 2001 (Vaughan et al., 2003; Henley et al., 2019). The mean warming recorded over the 20th century was 3.7±1.6°C, higher than that of other Antarctic continental regions and the rate of global warming (Vaughan et al., 2003). Several interlinked processes have been suggested to explain this warming, including the strength and location of low-high-latitude teleconnections, ozone depletion, sea ice loss and an increase in the strength of the westerly winds (Thompson and Solomon, 2002; Marshall et al., 2006; Turner et al., 2013; Turner et al., 2016). To date, the rapid warming observed over the twentieth century has not continued into the twenty-first century, with a plateau in atmospheric warming between 1999 and 2014 associated with the natural internal variability of the regional atmospheric circulation (Turner et al., 2016).

The near-surface ocean circulation of the central WAP includes a northeast flowing current on the outer continental shelf, driven by the Antarctic Circumpolar Current (ACC) and a southwest flowing current along the AP coast, the Antarctic Peninsula Coastal Current (APCC) (Moffat and Meredith, 2018). The APCC is driven by meltwater discharge and downwelling winds at the AP coast (Moffat et al., 2008; Moffat and Meredith, 2018). In places, the southern boundary of the ACC extends to the continental shelf edge of the AP and promotes upwelling of relatively warm and nutrient-rich Circumpolar Deep Water (CDW) (Hofmann et al., 1996; Martinson et al., 2008; Moffat and Meredith, 2018). CDW is generally split into upper CDW (UCDW; low oxygen and high nutrient concentrations) and lower CDW (LCDW; high salinity) (Orsi et al., 1995). On the AP shelf, CDW underlies Antarctic surface water (AASW) (Smith et al., 1999; Klinck et al., 2004; Meredith et al., 2008). There is a seasonal change in WAP shelf water mass structure (Smith et al., 1999). In the winter, cooling produces a deep thick AASW layer with temperatures near freezing (Smith et al., 1999; Meredith et al., 2008). Over the spring and summer, ice melt contributes fresh water to the AP shelf producing a seasonal pycnocline, with a thin (20-30 m) relatively fresh and warm surface layer (Smith et al., 1999). A remnant layer of the deep winter mixed layer (termed Winter Water) undercuts this summer surface water mass, this is gradually eroded over the summer as it is warmed from above and below (Hofmann and Klink, 1998; Meredith et al., 2008). As the summer progresses the pycnocline breaks down because of decreased warming and intensified storms (Hofmann and Klink, 1998; Smith et al., 1999).

The continental shelf bathymetry and small ocean eddies control the delivery of CDW on to the continental shelf and it's flow towards the ice sheet margin, whilst the volume of CDW intrusions is controlled by the strength of winds that drive the ACC (Walker et al., 2007; Thoma et al., 2008; Dinniman et al., 2011, 2012; Steig et al., 2012; Moffat and Meredith, 2018). The flux of CDW varies over time and is linked to westerly wind stresses over the continental slope, which is in turn linked to ocean/atmosphere variability in the Central Pacific Ocean (ENSO) and the SAM index (Jacobs, 2006; Steig et al., 2012; Paolo et al., 2015; 2018). CDW is modified (M-CDW) as it crosses the Antarctic continental shelf, as it is cooled and freshened by mixing with overlying AASW (Smith et al., 1999; Klinck et al., 2004; Martinson et al., 2008; Meredith et al., 2008). Upwelling of nutrient-rich CDW promotes diatom-dominated productivity and thus has an important impact on the AP ecosystem (Prézelin et al., 2000). Intrusions of warm CDW are considered to be the most important process for driving recent ice shelf and tidewater glacier retreat along the Pacific margin of APIS, West Antarctic Ice Sheet (WAIS) and East Antarctic Ice Sheet (EAIS) (Pritchard et al., 2012; Cook et al., 2016; Paolo et al., 2018).

2.3. Reconstructing ice sheet retreat and palaeoenvironmental conditions following the LGM

2.3.1. Sediment archives of ice sheet retreat

During the LGM the Antarctic Ice Sheet (AIS) extended to, or close to, the continental shelf break around much of its coastline (Fig. 1.1a) (RAISED Consortium, 2014). The sedimentary archives deposited during ice stream advance, and the subsequent deglaciation, provide an important record of past ice sheet behaviour that can be used to understand the processes active during ice sheet advance, as well the controls on grounding line retreat (Ó Cofaigh et al., 2014). Antarctic shelf sediments typically comprise a three part sedimentary sequence, representing the transition from subglacial (soft and stiff deformation tills) to seasonally open marine (biogenic-rich muds) conditions (e.g. Pudsey et al., 1994; Anderson, 1999; Domack et al., 1999; Evans et al., 2005; Heroy and Anderson, 2005; Heroy and Anderson, 2007). The change from subglacial to open marine sediments is often separated by a transitional sediment facies, representing the retreat or lift off of the ice sheet grounding line. Transitional sediment facies have been shown to be highly variable and reflect a range of processes active in grounding line proximal to distal settings (Evans et al., 2005). Powell (1984) proposed eight depositional regimes within transitional glaciomarine environments, predominantly controlled by combinations of three variables; (1) type of glacial ice source (ice sheet or valley glacier); (2) glacier thermal regime; and (3) type of glacier front (ice shelf vs. tidewater margin). Within

each regime, the rate of grounding line retreat, water depth, long and short-term grounding line oscillations, ocean current velocities, re-sedimentation processes and subglacial meltwater discharge, exert significant control on sedimentation and on the resulting sedimentary record (Powell, 1984). Eyles et al. (1985) highlighted the importance of basin margin relief, ice flow dynamics, seafloor bathymetry and the distance between the depositional site and grounding line for controlling the characteristics of transitional sediments. These ideas have subsequently been built upon by numerous workers, resulting in various conceptual models to help describe ice sheet-shelf sedimentation and aid the interpretation of the geological record (e.g., Alley et al., 1989; Powell et al., 1996; Powell and Alley, 1997; Domack and Harris, 1998; Domack et al., 1999; Howat and Domack, 2003; Prothro et al., 2018; Smith et al., in prep). Despite this progress, contemporary ice sheet grounding lines remain one of the least studied environments on Earth (cf. Powell et al., 1996), which is largely due to the logistical challenges associated with direct access, especially where large fringing ice shelves occur. The dearth of contemporary observations, together with the complex and often heterogeneous nature of transitional sediments (both temporally and spatially) deposited on the Antarctic shelf, mean that transitional sediment facies and their association with key processes and depositional environments (e.g. presence/absence of an ice shelf or grounding line proximity) are poorly understood. Understanding the full range of processes and the controls on sediment variability in the transitional environment, is essential if we are to utilise the geological record to accurately reconstruct palaeo-ice stream retreat and build reliable analogues between these and modern day ice streams and marine terminating glaciers. Furthermore, recognising the depositional environment of sediments within a transitional setting is important for selecting appropriate horizons for radiocarbon dating. Transitional sediments are assumed to represent the onset of glaciomarine sedimentation following the retreat of grounded ice and therefore radiocarbon dates from these sediments are used to date the retreat of grounded ice over a core site. Without a clear understanding of the variability in transitional sediment facies and associated depositional environments it is difficult to ensure that sediments representing grounding line retreat are correctly identified.

2.3.2. Chronological tools and limitations

A fundamental requirement of palaeoenvironmental reconstructions is to place them in a robust chronological framework. This allows key questions about the timing, rates and drivers of retreat to be answered. As outlined in the previous section, attempts to date ice sheet retreat in Antarctic sedimentary sequences ideally targets the contact between subglacial and transitional sedimentary units as this provides a minimum date for grounding line retreat

(Heroy and Anderson, 2007). Accelerator Mass Spectrometry (AMS) ^{14}C dating of calcareous (micro-)fossils are considered to produce the most reliable ages (e.g. Andrews et al., 1999; Heroy and Anderson, 2005, 2007; Hillenbrand et al., 2010a; Ó Cofaigh et al., 2014) and there is consensus within the community that if calcareous foraminifera are present within the horizons of interest, these are preferentially dated. However, the overall lack of calcareous (micro-)fossils in Antarctic sediments deposited since the LGM means that alternative dating methods are often utilised (Licht et al., 1998; Andrews et al., 1999; Heroy and Anderson, 2007; Hillenbrand et al., 2010a, 2010b; Smith et al., 2011). In the absence of calcareous (micro-)fossils, deglacial ages are often obtained by dating the acid insoluble organic matter (AIO) fraction of (bulk) sediments (Licht et al., 1999; Andrews et al., 1999). However, AIO ages are often contaminated by reworked fossil carbon that has been eroded and transported by ice streams and outlet glaciers (Andrews et al., 1999; Hillenbrand et al., 2010a). This problem is particularly acute in transitional glacier-proximal sediments where the input of modern carbon (from marine phytoplankton) is very low and the mainly terrigenous sediment flux from the glacier is very high. Traditionally, this error is corrected by subtracting seafloor surface AIO ages from down-core AIO ages. This correction assumes that the input of reworked fossil carbon has remained constant through time (Andrews et al., 1999), which although questionable, has been demonstrated to hold-true in certain settings (e.g. Amundsen Sea Embayment; Smith et al., 2011; 2014). A conclusion from previously published work has been that although the error of AIO-based deglacial chronologies can be high, reliable ages can be obtained through careful sample selection based on detailed stratigraphic information, provenance analysis of the fine-grained detrital fraction and measurements of sediment organic content (Andrews et al., 1999; Hillenbrand et al., 2010a; Smith et al., 2011, 2014).

To overcome the limitations associated with dating the AIO fraction, several studies have focussed on alternative dating methodologies such as compound specific ^{14}C dating (see Ohkouchi et al., 2003; Yokoyama et al., 2016), although this technique has not been universally applied. Progress has also been made by combusting sediments at gradually increasing temperatures to thermally break down the bulk organic matter (Ramped PyrOx method; Rosenheim et al., 2008). Here, bulk sedimentary organic matter is split into younger, more volatile components and older, more diagenetically stable components using stepped-temperature combustion (Rosenheim et al., 2008). The younger, more volatile components are assumed to consist of autochthonous algal-derived organic matter from the water column above the core site and this has been reflected in radiocarbon ages that are comparable to those obtained from calcareous (micro-)fossils (Rosenheim et al., 2008; Subt et al., 2016).

2.3.3. Glacial history of Anvers-Hugo Trough

In comparison to other well-studied palaeo-ice stream troughs on the WAP shelf (e.g. Marguerite Trough), the glacial history of the AHT is poorly documented. The existing geophysical, sediment core and chronological data sets for AHT are summarised below. Post-LGM/Holocene environmental changes are also considered.

2.3.3.1. Geophysical record

Primary acoustic profiles over the AHT demonstrated that the seabed of inner-AHT is characterised by outcropping bedrock, whilst the mid and outer-shelf seabed consists of prograding sequences of glacigenic sediments; deposited during multiple episodes of ice sheet advance (Larter and Barker 1989; Pudsey et al., 1994). The outcropping bedrock of the inner shelf, including the sill of Palmer Deep, features crescentic scours, anastomosing channels and northward-shoaling valleys, eroded by subglacial water flow over multiple glaciations (Domack et al., 2006; Larter et al., 2019). These features have been associated with a sub-glacial lake hosted within Palmer Deep basin that formed during, or prior to, the LGM and experienced several draining events (Domack et al., 2006; Larter et al., 2019). A recent study by Larter et al. (2019) using the newly acquired swath multibeam and sub-bottom profiler data collected during JR284, demonstrated that meltwater availability likely facilitated fast ice stream flow and controlled shear margin positions within AHT. The seafloor geomorphology of the mid and outer trough is dominated by mega-scale glacial lineations (MSGLs), highly elongated parallel ridges and grooves formed during ice streaming, and grounding zone wedges (GZWs), asymmetrical accumulations of sediment deposited at the grounding line of ice streams during still stands during episodic retreat (Pudsey et al., 1994; Evans et al., 2004; Heroy and Anderson 2005; Domack et al. 2006; Livingstone et al., 2012; Larter et al., 2019). The extension of MSGLs to the shelf break provides strong evidence that the APIS extended to this position during the LGM (Larter et al., 2019). Following deglaciation, icebergs gouged scour marks into sediment shallower than ~590 meters below sea level (mbsl) and overprinted glacial bedforms in certain places (Pudsey et al., 1994; Heroy and Anderson, 2005). The bathymetric high surrounding Hugo Island, west of AHT, and extending to the shelf break, is thought to have hosted a grounded ice dome during the LGM (Fig. 2.2) (Lavoie et al., 2015). Ice domes are additionally proposed to have been present to the east of AHT, with the Marr Dome sitting over Anvers Island and the Brabant Dome sitting between the Anvers and Smith Trough (Lavoie et al., 2015). These ice domes would have constrained and directed ice flow within the AHT (Fig. 2.2) (Lavoie et al., 2015).

2.3.3.2. Sedimentary and chronological record

The deglacial history of AHT is poorly constrained. Available chronological data suggests that deglaciation of the outer shelf started at ~16.4 calibrated kyr BP (calibrated years before present (cal. yr BP where BP is 1950) unless otherwise stated) (Fig. 2.1) (Pudsey et al., 1994; Nishimura et al., 1999; Domack et al., 2001; Yoon et al., 2002; Heroy and Anderson, 2005, 2007; Ó Cofaigh et al., 2014). By ~13.18 and ~8.40 cal. kyr BP, the Palmer Deep and the Gerlache Strait on the inner shelf were ice free (Fig. 2.1) (Harden et al., 1992; Domack et al., 2001, 2006). In a compilation of deglacial ages by Livingstone et al. (2012), deglaciation of the mid-shelf occurred by ~11.2 cal. kyr BP. However, given that age-data from Palmer Deep (Fig. 2.1) indicates ice free conditions as early as 12.85 cal. kyr BP, and possibly as early as 13.18 cal. kyr BP (Domack et al., 2001), this implies one of two things: (1) Current data does not accurately constrain ice sheet retreat across the mid-shelf, or (2) that the age-model for Palmer Deep is erroneous. A third scenario involves deglaciation of the inner shelf prior to the mid-shelf but this seems glaciologically implausible. Based on a retreat model that omits the deglacial age from Palmer Deep, calculated retreat rates are 2-15 m yr^{-1} across the outer shelf, and increasing to 47 m yr^{-1} on the inner most shelf (Livingstone et al., 2012). This increase in retreat rate has been attributed to the reverse slope morphology driving grounding line instability (Livingstone et al., 2012; Ó Cofaigh et al., 2014), although given the sparsity of available data, it is possible that periods of more rapid retreat or still-stands are not captured. As such, there is considerable scope for additional work to improve the deglacial chronology of AHT. Furthermore, ~50% of the available published deglacial ages rely on dating the AIO fraction of sediments that might carry considerable uncertainties (Ó Cofaigh et al., 2014).

2.3.3.3. Modelled LGM glacial history

Whole ice sheet-scale numerical models are typically too coarse (20 km) to accurately resolve individual ice stream systems such as AHT (Whitehouse et al., 2012). Golledge et al. (2013) present a higher resolution model (PISM; 5 km) that generally matches the ice flow direction inferred from geophysical evidence for the WAP. However, modelled flow lines do not reproduce the westward flowing Biscoe Island Ice Stream or the convergent Palmer Deep Ice Stream (Fig. 2.2), whereby the Palmer Deep Ice Stream is an inner-shelf branch of the Anvers-Hugo Ice Stream (AHIS) (e.g. Domack et al., 2006). Additionally, the model fails to reproduce the initial north-easterly flowing onset of the Gerlache and Boyd Strait Ice Stream (Fig. 2.2) (e.g. Canals et al., 2000; Evans et al., 2004; Amblas et al., 2006). These mismatches occur where the model underestimates the importance of topography for governing ice stream flow. This could result from an overestimation of ice thickness, which suppresses the effect of

topography (a consequence of using topographic grid that has become progressively smoothed during lower-resolution spin-up runs prior to the equilibrium simulation), or a model resolution that is too fine to capture the dynamic of ice streams of this size (Golledge et al., 2013). Furthermore, Golledge et al. (2013) notes that mapped bedforms might only provide a last snap-shot of grounded ice flow prior to deglaciation (e.g., Graham et al., 2009), and thus a discrepancy between flow directions inferred from marine geophysical and multibeam data and true flow-lines of the LGM ice sheet may exist. However, in the case of the Biscoe/Palmer-Deep/ Gerlache ice streams, subglacial bedforms on the inner shelf are in bedrock (Domack et al., 2006), and this record of flow likely reflects the LGM configuration rather than merely a footprint of ice flow during the last phases of deglaciation.

2.3.3.4. Post LGM environmental changes on the western Antarctic Peninsula and within Anvers-Hugo Trough

As noted above, the inner shelf areas of WAP were largely ice free by the early Holocene although this varies locally (see Ó Cofaigh et al., 2014). Piston cores recovered from (Ocean Drilling Program) ODP Site 1098 (Palmer Deep; Fig. 2.1) in innermost AHT indicate that the LGM diamicton was deposited prior to 13.18 cal. kyr BP, with the onset of high primary production and iceberg rafting after 13.18, to 11.46 cal. kyr BP (Domack et al., 2001). This period is characterised by high sea-surface temperatures (SST) (using the TEX_{86} proxy; Shevenell et al., 2011; Etourneau et al., 2013), high glacial discharge ($\delta^{18}O_{diatom}$ record; Pike et al., 2013) and the deposition of laminated diatomaceous oozes (Domack et al., 2001; Sjunneskog and Taylor, 2002; Taylor and Sjunneskog, 2002). Laminated diatomaceous oozes have been described in several deglacial sedimentary facies around Antarctica, often occurring directly above or within subglacial or transitional sediments (Leventer et al., 2002; Maddison et al., 2005; Stickley et al., 2005; Leventer et al., 2006). The oozes have been interpreted to reflect periods of high productivity and rapid export to the sea-floor, thought to be associated with meltwater induced stratification and nutrient delivery (i.e., iron fertilisation) within a calving bay re-entrant (Leventer et al., 2002). However, given that grounding line retreat within AHT is poorly constrained, the link between the onset of enhanced productivity and the drivers of such productivity (e.g. formation of a calving bay setting) is difficult to resolve. According to Domack et al. (2001) this period of high productivity was immediately followed by period of climatic cooling beginning at 11.46 cal. kyr BP and ending at 9.07 cal. kyr BP. However, the timing and structure of this cool interval is not consistent between proxies. For example, glacial discharge decreases between 12.1 and 11.5 cal. kyr BP before increasing between 11.5 and 9.0 cal. kyr BP (Pike et al., 2013). Increases in glacial discharge are broadly

in phase with changes in SST, which show relatively high SSTs until ~9 cal. kyr BP (Shevenell et al., 2011).

From 9.07 to 3.36 cal. kyr BP, Domack et al. (2001) suggest a period of climatic warming (mid-Holocene hypsithermal (MHH)). However, the timing and expression of climatic changes during this time-interval vary depending on the proxy analysed (see Bentley et al., 2009 and references therein). In a comprehensive review of Holocene palaeoclimatic records from the AP, Bentley et al. (2009) recognised two warm periods, the first during the early Holocene (11-9.5 cal. kyr BP) and the second, during the mid-Holocene (MHH; 4.5-2.8 cal. kyr BP). The SST record from Palmer Deep (Shevenell et al., 2011) shows an overall cooling of ~3–4 °C throughout the Holocene which is consistent with a strong reduction and stabilisation of glacial discharge until 3.6 cal. kyr BP, prior to enhanced variability and a second period of strong melting during the late Holocene (Pike et al., 2013). The James Ross Island (JRI) ice core, EAP (Fig. 1.1b) indicates a relative cooling of ~1 °C from ~9.20 to 5.0 cal. kyr BP, slightly warmer temperatures from 5.0 to 3.0 cal. kyr BP (corresponding to the MHH), and a second gradual cooling of ~1 °C throughout the late Holocene. The JRI ice core also shows warming during the past 500 years (Mulvaney et al., 2012). A more recent TEX-based SST record from Palmer Deep using a revised calibration ($TEXL_{86}$; Etourneau et al., 2013) shows broadly the same trend as Shevenell et al. (2011), although the amplitude of changes are much lower. This record indicates warmer SSTs between 10.0-7.0 cal. kyr BP, a cooling trend from 7.0 to 3.8 cal. kyr BP, following by an increase in variability from 3.8 cal. kyr BP and a general shift to cooler conditions (Etourneau et al., 2013). This overall structure is consistent with a multi-proxy marine record from Marguerite Bay (Fig. 1.1b) (Peck et al., 2015) that indicates cooling from 6.9-4.2 cal. kyr BP, reflected in an increased abundance of ice-tolerant diatom species and a decreased flux of phytodetritus to the sea floor. This is associated with decreased frontal melting of glaciers and associated primary productivity (Peck et al., 2015). A similar signal is recorded at nearby Neny Fjord (Fig. 1.1b), where a relatively high proportion of cool-water associated species, indicative of late summer to autumn productivity, is thought to be associated with persistent sea-ice through the spring and summer (Allen et al., 2010).

The increased climate variability during the late Holocene (from ~4.2 cal. kyr BP to present) is seen in multiple proxy records (Domack et al., 2001; Sjunneskog and Taylor, 2002; Taylor and Sjunneskog, 2002; Shevenell et al., 2011; Etourneau et al., 2013; Pike et al., 2013). Diatom abundance and species assemblage records from the Palmer Deep and Lallemend Fjord, show that these regions experienced cool neoglacial conditions with more extensive sea ice from 3.7

and 3.9 cal. kyr BP, respectively (Shevenell et al., 1996; Domack et al., 2001; Taylor et al., 2001; Sjunneskog and Taylor, 2002; Taylor and Sjunneskog, 2002; Etourneau et al., 2013). During the same time (from ~4.2 cal. kyr BP to present), Marguerite Bay experienced reduced glacial meltwater discharge, increased sea ice cover and relatively low SSTs (Peck et al., 2015).

The climatic drivers of ice sheet retreat and Holocene climate variability are complex and often contradictory (cf. Ishman and Sperling, 2002; Shevenell and Kennett, 2002). Ice sheet retreat is typically associated with sea-level rise, together with oceanic and atmospheric forcing. A retrograde slope may also introduce positive feedbacks, whereby ice retreat into deeper inner shelf areas exposes more of ice sheet base to warmer water (e.g., Smith et al., 2011). Deglaciation of the APIS and AIS more generally, has been attributed to both global (sea-level) and more regional drivers, such as increasing atmospheric oceanic temperatures, and it is likely that it was the interplay between these variables which drove grounding line retreat in AHT. Thus initial post-LGM retreat of AHT was likely caused by raising global sea-level associated with deglaciation of Northern Hemisphere ice sheets after ~21 kyr (Denton et al., 1991). Coeval with raising global sea-level, ice core records indicate that warming of West Antarctica began around 20 kyr (WAIS Divide Project Members, 2013) attributed to orbital forcing as well as potential bi-polar see-saw effects (Blunier et al., 1998; Anderson et al., 2009; Steig and Alley, 2002; Weber et al., 2011; WAIS Divide Project Members, 2013). In this context, a southward shift of the SHWW in parallel with well-documented shifts of the intertropical convergence zone (Schneider et al., 2014) has been inferred in numerous reconstructions (Anderson et al., 2009; Kaiser and Lamy, 2005; Buizert et al., 2018). This is thought to have driven enhanced Southern Ocean upwelling, a rise in atmospheric CO_2 (Anderson et al., 2009) and further warming of Antarctica until ~14.5 ka (Pedro et al., 2016; WAIS Divide Project Members, 2015). Support for intensified CDW advection along the Pacific margin of Antarctica during the early Holocene (at least 10.4-7.5 cal. yrs BP) comes from a multi-proxy based record from Pine Island Bay on the inner shelf of the eastern Amundsen Sea Embayment (Hillenbrand et al., 2017). From ~7.0 cal. yr BP, Peck et al. (2015) suggest a decreasing influence of CDW and greater sea-ice formation, linked to a northward shift in the SHWW. Warmer atmospheric temperatures recorded in the JRI ice core (Mulvaney et al., 2012) during this interval, indicate that the climate of WAP and EAP might have been driven by different climate forcing. Simplistically, it would suggest that the climate of WAP was largely forced by the ocean, whilst the EAP was more susceptible to atmospheric warming (Peck et al., 2015). Cooling and increased climate variability during the late Holocene (after 4.2 cal. yr BP) have been attributed to the increasing influence of the ENSO and waning of the

SHWW influence on AP climate (Etourneau et al., 2013; Pike et al., 2013). Presently, the onset of modern warming is poorly resolved in most available proxy records. The JRI ice core shows warming during the past 500 years (Mulvaney et al., 2012), which is broadly coincident with a trend to increasing glacial discharge observed in the Palmer Deep record (Pike et al., 2013).

2.3.3.5. Summary of previous research into the glacial history of Anvers-Hugo Trough

In summary, extensive geophysical surveying and mapping of seabed features (e.g. MSGL) provide strong evidence that the APIS extended to the shelf edge during the LGM and possibly during previous glacial periods (Pudsey et al., 1994; Evans et al., 2004; Heroy and Anderson 2005; Domack et al. 2006; Livingstone et al., 2012; Larter et al., 2019). The presence of GZWs within AHT are indicative of episodic retreat following the LGM (Heroy and Anderson, 2005; Domack et al. 2006; Livingstone et al., 2012; Larter et al., 2019). On the inner-shelf, crescentic scours, anastomosing channels and northward-shoaling valleys, have been associated with a sub-glacial lake hosted within Palmer Deep basin that formed during, or prior to, the LGM and experienced several draining events (Domack et al., 2006; Larter et al., 2019). Meltwater sourced from within Palmer Deep likely facilitated fast ice stream flow and controlled shear margin positions within AHT (Larter et al., 2019). In contrast to the geophysical record, the deglacial chronology of AHT is poorly constrained. Available chronological data suggests that deglaciation following the LGM started at ~16.4 cal. yr BP (Heroy and Anderson, 2007), with deglaciation of the inner shelf by ~13.18 and ~8.40 cal. kyr BP, for the Palmer Deep and the Gerlache Strait, respectively (Harden et al., 1992; Domack et al., 2001, 2006). In a compilation of deglacial ages by Livingstone et al. (2012), deglaciation of the mid-shelf occurred by ~11.2 cal. kyr BP (Livingstone et al., 2012), although this is incompatible with earlier deglaciation of the inner shelf, prior to ~13.18 cal. kyr BP. Issues with the current deglacial chronology may result from a lack of core sites, the grouping of transitional sediment facies and, as a result, radiocarbon dating sediments deposited at an unknown time after grounding line retreat, as well as reliance on AIO dating without adequate investigation into its reliability. A period of high productivity is observed at Palmer Deep following deglaciation and is associated with meltwater induced stratification and nutrient delivery within a calving bay setting. However, the lack of a concise deglacial chronology for AHT makes it difficult to understand the link between deglaciation and the onset of enhanced productivity at Palmer Deep, including if and when a calving bay was established. Improving our understanding of the link between deglaciation and primary productivity, will provide an insight into the environmental impacts of future ice sheet change.

More generally, the grounding line of ice streams remain poorly understood due to the lack of modern grounding line observations and a reliance on conceptual models that may not necessarily reflect the variability in grounding line processes and environments that exist in natural settings. Correctly identifying the environment within which transitional sediments are deposited is of particular importance when sediments are targeted for radiocarbon dating, or when a link between the rate and style of ice stream retreat and the nature of the grounding line or ice margin environment (e.g. presence of absence of an ice shelf), is deemed important. The extensive network of sediment cores recovered for this study will allow variability in transitional sediment facies to be investigated.

2.4. Research questions

The presented literature review outlined key gaps in our knowledge of transitional sediment facies, as well the deglacial and palaeoenvironmental history of AHT. This includes (1) a lack of detailed information about the variability in processes and depositional environments that can occur at a retreating ice stream grounding line and the signal these processes and environments leave in the sedimentological record. (2) The link between grounding line retreat in AHT and enhanced primary productivity, as observed in Palmer Deep ODP Site 1098, is poorly understood. This is hindered by a third knowledge gap; (3) the timing of deglaciation, especially the outer and mid-shelf, is poorly constrained due to lack of core sites and reliance on AIO dating. The age and significance of GZWs in AHT is also not well constrained, yet their formation is likely to exert significant influence on the sedimentary signature seaward of these features. These key knowledge gaps are investigated within this thesis under three key research questions:

I. What controls the variability in sediments at a retreating ice stream grounding line? (Chapter 4)
II. What are the palaeoenvironmental conditions of the AHT during and after deglaciation? (Chapter 5)
III. What are the timings of environmental change(s) within AHT? (Chapter 6)

2.5. Thesis structure

Chapter 3 will present the methodology used to address the key thesis objectives. The data are first used to understand sediment variability at a retreating grounding line using multi-proxy sediment core analysis to identify the sedimentary units deposited in AHT during deglaciation following the LGM (Ch. 4). Particular focus will be paid to investigating the variability in

sediments deposited in the transitional (grounding line proximal to distal) environment. The dearth of contemporary observations of ice sheet grounding lines, together with the complex and often heterogeneous nature of transitional sediments (both temporally and spatially) deposited on the Antarctic shelf, means that detailed information about key processes can be overlooked. In this study, detailed analysis of transitional sediments will be used to identify spatial variability in the distribution of transitional sediments and identify if this is related to the rate of grounding line retreat (including still-stands), presence or absence of an ice shelf, or variable internal/external dynamics (e.g. variations in marine processes). Data presented and analysed in Chapter 4, in addition to new absolute diatom abundance (ADA) and species assemblage data, will be used to investigate the palaeoenvironmental conditions of the AHT over and following deglaciation in order to assess the link between deglaciation and primary productivity (Ch. 5). Finally, new radiocarbon dates from AHT sediment cores will be used to (i) constrain the timing of grounded ice retreat following the LGM, and (ii) constrain the timing of key palaeoenvironmental changes following deglaciation (Ch. 6). The key findings of this thesis will be summarised in Chapter 7 and will include reflection on the limitations of this study and perspectives for future work.

Chapter 3

3. Data sets and methods

3.1. Primary data set collection

Extensive marine geological and geophysical data was collected prior to this PhD work during RRS *James Clark Ross* cruise JR284 in January 2014. Detailed bathymetric data was collected using the hull-mounted Kongsberg-Simrad EM122 and a TOPAS PS018 parametric echo sounder was used to collect sub-bottom profile data (Fig. 3.1) (Larter et al., 2019). The bathymetric and sub-bottom profiler data were used to select core sites. Sediment cores were recovered using the British Antarctic Survey (BAS) wide-diameter (11 cm) gravity corer (GC) along two transects, one running along and one across AHT (Fig. 3.1 and Table 3.1). Cores were collected in 3, 6 or 9 m barrels and were split into ~100 cm sections once on board the ship. Box cores (BC) were additionally recovered at several GC sites in order to ensure surface sediments were sampled. The coring strategy primarily focussed on prominent GZWs; with three pairs of sediment cores recovered from the stoss and lee sides of three wedges. Cores GC703 and GC702 were collected perpendicular to the along trough core transect in order to assess across trough sediment variability (Fig. 3.1). Sediment cores are analysed using visual core description, X-radiographs, and a multi-proxy approach (water content, shear strength, grain size distribution, clay mineral analysis, magnetic susceptibility, density, contents of biogenic opal, total organic carbon (TOC) and calcium carbonate ($CaCO_3$)). Quantitative assessment of ADA and diatom species assemblage was additionally carried out on two sediment cores (GC695 and GC697). Twenty-seven new radiocarbon dates were obtained from calcareous (micro-) fossils, the AIO fraction of sediments and Ramped PyrOx ^{14}C dating. With the exception of clay mineral analysis and data acquired during cruise JR284, all presented sediment core analysis and acquisition of data were carried out as part of this PhD. Detailed methodology and justification of techniques utilised for this study are outlined below.

3.2. Geophysical data

Detailed bathymetry was collected using the hull-mounted Kongsberg-Simrad EM122 which emits soundings within a beam, with up to 432 beams per swath, with a normal operating frequency of 12 kHz. The spatial resolution is 10-70 m, depending on the water depth. The swath width is six times the water depth, to up to 4000 mbsl, when the full beam angle of 75° on the port and starboard side is utilised. The bathymetric data set utilised for this study was processed and gridded for Larter et al (2019). The bathymetric data set collected on JR284 was

gridded alongside pre-existing multibeam data sets, collected on RVIB *Nathaniel B. Palmer*, previous cruises of RRS *James Clark Ross* and HMS *Protector* (Fig. 3.1) (Anderson, 2005; Domack, 2005; Lavoie et al., 2015). Bathymetric data sets were mapped and analysed in ArcGIS (ArcMap). Within ArcMap, bathymetric data was manipulated to aid analysis through applying a colour ramp and Hillshade. 3D Analyst 'tools' were used to identify and analyse trough bathymetry and individual bedforms, through creating bathymetric profiles.

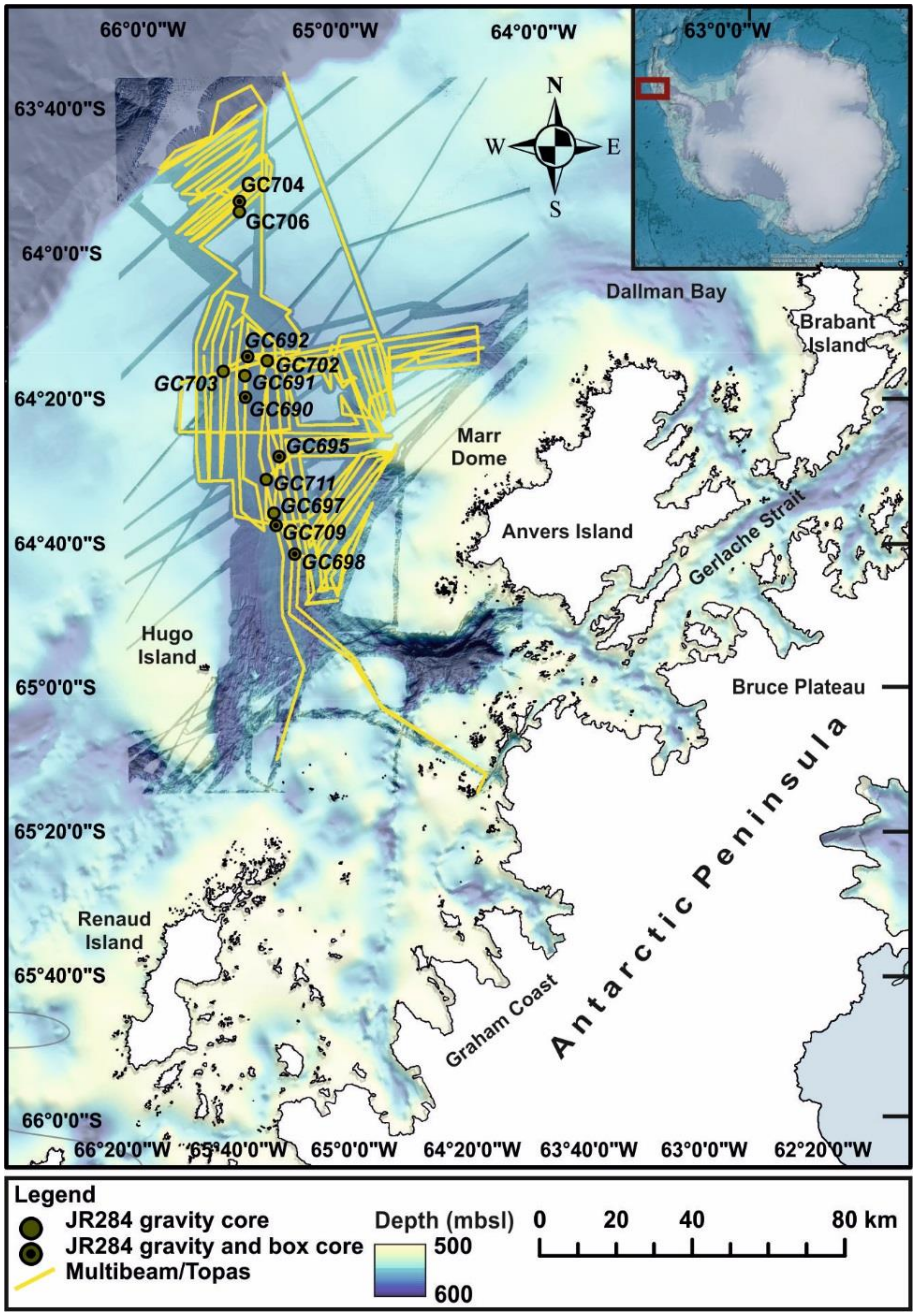

Figure 3.1: Map of the Antarctic Peninsula and Anvers-Hugo Trough with JR284 gravity core sites (green points), box core sites (black points) and the JR284 cruise track (yellow line).

3.3. Geological data

3.3.1. Core description and lithological units

Cores were split along their longitudinal axis, producing a working half and an archive half. The working half was sampled for multi-proxy analysis (water content, shear strength, clay mineral analysis, grain size analysis, analysis of biogenic opal, TOC and $CaCO_3$ content and quantitative assessment of ADA and diatom species assemblage) and for obtaining material for radiocarbon dating. Both the working and archive halves were photographed. For each core section, individual lithological units were measured and their texture (clay/silt/sand/gravel/diamicton), structure, colour and contacts between under/overlying lithological unit (sharp/gradational) were described. Initial determination of diatom abundance and species assemblages was carried out on a qualitative basis through smear slide analysis. Based on diatom abundance, sediments are defined as diatom bearing (15-30% diatoms), diatomaceous (30-50% diatoms), or were described as diatomaceous ooze (50-100%). Additional descriptors including trace (<2%), some (5%) or minor (10%) diatom content were also used.

Core ID	**Latitude (°)**	**Longitude (°)**	**Water depth (mbsl)**	**Core Recovery (m)**
GC690	-64.337167	-65.489500	584	6.08
BC689	-64.337167	-65.489500	584	0.34
GC691	-64.287333	-65.491500	604	4.10
GC692	-64.243000	-65.478000	578	4.73
BC693	-64.243000	-65.478000	577	0.32
GC695	-64.473833	-65.313000	629	6.74
BC696	-64.473833	-65.313000	628	0.30
GC697	-64.605000	-65.343333	583	7.24
GC698	-64.700000	-65.233333	607	6.34
BC699	-64.700000	-65.233333	605	0.33
GC702	-64.254500	-65.371833	560	4.93
GC703	-64.276667	-65.603500	564	3.86
GC704	-63.886833	-65.511333	475	4.17
BC705	-63.886833	-65.511667	476	0.40
GC706	-63.910833	-65.513833	453	2.38
GC709	-64.632333	-65.330333	556	3.59
BC710	-64.632333	-65.330167	555	0.26
GC711	-64.527333	-65.381333	614	5.88

Table 3.1: JR284 sediment core IDs, latitude, longitude, water depth (mbsl) and core recovery (m).

3.3.2. Physical properties and X-radiographs

Magnetic susceptibility (MS), density and p-wave velocity were measured on whole cores using a GEOTEK multi-sensor core logger (mscl) at the British Ocean Sediment Core Research Facility (BOSCORF, Southampton, UK). This data was plotted and analysed in GraphPad Prism 7. To refine lithological units and assess sedimentary structure in more detail, a sub-set of core sections were additionally X-rayed at Intertek NDT (Derby).

3.3.3. X-ray fluorescence analysis

Down core elemental data was collected on the archive half of sediment cores (GC711, GC698, GC695, GC697, GC691, GC692) using an ITRAX Core Scanner at the BOSCORF. This produces a high-resolution (2 mm), non-destructive profile of semi-quantitative element counts that can be used to assess palaeoenvironmental conditions. In addition to elemental data, the ITRAX Core Scanner produced an image of the core section and a 22 mm width X-radiograph down the length of the core. Elemental data was cleaned based on the data validity of the exported data set, which highlights erroneous data points typically at the end of core sections. This data is semi-quantitative because it is not measuring element concentration, rather element counts or element intensities. The basis of element selection and their application for reconstructing particular environmental conditions was based on Croudace and Rothwell (2015); e.g. Silicon/Titanium (Si/Ti) ratios are used as a semi-quantitative proxy for siliceous productivity. Data was analysed as raw element profiles and as element ratios. Element ratios help to avoid closed sum effects because the absolute counts received by the X-ray fluorescence (XRF)-detector will vary depending on the sediment composition (Rollinson, 1993; Weijden, 2002; Löwemark et al., 2011). For example, a high proportion of light elements that are outside the measuring range of the XRF-detector will reduce the absolute counts detected for all other elements, this is the case for sediments with a high organic content (Löwemark et al., 2011). Element counts are typically normalised to an element that represents the siliclastic component of sediment such as Titanium (e.g. Löwemark et al., 2011). Data plots were produced for ITRAX data using GraphPad Prism. Additionally, cluster analysis on ITRAX data was attempted in Multi-Variate Statistical Package (MSVP) v.3.1, in order to condense multiple element data sets into one plot, so to visualise the data and identify changes in palaeo-environmental conditions. This was particularly of interest over laminated oozes, where the high-resolution XRF data (2 mm) could identify the elemental composition of individual laminae. This work was eventually superseded by quantitative assessment of ADA and diatom species assemblage over the same stratigraphic intervals,

which provided quantitative data for assessing palaeo-environmental changes. Results of preliminary XRF data cluster analysis are presented in the thesis appendix (Appendix A).

3.3.4. Shear strength and water content

Shear strength and water content data was collected every 20 cm along each core. Sediment shear strength is used as an indication of sediment compaction, and is typically used in the identification of sediments deposited subglacially vs. sediments deposited seawards of the grounding line (e.g. Evans et al., 2005; Ó Cofaigh et al., 2005; Smith et al., 2009; Hillenbrand et al., 2012). Water content additionally indicates the degree of sediment compaction and can be used to identify units with a higher organic content (e.g. Evans et al., 2005; Hillenbrand et al., 2012). Shear strength was measured every 20 cm using a hand held shear vane. For the analysis of water content, 1 cm slices of sediment were taken and weighed (wet weight). The sediment was then freeze-dried and re-weighed to find the sediment dry weight. Water content was calculated by subtracting the weight of the dry sediment from the weight of the wet sediment and converted to a percentage.

3.3.5. Grain size analysis

Within glaciomarine settings, sediment grain size is typically used to identify the proximity of the sediment source (e.g., grounding line) but can also be used to identify sediment winnowing from ocean currents and input of ice rafted debris (IRD) (Powell, 1984; Light et al., 1999; Evans et al., 2005; Ó Cofaigh et al., 2005; Smith et al., 2011). Analysis of the contribution of gravel, sand and mud to sediments was determined through wet and dry sieving. In order to carry out this analysis 2 g of sediment was weighed out, and then sodium hexametaphosphate was used to disperse the sediment, which was wet sieved through a 63 μm sieve to remove any fine material. This was dried and one beaker of the fine sediment was retained for further analysis. The sediment >63 μm was dry sieved through a 2 mm and another 63 μm sieve in order to separate out gravel, sand and any remaining mud sized particles. The gravel and sand sized fractions were weighed and the weight of mud was derived from subtracting the cumulative weight of sand and gravel from the total weight. These values were converted to a percentage. The gravel content of sediments was additionally assessed through qualitative analysis of X-radiographs.

The grain size distribution of the fine fraction (63 μm) of sediments was determined using a Beckman Coulter LS 13 320 Laser Diffraction Particle Size Analyser. First, 20 ml of 20% Hydrogen Peroxide was added to each sample (0.5 g of sediment) in order to digest organic

matter. Samples were then placed in a hot water bath to aid digestion. For samples with very high organic matter content, this process was repeated several times until the reaction had completely ceased. Samples were then centrifuged and the supernatant liquid decanted. Distilled water was added and the centrifuge step was repeated. Prior to analysis, 2 ml of sodium hexametaphosphate was added to the sample to prevent flocculation. In order to assess the influence of biogenic silica on the <63 µm grain size analysis, it was removed from a sub-set of the samples using the method of Mortlock and Froelich (1989). 40 ml of 2 M sodium carbonate ($NaCO_3$) was added to each test tube. The samples were then placed in a hot bath at 80°C for a total time of five hours and were stirred every 30 minutes and shaken half way through. Samples were rinsed with nanopure water, placed in the centrifuge for 20 minutes at 400 rpm and decanted to remove $NaCO_3$. The last step was repeated three times to ensure that all $NaCO_3$ was removed. Sediment smear slides were used to ensure that all biogenic silica (diatoms) was removed prior to grain size analysis.

3.3.6. Clay mineral analysis

The clay mineral assemblage of sediments reflect the rocks from which they were sourced and can therefore be used to identify the source of sediments and reconstruct transport pathways (Hillenbrand and Ehrmann, 2001; Hillenbrand et al., 2009). The clay mineral assemblage of sediments was carried out at the Institute for Geophysics and Geology, University of Leipzig, Germany. The relative contents of chlorite, illite, smectite and kaolinite were determined from the <63µm fraction using x-ray diffraction following Ehrmann et al. (1992).

3.3.7. Biogenic opal, total organic carbon (TOC) and calcium carbonate ($CaCO_3$) content

Biogenic opal, TOC and $CaCO_3$ content are used in this study as proxies for primary productivity (e.g. Domack et al., 1999; Hillenbrand et al., 2010b; Hillenbrand et al., 2012; Smith et al., 2014). Biogenic opal content was measured using the automated leaching method of Müller and Schneider (1993). This data, as well as that for TOC and $CaCO_3$, were analysed at the Alfred Wegener Institute for Polar and Marine Science (AWI, Bremerhaven, Germany) during a research visit in August 2016. TOC and Total Carbon (TC) were analysed using a LECO CS-125 and Elemetar Vario EL III carbon-nitrogen-sulphur analyser, with an analytical error of 3% and 1% respectively. $CaCO_3$ was calculated using equation:

$$\boldsymbol{CaCO_3 = (TC - TOC) \times 8.3}$$

3.3.8. ^{14}C dating strategy

To ensure that the key glaciological and environmental changes are placed in a robust chronological framework a combination of traditional (^{14}C dating of AIO and foraminifera) and state-of-the art (Ramped PyrOx ^{14}C) dating techniques were employed in this thesis. Where preserved in sufficient quantities, calcareous foraminifera were preferentially targeted for dating. However, the overall lack of foraminifera in key horizons (i.e., sediments directly above subglacial facies) meant that age-data was also obtained from the AIO fraction. The reliability of AIO ages was assessed by performing paired foraminifera-AIO dating. In addition, the Ramped PyrOx ^{14}C method was also employed, because this technique can overcome contamination issues associated with dating the AIO fraction of sediments (see section 2.3.2). In total, twenty-seven new radiocarbon ages were acquired for this thesis; seven from benthic and planktonic foraminifera, thirteen from the AIO fraction of sediments and seven ages were obtained using the Ramped PyrOx ^{14}C method. All conventional ^{14}C ages were calibrated in Calib v.7.0.4, using the Marine13 calibration curve and a marine reservoir effect (MRE) of 1,230±100 yrs (Ó Cofaigh et al., 2014). For downcore AIO ages, a local contamination offset (LCO = surface AIO age – MRE) was calculated by dating seafloor surface sediments at two sites. This allows down-core AIO ages to be corrected for reworked fossil carbon that has been transported to the core site (Andrews et al., 1999; Hillenbrand et al., 2010a) (see section 2.3.2). When referred to in the text ages are presented as calibrated years before present (cal. yrs BP) where present corresponds to A.D. 1950. The ages are reported as the mid-point between the 2σ standard deviation, with the total 2σ standard deviation representing the error.

3.3.8.1. Calcareous (micro-)fossils

Sediment was sieved at 125 µm, dried and ~5 mg of foraminifera were picked from the >125 µm fraction and sent to BETA Analytic, Florida, for radiocarbon dating. Four dates were obtained from planktonic foraminifera (*Neogloboquadrina pachyderma* (sin.)), one from benthic foraminifera (*Globocassidulina crassa*) and two from mixed planktonic and benthic foraminifera (*N. pachyderma* (sin.), *Cibicoides* spp. and *Fursenkoina fusiformis*). As Calib automatically includes the average ocean reservoir correction of 400 yrs, a ΔR of 830 years is used in this study to account for the difference between the average ocean reservoir correction and the regional one of 1,230±100 yrs (Ó Cofaigh et al., 2014). At 445 and 541 cm depth within cores GC698 and GC695 respectively, foraminifera were in high enough abundance to date a paired set of foraminifera and AIO samples. These paired samples were used to test the assumption that (a) AIO ages are older than foraminifera ages obtained from the same horizon

due to contamination with terrigenous sediment and that (b) contribution of reworked fossil carbon has stayed constant over time.

3.3.8.2. Acid-insoluble organic matter (AIO)

Approximately 10-15 g of wet sediment was sampled and submitted to BETA Analytic for AIO dating. Prior to calibration, downcore ^{14}C ages were corrected using a LCO. However, in some special cases (e.g., samples from diatomaceous oozes) AIO ages were simply calibrated using the MRE (see section 6.2).

3.3.8.3. Ramped PyrOx

Samples were prepared for ^{14}C dating at University of South Florida, College of Marine Sciences during a research visit throughout June and July 2017 (hosted by Professor Brad Rosenheim). Sample preparation followed Rosenheim et al. (2008) and Subt et al. (2016) and involved splitting CO_2 gas into ~10-25 µmol aliquots as the sediment was gradually heated and CO_2 was produced. The CO_2 was separated from other gases using a series of liquid nitrogen and liquid nitrogen–cooled isopropanol traps and was sealed into pre-combusted, evacuated Pyrex tubes. These Pyrex tubes contain pre-combusted copper oxide and granulated silver; this allowed the CO_2 gas to be graphitised prior to ^{14}C dating at the National Ocean Sciences Accelerator Mass Spectrometry Facility, Woods Hole Oceanographic Institution. Where samples did not contain enough young organic carbon to be captured in a normal Ramped PyrOx aliquot (~10-15 µmol CO_2), a composite Ramped PyrOx technique was applied. This involved applying the Ramped PyrOx method to portions of the same sediment sample two times; CO_2 obtained from the first split over these two runs was combined to produce ~10-15 µmol CO_2 for ^{14}C dating (Subt et al., 2017). As with ages obtained from foraminifera, the returned conventional radiocarbon ages were calibrated using a MRE of 1,230±100 yrs.

3.3.9. Diatom absolute abundance and species assemblage analysis

Diatom abundance and relative diatom assemblage data were obtained as a proxy for marine productivity and palaeoenvironmental conditions (Scherer, 1994; Sjunneskog and Taylor, 2002; Taylor and Sjunneskog, 2002). Diatom abundance and relative diatom assemblage were initially assessed using smear slides and Scanning Electron Microscope (SEM) analysis. For SEM analysis ~0.5 x 0.5 cm ‘cubes’ of sediment were extracted from the sediment core and were split, exposing a clean sediment surface to be imaged by the SEM. Smear slides were

made using toothpick samples of sediment which were diluted with water and spread over a glass slide. Cover slips were adhered to the slide using Norland Optical Adhesive #61. The smear slides were analysed using light microscopy. Based on qualitative assessment of smear slides, sediments are defined as diatom bearing (15-30% diatoms), diatomaceous (30-50% diatoms) or diatomaceous ooze (50-100%). Sediments can additionally have trace (<2%), some (5%) or minor diatom content (10%).

Quantitative diatom slides for ADA and species assemblage analysis were prepared following the settling technique of Warnock and Scherer (2015); permanent slides were made using Norland Optical Adhesive. Quantitative slides were examined using light microscopy. Due to the dominance of *Chaetoceros subg. Hyalochaete (Chs)* resting spores and vegetative cells, 400 valves or 10 transects were counted for each slide twice; once including *Chs*, which provided information about the total assemblage and ADA, and a second time excluding *Chs*, in order to evaluate the contribution of minor species to the total assemblage (Leventer et al., 2002). Quantitative ADA and assemblage analysis were carried out on cores GC695 and GC697 and samples were taken at 10-20 cm intervals with toothpicks. Core GC695 contains a unit of highly laminated sediment. In order to accurately determine the composition of individual lamina, a detailed quantitative analysis of ADA and diatom assemblages was carried out on a 20 cm section of this laminated unit using toothpick samples, allowing the species assemblage of the laminations to be analysed individually. Samples were homogenised before analysis. Following diatom counts, ADA was calculated using the following equation:

$$\boldsymbol{T = (\frac{NB}{AF})/M}$$

T: Number of microfossils per unit mass
N: Total number of microfossils counted
B: Area of bottom of beaker (mm^2),
A: Area per field of view or transect (mm^2)
F: Number of fields of view or transects counted
M: Mass of sample (g)
(Scherer, 1994)

The percentage contribution of *Chs* to the total assemblage was obtained from counts including *Chs* and the percentage contribution of all other species were from *Chs* free counts. *Chs* are present within sediments in a resting spore (*Chs*-RS) and vegetative (*Chs*-veg) form. Many

diatom cells are present in a broken state, therefore so not to over-predict the relative abundance of a particular species, only diatom valves that were more than 50% complete were counted. In the case of araphid pennate diatoms (*Thalassiothrix* and *Thalassionema*), each frustule point/end identified counted as a half count. This counting method is illustrated in Figure 3.2.

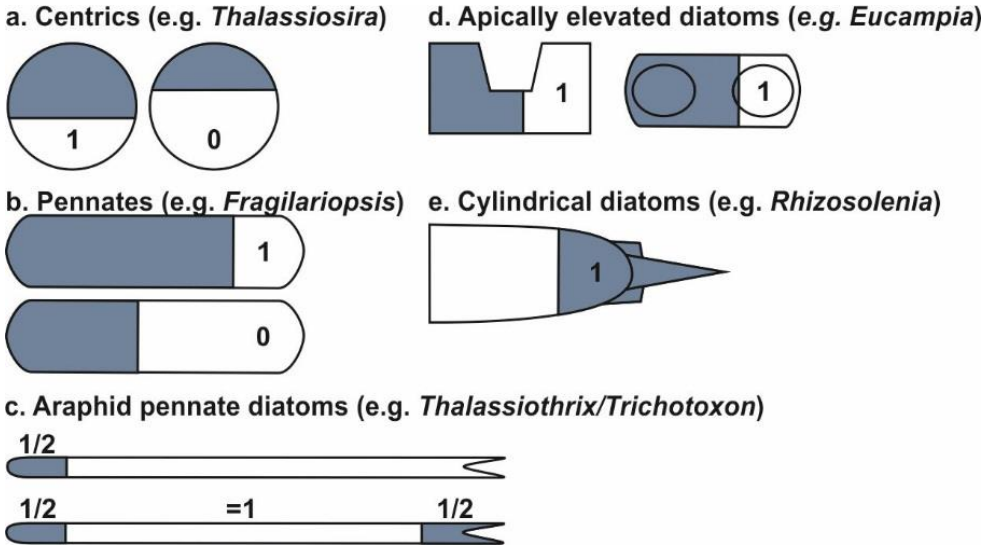

Figure 3.2: Schematic diagram outlining the counting method used for different diatom forms. Numbers indicate the count given depending on the state of the valve, with the shaded area indicating the fragment present. Typically, valves more than 50% complete are given a count of one (after Allen, 2003).

In some previous publications, certain diatom species and species morphotypes are combined under one name/type. This reflects difficulties in observing their identifying features. However, identifying these different species and morphotypes can provide important information on palaeoenvironmental conditions (Fryxell, 1989; Fryxell, 1990; Fryxell et al., 1994; Leventer et al., 2002; Allen, 2014). *T.antarctica* and *T. scotia* are closely related (Johansen and Fryxell, 1985) and these species are often combined in diatom assemblage counts (Zielinski and Gersonde, 1997). Although the environmental niche that these species occupy remains difficult to discern, in this study *T. antarctica* and *T. scotia* are separated in the hope that this treatment will allow any differences in the environments they occupy to be identified. *T. antarctica* morphotypes T1 and T2 are also identified and counted separately. These two types of *T. antarctica* are distinguished based on their size, coarseness of areolae and the absence or presence of marginal processes (Villareal and Fryxell, 1983; Taylor et al., 2001; Buffen et al., 2007). These two morphotypes, T1 and T2, are considered to dwell in relatively cool and relatively warm waters, respectively and are thus important environmental indicators (Villareal and Fryxell, 1983; Buffen et al., 2007). *Eucampia* spp. are additionally separated into symmetrical and asymmetrical morphotypes. The symmetrical morphotype is

the southern variety, tolerating sea-ice, whilst the asymmetrical morphotype is associated with relatively warm sub-polar environments (Fryxell, 1989; Fryxell, 1990; Leventer et al., 2002; Allen, 2014). Photomicrographs of common diatom taxa within core GC695 are presented in Appendix B.

Chapter 4

4. Controls on the variability of sediments deposited at the grounding line of a retreating ice stream

Abstract

Understanding the future response of ice streams and glaciers to climate change is of high importance but remains uncertain, due to the limited timescales over which we have recorded observational and satellite data. Sedimentary sequences, deposited on polar continental shelves during past episodes of ice sheet advance and retreat, can be used to improve our understanding of long-term changes. Past studies on marine sediment cores have typically identified three sediment facies assemblages: sub-glacial, transitional and seasonally open marine. Transitional sediment facies, deposited proximal to the ice stream grounding line, capture ice-proximal to distal depositional processes and environments, however their variability in a natural setting remains poorly understood. This is due the scarcity of grounding line observations and a reliance on conceptual models. Detailed analysis of transitional sediment facies, within sediment cores that capture an evolving ice stream grounding line over space and time, would allow us to understand variability in these sediments and the insight they provide into reconstructing palaeo-ice stream behaviour. Furthermore, recognising the depositional environment of sediments within a transitional setting is important for selecting appropriate horizons for radiocarbon dating. Transitional sediments are assumed to represent the onset of glaciomarine sedimentation following the retreat of grounded ice and therefore radiocarbon dates from these sediments are used to date the retreat of grounded ice over a core site. Here we use a multi-proxy approach on an extensive network of marine sediment cores recovered from the Anvers-Hugo palaeo-ice stream trough, western Antarctic Peninsula shelf, to identify the variability in transitional sediment facies deposited along and across the trough. Our data reveal systematic variability in transitional sediments, resulting from changes in retreat rate, bathymetry, grounding line oscillations and the evolving nature of the ice margin over deglaciation.

4.1. Introduction

Sediments deposited at the grounding line of a retreating ice stream are often heterogeneous, reflecting several overlapping depositional processes as well as multiple sediment pathways (e.g., Evans and Pudsey, 2002). Such sediments are often grouped together as transitional glacial marine facies, where 'transitional' defines the switch from sub-glacial to open marine conditions, often under ice-shelf cover. This means that not all processes are captured and that important information about glacier dynamics can be missed. The grounding line of ice streams remain poorly understood due to the lack of modern grounding line observations and a reliance on conceptual models that may not necessarily reflect the variability in grounding line processes and environments that exist in natural settings. Correctly identifying the environment within which transitional sediments are deposited is of particular important when sediments are targeted for radiocarbon dating, or when a link between the rate and style of ice stream retreat and the nature of the grounding line or ice margin environment (e.g. presence of absence of an ice shelf), is deemed important. In this chapter, a multi-proxy approach is used to investigate sediment variability within an extensive network of cores recovered from AHT. The aim is to investigate the dominant depositional processes active at the grounding line and how these vary spatially and temporally during ice stream retreat. Understanding the full range of processes is essential if we are to utilise sediment cores to accurately reconstruct ice sheet histories and consequently build analogues between these and modern day ice streams. Well-constrained palaeo studies will allow us to extend the timescales over which we understand ice stream and glacier behaviour, which aids predictions regarding the future of the AIS. A particular advantage of the AHT system that it is one of the best-surveyed palaeo-ice streams in Antarctica (Larter et al., 2019), which enabled sediment coring and subsequent core interpretation within a well-known geomorphic context (e.g. landward and seaward of GZWs).

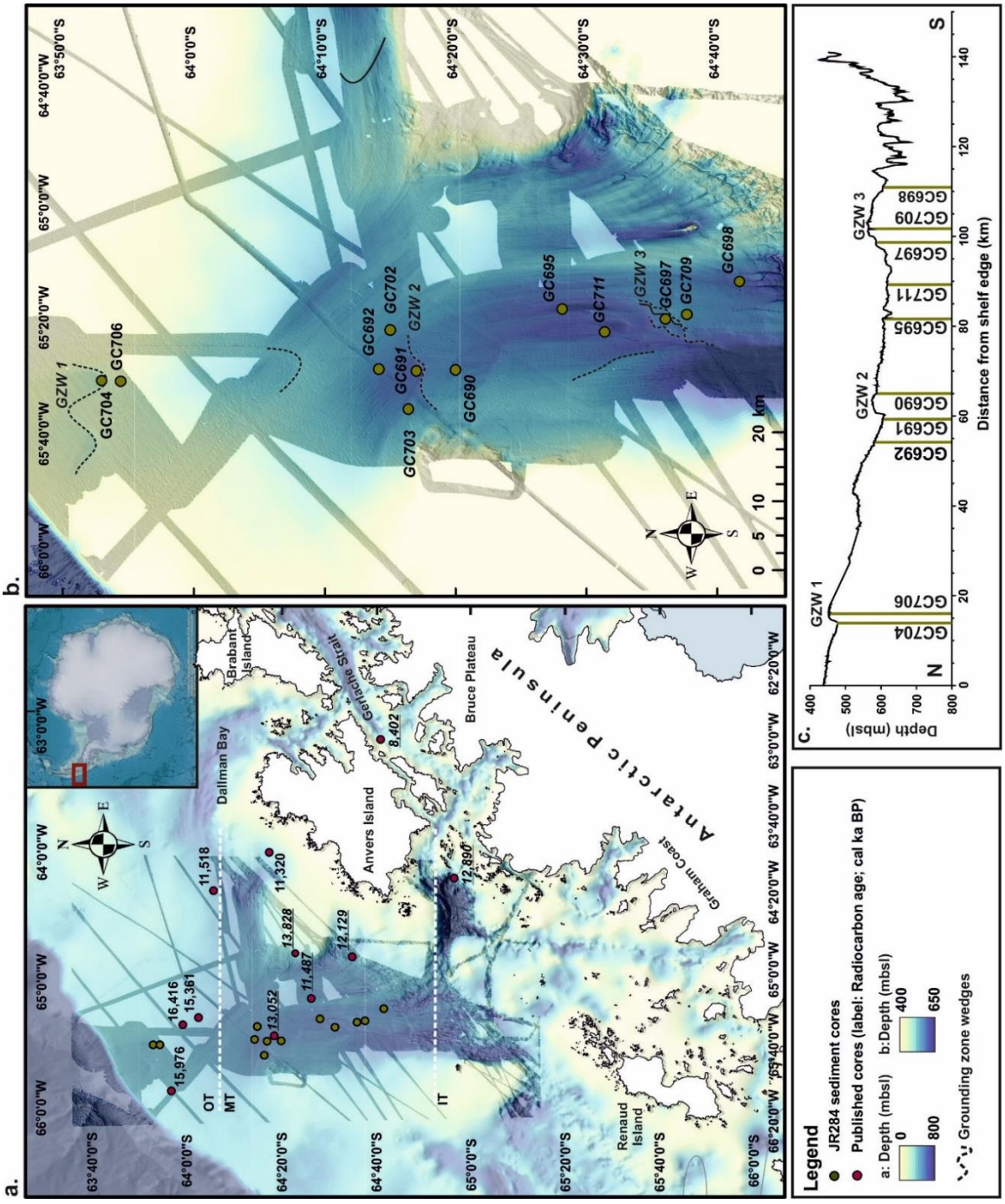

Figure 4.1: (a) Map of Anvers-Hugo Trough (AHT). White dashed lines indicate the division of the trough into an Outer Trough (OT), Mid-Trough (MT) and Inner-Trough (IT) region. Red dots denote available published deglacial ages (in cal. kyrs. BP) (from Harden et al., 1992; Domack et al., 2001; Heroy and Anderson, 2005, 2007; Nishimura et al., 1999; Ó Cofaigh et al., 2014; Pudsey et al., 1994; Yoon et al., 2002). Ages derived from calcareous foraminifera are in normal font; those derived from the acid-insoluble fraction of organic matter are italicised and underlined. (b) AHT with JR284 core locations (green dots) and location of GZWs 1-3 referred to in the text (c) Bathymetric cross sections of the AHT trough with GZWs 1-3 and core locations labelled.

4.2. Results

4.2.1. Geomorphological context of sediment cores

Near continuous multi-beam coverage of the AHT has allowed glacial bedforms to be mapped in high detail (Larter et al., 2019). The inner shelf, including the sill separating Palmer Deep and AHT, features anastomising channels and cresentic scours. These features are associated with periodic meltwater outflows from the subglacial lake hosted in Palmer Deep at the beginning of the last glacial period and during previous glacial periods (Alley et al., 2006; Domack et al., 2006; Larter et al., 2019). Northward shoaling and narrowing valleys additionally cut across the inner shelf; these become narrower and shallower northwards, being up to 1,100 m wide and 60 m deep at their southern end. From the termination of the valleys, the main trough is dominated by a series of well-developed GZWs and near-continuous MSGL (Fig. 4.2 and 4.3). MSGL extend to the outer continental shelf (see Fig. 4d in Heroy and Anderson, 2005; Larter et al., 2019) and usually their presence indicates the occurrence and direction of past ice streaming (e.g. Clark, 1993; Ó Cofaigh et al., 2002; Heroy and Anderson, 2005; Larter et al., 2019). In areas of the trough shallower than ~590 mbsl, south-west to north-east oriented iceberg scours cut across the MSGL and appear to have removed them entirely on the outermost shelf (Fig. 4.2) (see Fig. 6 in Heroy and Anderson 2005; see Fig. 4a in Convey et al., 2009; Larter et al., 2019). Within the deep central trough, iceberg scour marks occur north of 64°22’2’’S, on the shallower trough flanks these are present north of 64°32’19’’S.

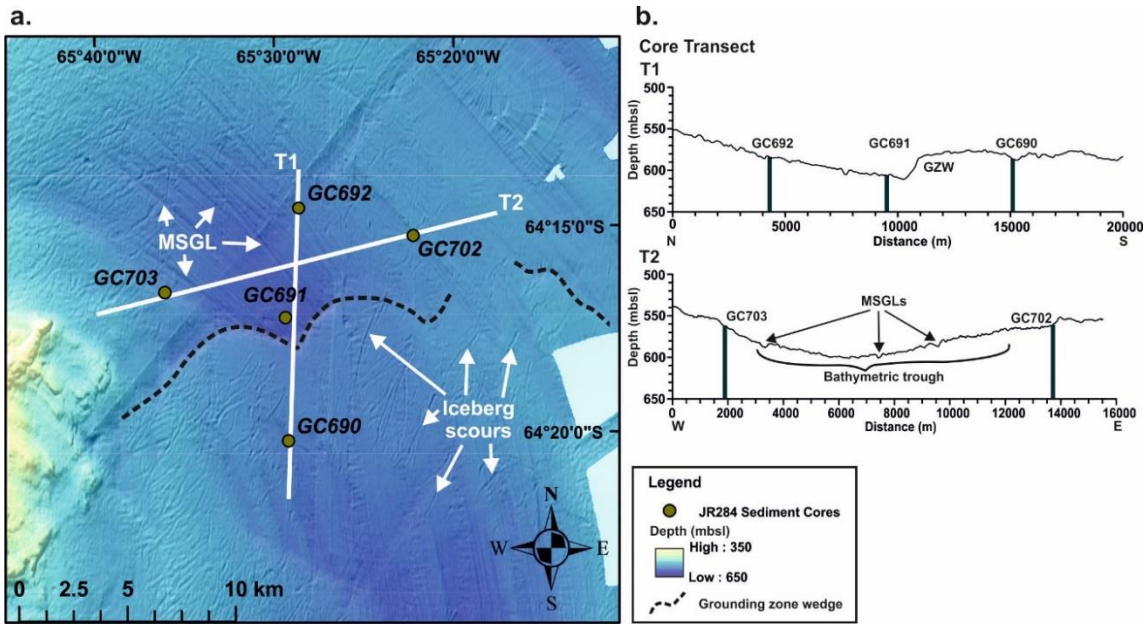

Figure 4.2: (a) Multibeam coverage of GZW 2, with interpreted glacial bedforms and sediment core locations (green circles). GZWs (dashed black lines) are also shown. (b) The bathymetric profiles of the along trough (T1) and across trough (T2) profiles are presented and include the position of the sediment cores as well as the position of the GZW and MSGLs.

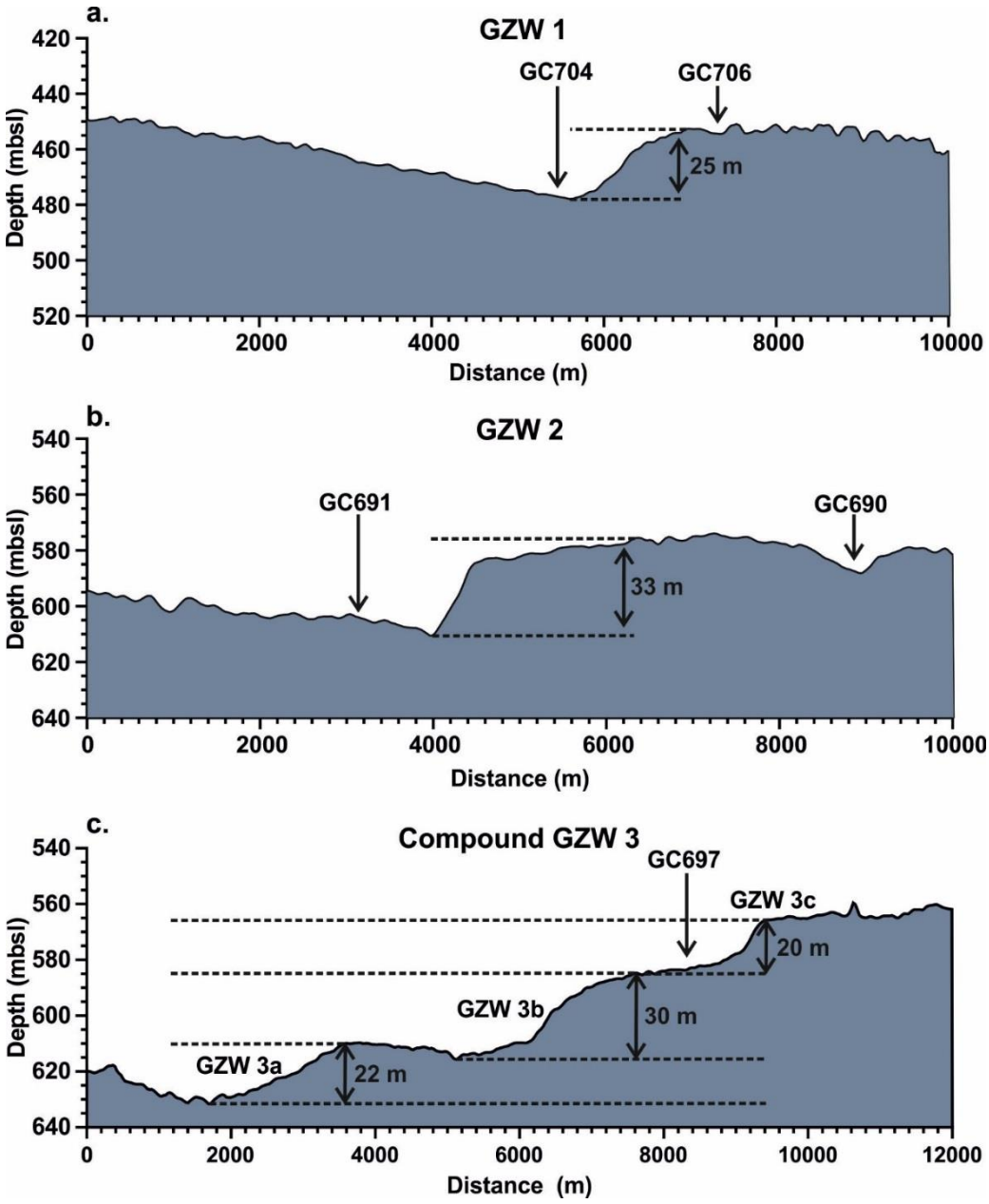

Figure 4.3: Bathymetric profiles, core locations and heights of (a) GZW 1 (b) GZW 2 and (c) GZW 3 (a-c).

MSGL are preserved seawards and do not overprint GZWs (Fig. 4.2a). This indicates that these GZWs were deposited during the last deglaciation of the trough and have not been overridden by an advancing ice stream. GZWs are present on the outer and mid-trough. The three GZWs, including one compound-GZW (Bart et al., 2017) labelled 1-3(a-c) in Figure 4.3, will be discussed further in relation to the sediment cores recovered seawards and on the landward, gentle slope of each wedge. Based on bathymetric profiles, the crest of GZW 1 is 25 m high and that of GZW 2 is 33 m high (Fig. 4.3)**.** There is a step-like bathymetry on the mid-shelf caused by the presence of three stacked GZWs (3a, b and c), representing three

phases of grounding line stills stands, similar to what was concluded for other stacked GZWs observed on polar continental shelves (Batchelor and Dowdeswell, 2015; Dowdeswell et al., 2016; Bart et al., 2017). From north to south (a-c), the highest parts of the steps are 22, 30 and 20 m high respectively (Fig. 4.3c). The location of GZW 2 coincides with a narrowing of AHT and extends from a bathymetric high (Fig. 4.2); this observation is consistent with the location of GZWs in Marguerite Trough (Fig. 1.1b), another major and well mapped palaeo-ice stream trough on the western Antarctic Peninsula continental shelf (Jamieson et al., 2012).

4.2.2. Lithological units

Lithological units were defined on the basis of core description, X-radiographs, physical properties (magnetic susceptibility and wet bulk density), grain size distributions, clay mineral assemblage, shear strength and water, biogenic opal, $CaCO_3$ and TOC content (Fig. 4.4 and 4.5). Seven lithological units are identified: (1) massive diamicton, (2) stratified diamicton, (3) mud alternating with gravel and sand, (4) mud alternating with silt laminae, (5) bioturbated to massive mud with dispersed gravel, (6) laminated to stratified diatomaceous ooze and (7) bioturbated diatomaceous ooze. It should be noted that these lithological units are not stratigraphic in nature.

4.2.2.1. Unit 1: Massive diamicton

Unit 1 is a massive, dark grey, matrix-supported diamicton with sub-angular to sub-rounded gravel-to pebble-sized clasts and is present in the lower section of most sediment cores (Fig. 4.4 and 4.5). Additionally, core GC703, recovered from the shallower trough flank, contains two massive diamictons, one at the base and one between 66 and 122 cm (Fig. 4.4l). Unit 1 has a water content of 17-26%, magnetic susceptibility of 401-960 (10^{-5} SI Units), a biogenic opal content of 2-4%, a TOC content of 0.1-0.2% and a $CaCO_3$ content of 1.1-3.2%. Shear strength varies between 10-35 kPa (mean 16 kPa, n=11), but is typically less than 26 kPa except towards the base of cores GC692, GC690, GC711 and GC703 (Fig. 4.4c, 4.4e, 4.4g and 4.4l). Core GC711 recovered two massive diamicton units, which are indistinguishable in terms of structure, grain size and physical properties. However, the upper diamicton (370-440 cm) has shear strengths of ~9 kPa and a water content of 21%, whilst the underlying diamicton has a much higher shear strength of up to 42 kPa and lower water content (~19%) (Fig. 4.4g). Smear slide analysis indicates that the unit contains trace fragments of diatoms, with a microfossil content of just 2-5%. Gravel abundance within Unit 1 varies considerably within and between cores. Core GC692 contains less coarse-gravel (16-32 mm; pebbles) relative to other cores (Fig. 4.4c). Unit 1 in this core also has the lowest magnetic susceptibility values.

Contacts with overlying units also vary between cores, from sharp to gradational. The clay mineral assemblage of Unit 1 varies between cores but is typically dominated by smectite, chlorite and illite, with minor concentrations of kaolinite (<1%) (Fig. 4.4c, d, e, g, h, j, k and l). The base of cores GC691 and GC698 have higher concentrations of chlorite (62-64%), similar to the stratified diamictons in cores GC697, GC703, GC711 and GC698. GC692 has a higher illite concentration (38%) whilst cores GC711, GC703 and GC692 contain a higher concentration of smectite (>45%).

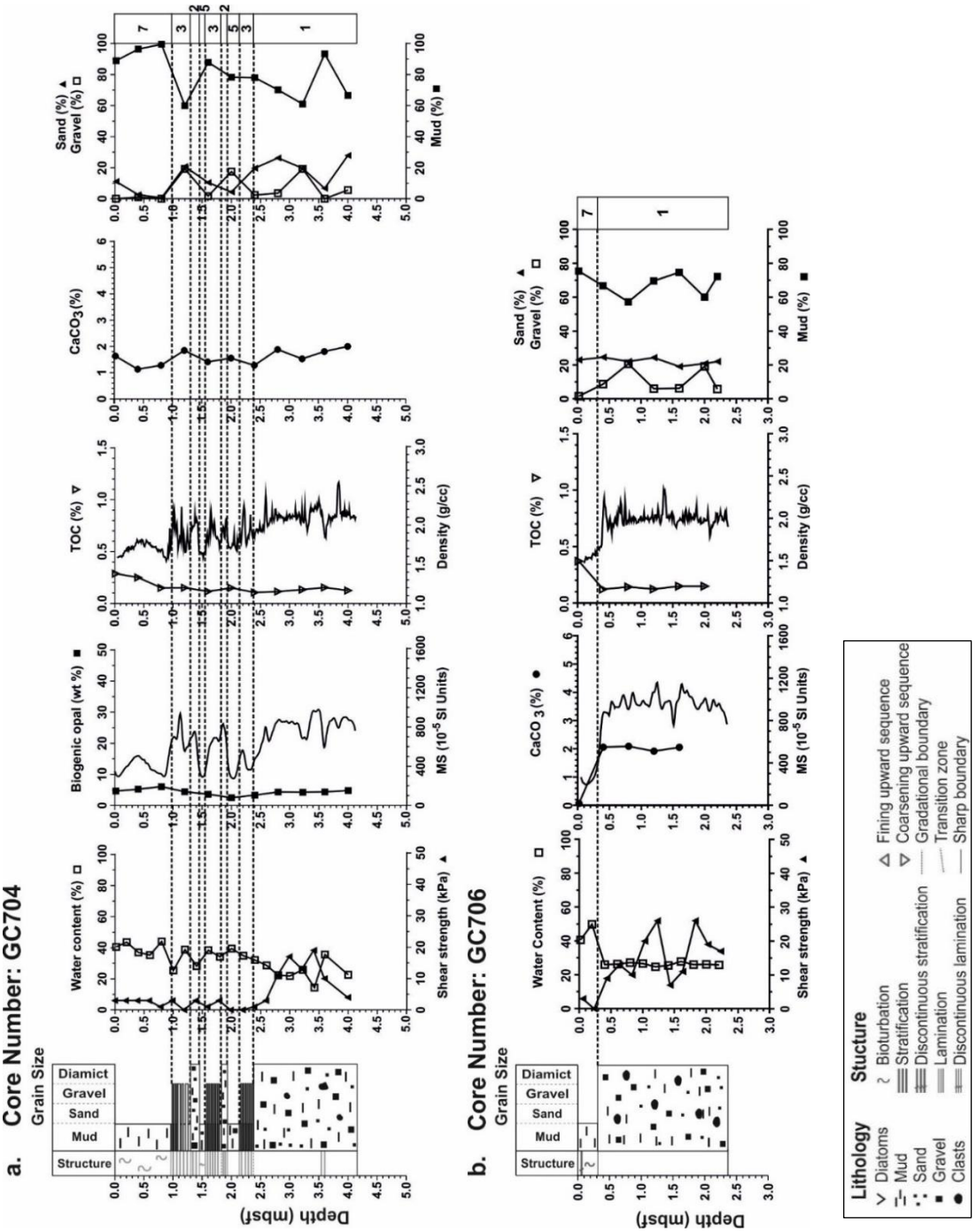

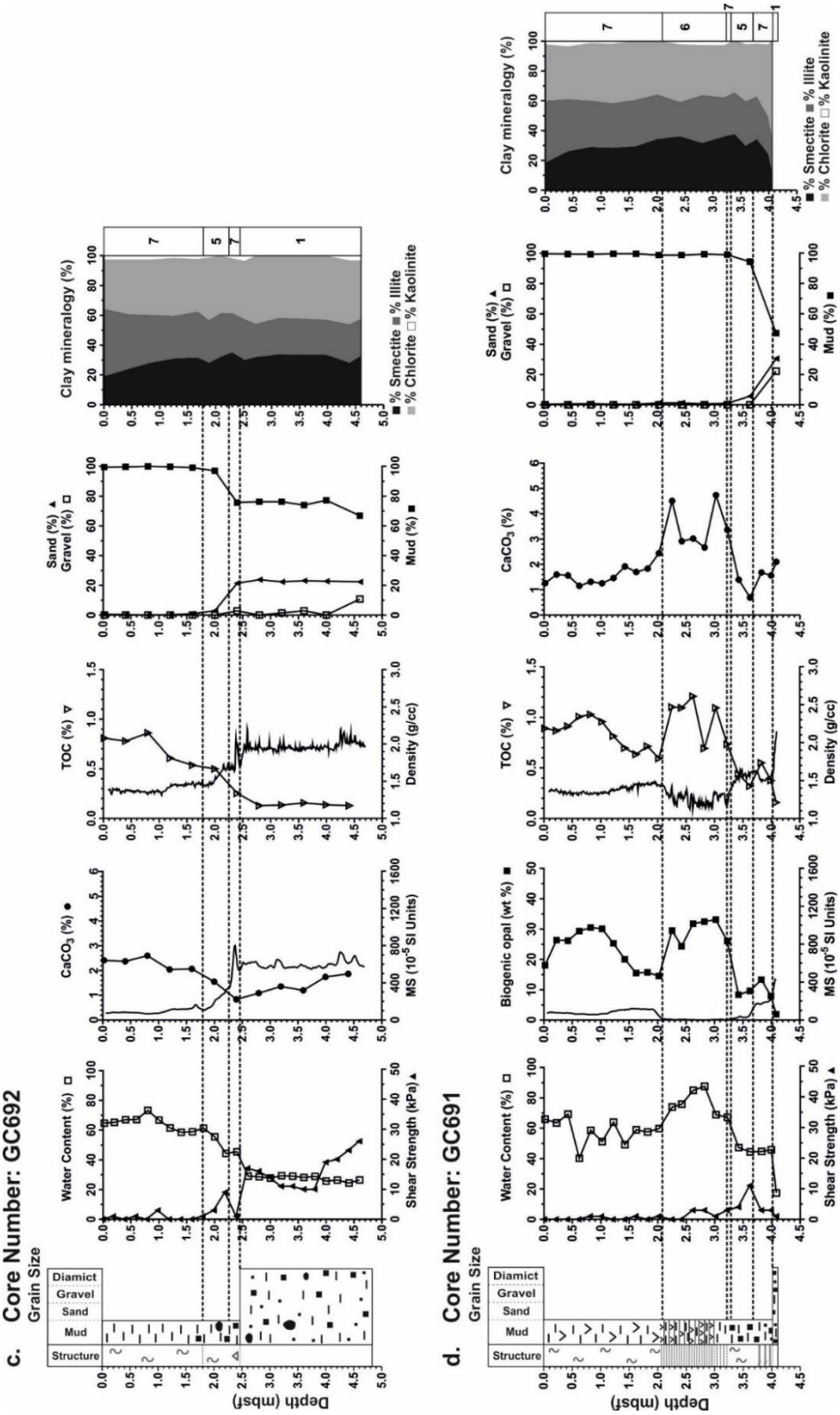
c. Core Number: GC692
Grain Size
Diamict
Gravel
Sand
Mud
Structure
Depth (mbsf)
Water Content (%)
Shear Strength (kPa)
CaCO3 (%)
MS (10-5 SI Units)
TOC (%)
Density (g/cc)
Sand (%)
Gravel (%)
Mud (%)
Clay mineralogy (%)
% Smectite
% Illite
% Chlorite
% Kaolinite
d. Core Number: GC691
Biogenic opal (wt %)

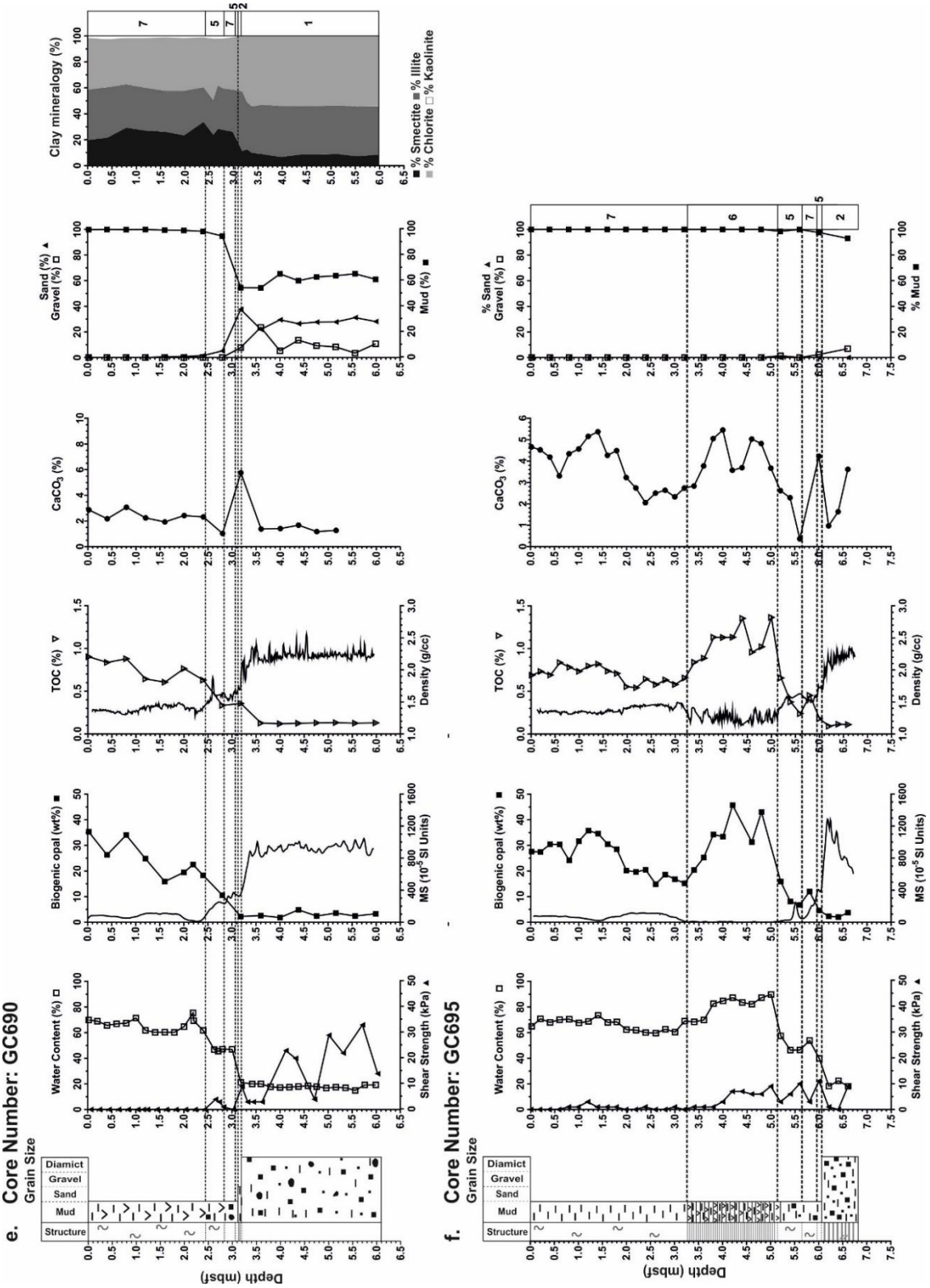
e. Core Number: GC690
f. Core Number: GC695
Grain Size
Diamict
Gravel
Sand
Mud
Structure
Depth (mbsf)
Water Content (%)
Shear Strength (kPa)
Biogenic opal (wt%)
MS (10⁻⁵ SI Units)
TOC (%)
Density (g/cc)
CaCO3 (%)
Sand (%)
Gravel (%)
Mud (%)
% Sand
% Gravel
% Mud
Clay mineralogy (%)
% Smectite
% Illite
% Chlorite
% Kaolinite

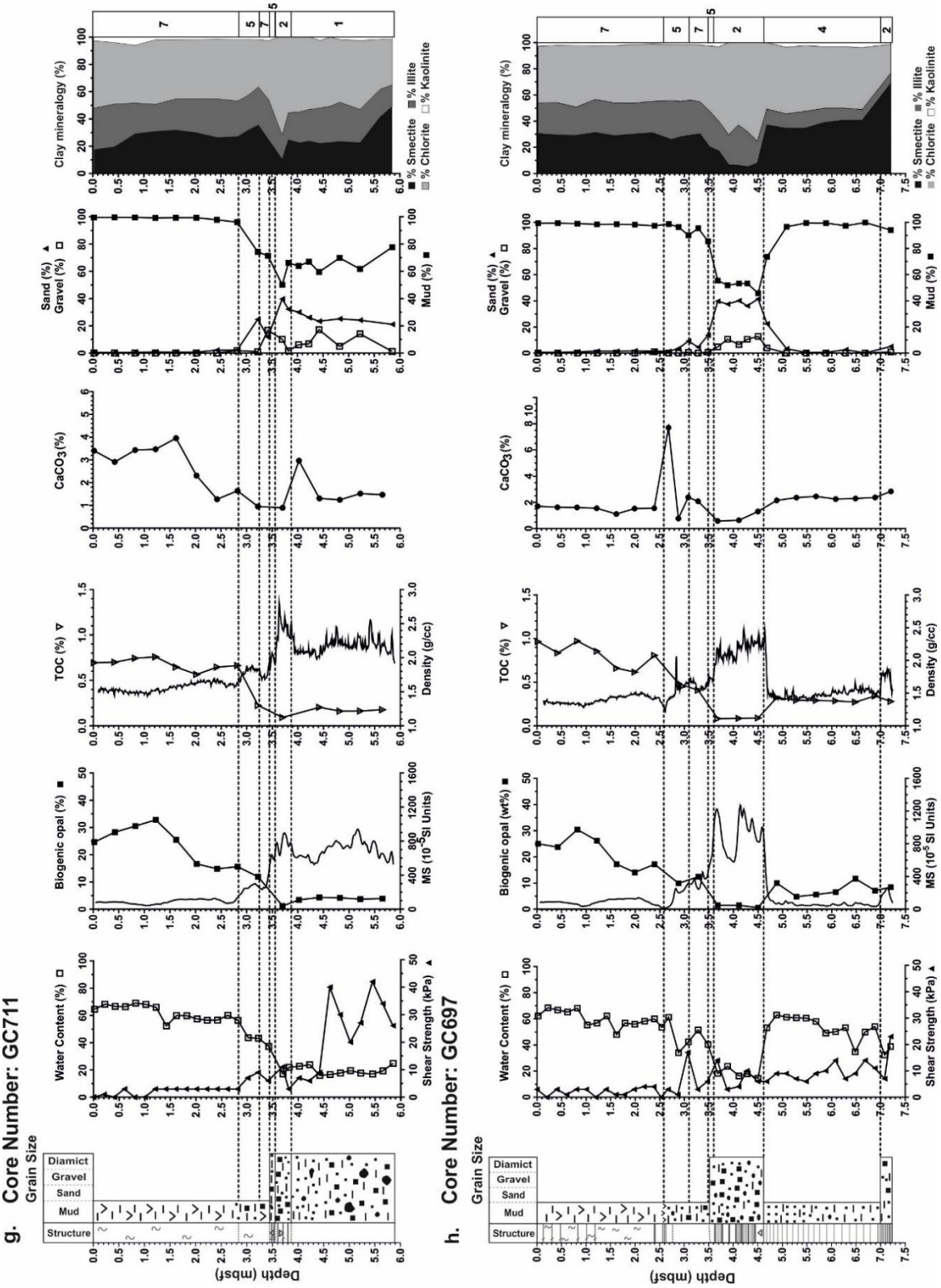
g. Core Number: GC711
h. Core Number: GC697
Grain Size
Diamict
Gravel
Sand
Mud
Structure
Depth (mbsf)
Water Content (%)
Shear Strength (kPa)
Biogenic opal (%)
Biogenic opal (wt%)
MS (10^{-5}SI Units)
TOC (%)
Density (g/cc)
$CaCO_3$(%)
Sand (%)
Gravel (%)
Mud (%)
Clay mineralogy (%)
% Smectite
% Illite
% Chlorite
% Kaolinite

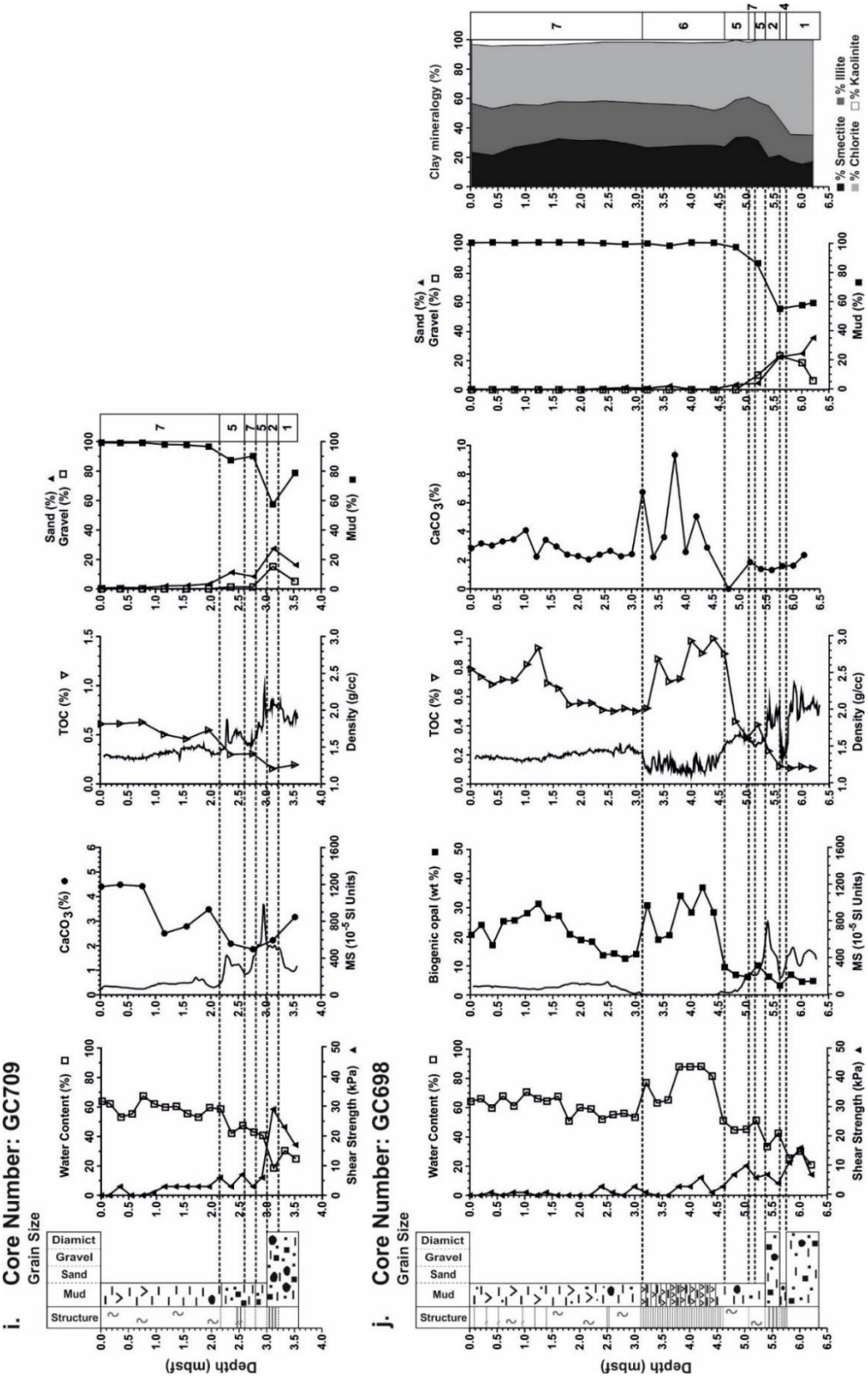
i. Core Number: GC709
j. Core Number: GC698
Grain Size
Diamict
Gravel
Sand
Mud
Structure
Depth (mbsf)
Water Content (%)
Shear Strength (kPa)
CaCO3 (%)
MS (10-5 SI Units)
TOC (%)
Density (g/cc)
Sand (%)
Gravel (%)
Mud (%)
Biogenic opal (wt %)
Clay mineralogy (%)
% Smectite
% Illite
% Chlorite
% Kaolinite

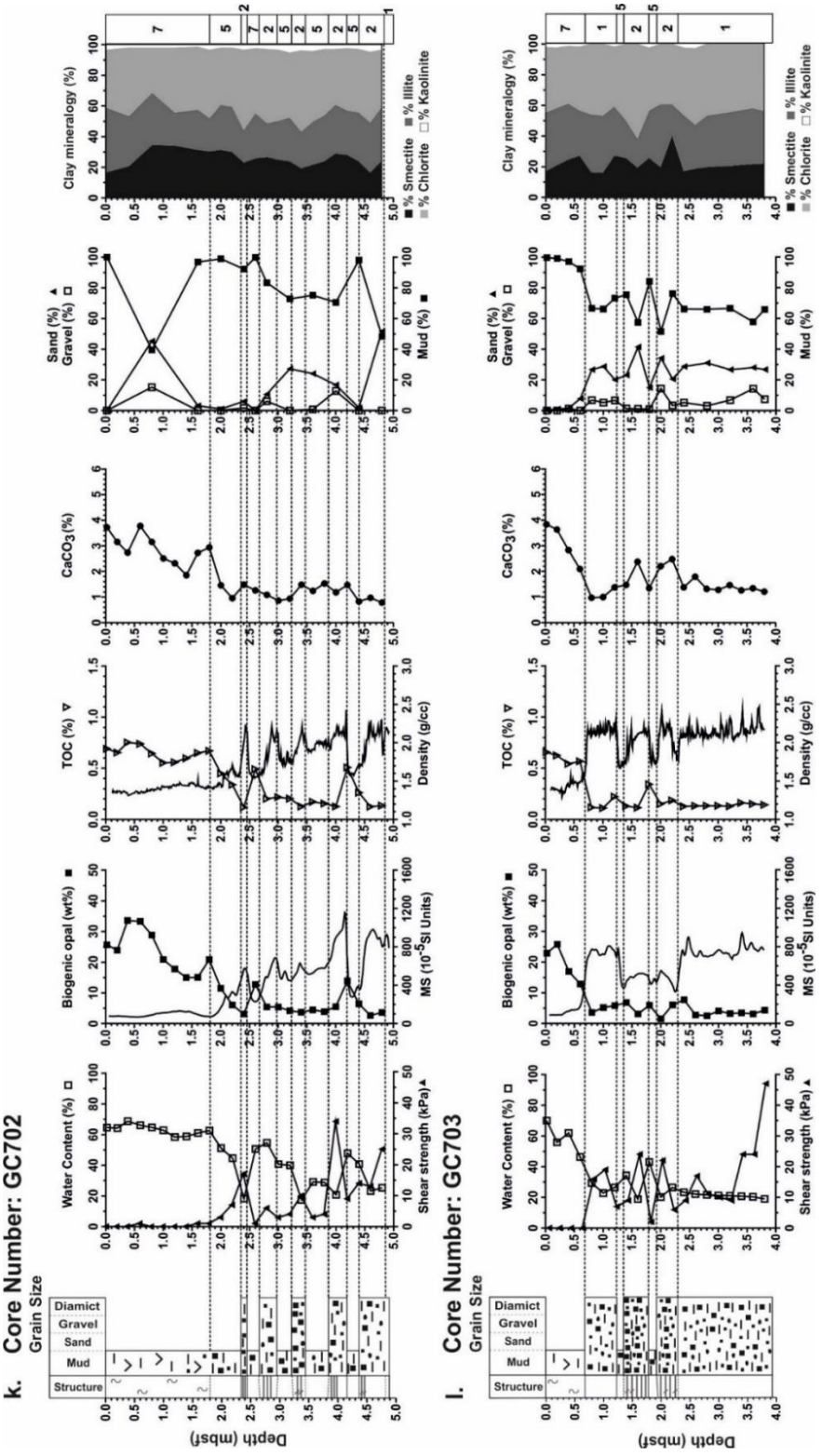

Figure 4.4: Core lithology and down core data including; water content (open squares), shear strength (closed triangles), magnetic susceptibility (MS), biogenic opal (closed squares), TOC (open triangles), $CaCO_3$ (closed circles), density, contents of mud (<63µm, closed squares), sand (63 µm-2mm, closed triangles) and gravel (>2 mm, open squares). Clay mineral assemblages are also shown where measured. Sedimentary structure was identified using X-radiographs. Dashed lines and numbered boxes (far right) indicate the boundary between lithological units: (1) massive diamicton, (2) stratified diamicton, (3) mud alternating with sand and gravel, (4) mud alternating with silt laminae, (5) bioturbated mud with dispersed gravel, (6) laminated to stratified diatomaceous ooze and (7) bioturbated diatomaceous ooze. Unit depths are given in Appendix C and core images in Appendix D.

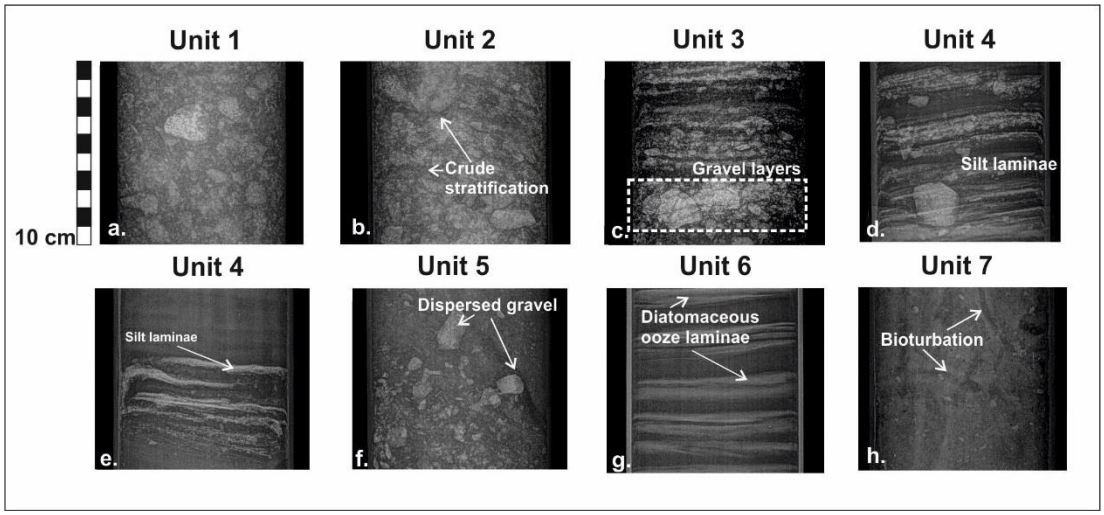

Figure 4.5: X-radiographs (negatives) showing examples of the lithological units identified in the sediment cores. Bright layers are coarse and the darker layers are finer. (a) Unit 1: Massive diamicton in core GC690. (b) Unit 2: Stratified diamicton in core GC704. (c) Unit 3: Mud alternating with sand and gravel in core GC704. (d) Unit 4: Mud alternating with silt laminae in core GC698. (e) Unit 4: Mud alternating with silt laminae in core GC697. (f) Unit 5: Bioturbated mud with dispersed gravel in core GC698. (g) Unit 6: Laminated to stratified diatomaceous ooze in core GC691. (h) Unit 7: Bioturbated mud in core GC704. Full X-radiographs are given in Appendix E.

4.2.2.2. Unit 2: Stratified diamicton

Unit 2 is a grey to dark grey laminated to stratified, matrix-supported diamicton, present in all but three cores (GC691, GC692, GC706; Table 4.1). Unit 2 typically forms the basal unit or overlies Unit 1, although this is not always the case, e.g. in GC697 this unit occurs at the base and between 360 - 460 cm (Fig. 4.4h and 4.6). The thickness of Unit 2 ranges from 10 to 100 cm. Unit 2 has a water content of 18-38%, a shear strength of 3-17 kPa, magnetic susceptibility values of 70-920 10^{-5} SI Units, a biogenic opal content of 1-6%, a TOC content of 0.1-0.3%, a $CaCO_3$ content of 0.8-2.3% and a microfossil content of 2-10%. The X-radiographs show the unit is crudely stratified (Fig. 4.5 and 4.6), and that the upper and lower boundaries to other lithological units are generally gradational. Stratification is variable within and between the cores. Figure 4.6 illustrates the details of the cm-scale stratification in core GC697, including coarser and finer 10-30 cm sub-units, some of which include mm-scale laminations (Fig. 4.6). Unit 2 has a higher water, biogenic opal, TOC and $CaCO_3$ content, as well as lower shear strength, magnetic susceptibility and mud content, relative to Unit 1, although these differences are subtle and the ranges of their various physical properties often overlap (Fig. 4.7). The clay mineral assemblage of Unit 2 is again dominated by chlorite, smectite and illite, with minor concentrations of kaolinite (<1%) (Fig. 4.4e, g, h, j, k and l). Cores GC697, GC703, GC711 and GC698 contain high concentrations of chlorite (57-71%). Higher smectite contents are observed in core GC702 (21-35%) and at 220 cm in core GC703 (40%) and at the base of core GC697 (69%).

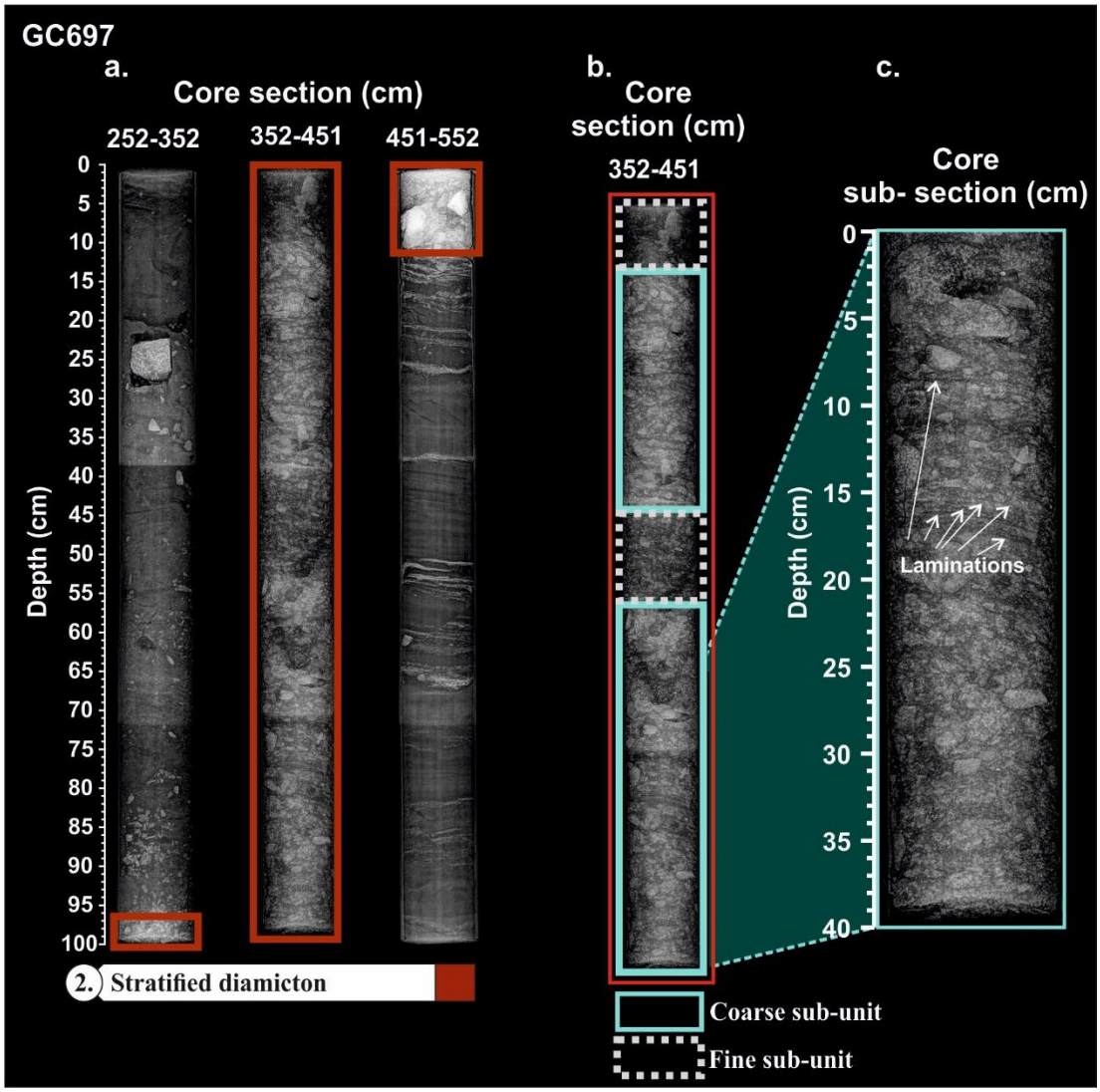

Figure 4.6: X-radiograph (negatives) of GC697 illustrating the stratification within Unit 2. (a) The whole of Unit 2 (red, solid border; 352-451 cm); including its contacts to under (Unit 4) and overlying (Unit 5) lithological units. (b) Illustration of coarser-grained (light blue, solid border) and finer-grained (white, dashed border) intervals. (c) The coarser-grained crudely stratified intervals often include millimetre-scale laminations (white arrows).

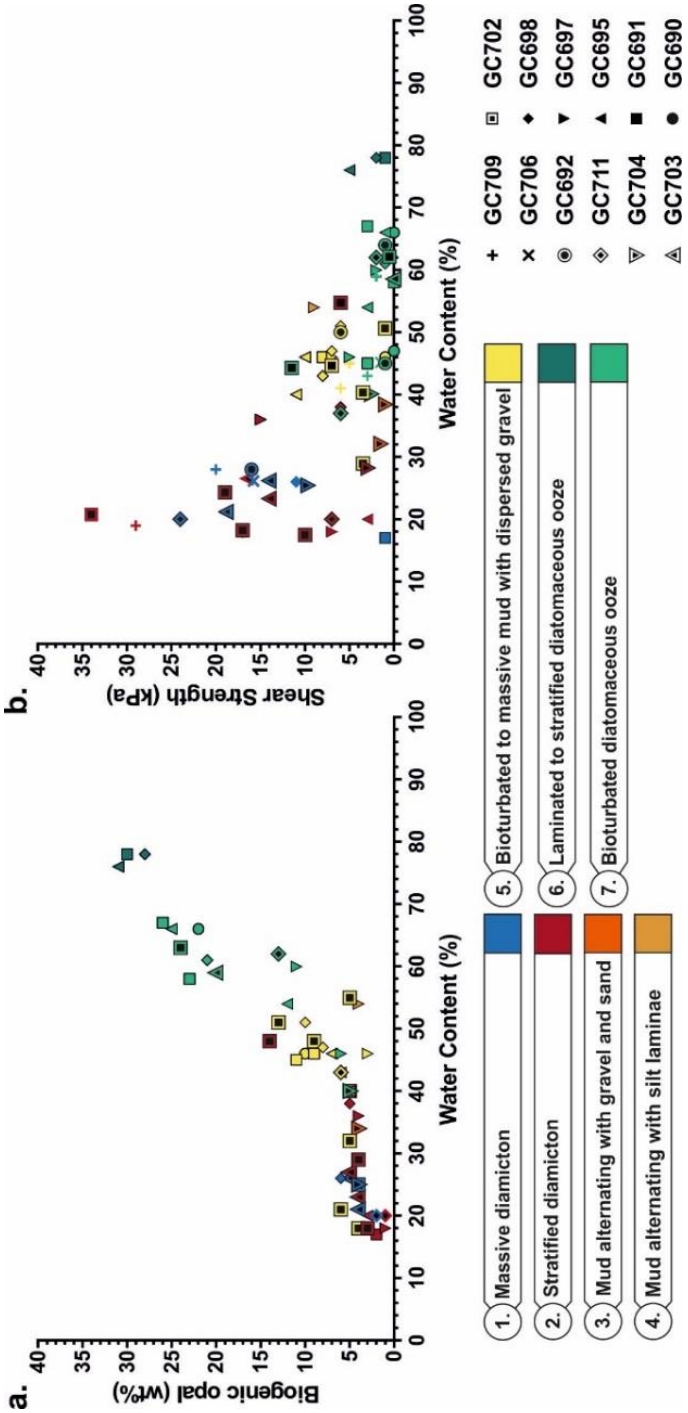

Figure 4.7: Cross-plots illustrating key differences/similarities between lithological units. (a) Biogenic opal (wt%) vs. water content (%) and (b) shear strength (kPa) vs. water content (%). Each data point represents the average value for each unit and has a corresponding core number (shape) and lithological unit (colour).

4.2.2.3. Unit 3: Mud alternating with gravel and sand

Unit 3 is a laminated to stratified, grey to dark grey mud with mm-to cm-scale sand and gravel layers (Fig. 4.5c). This unit is present in core GC704 only (Fig. 4.4a); the outermost shelf core analysed for this study. Sand and gravel content varies between individual laminae. Unit 3 has a water content of 32-38%, a shear strength of 1 kPa, magnetic susceptibility values of 250-

680 10^{-5} SI Units, a biogenic opal content of 4%, a TOC content of 0.1-0.2%, a $CaCO_3$ content of 1.4-1.8% and a microfossil content of 0-5%. In sediment core GC704, beds of Unit 3 alternate with beds of Unit 2 and 5 (Fig. 4.4a).

4.2.2.4. Unit 4: Mud alternating with silt laminae

Unit 4 is a grey mud with silt laminae. It is present in cores GC697 and GC698. Within core GC697, this unit is 234 cm thick and sits between two intervals of stratified diamicton (Unit 2) (Fig. 4.4h). Within core GC698, Unit 4 occurs between a massive diamicton (Unit 1) at its base and a stratified diamicton (Unit 2) above (Fig. 4.4j). In both cores, X-radiographs reveal that the laminae coarsen up-core, are continuous to discontinuous, contorted and occasionally faulted (Fig. 4.5d and 4.5e). They additionally show dispersed gravel-sized clasts, which are occasionally "floating" within and between the laminae and, in some places, contort the laminae (Fig. 4.5d). Unit 4 has a water content of 54% (n=1; Table 4.1), a shear strength of 9 kPa, magnetic susceptibility values of 175-252 10^{-5} SI Units, a biogenic opal content of 4%, a TOC content of 0.3%, a $CaCO_3$ content of 2.3% and a microfossil content of 0%. Unit 4 within core GC697 has a relatively high smectite content (Fig. 4.4h) (38% smectite, 11% illite, 49% chlorite and 2% kaolinite) comparable with smectite-enriched layers of Unit 1 core GC711 and Unit 2 in cores GC697 and GC703.

The shear strength and microfossil, biogenic opal, TOC and $CaCO_3$ content of this unit are comparable to Units 1-3, however the magnetic susceptibility values are considerably lower and the water content is higher. The grain size of the grey mud with silt laminae varies from clays to very fine silt, with peaks in grain size at 0.35, 1.7 (clay) and 4.9 µm (very fine silt) (Fig. 4.8a). These peaks also correspond with the distribution of the fine (clay/silt) fraction of Units 1 (Fig. 4.8b).

4.2.2.5. Unit 5: Bioturbated to massive mud with dispersed gravel

Unit 5 is grey, bioturbated to massive, diatom bearing mud with dispersed gravel. Unit 5 is present in most cores (Fig. 4.4) and generally has a gradational lower boundary with Unit 2 or 1. The water content of Unit 5 is 17-55%, its shear strength is 0-34 kPa, its magnetic susceptibility values range from 76-319 10^{-5} SI Units, its biogenic opal content is 2-10%, its TOC content 0.1-0.6% and its $CaCO_3$ content is 0.4-5.6%. Water content and concentrations of diatom, biogenic opal, TOC and $CaCO_3$ are typically higher than those of Units 1 and 2 (Fig. 4.7), and these values generally increase up-unit, whilst shear strength and magnetic susceptibility both decrease. Gravel concentrations (ø up to 4 cm) decrease towards the top of

the unit and Unit 5 typically has a gradational upper contact with Unit 7 (Fig. 4.5f). Smear slide analysis shows that this lithological unit has a diatom content of 20-30%. Unit 5 is characterised by a decrease in the percentage of chlorite and illite and an increase in smectite.

Within cores GC690, GC695, GC711, GC697, GC709 and GC698 an initial interval of bioturbated to massive mud with dispersed gravel (Unit 5) overlies stratified diamicton (Unit 2) (Fig. 4.4e, f, g, h, i and j). These cores have an additional 20-40 cm thick interval of bioturbated to massive grey mud with dispersed gravel (Unit 5), overlying an initial interval of bioturbated diatomaceous ooze (Unit 7). Cores GC692 and GC691 additionally have an interval of Unit 5 overlying Unit 7 (Fig. 4.4c and Fig. 4.4d). Cores GC702 and GC703 contain multiple Unit 5 intervals, interbedded with layers of massive (Unit 1) and stratified (Unit 2) diamictons (Fig. 4.4k and 4.4l).

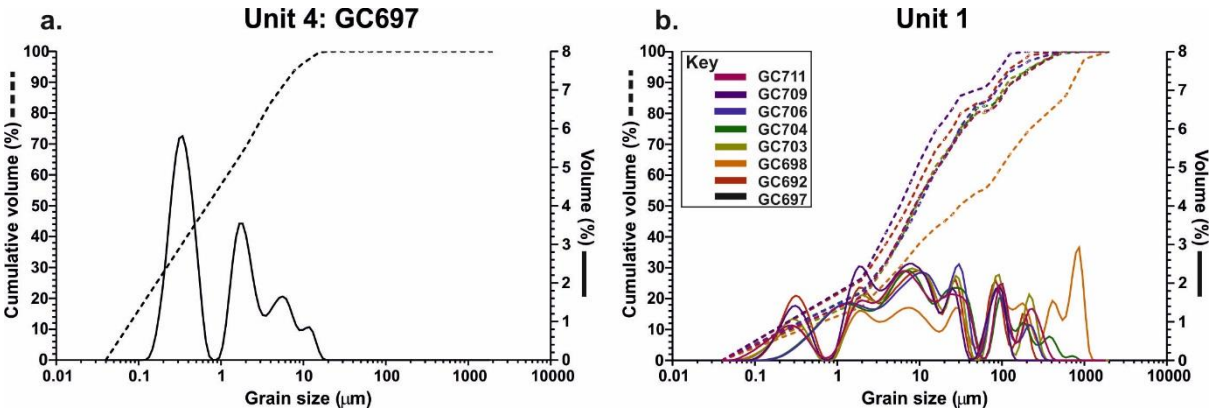

Figure 4.8: Grain-size distributions within (a) Unit 4 (mud alternating with silt laminae) and (b) Unit 1 (massive diamicton).

Unit	Description	Cores present	Water content (%)	Shear strength (kPa)	Magnetic susceptibility (10^{-5} SI Units)	Biogenic opal content (%)	TOC (%)	$CaCO_3$ (%)	Microfossil content (%)
1	Massive diamicton	GC704, GC706, GC692, GC691, GC690, GC711, GC709, GC698, GC703, GC702	17-26 (n=11, $\bar{x}$= 24, σ= 4)	10-35 (n=11, $\bar{x}$= 16, σ= 7)	401-960 (n=11, $\bar{x}$= 668, σ= 219)	2-4 (n=7, $\bar{x}$= 4, σ= 1)	0.1-0.2 (n=10, $\bar{x}$= 0.1, σ= 0)	1.1-3.2 (n=10, $\bar{x}$= 1.7, σ= 0.6)	2-5
2	Stratified diamicton	GC704, GC690, GC695, GC711, GC697, GC709, GC698, GC702, GC703	18-38 (n=15, $\bar{x}$= 26, σ= 10)	3-17 (n=15, $\bar{x}$= 12, σ= 9)	70-920 (n=16, $\bar{x}$= 609, σ= 226)	1-6 (n=13, $\bar{x}$= 4, σ= 2)	0.1-0.3 (n=14, $\bar{x}$= 0.2, σ=0.1)	0.8-2.3 (n=14, $\bar{x}$= 1.9, σ= 1.3)	2-10
3	Laminated to Stratified mud alternating with gravel and sand	GC704	32-38 (n=3, $\bar{x}$= 35, σ= 3)	1 (n=2, $\bar{x}$= 1, σ= 0)	250-680 (n=3, $\bar{x}$= 571, σ= 127)	4 (n=2, $\bar{x}$=4, σ= 1)	0.1-0.2 (n=2, $\bar{x}$= 0.1, σ= 0)	1.4-1.8 (n=2, $\bar{x}$= 1.6, σ= 0.3)	0-5
4	Mud alternating with silt laminae	GC697, GC698	54 (n=1)	9 (n=1)	175-252 (n=2, $\bar{x}$= 214, σ= 54)	4 (n=1)	0.3 (n=1)	2.3 (n=1)	0
5	Bioturbated mud with dispersed gravel	GC704, GC692, GC690, GC695, GC711, GC697, GC709, GC698, GC792, GC703	17-55 (n=17, $\bar{x}$= 45, σ= 6)	0-34 (n=16, $\bar{x}$= 6, σ= 3)	76-319 (n=16, $\bar{x}$= 355, σ= 162)	2-10 (n=13, $\bar{x}$= 7, σ= 4)	0.1-0.6 (n=14, $\bar{x}$= 0.3, σ= 0.1)	0.4-5.6 (n=16, $\bar{x}$= 1.1, σ= 0.6)	20-30
6	Laminated to stratified diatomaceous ooze	GC691, GC695, GC698	76-78 (n=3, $\bar{x}$= 77, σ= 1)	2-5 (n=3, $\bar{x}$= 3, σ= 2)	3-8 (n=3, $\bar{x}$= 5, σ= 3)	28-31 (n=3, $\bar{x}$= 30, σ= 2)	0.8-1 (n=3, $\bar{x}$= 0.9, σ= 0.1)	3.5- 4.6 (n=3, $\bar{x}$= 4.0, σ= 0.6)	80-100
7	Bioturbated diatomaceous ooze	GC704, GC706, GC692, GC692, GC690, GC695, GC711, GC697, GC709, GC698, GC702, GC703	37-67 (n=21, $\bar{x}$= 54, σ= 10)	0-9 (n=21, $\bar{x}$= 2, σ= 2)	71-481 (n=16, $\bar{x}$= 157, σ= 116)	5-26 (n=16, $\bar{x}$= 15, σ= 9)	0.2-0.8 (n=15, $\bar{x}$= 0.6, σ= 0.2)	0.1-3.7 (n=15, $\bar{x}$= 2.2, σ= 1.0)	50-100

Table 4.1: Characteristics of each lithological unit based on water content (%), shear strength (kPa), magnetic susceptibility (10^{-5} SI Units) and biogenic opal, TOC, $CaCO_3$ and diatom content (%). The number of units measured (n), the mean value ($\bar{x}$) and standard deviation (σ) are given.

4.2.2.6. Unit 6: Laminated to stratified diatomaceous ooze

Unit 6 is present in cores GC691, GC695 and GC698 and consists of laminated and stratified diatomaceous ooze (Fig. 4.4d, f and j, 4.5g). There are 83, 68 and 44 laminae of near-pure diatomaceous ooze ranging in size from 0.1-3.7 cm within cores GC695, GC698 and GC691, respectively. *Chs*, including *Chs*-veg and *Chs*-RS, dominate the ooze layers. These laminae alternate with layers of grey mud. Cores containing Unit 6 were all recovered from bathymetric low points (Fig. 4.1b). Unit 6 has a water content of 76-78%, a shear strength of 2-5 kPa, magnetic susceptibility values of 3-8 10^{-5} SI Units, a biogenic opal content of 28-31%, a TOC content of 0.8-1% and a $CaCO_3$ content of 3.5-4.6%. The biogenic opal content measured on the bulk sediment of this unit is surprisingly low (28-31%), when compared to the estimated diatom content from smear slide analyses (80-100%). This may reflect a sampling bias whereby muddier sediments were sampled or, more likely, an over/under-estimation of diatom/biogenic opal content from the smear slide analysis and automated leaching technique, respectively (e.g., Pudsey, 2002; Hillenbrand et al., 2010a).

Although this unit is only observed in three cores, sediments with a similar magnetic susceptibility signature (i.e., low/zero SI Units) are observed at the same stratigraphic interval in several other cores, although the unit is much thinner (<10 cm). This magnetic susceptibility low is observed overlying the upper interval of bioturbated to massive grey mud with dispersed gravel (Unit 5) in cores GC692, GC690, GC697, GC709, GC711 and GC702 (Fig. 4.4c, e, h, i, g and k). These sediments (and consequently, environmental conditions) therefore appear to be pervasive across AHT, represented as both thick (GC691, GC695 and GC691) and thinner drapes (GC690, GC697, GC709, GC711, GC692 and GC702).

4.2.2.7. Unit 7: Bioturbated diatomaceous ooze

The uppermost unit (Unit 7) in all cores is an olive-green, bioturbated diatomaceous ooze with dispersed gravel-sized grains (Fig. 4.5h). As well as being present as the uppermost unit in all cores, there is a thin (18-34 cm) interval of Unit 7 overlying massive diamicton (Unit 1) and underlying an interval of bioturbated to massive mud with dispersed gravel (Unit 5) in cores GC692 and GC691 (Fig. 4.4c and d) and sandwiched between two intervals of Unit 5 in cores GC690, GC695, GC711, GC697, GC709 and GC698 (Fig. 4.4e, f, g, h, i and j). Core GC702 contains multiple Unit 7 intervals interbedded with layers of stratified diamicton (Unit 2) and bioturbated to massive grey mud with dispersed gravel (Unit 5) (Fig. 4.4k). The diatom content of Unit 7 varies between 50 and 100% with occasional ~3 mm thick layers of near pure diatomaceous ooze. Based on smear slide analysis, Unit 7 contains a mixed diatom

assemblage, whilst the near-pure ooze layers are dominated by *Chs*-veg and *Chs*-RS. Unit 7 has a water content of 37-67%, a shear strength of 0-9 kPa, magnetic susceptibility values of 71-481 10^{-5} SI Units, a biogenic opal content of 5-26%, a TOC content of 0.2-0.8% and a $CaCO_3$ content of 0.1-3.7%. In cores recovered from the outer shelf, the unit is greyer and has lower concentrations of biogenic opal, TOC and $CaCO_3$ compared to cores from the mid shelf. The thickness of Unit 7 thins towards the outer shelf. Unit 7 has a similar clay mineral assemblage as Unit 6, with 17-37% smectite, 20-45% illite, 30-50% chlorite and 0-6% kaolinite.

4.3. Interpretation

4.3.1. Unit 1: Massive diamicton

Unit 1 occurs at the base of all recovered sediment cores, with the exception of cores GC695 and GC697, which instead bottom-out in Unit 2 (Figure 4.9). In all instances, cores containing Unit 1 were recovered from areas of MSGL. The massive structure, low biogenic content and shear strength values are indicative of deposition in a subglacial setting with no marine influence (Evans et al., 2005; Ó Cofaigh et al., 2005). Based on these properties, and its association with MSGL, Unit 1 is interpreted as a subglacial deformation till. The presence of diatom fragments indicates the incorporation/re-working of glaciomarine sediments during ice stream advance (e.g., Ó Cofaigh et al., 2005). Similar diamictons described from other areas of the Antarctic continental shelf have been divided into soft and stiff tills, based on shear strength (Evans et al., 2005; Ó Cofaigh et al., 2005; Reinardy et al., 2011). Whilst the boundary between soft and stiff till is often ambiguous, it typically falls between 20 and 25 kPa (Evans et al., 2005; Reinardy et al., 2011). In most instances the massive diamictons described in this study have shear strength values <26 kPa; this is used as the boundary between soft and stiff tills. Shear strength values of >26 kPa occur towards the base of cores GC692, GC690, GC711 and GC703. It has been speculated that such areas of stiff till represent regions of enhanced basal roughness and friction, which might promote the development of bed instabilities that form MSGL (Ó Cofaigh et al., 2005). It is also generally accepted that the stiff tills represent initial ice advance across the shelf, prior to the establishment of ice streaming (Ó Cofaigh et al., 2005). Sediment core GC703, recovered from a shallower trough flank, contains two packages of massive diamicton, one at the base (229-386 cm) and the other between 66 and 122 cm (Fig. 4.4l). This core was recovered from the relatively shallow trough flank west of AHT, in an area characterised by abundant iceberg scours (4.2a). Given its location and the fact that iceberg turbates are often indistinguishable from deformation tills (Hillenbrand et al., 2005), Unit 1 in this core is interpreted as an iceberg turbate.

The clay mineral assemblage of sediments, reflect the rocks from which they were sourced and can therefore be used to identify the source of sediments and reconstruct transport pathways (Hillenbrand and Ehrmann, 2002; Hillenbrand et al., 2009). Sediment samples within AHT are dominated by chlorite, illite and smectite, with chlorite being the most abundant mineral. These clay minerals reflect the Jurassic-Palaeogene arc volcanic rocks exposed on the Antarctic Peninsula (British Antarctic Survey, 1981a; British Antarctic Survey, 1981b) (Fig. 2.1). Enrichment of smectite in some samples could reflect supply of non-metamorphised intrusive rocks from Anvers Island. Variability in the clay mineral assemblage of diamictons within and between cores could result from the spatial distribution of source rock outcrops or temporal changes in transport pathways.

4.3.2. Unit 2: Stratified diamicton

The transition from massive diamictons to stratified diamicton represents a change in depositional environment. The high concentration of sand and gravel imply a grounding line-proximal setting (Powell, 1984; Light et al., 1999; Evans et al., 2005; Ó Cofaigh et al., 2005; Smith et al., 2011) whilst the decrease in the mud content relative to Unit 1, indicates an increasing marine influence (e.g. stronger currents/winnowing of fine sediments post-deposition). Unit 2 is thus interpreted as a glaciomarine facies, deposited in a grounding line proximal setting. Discerning whether Unit 2 was deposited beneath an ice canopy (ice shelf or permanent sea-ice) is less straightforward but is important for two reasons. Firstly, ice shelves exert a significant control on the depositional processes which operate at the grounding line and beyond (Smith et al., in press). Secondly, the presence or absence of an ice shelf is thought to exert a significant control on the rate of grounding line retreat (e.g., marine ice cliff instability; Pollard et al., 2015; DeConto and Pollard, 2016). Traditionally ice shelf cover has been inferred based on the presence of so-called pelletized muds together with low biogenic content (Domack and Harris, 1998; Domack et al., 1999). Conversely, stratified diamictons (directly above subglacial till) that contain higher contents of biogenic detritus are more likely to have been deposited in a tidewater/ice cliff setting where coarse grained and biogenic-rich facies can be deposited simultaneously (Domack et al., 1998). However, pelletized muds are regionally patchy and not always found in sub-ice-shelf sediments (e.g., Kilfeather et al., 2011; Smith et al., 2017; this study). Furthermore, biogenic material and suspended sediments can be advected beneath the ice shelf from the open-ocean (Hemer and Harris, 2003; Hemer et al., 2007; Post et al., 2014), meaning that high-biogenic content cannot be used to rule out ice shelf cover. In instances where advection of biogenic detritus cannot be ruled out, greater

diversity of exotic lithologies (transported via icebergs) might help differentiate between stratified diamictons deposited in a sub-ice shelf or tidewater/ice cliff setting. Sediments deposited in a sub-ice-shelf environment are more likely to have a restricted provenance, largely comparable to the underlying subglacial till.

In most instances the clay mineral assemblage of the stratified diamictons comprising Unit 2 is similar to that of the underlying till, suggesting a shared provenance/source area. Exceptions to this is a smectite enriched (41 %) layer of Unit 2 at 220 cm depth within core GC703 (Fig. 4.4l) which indicates input of sediments from a different source area, either by icebergs or ocean currents or erosion of different sea-floor sediments and/or changing glacier flow (Domack and Harris, 1998; Domack et al., 1998; Domack et al., 1999; Hillenbrand et al., 2009). The biogenic content of Unit 2 remains comparable to Unit 1, indicative of low biological productivity. Based on the low biogenic content of sediment and the overall lack of exotic debris, sediments are interpreted to have been deposited within a sub-ice shelf cavity. The laminated to stratified structure likely reflects a number of processes, some of which may happen simultaneously; including rain-out of debris from overhanging dirty ice, meltwater discharge and the settling out of fine grained sediment, changes in current activity, variations in the flux of debris at the grounding line and glaciogenic debris flows (Powell et al., 1984, 1996; Ó Cofaigh et al., 2005).

The stratified diamicton in GC697 (360-460 cm) differs from other cores in that it has a sharp lower boundary and coarsens upwards from its base (Fig. 4.6a). Its upper boundary is gradational. Although debris flows have the potential to deliver coarse debris, they are typically massive and are characterised by sharp upper and lower (erosional) boundaries (Kurtz and Anderson, 1979; Evans et al., 2005; Hillenbrand et al., 2005; Ó Cofaigh et al., 2005). Furthermore, the graded nature of this unit is indicative of sorting during dumping of sediment rather than representing the tail of debris flow. Such sorting could occur at a calving line, where icebergs melt and/or roll-over producing graded deposits (Drewry and Cooper, 1981; Powell, 1984; Evans and Ó Cofaigh, 2003). Unit 2 in core GC697 is thus interpreted to have been deposited at the ice shelf calving line, which also implies that an ice shelf must have existed inboard of GC697 at some point during deglaciation.

4.3.3. Unit 3: Mud alternating with gravel and sand

Unit 3 is present in core GC704 only (Figure 4.9). The sand and gravel layers, within an otherwise muddy unit, indicate episodic delivery of coarse sediment either through melt-out

of englacial debris within an ice cavity or melt-out from icebergs (Powell, 1984, 1996). Inspection of the X-radiographs reveals that the coarser sand and gravels layers are clast supported, suggesting that fine sediments have been transported away during deposition, or winnowed post deposition (Fig. 4.5c). This finding, together with the proximity of core GC704 to the shelf edge, where high bottom currents are common (Pudsey et al., 1994; Pirrung et al., 2002; Hillenbrand et al., 2010b), supports the interpretation that Unit 3 is the result of winnowing.

4.3.4. Unit 4: Mud alternating with silt laminae

Unit 4 is present in cores GC697 and GC698 (Figure 4.9). The fine-grained nature of the sediment suggests deposition in a grounding line-distal setting (Domack and Harris, 1998). Silt laminae may be introduced through the lateral sorting of sediment-rich meltwater plumes by tidal/ocean currents (Jacobs et al., 2011; Kilfeather et al., 2011; Witus et al., 2014; McKay et al., 2016; Smith et al., 2017). The grain size of the laminated sandy muds varies from clays to very fine silt, with peaks in grain size comparable to the fine fraction of the massive diamictons deposited subglacially (Unit 1) (Fig. 4.8). This is indicative of a grounding line source (Prothro et al., 2018). The predominantly terrigenous composition of Unit 4, with low biogenic content relative to Units 5-7, indicates deposition in a low productivity environment associated with the presence of an ice shelf (Domack and Harris, 1998; Kilfeather et al., 2011; Smith et al., 2014; Smith et al., 2017). The lack of coarse grained material is also indicative of a grounding line distal setting, as basal debris tends to be preferentially melted out of the ice shelf base within ~10 km of the grounding line (Domack and Powell, 2018). The properties of Unit 4 are consistent with grounding line-distal sediments deposited beneath the Pine Island Glacier ice shelf, >1.5 km from the grounding line (Smith et al., 2017).

Within core GC697, Unit 4 is 234 cm thick. Furthermore, core site GC697 is located directly seaward of GZW 3b indicating that (a) the grounding line was stable for some time and (b) that the ice shelf existed during wedge formation. Similar deposits are observed in GC698, this implies that an ice shelf existed after the grounding line had retreated further inshore. However, unlike GC697, Unit 4 is relatively thin in GC698, which could suggest that any period of ice shelf cover on the innermost part of the shelf was relatively brief, or that sedimentation rates were much lower.

4.3.5. Unit 5: Bioturbated mud with dispersed gravel

The fine-grained nature of Unit 5 also indicates deposition in a grounding line distal setting (Domack and Harris, 1998). The biogenic content, in particular the diatom component, of this unit is higher than that of Units 1, 2 and 4; however, it is lower than that of Units 6 and 7. This could represent a relatively higher terrigenous sediment input relative to Units 6 and 7, diluting the diatom component of the sediments, or relatively low primary productivity relative to Units 6 and 7. Terrigenous sediment supply could be increased through a relatively ice-proximal position compared to Units 6 and 7 or high rates of iceberg rafting (MacAyeal, 1985; Domack and Harris, 1998; Domack et al., 1999; Le Brocq et al., 2013), whilst a decrease in biogenic content could relate to a pervasive ice canopy and/or unfavourable climatic conditions which suppress biological production (e.g., cooling) (Maddison et al., 2005; Leventer et al., 2006). Unit 5 has a clay mineral assemblage indicative of well-mixed sediments, derived from various source regions within or out of the AHT (Hillenbrand et al., 2009). Within core GC690, this layer (260 cm) has a clay mineral assemblage that is characterised by higher chlorite and illite content, possibly indicating sediment delivery sourced from basement metamorphic and igneous rocks on the AP (British Antarctic Survey, 1981a; British Antarctic Survey, 1981b).

Within cores GC690, GC695, GC711, GC697, GC709 and GC698, this unit overlies stratified diamicton (Unit 2). These cores have an additional 20-40 cm thick interval of bioturbated to massive grey mud with dispersed gravel (Unit 5), overlying an initial interval of bioturbated diatomaceous ooze (Unit 7). Cores GC692 and GC691 additionally have an interval of bioturbated to massive grey mud with dispersed gravel (Unit 5), overlying an initial interval of bioturbated diatomaceous ooze (Unit 7). This suggests that environmental conditions that led to the deposition of bioturbated to massive grey mud with dispersed gravel re-occurred across much of AHT, following environmental conditions that led to the deposition of bioturbated diatomaceous ooze. This will be discussed in more detail in Chapter 5, with support of quantitative ADA and assemblage data.

4.3.6. Unit 6: Laminated to stratified diatomaceous ooze

Unit 6 (GC691, GC695 and GC698), is comprised of laminated diatomaceous ooze and is interpreted to have been deposited in a seasonally open and productive water column. *Chs*-RS and *Chs*-veg dominate the ooze layers. This subgenus is associated with early spring conditions, when melting sea ice induces stratification of the water column, concentrating nutrient delivery in the surface waters and promoting high primary productivity (Leventer, 1991; Leventer et al., 1996; Leventer et al., 2002; Maddison et al., 2005; Leventer et al., 2006).

Such conditions are typical of calving bay re-entrants (e.g., Leventer et al., 2006). Furthermore, magnetic susceptibility data indicates that this unit may be more pervasive across AHT, preserved as both thick (GC691, GC695 and GC698) and thin drapes (GC690, GC697, GC709, GC711, GC692 and GC702), depending on the bathymetry. The significance of this unit, together with controls on its deposition are discussed in Chapter 5.

4.3.7. Unit 7: Bioturbated diatomaceous ooze

Unit 7 is a diatomaceous bioturbated ooze with dispersed gravel, indicative of seasonally open marine conditions, comparable to modern-day sedimentation on the Antarctic continental shelf. It is the product of the slow settling of fine-grained hemipelagic sediment through the water column. Primary productivity is driven by high nutrient and sunlight availability, the latter of which is associated with seasonally sea ice-free conditions. Diatoms thrive in Antarctic surface waters because of nutrient delivery through meltwater discharge and the upwelling of nutrient-rich waters (Maddison et al., 2005). Variability in the contents of microfossils, biogenic opal, TOC and $CaCO_3$ over time may reflect temporal changes in oceanographic and/or climatic conditions promoting or diminishing diatom bloom events (Maddison et al., 2005; Leventer et al., 2006). Unit 7 generally thins offshore, which is consistent with previous observations on Holocene sediments deposited in Anvers Trough and which can be attributed to stronger ocean currents on the outer continental shelf (Pudsey et al., 1994). Icebergs are considered responsible for the delivery of gravel (IRD) to the core sites (Powell, 1984).

In several cores, Unit 7 is not only present as the uppermost unit but it also occurs above the overlying massive diamicton (Unit 1) and underlying bioturbated to massive grey mud with dispersed gravel (Unit 5) in cores GC692 and GC691, or sandwiched between two intervals of Unit 5 in cores GC690, GC695, GC711, GC697, GC709 and GC698 (Figure 4.9). It's presence likely reflects initial onset of open marine conditions following deglaciation, which in some cases was followed by a phase of reduced primary productivity and/or a greater influx of terrigenous sediment (e.g., deposition of Unit 5) before returning to seasonally open-marine conditions.

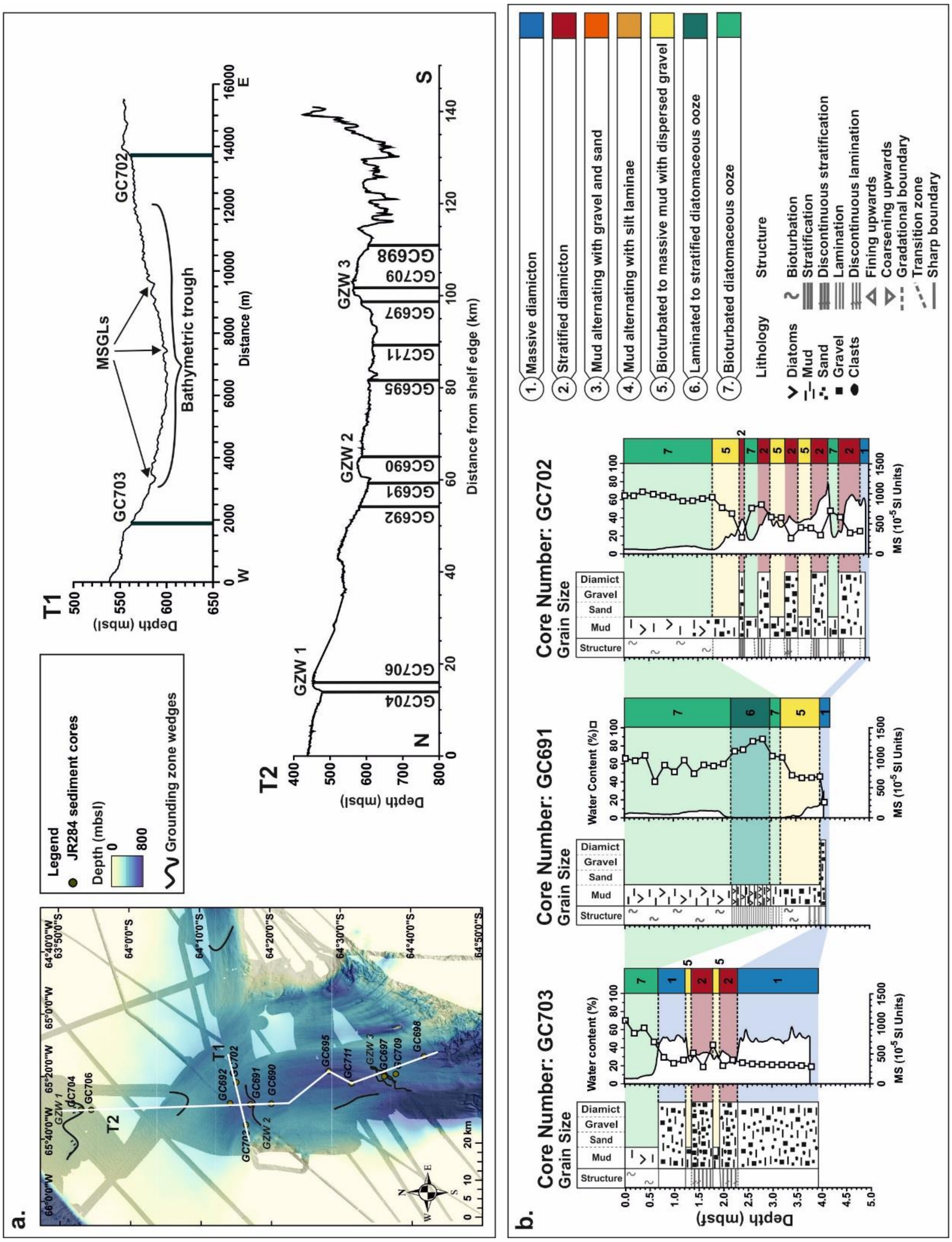
a.
Legend
JR284 sediment cores
Depth (mbsl)
0
800
Grounding zone wedges
T1
T2
GZW 1
GZW 2
GZW 3
MSGLs
Bathymetric trough
Depth (mbsl)
Distance (m)
Distance from shelf edge (km)
GC703
GC702
b.
Core Number: GC703
Core Number: GC691
Core Number: GC702
Grain Size
Structure
Mud
Sand
Gravel
Diamict
Water content (%)
MS (10^-5 SI Units)
Depth (mbsf)
1. Massive diamicton
2. Stratified diamicton
3. Mud alternating with gravel and sand
4. Mud alternating with silt laminae
5. Bioturbated to massive mud with dispersed gravel
6. Laminated to stratified diatomaceous ooze
7. Bioturbated diatomaceous ooze
Lithology
Diatoms
Mud
Sand
Gravel
Clasts
Structure
Bioturbation
Stratification
Discontinuous stratification
Lamination
Discontinuous lamination
Fining upwards
Coarsening upwards
Gradational boundary
Transition zone
Sharp boundary

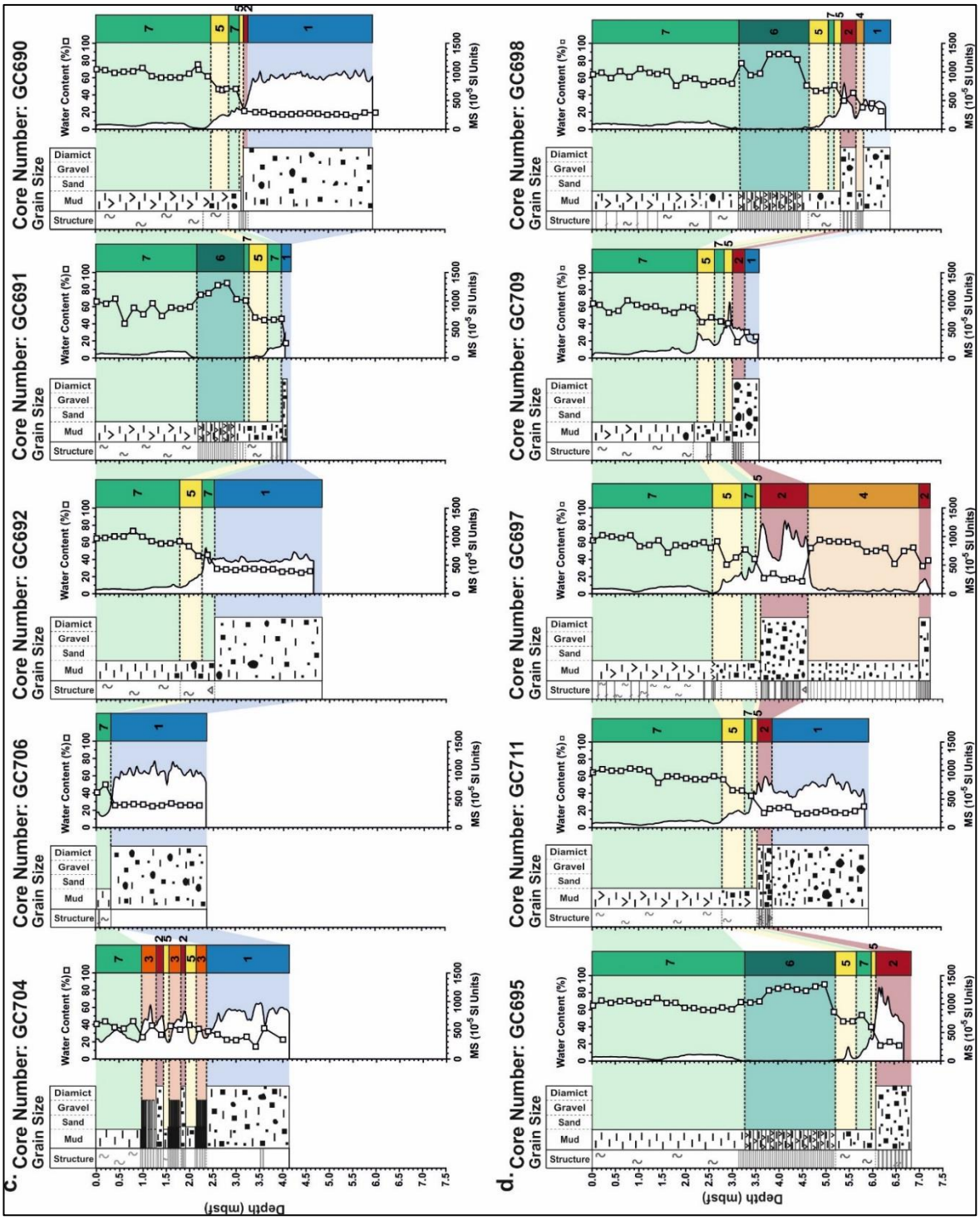

Figure 4.9: (a) Map of AHT with bathymetric profiles of the across trough transect (T1) and the along trough transect (T2). (b-d) Fence diagrams summarising the spatial distribution of lithological units within AHT. The cores recovered from the across trough transect (T1) are shown in Panel b. The cores recovered from the along trough transect (T2) are split into two panels, c and d. Also shown are magnetic susceptibility values and water contents for each core.

4.4. Discussion

4.4.1. Processes and influences controlling transitional sediment variability

Detailed sedimentological analyses of cores recovered from AHT reveal that transitional subglacial to glaciomarine facies are highly variable. This heterogeneity, also identified in other studies (e.g., Evans and Pudsey, 2002; Kilfeather et al., 2011), likely reflects several overlapping depositional processes and sediment pathways, operating over a range of temporal and spatial scales (Fig. 4.10). The ultimate aim of this section is to identify sediment end-members (Fig. 4.11) which are representative of key processes and modes of sedimentation and which can be used to help refine future palaeo-studies. These end-members are described in terms of the key physical and environmental processes identified below, including marine processes, the rate and style of grounding line retreat, the presence or absence of an ice shelf and bathymetric context (e.g., along/across trough position). On the basis of detailed sedimentological information outlined in sections 4.2 and 4.3, six broad depositional environments are identified and summarised below. Note that the distances (from grounding line) given in parenthesis below are best estimates based on published literature (e.g., Powell et al., 1996; Domack and Powell, 2018). However, these distances are poorly constrained due to a lack of data from extant ice shelves so may not be applicable for all grounding-line/ice shelf systems.

a. Subglacial: Sediment deformation produces both stiff and soft till (Powell, 1984; Boulton, 1996; Ó Cofaigh et al., 2005; Anandakrishnan et al., 2007) (Fig. 4.10; no. 3 and 4) (Fig. 4.11i). This corresponds to Unit 1: Massive diamicton.
b. Grounding line (<1 km): Processes active in this setting are variation in sediment flux including from glaciogenic debris flows, melt/rain-out of englacial debris from overhanging dirty ice, meltwater-sediment discharge (including steady-state and catastrophic release(s)). Current/tidal activity can modify both suspended sediment in the water-column (i.e., before it is deposited) as well as sediment already deposited on the seabed. Remobilisation of sea-floor sediment by grounding line oscillation is also likely (Drewry and Cooper, 1981; Powell, 1984; Powell et al., 1996; Ó Cofaigh et al., 2005; Christianson et al., 2017) (Fig. 4.10; no. 2, 5, 6, 7, 8 and 9) (Fig. 4.11ii). This corresponds to Unit 2: Stratified diamicton.
c. Grounding line proximal (~1-10 km): Sedimentation is likely to dominated by the melt/rain out of englacial debris (ice shelf setting), depositing a wide-range of grain-sizes from mud to gravel (Fig. 4.10; no. 2 and 7) (Drewry and Cooper, 1981; Powell, 1984; Powell et al., 1996; Domack and Harris, 1998). Additionally, deposition of sediments suspended in sediment-laden plumes, produce fine (silt/clay) laminated

muds. Ocean and tidal currents are also important in proximal settings (Fig. 4.10; no. 8 and 9). Sediments are entirely terrigenous, except in special circumstances (e.g., strong advection/inflow) (Powell, 1984; MacAyeal, 1985; Domack and Williams, 1990; Powell et al., 1996; Domack et al., 1999; Evans et al., 2005; Kilfeather et al., 2011; Witus et al., 2014; Smith et al., 2017) (Fig. 4.11iii). This corresponds to Unit 3: Mud alternating with sand and gravel.

d. Grounding line distal (>10 km): Deposition is dominated by sediment-laden meltwater plumes, which produce fine (silt/clay) laminated muds (Fig. 4.10; no. 7) (Powell, 1984; MacAyeal, 1985; Domack and Williams, 1990; Powell et al., 1996; Domack et al., 1999; Evans et al., 2005; Kilfeather et al., 2011; Witus et al., 2014; Smith et al., 2017). Whilst mostly terrigenous, biogenic detritus increases due to advection (Fig. 4.10; no. 9). Ultimately the laminated muds likely grade into massive muds (Fig. 4.11iv). This corresponds to Unit 4: Mud alternating with silt laminae.
e. Calving line: Dominated by melt out of iceberg basal debris, depositing layers of mud, sand and gravel. These deposits may be distinguishable from melt out of englacial debris (an ice shelf setting) by a higher biogenic content and greater diversity of lithologies from a wider area, brought in by icebergs calved from different glaciers or ice streams (Drewry and Cooper, 1981; Powell, 1984; Powell et al., 1996). Supra-glacial debris can be deposited at the calving line and from iceberg melting/tipping. In the case of supraglacial debris, sediments can be dumped as a result of iceberg tipping; this can cause sediments to be sorted as they fall through the water column, producing an upwards fining unit (Drewry and Cooper, 1981; Powell, 1984; Evans and Ó Cofaigh, 2003) (Fig. 4.10; no. 10) (Fig. 4.11v). This could correspond to Unit 2: Stratified diamicton, or Unit 5: Bioturbated to massive mud with dispersed gravel.
f. Seasonally open marine: Deposition of biogenic material produces diatomaceous muds. Gravel-size grains are supplied by icebergs; iceberg-rafted debris (Fig. 4.10; no. 10, 11 and 12) (Fig. 4.11vi). This could correspond to Unit 7: Bioturbated diatomaceous ooze, or Unit 5: Bioturbated to massive mud with dispersed gravel, when diatom productivity is low. When productivity is particularly enhanced, deposition of Unit 6: Laminated diatomaceous ooze, may occur.

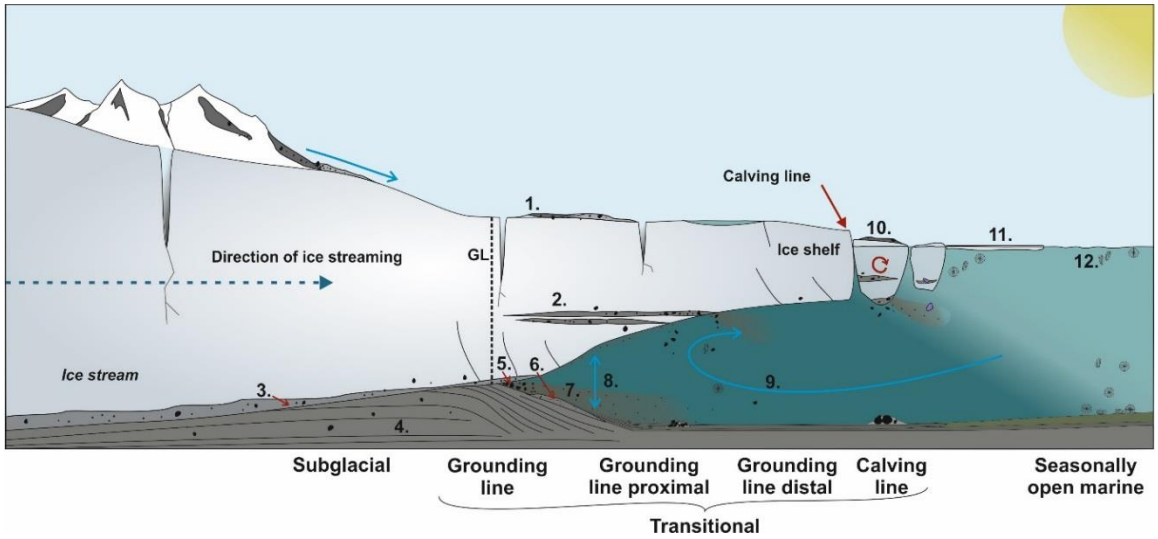

Figure 4.10: Schematic model illustrating subglacial, transitional and open marine depositional environments of an ice stream with fringing ice shelf (not to scale). Shown are the location of the grounding line (GL), ice shelf and calving line, sediment sources and processes active. These include (1) supraglacial debris, (2) englacial debris, (3) debris entrainment within basal ice, (4) subglacial deformation, (5) sediment melt-out at the grounding line (GL), (6) sediment gravity flows, (7) meltwater plumes, (8) tidal motion, (9) ocean currents, (10) iceberg rafting, tipping and debris release, (11) sea ice production and (12) biological productivity (after Domack and Harris, 1998).

4.4.2. Marine processes

As sediment enters the marine environment it is influenced by several marine processes, including temporal and spatial variations in oceanic properties (e.g., temperature, current velocity and direction) (Powell, 1984). Weak currents will allow fine sediments to settle out of suspension (Fig. 4.11; row a), whilst strong currents can prevent fine sediments from being deposited and can also winnow fine sediments from deposited material to produce a relatively coarse lag deposit (Fig. 4.11; row b). Core GC704, recovered from the outermost shelf position, contains layers of well-sorted gravel and sand, interpreted to result from variation in sediment delivery at the ice sheet grounding-line. The well-sorted nature of these sediments suggests currents are transporting the fine fraction away, likely as a result of high bottom current activity at the shelf edge (e.g. 4.11; bii and biii) (Pudsey et al., 1994). In contrast, the silty-laminae in cores GC697 and GC698, recovered from the mid-shelf, suggest deposition in a quiescent (sub-ice shelf setting) and potentially more grounding line distal environment (e.g. 4.11; aiv). In addition to shelf edge proximity, current activity will also vary with distance from the grounding line. Tidal/traction currents are likely to exert strongest influence close to the grounding line where the ocean cavity (beneath and ice shelf) is at its narrowest. In this environment, coarse-grained sediments are likely (e.g., Figure 4.11; iii). This will contrast with more grounding line-distal facies, where current velocity is reduced and fine sediments can settle out of suspension, producing submillimetre-to millimetre-scale laminae. Sediments are

also likely to be muddier and lack significant concentrations of coarse-grained material (e.g., Figure 4.11; iV). McKay et al. (2016) observed comparable mud with subtle, rhythmic, laminae in cores recovered from below the Ross Ice Shelf. On the basis of similar sediments in other Antarctic glacial retreat sequences (e.g., Domack and Williams, 1990), they interpreted the silty laminae to reflect tidally-regulated traction currents or sediment delivery by meltwater plumes sourced from a proximal grounding line. This apparent disagreement (proximal vs. distal) reflects a lack of observational data at modern day grounding lines and from beneath modern ocean shelves.

The situation is also likely to vary depending on basal melt rates. Conceptually, enhanced melting will be characterised by a thicker and/or higher concentrations of coarse-grained material from melt-out, and this is likely to be more pronounced near the grounding line where most melt occurs (Jacobs et al., 2011) and where basal ice is likely to be dirtiest. Observations beneath McKay Glacier floating tongue (Powell et al., 1996) revealed that the majority of coarse-grained material melts out of the ice shelf base within ~1.5 km of the grounding line, although later studies suggested this could be as far as 10 km (Domack and Powell, 2018) (Fig. 4.11; column iii vs. iV).

Other important factors in this equation are the amount of sediment frozen or entrained within the ice and its distribution (Evans and Ó Cofaigh, 2003) (which will depend on local geology, thermal regime of the inflowing glacier as well as availability of supraglacial debris), together with the duration that the sediment source is stable. These factors can influence the nature (coarse or fine, thick or thin) of deposition. Sediments deposited at a rapidly retreating grounding line with a low-basal melt rate will clearly differ from a grounding line that is relatively stable and subject to high melt rates.

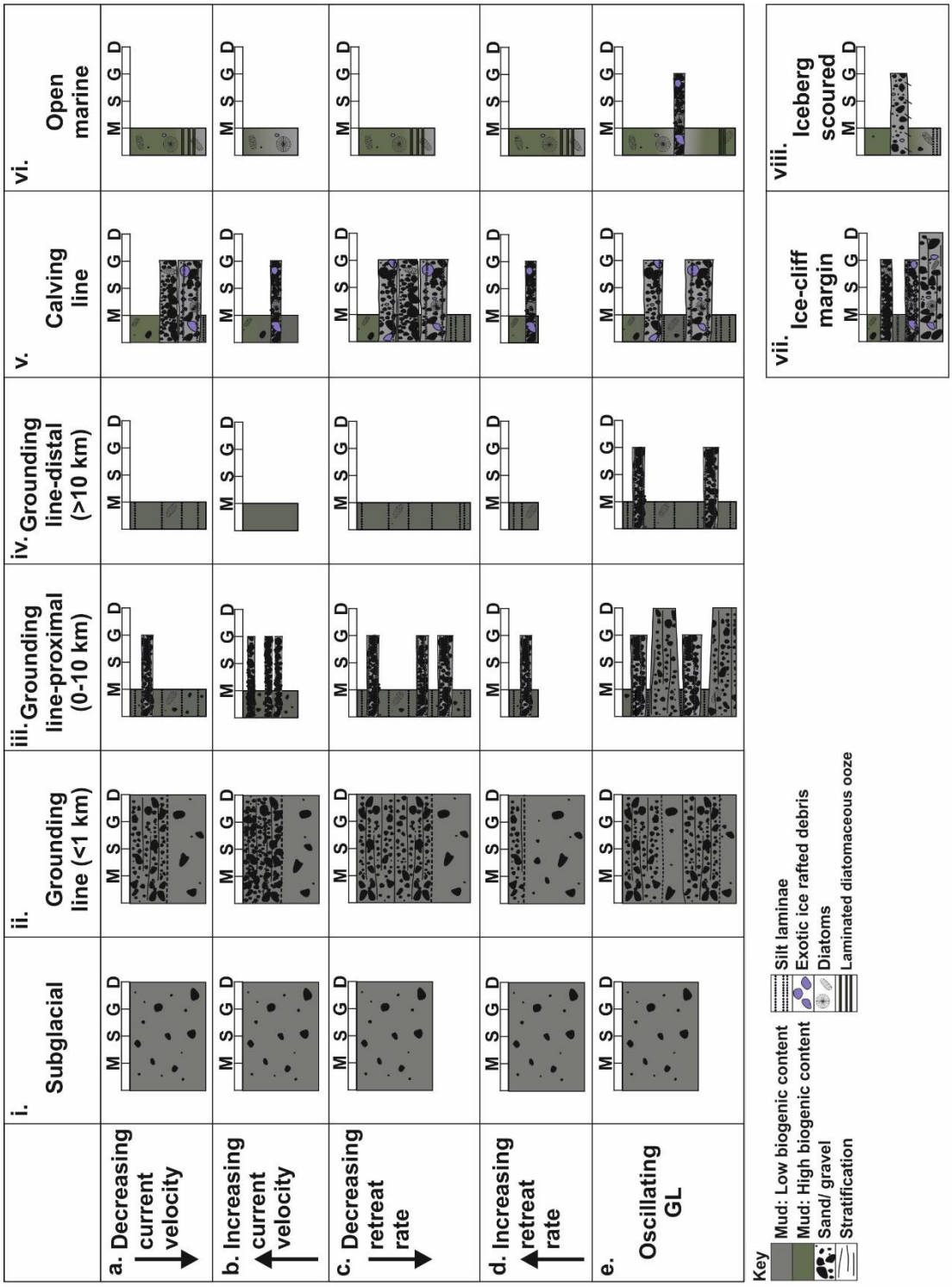

Figure 4.11: (a-e and i-vi) Sediment endmembers for sediments deposited in subglacial, grounding line (<1 km from grounding line), grounding line proximal (up to 10 km from the grounding line), grounding line distal (>10 km), calving line and seasonally open marine environments and how they are altered with changing current velocity, grounding line retreat rate and grounding line oscillations where an ice stream terminates in an ice shelf. (vii) Sediment endmember for sediments deposited at the grounding line/calving line, where an ice stream terminates in an ice cliff. (viii) Sediment endmember for shallow trough settings that experience iceberg scouring. Sediment grain size is indicated: M=mud, S=sand, G= gravel and D= diamicton.

4.4.3. Rate of grounding line retreat

Grounding zone wedges develop during quasi-stable still-stands during ice-stream retreat, with the volume of a wedge controlled by the delivery of sediment to the grounding line and the duration of the still stand (Batchelor and Dowdeswell, 2015; Dowdeswell et al., 2016). The thickness of transitional units (Units 2-4) along the AHT are highly variable, but appear to correlate with the location of GZWs; with thicker transitional sediments seawards of GZWs (e.g. GC697, GC704, GC703 and GC702), and thinner sequences of transitional sediments between GZWs (i.e. between GZW 1 and 2) (Fig. 4.9). Thus, assuming that sediment delivery to the grounding line is constant through time, we interpret the variable thickness of transitional sediment facies in AHT as a function of retreat rate (Fig. 4.11; row c vs. row d). In this context, the duration of still-stands appears to be the most important factor in controlling sediment thicknesses. Minor oscillations of the grounding line and/or varying sediment flux are reflected in the interbedded coarser and finer units (GC704 and GC702) (Fig. 4.11; row e). During fast ice stream retreat (e.g. between the GZWs), the sediment source (both from the grounding line and melt-out of englacial sediments from an overhanging ice shelf) is constantly retreating so there is insufficient time for thick deposits to accumulate. Further verification of this hypothesis requires accurate dating. Current estimates based on sediment flux data, suggest the GZWs form over a very broad time-range from 3,700 (Whales Deep, Ross Sea; Bart et al., 2017) to as little as ~120 years (Pine Island Trough, Amundsen Sea; Graham et al., 2010).

4.4.4. Presence or absence of an ice shelf

As discussed, the geometry of the ice stream margin, and specifically whether it has a fringing ice shelf, exerts a significant control on the depositional processes which operate at the grounding line and beyond. Furthermore, the presence or absence of an ice shelf is also thought to exert a significant control on the rate of grounding line retreat (Pollard et al., 2015; DeConto and Pollard, 2016), which, as noted above, also has the potential to influence debris release. In this study, the clay mineral assemblage and biogenic content of sediments are used to identify the presence or absence of an ice shelf during the last deglaciation of AHT. Ultimately, at a tidewater/ice cliff, siliceous and calcareous microfossils together with coarse-grained terrigenous sediments would be deposited simultaneously (Domack et al., 1998) (Fig. 4.11; vii and Fig. 4.12). It also follows that stratified diamicton deposited at the grounding line of tidewater margin/ice cliff would contain a higher proportion of exotic lithologies (transported via icebergs) compared to a stratified diamicton deposited in an ocean cavity beneath an ice shelf (Fig. 4.12) (Drewry and Cooper, 1881; Domack and Harris, 1998; Domack et al., 1998;

Domack et al., 1999). In this study, the majority of stratified diamictons (Unit 2) are characterised by low biogenic content and a clay mineral assemblage that is comparable to underlying sub-glacial sediments and because of this are interpreted to have been deposited in a sub-ice shelf environment.

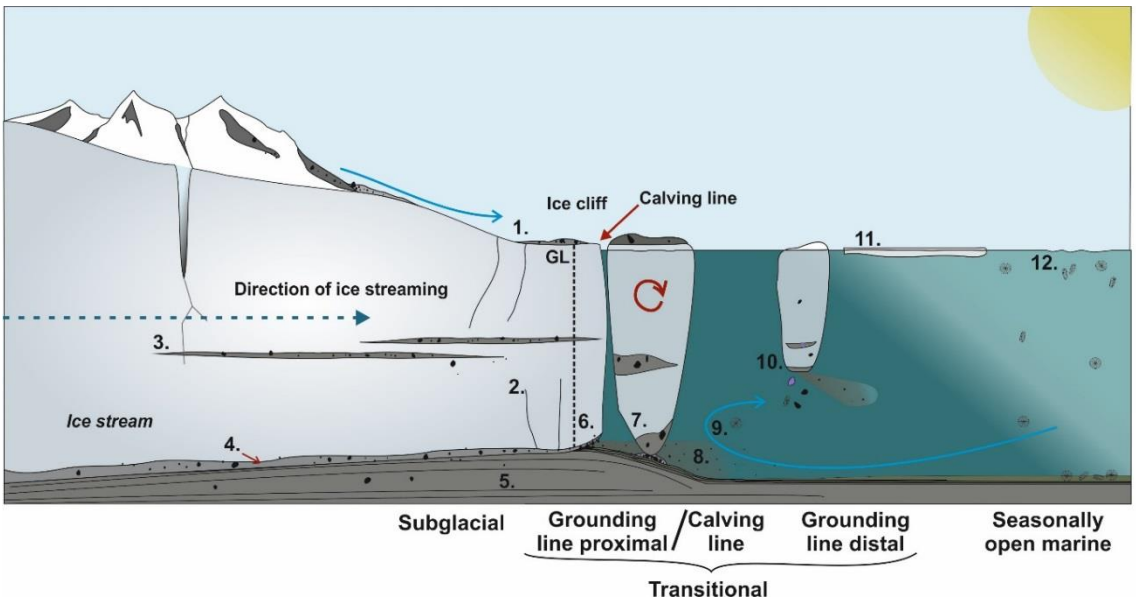

Figure 4.12: Schematic model illustrating the location of the subglacial, transitional and open marine depositional environments when an ice stream is grounded on a polar continental shelf with an ice cliff margin (not to scale). Diagram includes the location of the ice stream grounding line (GL), ice shelf and calving line, sediment sources and processes active. These include (1) supraglacial debris, (2) ice crevassing, (3) englacial debris, (4) debris entrainment within basal ice, (5) subglacial deformation, (6) sediment melt-out at the grounding line (GL), (7) iceberg rafting, tipping and debris release with potential seafloor scouring, (8) meltwater plumes, (9) ocean currents, (10) exotic iceberg rafted debris release (11) sea ice production and (12) biological productivity.

Away from these grounding-line proximal ice shelf facies, the most expanded sub-ice shelf sediments occurs in GC697. GC697 contains a 234 cm-thick unit of mud/silt laminae (Unit 4), which is interpreted to reflect deposition by sediment-rich meltwater plumes distal from the grounding line (Fig. 4.11; column iv). This core site coincides with a narrowing of the AHT between Anvers and Hugo Islands; a setting that would provide ice shelf pinning points and shelter from wind, waves and currents. These conditions favour ice shelf formation and stability (Powell, 1984). Core site GC697, is also seaward of GZW 3b (Fig. 4.1 and 4.3c), which also indicates that the grounding-line, and thus the sediment source, was stationary for a prolonged period of time. The fact that comparable sequences were not recovered in other cores suggests that (a) retreat was rapid until it reached the rugged seafloor of the inner shelf which provided stabilising pinning points and allowed a large ice shelf to develop, or (b) episodes of ice shelf cover elsewhere on the shelf were relatively short-lived and thus only characterised by coarse-grained sub-ice shelf facies (e.g. Units 2, 3).

Thus, the evolution of the ice shelf during grounding-line retreat, both spatially and temporally, represents ongoing challenges for identifying ice shelf sediments in geological records. In this respect, additional work on modern sub-ice shelf environments is required in order to refine our understanding of sub-ice shelf facies for a range of ice shelves (from small to large). In addition, targeted coring of GZWs (Simkins et al., 2018; Bart et al., 2018) and former grounding lines that have been associated with an marine ice cliff collapse (e.g., Wise et al., 2017), are also needed in order to characterise its sedimentological and geomorphological signature.

4.4.5. Across trough position

Cores GC703 and GC702 were collected perpendicular to the along trough core transect in order to assess across trough sediment variability. These cores both contained interbedded subglacial (Unit 1) and transitional (Units 2 and 5) sediments. As discussed, the interbedded layers of stratified diamicton and bioturbated/massive mud in core GC702 (Fig. 4.4k), are interpreted to result from glacier oscillations at a temporarily stable grounding line (Fig. 4.11e); these generally have gradational contacts. GC703 also contains interbedded, albeit fewer, units of 1, 2 and 5, typically with sharp contacts, which may also represent grounding line oscillations (Fig. 4.4l). As discussed previously, the uppermost massive diamicton in core GC703 is interpreted as an iceberg turbate (Fig. 4.11; viii). This interpretation is consistent with bathymetric data from AHT, which reveal that the trough flanks, where water depths are shallower than approximately 590 mbsl are heavily scoured. It remains unclear if the sediments analysed in this study are representative of other palaeo-ice stream trough flanks. Both cores indicate an oscillating ice margin, although it is unclear why ice on the trough flanks would step back and forth while ice in the trough axis is assumed to have remained relatively stationary (during GZW formation). It is assumed that Unit 6 (laminated/stratified diatomaceous ooze) was deposited after a calving bay was established. Therefore, ice remaining on the trough flanks might have been more susceptible to changes in mass balance and/or climate forcing. Additionally, both GC703 and GC702 sit at the confluence between ice discharging from AHT and Dallman Bay and the inferred position of local ice domes (Hugo Island and Marr Dome respectively; Fig. 2.2) so it is possible that interactions between ice in the main trough and ice draining these domes led to a more dynamic setting (Lavoie et al., 2015).

4.5. Conclusions

- This chapter has provided a detailed analysis of the temporal and spatial variability within transitional sediment facies, deposited at the grounding line of a retreating ice stream, and builds on previously published conceptual models.
- Sedimentological analyses of cores recovered from AHT reveal that sediments can be divided into six broad depositional environments; subglacial, grounding line, grounding line proximal, grounding line distal, calving line and seasonally open marine.
- Detailed sedimentological information have been used to identify sediment end-members which are representative of key processes and modes of sedimentation in these depositional environments, these can be used to help refine future palaeo-studies.
- Sediments deposited in the transitional environment (grounding line-proximal to grounding line-distal) are often considered to be heterogeneous. Within core recovered from AHT, transitional sedimentary units are found to be deposited systematically, varying with:
    - Marine processes: Current activity is enhanced at the outermost shelf and at the grounding line of ice streams. Strong current activity preferentially removes the fine fraction, producing layers of well-sorted gravel and sand in a grounding line proximal setting. In contrast, units of fine silty-laminae deposited on the mid-shelf represent deposition in a quiescent and potentially more grounding line distal environment.
    - Grounding line retreat rate: The thickness of transitional units along AHT are highly variable, but the presence of thicker units appear to correlate with the location of GZWs. Assuming that sediment delivery to the grounding line is constant through time, the variable thickness of transitional sediment facies in AHT is interpreted to be a function of retreat rate. Thus, the variable thickness in transitional units and the GZWs themselves are indicative of episodic grounding line retreat through AHT, with the ice stream retreating rapidly between stable phases. Minor oscillations at the temporarily stable grounding line and/or varying sediment flux are reflected in the interbedded coarser and finer units deposited proximal to GZWs.
    - Ice shelf presence: The low biogenic content of sediments deposited at the ice stream grounding line and a clay mineral assemblage that is comparable to underlying sub-glacial sediments, indicate that the AHIS had an ice shelf at

its margin over deglaciation. Expanded sub-ice shelf sediments on the mid-shelf reflect deposition by sediment-rich meltwater plumes distal from the grounding line. This coincides with a narrowing of the AHT between Anvers and Hugo Islands; a setting that would provide ice shelf pinning points and shelter from wind, waves and currents.

  - Bathymetric position: Cores recovered from bathymetric high points are subject to intense iceberg scouring, thus forming interbedded layers of massive diamicton and bioturbated/massive mud. This is observed on the flanks of the ice stream trough.
  - Across trough position: It remains unclear if the sediments within cores recovered from the confluence between ice discharging from AHT and the inferred position of local ice domes, are influenced by ice in the main trough and ice draining these domes. Further work is required to fully understand if there are key differences between trough flank/trough axis sedimentation.

- These observations will ultimately allow us to better utilise sediment cores to accurately reconstruct the history of palaeo-ice streams and consequently build analogues between these and modern day ice streams and marine terminating glaciers.

Chapter 5

5. Palaeoenvironmental conditions of the AHT over and following deglaciation

Abstract

Glacial melt with freshwater, nutrient and sediment contributions to coastal regions, as well as changes to sea ice extent and windiness, influence diatom biomass and the dependant food chain in the modern Southern Ocean. As we attempt to predict the future of the Antarctic Peninsula ecosystem in a warming world, we are limited by the decadal timescales over which we have monitored Antarctica and its surrounding seas. Sediment cores recovered from the Antarctic margin allow us to reconstruct the style and timing of post-LGM ice sheet retreat and environmental changes following deglaciation. Several studies address drivers of enhanced primary productivity following the LGM, in particular, focussing on the analysis of laminated and varved diatomaceous sediments that provide high-resolution reconstructions of Antarctic climatic history. These ooze deposits are associated with periods of enhanced productivity, triggered by meltwater induced stratification and nutrient delivery within a calving bay setting. These studies are often focussed on the composition of laminated diatomaceous ooze, but the transition to the underlying deglacial sediments is often overlooked. The relative importance of the drivers of enhanced productivity i.e. oceanographic/climatic conditions or the establishment of a calving bay setting may, therefore, not be fully resolved. This study will utilise cores and quantitative assessment of absolute diatom abundance and species assemblages, which extend to sediments deposited during the LGM and the subsequent deglaciation, to investigate the context of laminated diatomaceous ooze deposition over deglaciation. Furthermore, the suite of cores recovered for this study, including cores that do and do not contain units of laminated diatomaceous ooze, as well as extensive bathymetric mapping, can be used to investigate the spatial extent of diatom bloom production and the controls on laminated diatomaceous ooze deposition and accumulation. Deposition of laminated diatomaceous ooze is associated with meltwater discharge and nutrient input from sea and glacial ice melt. This led to deposition of laminated diatomaceous oozes, with their spatial distribution and accumulation influenced by seafloor bathymetry. This indicates that the distribution of laminated oozes does not necessarily reflect the spatial extent of surface productivity. Grounding line retreat within AHT and the formation of a calving bay were not solely responsible for the enhanced productivity and formation of laminated diatomaceous ooze units within AHT, as laminated diatomaceous ooze units do not directly overly sub-glacial to grounding-line proximal sediments in these cores.

5.1. Introduction

The previous chapter provided a detailed sedimentological investigation of cores recovered from AHT. Sediments were interpreted in the context of ice stream advance and subsequent retreat following the LGM. It established that a range of processes are active at the grounding line of a retreating ice-stream. In addition to information about grounding line processes and the relative rates of ice stream retreat, it also identified a post-glacial sequence of mainly diatomaceous sediments (Unit 7). In several cores (GC691, GC695, and GC698), a unit of laminated diatomaceous ooze (Unit 6) occurs above the glacial sediments, interpreted to have been deposited during a period of high-productivity following grounding line retreat (Fig. 5.1). Laminated diatomaceous oozes have been described in several deglacial sequences around Antarctica, often occurring directly above or within the deglacial sediments (Leventer et al., 2002; Maddison et al., 2005; Stickley et al., 2005; Leventer et al., 2006). The oozes have been interpreted to reflect periods of high productivity and rapid export to the sea-floor, thought to be associated with meltwater induced stratification and nutrient delivery (i.e. iron fertilisation) within a calving bay re-entrant (Leventer, 2002). To explore these sediments in more detail, this chapter presents new ADA and diatom assemblage data for two cores, one containing a laminated unit (GC695) and one without (GC697), in order to reconstruct the palaeoceanographic and climatic setting of the AHT during deglaciation. The factors controlling production and preservation of laminated diatomaceous ooze deposits in this region will be investigated and then discussed in the context of similar deposits found elsewhere around Antarctica.

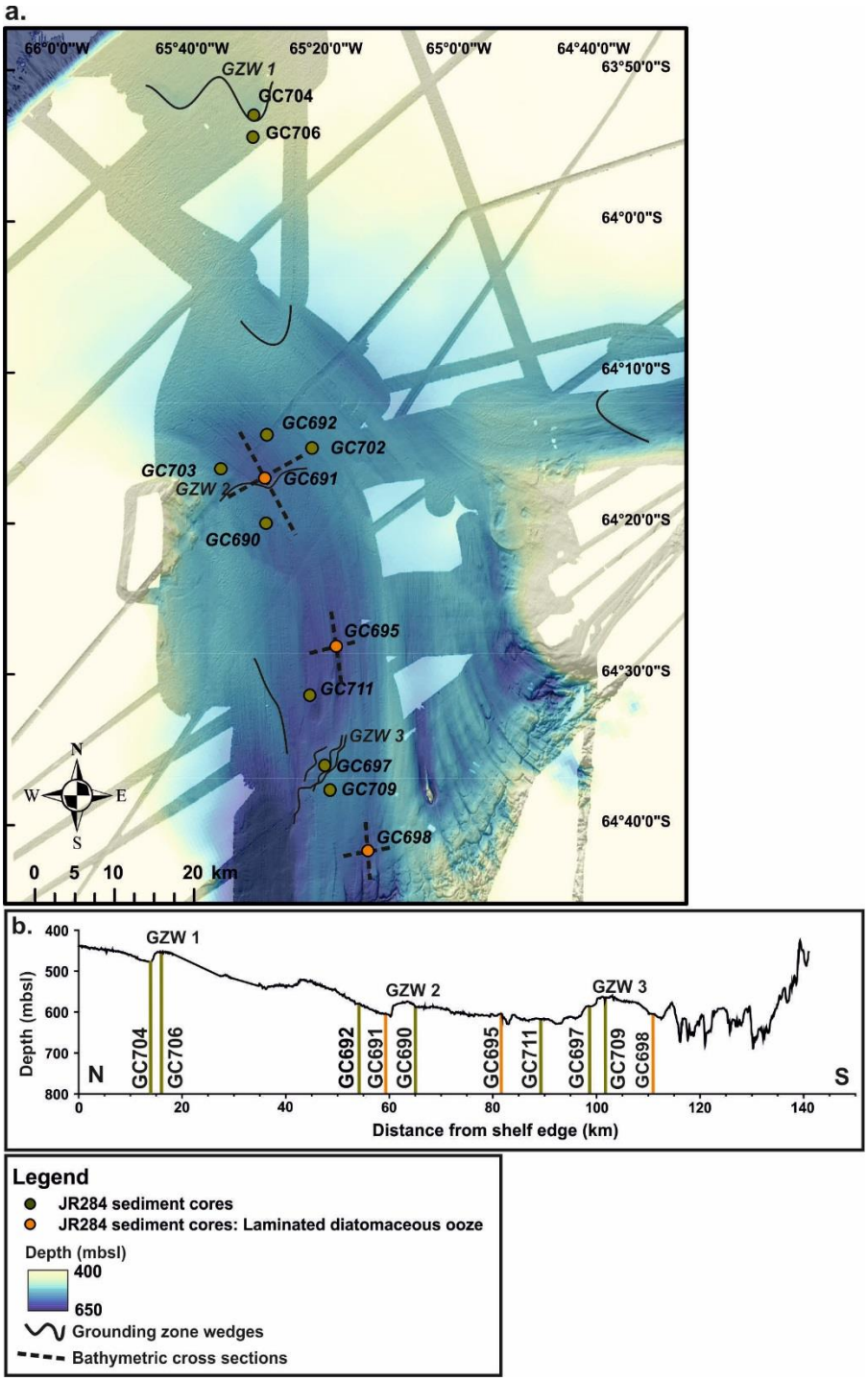

Figure 5.1: ((a) Detailed bathymetric map of AHT showing cores containing laminated diatomaceous ooze (orange circles), location of bathymetric cross sections (dashed lines; Fig. 5.5) and GZWs. (b) Bathymetric cross sections of the AHT trough with GZWs 1-3 and core locations labelled.

5.2. Results and Interpretation

5.2.1. Description of laminations

Cores GC691, GC695 and GC698 contain 1-2 m thick units of laminated sediment (Ch. 4; Unit 6). Preliminary smear slide and SEM analysis confirmed that these laminations consist

of alternating layers of grey mud, with a greater proportion of terrigenous sediment (hereafter referred to as terrigenous), and olive, olive grey and light olive brown diatomaceous ooze (hereafter referred to as biogenic) (Fig. 5.2). Although containing a higher proportion of terrigenous sediment, terrigenous laminae are not devoid of biogenic material. The terrigenous layers are typically fine-grained (Ch. 4) but are occasionally gravel-rich (e.g. Fig. 5.2; 415 cm). Boundaries between biogenic and terrigenous laminae are generally sharp in the middle of the unit and gradational and/or bioturbated towards the top and bottom (Fig. 5.3; laminated unit between 346 and 512 cm). There are 83, 68 and 44 laminae of diatomaceous ooze, intervening terrigenous laminations, ranging in thickness from 0.1-3.7 cm within cores GC695, GC698 and GC691, respectively (Fig. 5.4). The thickness of the laminations does not change systematically, i.e. thin or thicken, up or down unit (see R^2 values in Fig. 5.4).

5.2.2. Bathymetric setting of cores containing laminated diatomaceous ooze units

Along trough (N-S) and cross-trough (W-E) profiles for core sites GC695, GC691 and GC698 show that these cores were recovered from bathymetric depressions, indicating a link between shelf bathymetry and accumulation/preservation of laminated diatomaceous oozes (Fig. 5.5). The control of basin geometry and water depth on the thickness of deglacial varved sediments has been suggested previously in relation to sediments recovered from Iceberg Alley, East Antarctica (Stickley et al., 2005) and will be discussed in more detail in section 5.3.3.

5.2.3. Stratigraphic and chronological context of laminated diatomaceous ooze units

Quantitative diatom analysis of core GC695 provides insight into environmental change(s) that occurred immediately following grounding line retreat through to the modern day depositional environment of the AHT, as well as the properties and stratigraphic context of the unit of laminated diatomaceous ooze. Core GC695 is described in terms of zones, with each zone characterised by its sediment properties and diatom assemblages. Zones do not directly correlate with sedimentological units defined in Chapter 4, as some sedimentological units (e.g. Unit 7: Bioturbated diatomaceous ooze) are subdivided into multiple diatom zones here. Diatom assemblage analysis is focussed on the sediments deposited following grounding line retreat, thus sample resolution is higher for sediments underlying and within the unit of laminated diatomaceous ooze, than above.

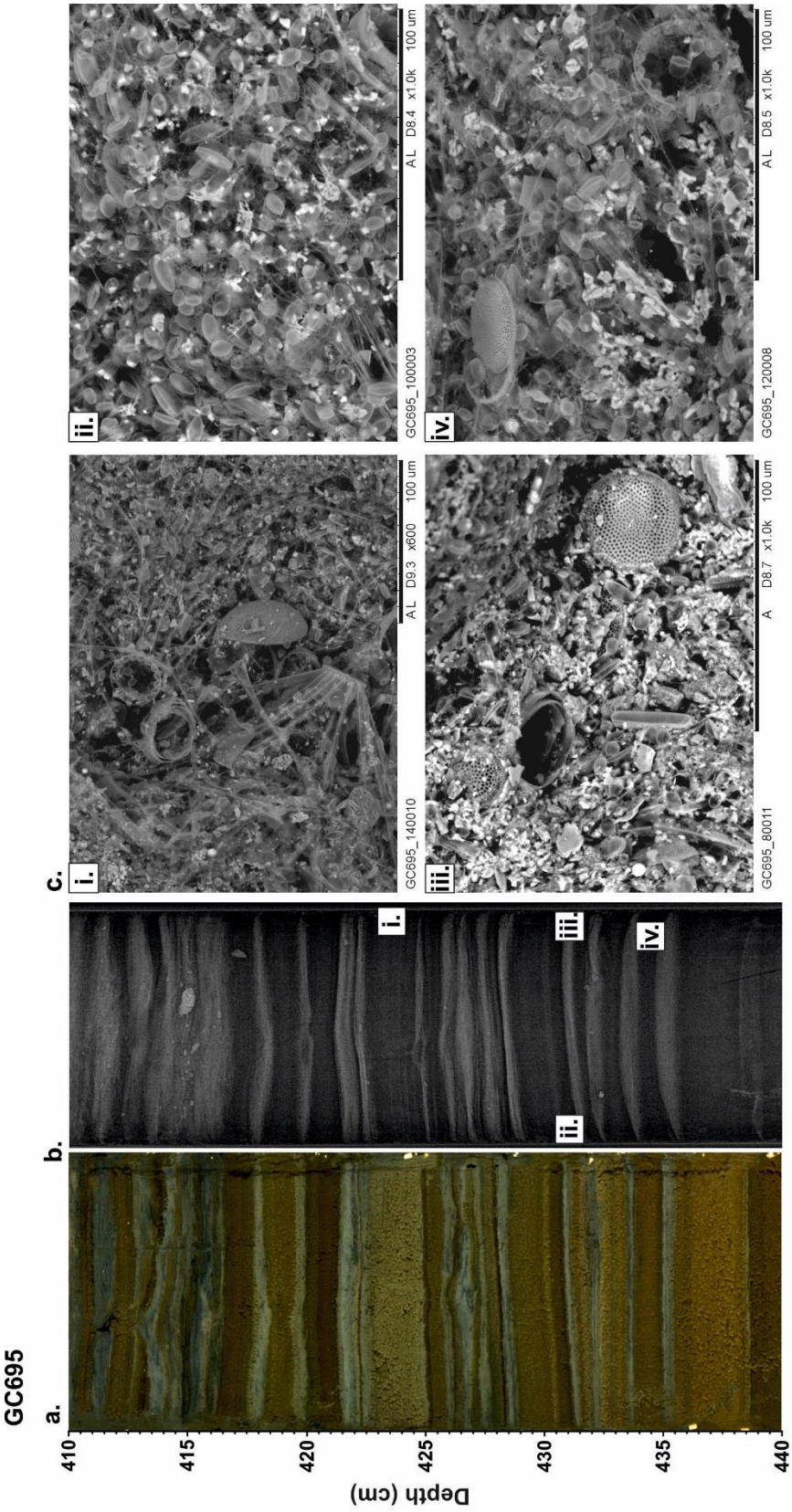

Figure 5.2: (a) Line-scan image and (b) X-radiograph (negative) of core GC695, 420-440cm, showing 'biogenic' (olive/dark layers) and 'terrigenous' (grey/light layers) laminae. (c) SEM images of biogenic laminae (i, ii, iv) and terrigenous laminae (iii). Darker shades generally indicate higher biogenic content, while lighter shades indicates higher terrigenous content.

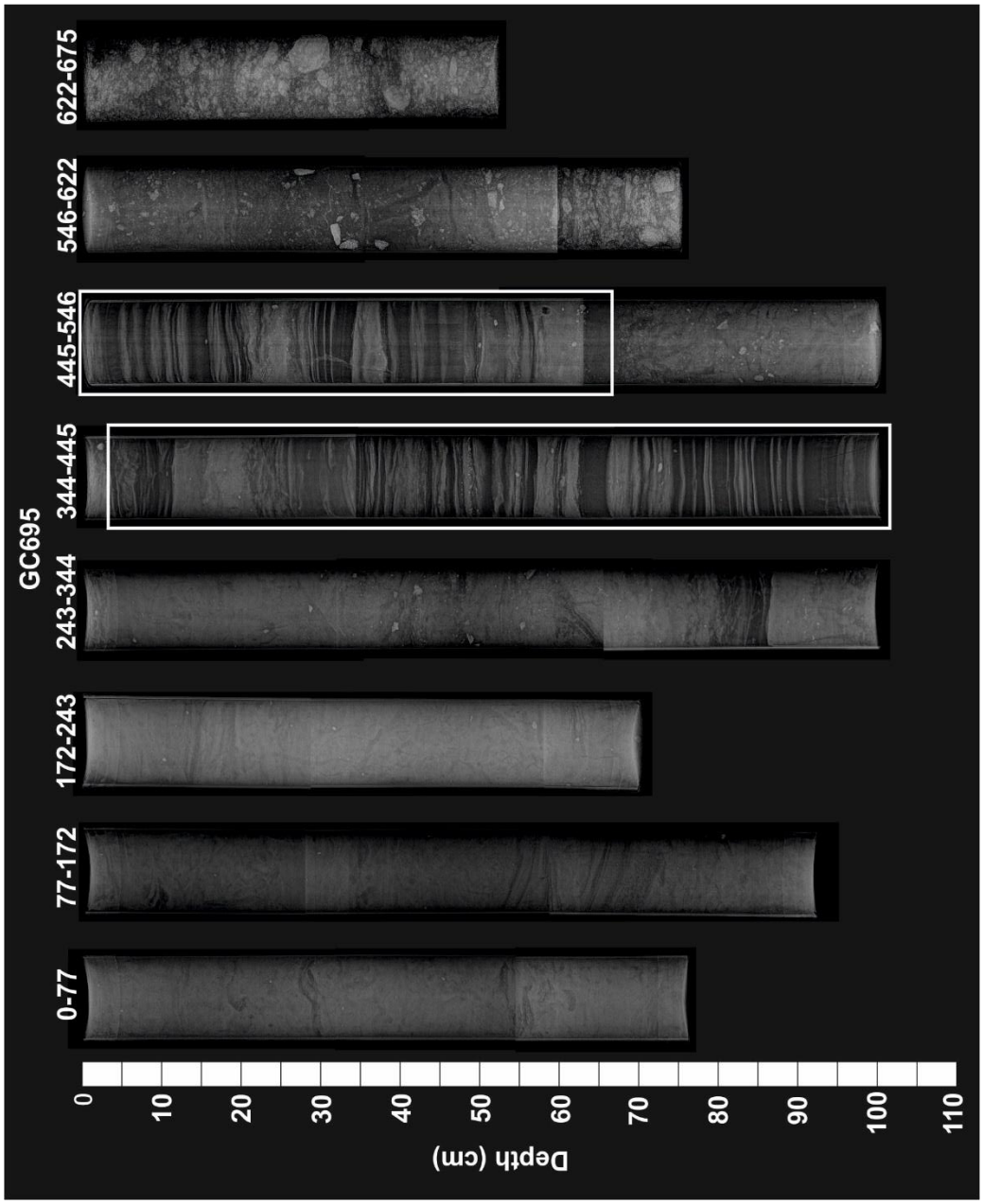

Figure 5.3: X-radiograph (negative) of core GC695. Darker shades indicate biogenic rich sediments and lighter shade indicates sediment with higher terrigenous content. The white box indicates the unit of laminated diatomaceous ooze.

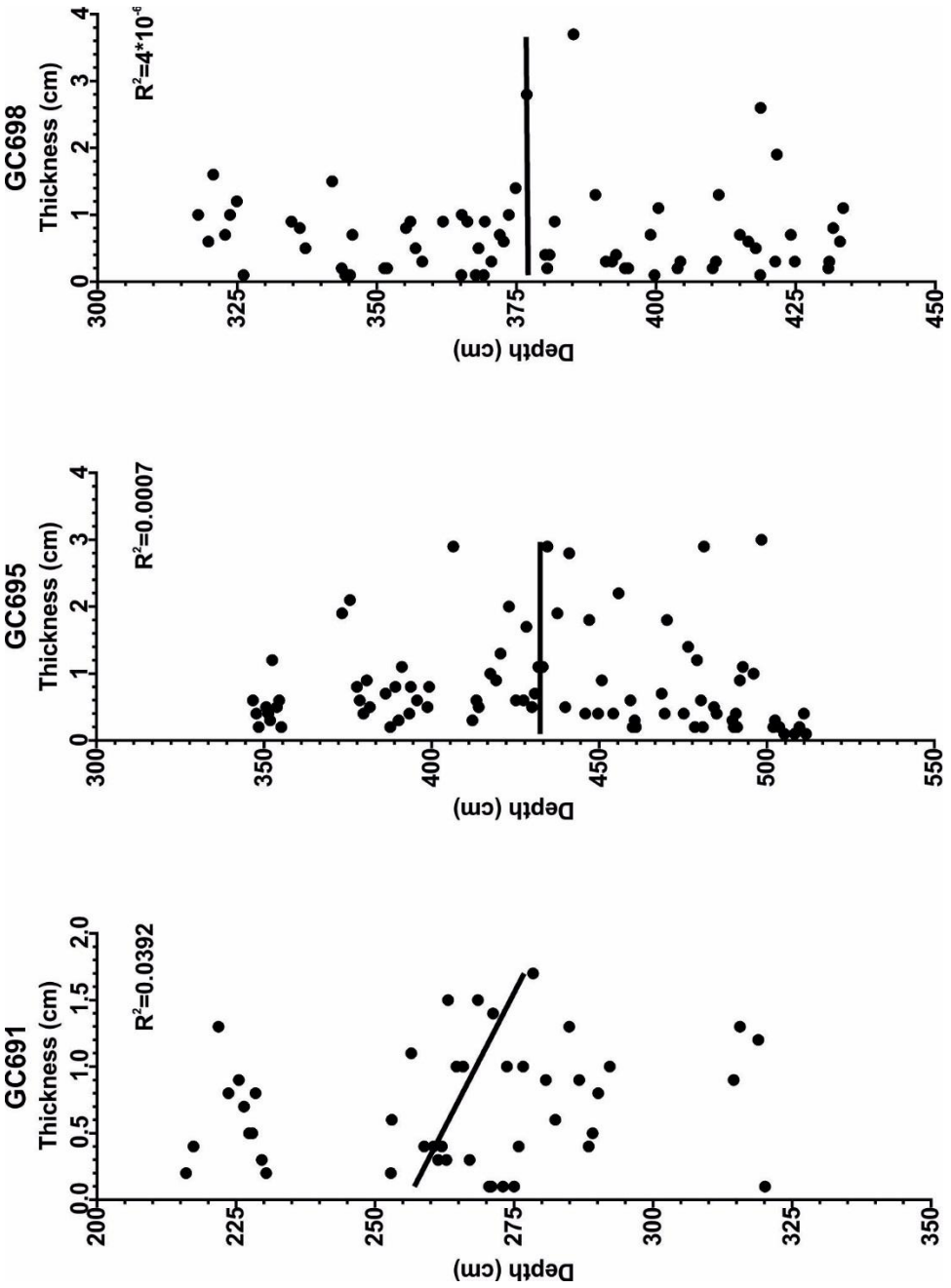

Figure 5.4: Thickness of biogenic laminae through the laminated sections of cores GC695, GC698 and GC691. R^2 values and regression line are also shown (Pearson correlation coefficient).

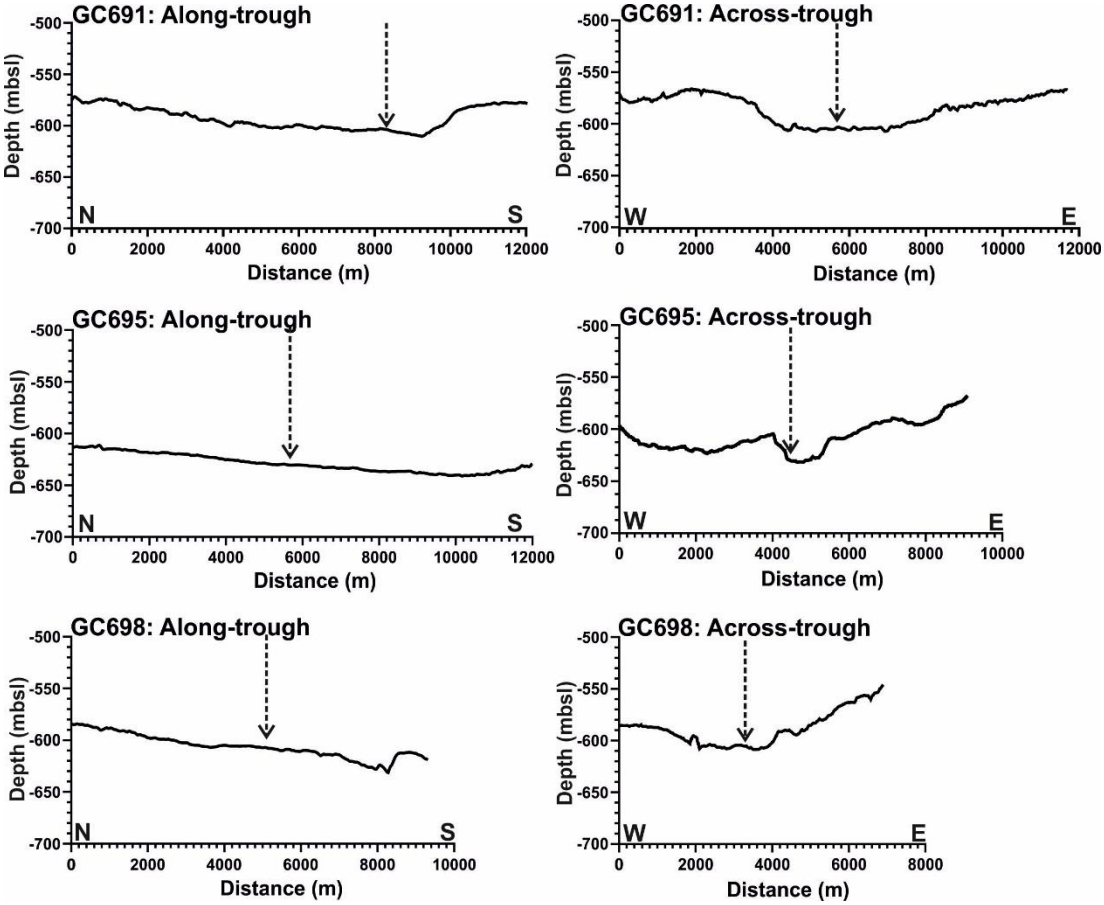

Figure 5.5: Along tough and cross-trough profiles for cores GC691, GC695 and GC698 (vertical arrow) within AHT. Locations of transects are shown in Fig. 5.1a.

5.2.3.1. GC695 Zone 1

5.2.3.1.1. Result

Zone 1 extends between 675 and 607 cm and consists of stratified diamicton. Zone 1 has an ADA of 0.02 million valves per gram (mvpg) and a total *Chs* content of 37% (Fig. 5.6). Diatom data is averaged for each zone (Table 5.1). *Fragilariopsis kerguelensis* (29%), *Thalassiosira antarctica* T2 RS (14%), *Eucampia antarctica* (14%) and *Thalassiosira lentiginosa* (7%) dominate the *Chaetoceros*-free assemblage (Fig. 5.6), with minor amounts of *Actinocyclus actinochilus* (4%), *Thalassiosira scotia* RS (3%), *Fragilariopsis curta* (4%), *Rhizosolenia* spp. (5%), *Stellarima microtrias* (3%), and *Shionodiscus gracilis* var. *expecta* (3%) (previously *Thalassiosira gracilis*; Alverson et al., 2006). It should be noted that <400 specimens/valves were identified over the 10 transects over which diatoms were counted and identified. The three samples taken in this unit at depths of 622, 642 and 666 cm had total (*Chs*-free) counts of 22 (13), 132 (67) and 64 (50) individuals, respectively.

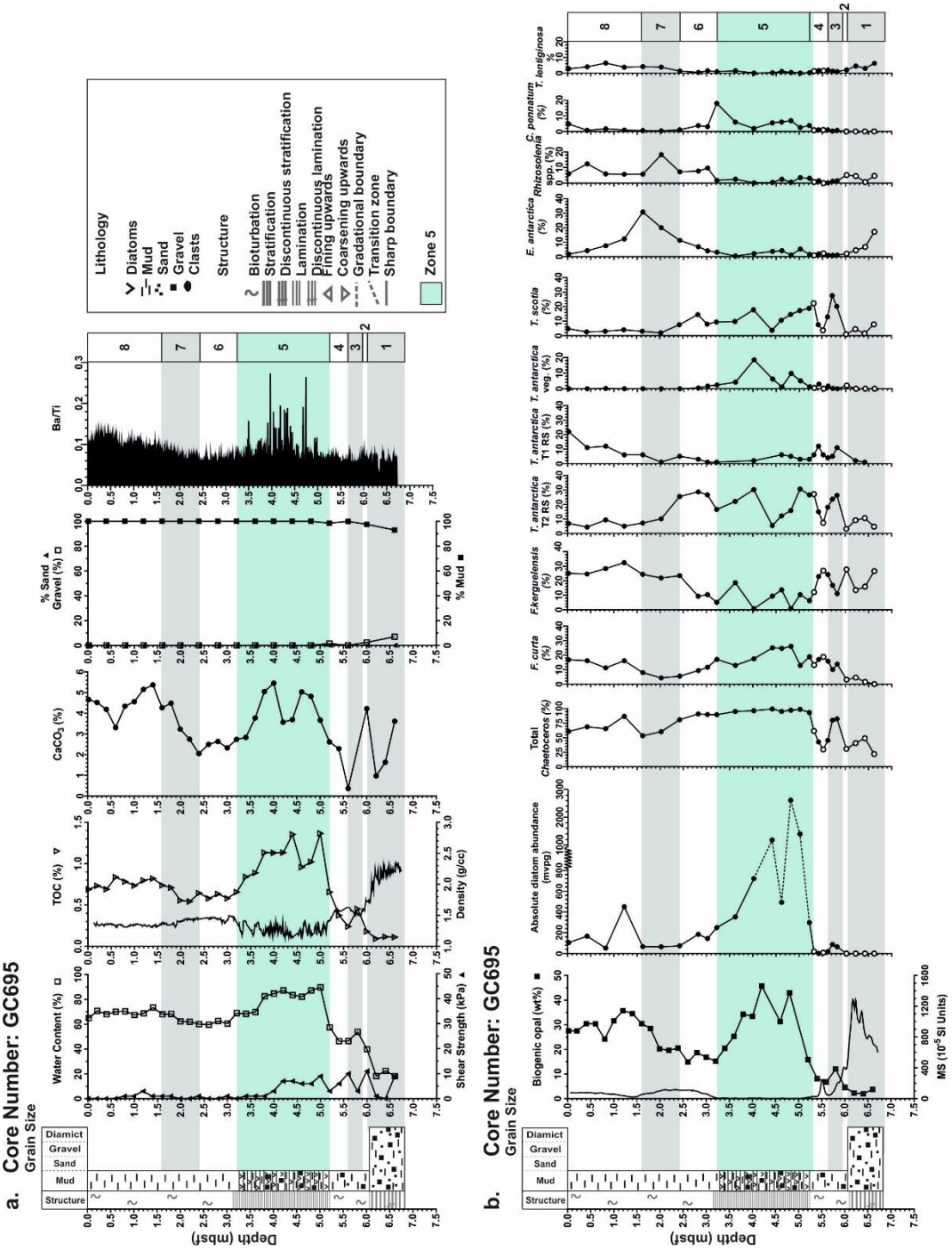

*Figure 5.6: (a) Simplified core logs and multi-proxy data for core GC695, including water content (open squares), she*ar strength (closed triangles), *TOC (open triangles), $CaCO_3$ (closed circles), density, contents of mud (<63µm, closed squares), sand (63 µm-2mm; closed triangles) and gravel (>2 mm; open squares) and Ba/Ti ratios. The laminated diatomaceous ooze unit is highlighted in green. Diatom zones (1-8) are shown on right of panel. (b) Quantitative diatom data, magnetic susceptibility (MS), and biogenic opal content (closed squares) for core GC695. Absolute diatom abundance and total* Chaetoceros *subg.* Hyalochaete *(Chs) data were collected from total diatom counts including Chs. The relative abundance data for the species* Fragilariopsis curta, Fragilariopsis kerguelensis, Thalassiosira antarctica *T2 RS*, Thalassiosira antarctica *T1 RS*, Thalassiosira antarctica *(veg)*, Thalassiosira scotia *RS*, Eucampia *spp*., Rhizosolenia *spp.*, Corethron pennatum *and* Thalassiosira lentiginosa *were collected from Chs-free counts. Samples from which <400 whole valves were counted are indicated (white circles). Diatom zones (1-8) are shown on right of panel. Full quantitative ADA and diatom species data are given in Appendix F.*

Depth (cm)	No. of samples	Absolute diatom abundance (mvpg)		Total *Chaetoceros* subg. *Hyalochaete* (%)		*Corethron pennatum* (%)		*Fragilariopsis curta* (%)		*Fragilariopsis kerguelensis* (%)		*Rhizosolenia* spp. (%)		*Thalassiosira antarctica* (T2) (%)		*Thalassiosira antarctica* vegetative (%)		*Thalassiosira scotia* (%)		*Eucampia antarctica* (total) (%)		*Eucampia antarctica* (symmetrical) (%)		*Eucampia antarctica* (asymmetrical) (%)		*Thalassiosira lentiginosa* (%)	
		Mean	SD	Mean	SD	Mean	SD	Mean	SD	Mean	SD	Mean	SD	Mean	SD	Mean	SD	Mean	SD	Mean	SD	Mean	SD	Mean	SD	Mean	SD
675-607	3	0.02	0.02	37	11	0	0	4	3	29	5	5	3	14	6	0	7	3	3	14	6	2	2	0	0	7	1
607-598	*1*	*0.03*	*0.00*	*31*	*0*	*0*	*0*	*4*	*0*	*40*	*0*	*7*	*0*	*4*	*0*	*0*	*0*	*1*	*0*	*3*	*0*	*0*	*0*	*0*	*0*	*3*	*0*
598-565	2	76	11	81	1	0	0	12	2	14	3	1	0	25	1	0	0	24	4	1	1	0	0	0	0	1	0
565-526	5	12	8	45	11	1	0	16	2	22	6	1	1	17	7	1	1	12	7	2	1	1	0	0	0	2	0
526-322	6	912	751	96	3	6	5	19	5	8	6	2	1	20	8	6	5	13	5	3	2	1	1	0	0	1	1
322-240	4	135	46	87	4	3	1	9	3	14	6	8	1	27	1	1	1	10	3	7	3	4	1	0	0	1	0
240-160	2	66	1	57	4	0	0	6	2	23	1	12	6	9	1	0	0	2	1	25	5	9	1	1	1	4	0
160-0	4	194	154	71	10	2	2	15	2	28	3	7	3	6	2	0	0	4	1	6	4	2	2	0	1	4	1

Table 5.1: Absolute diatom abundance and relative species assemblage data for most common diatoms in core GC695 (mean and standard deviation for each zone), including number of samples analysed for each diatom zone. Values for Zone 2 (italicised) are from one sample and are therefore not an average. Full quantitative ADA and diatom species data are given in Appendix F.

5.2.3.1.2. Interpretation

In Chapter 3, stratified diamictons (Unit 2 equivalent to Zone 1) were interpreted to have been deposited in a grounding line-proximal depositional setting. The low biogenic content of Unit 2 and a clay mineral assemblage that is comparable to underlying sub-glacial sediments were used to interpret stratified diamictons as having been deposited in a sub-ice shelf environment (Drewry and Cooper, 1881; Domack and Harris, 1998; Domack et al., 1998; Domack et al., 1999; Minzoni et al., 2015; Rebesco et al., 2014). This interpretation is supported by the extremely low ADA, which suggests deposition in an environment with a very limited marine influence, extremely low biological productivity and a high terrigenous sediment contribution (Licht et al., 1999; Minzoni et al., 2015). Although the ADA of sediments is primarily linked to surface productivity, diatom assemblages can be influenced by advection by currents, dissolution, or dilution with variable terrigenous sediment input (Shemesh et al., 1989; Scherer et al., 1994). Following deposition sediments can be bioturbated or re-mobilised by bottom currents (Scherer et al., 1994). Therefore, ADA data is utilised here as a proxy of surface productivity, in combination with other proxies for palaeo-productivity (biogenic opal, TOC and $CaCO_3$ content) and corresponding quantitative diatom assemblage data.

The dominant species in this sample is *Fragilariopsis kerguelensis*, the most abundant diatom species in Southern Ocean sediments and associated with open ocean environments (Burckle, 1972; Leventer, 1992; Zielinski and Gersonde, 1997). Surface water samples recovered between New Zealand and the Ross Sea show a negative correlation between sea ice concentration and *F. kerguelensis* abundance (Burckle, 1972). Although *F. kerguelensis* can be found within sea ice, its concentration increases offshore (Tanimura, 1992; Taylor et al., 1997). It is coarsely silicified and preferentially preserved; therefore, *F. kerguelensis* has been used to trace incursions of CDW onto the Antarctic continental shelf (Zielinski and Gersonde, 1997; Allen et al., 2010; Peck et al., 2015). As well as *F. kerguelensis*, *Thalassiosira lentiginosa* is considered to be a permanently open water indicator species, whilst *Thalassiosira antarctica* T2 is associated with open water conditions during the austral summer (Abelmann and Gersonde, 1991; Burckle, 1972; Leventer, 1992; Taylor et al., 1997; Zielinski and Gersonde, 1997; Crosta et al., 2005; Armand et al., 2008). Finally, the symmetrical *Eucampia antarctica* morphotype observed in these samples is the 'cold' polar variety, found proximal to the sea ice edge (Table 5.1) (Fryxell, 1989; Fryxell, 1990; Leventer et al., 2002; Allen, 2014). Whilst most of these species are associated with open water environments, the dominant species in these samples, *F. kerguelensis, E. antarctica., T. antarctica T2, Thalassiosira scotia* and *T. lentiginosa*, are all highly silicified and robust

species, allowing them to be preferentially preserved (Abelmann and Gersonde, 1991; Zielinski and Gersonde, 1997; Crosta et al., 2005; Shukla et al., 2016).

The scarcity of diatoms within Zone 1 (0.02 mvpg), the prevalence of heavily silicified taxa and the influx of coarse-grained material (gravel and sand), support deposition in a grounding line proximal depositional setting. The observed diatoms are likely to have either been incorporated into glacially reworked sediments during glacial advance, or delivered to the core site by currents that transport diatoms beyond the ice shelf or perennial sea ice margin (Ó Cofaigh et al., 2005). The low number of these robust species mean that they are not utilised as environmental indicators in this study; e.g. for inferring an influx of CDW over deglaciation. Additional proxies would be required to support such an interpretation, such as magnesium/calcium (Mg/Ca) ratio of calcareous (micro-)fossils (Hillenbrand et al., 2017). However, this is reliant on preservation of foraminifera at horizons of interest, which has been a challenge in this setting.

5.2.3.2. GC695 Zone 2

5.2.3.2.1. Result

Zone 2 extends between 607 and 598 cm and consists of grey mud with dispersed gravel. Zone 2 has an ADA of 0.03 mvpg and a total *Chs* content of 31% (Table 5.1). *Fragilariopsis kerguelensis* (40%), *Actinocyclus actinochilus* (9%), *Fragilariopsis peragallii*, (7%), *Rhizosolenia* spp. (7%) and *Shionodiscus gracilis* var. *gracilis* (10%) dominate the *Chs*-free assemblage (Fig. 5.6). As with Zone 1, the one sample analysed from this interval contained <400 individuals (97 including *Chs*.), counted over 10 transects.

5.2.3.2.2. Interpretation

The overall fine-grained nature of the sediment relative to Zone 1 suggests deposition in a more grounding line distal setting. The clay mineral assemblage of this unit indicates well-mixed sediments, derived from various source regions within or out of the AHT and is comparable to those deposited in an seasonally-open marine setting (Ch. 4; Unit 5) (Hillenbrand et al., 2009). The very low ADA (0.03 mvpg), as well as low biogenic opal, TOC and $CaCO_3$ content, indicates the presence of an ice canopy that would suppress primary productivity (Minzoni et al., 2015; Rebesco et al., 2014). Based on the assemblage of diatoms and mixed sediment provenance, is difficult to infer if sediments were deposited in sub-ice shelf or sea ice setting and thus the term ice canopy is utilised (Minzoni et al., 2015; Rebesco

et al., 2014). The continuous presence of 2-40 mm clasts dispersed throughout Zone 2, suggests that rain out of debris from an ice shelf or icebergs is taking place during and following grounding line retreat (Powell et al., 1984; Evans et al., 2005). As with Zone 1, the dominant species in Zone 2 is *Fragilariopsis kerguelensis*, an open water and CDW upwelling indicator species (Burckle, 1972; Abelmann and Gersonde, 1991; Leventer, 1992; Taylor et al., 1997; Zielinski and Gersonde, 1997; Crosta et al., 2005). The very low ADA within Zones 1 & 2, are comparable to subglacial tills recovered from Marguerite Bay (~2 mvpg) and Herbert Sound (0.7 mvpg), and samples recovered from sub-ice shelf sediments deposited prior to the collapse of the Larsen B Ice Shelf (~0 mvpg) (Ó Cofaigh et al., 2005; Minzoni et al., 2015; Sañé et al., 2011; Rebesco et al., 2014). As with Zone 1, the low ADAs in Zone 2 imply that they were not deposited in situ, and were either (i) reworked from pre-LGM diatomaceous sediments, or (ii) delivered to the core site by currents that transport diatoms from the open ocean seaward of the ice canopy.

5.2.3.3. GC695 Zone 3

5.2.3.3.1. Result

Zone 3 extends between 598 and 565 cm and consists of bioturbated olive grey mud with dispersed gravel (Unit 7). Zone 3 has an ADA of 76 mvpg and a total *Chs* content of 81% (Table 5.1). *Fragilariopsis curta* (12%), *Fragilariopsis kerguelensis* (14%), *Thalassiosira antarctica* T2 RS (25%), *Thalassiosira scotia* RS (24%) and *Actinocyclus actinochilus* (5%) dominate the *Chs* free counts (Table 5.1 and Fig. 5.6). More than 400 specimens/valves were identified in all samples during counts including and excluding *Chs*.

5.2.3.3.2. Interpretation

As with Zone 2, the predominantly fine-grain nature of sediments comprising Zone 3 is indicative of deposition in a grounding line distal setting (Domack and Harris, 1998). The increase in ADA and in the content of biogenic opal and TOC, relative to Zone 2 (Table 5.1 and Fig. 5.6) suggests the onset of oceanographic and/or climatic conditions supporting biological production (Maddison et al., 2005; Leventer et al., 2006). This also coincides with a change in species assemblage, including an increase in *Chs*, *Fragilariopsis curta*, *Thalassiosira antarctica* T2 RS, *Thalassiosira scotia* RS (Fig. 5.6). There is a 50% increase in the relative abundance of total *Chs* (vegetative cells and resting spores) within Zone 3, relative to Zone 2. This subgenus is associated with early austral spring conditions, when melting sea ice induces stratification of the water column, concentrating nutrient delivery in the surface waters and promoting high primary productivity (Leventer, 1991; Leventer et al.,

1996; Leventer et al., 2002; Crosta et al., 2005; Maddison et al., 2005; Stickley et al., 2005; Leventer et al., 2006). The formation of heavily silicified resting spores, triggered by environmental stresses such as nutrient depletion, may facilitate rapid sinking and the transfer of *Chs*-RS to the seafloor (Smetacek, 1985; Leventer, 1991; Leventer, 1992). Sea ice and sea ice melt associated productivity is supported by the presence of *F. curta*, a well-documented sea ice associated diatom, found in fast and pack ice as well as waters adjacent to the sea ice (Garrison, 1991; Leventer, 1992; Taylor et al., 1997; Zielinski and Gersonde, 1997; Cunningham and Leventer, 1998; Leventer; 1998; Armand et al., 2005; Peck et al., 2015).

Thalassiosira antarctica and *Thalassiosira scotia* are closely related (Johansen and Fryxell, 1985) and these species are often combined in diatom assemblage counts (Zielinski and Gersonde, 1997). They are believed to dwell in waters ranging in temperature from -2 to 9.5°C (Zielinski and Gersonde, 1997). In this study, *T. antarctica* and *T. scotia* resting spores are separated (Fig. 5.6). They appear to fill a similar environmental niche with only minor variations in their abundance relative to each other (Fig. 5.6). Further investigations into the modern ecological preferences of these species would allow better understanding of the environments these taxa represent in the fossil record. *T. antarctica* and *T. scotia* vegetative cells are not identified separately in this study as their similar morphology impairs distinction. *T. antarctica* morphotypes T1 and T2 are also identified and counted separately. These two forms of *T. antarctica* are distinguished based on their size, coarseness of areolae and the absence or presence of marginal strutted processes (Villareal and Fryxell, 1983; Taylor et al., 2001; Buffen et al., 2007). These two morphotypes T1 and T2, are considered to dwell in relatively cool and relatively warm waters, respectively (Villareal and Fryxell, 1983; Buffen et al., 2007). A study of species distribution along the eastern Antarctic Peninsula showed that *T. antarctica* T1 is more abundant in the southernmost sample sites (65°00'S), dwelling in waters abundant in *F. curta*; a sea ice associated species (Buffen et al., 2007). Inversely, *T. antarctica* T2 is more common in the northernmost sites, at the tip of the Antarctic Peninsula, dwelling in waters abundant in *Chs* (Buffen et al., 2007). This region experiences a shorter duration of sea ice cover relative to the southern samples sites, thus *T. antarctica* T2 is associated with relatively warm and more open marine environments (Villareal and Fryxell, 1983; Buffen et al., 2007). Previous work on laminated diatomaceous ooze units, also noted that *T. antarctica* T2 RS are deposited near the top of terrigenous laminae, indicating blooming in summer/autumn in a seasonally open marine setting (Maddison et al., 2005). Therefore, within samples analysed from core GC695, the high *T. antarctica* T2 content of Zone 3 (25 %) could be indicative of higher productivity and bloom formation in the summer and/or a longer ice-free summer season (Pike et al., 2009). Resting spore formation of *T. antarctica* T2

is associated with environmental stress at the end of the summer, associated with nutrient depletion, a drop in temperature, sea ice growth and associated increase in salinity of surface waters adjacent to freshly formed sea ice (Hargraves and French, 1983; Maddison et al., 2005; Maddison et al., 2006).

Overall, Zone 3 is interpreted to reflect the beginning of a seasonally sea ice covered ocean with elevated primary productivity relative to Zones 1 and 2, with icebergs delivering dispersed sand and gravel to the core site.

5.2.3.4. GC695 Zone 4

5.2.3.4.1. Result

Zone 4 extends between 565 and 526 cm and consists of bioturbated dark greenish grey to grey mud with dispersed gravel. Zone 4 has an ADA of 12 mvpg and a total *Chs* content of 45% (Table 5.1). *Fragilariopsis curta* (16%), *Fragilariopsis kerguelensis* (22%), *Thalassiosira antarctica* T2 RS (17%), *Thalassiosira scotia* RS (12%), *Actinocyclus actinochilus* (9%) and *Fragilariopsis vanheurckii* (6%) dominate the *Chs*-free counts (Fig. 5.6). Less than 400 individuals were identified over 10 transects of the *Chs*-free counts. At 552 cm, 330 individuals were identified over 10 transects, and at 532 cm, 390 individuals were identified over 10 transects.

5.2.3.4.2. Interpretation

Zone 4 has a lower ADA, biogenic opal and TOC content than Zone 3 (64 mvpg ADA decrease). This decline is indicative of reduced biological productivity or greater dilution of the diatom component by terrigenous material (Maddison et al., 2005; Leventer et al., 2006). The decrease in *Chs* (from 85 to 45%) could indicate reduced austral spring productivity. This could be explained by a longer sea ice season that would inhibit meltwater input in the spring and associated with this, *Chs* blooms (Leventer, 1991; Leventer et al., 1996; Leventer et al., 2002; Leventer et al., 2006; Crosta et al., 2005; Maddison et al., 2005). A longer sea ice season would also lead to ice break-up or melting later in the year, when other environmental factors such as light availability would differ; this might make other species out-compete *Chs*. A longer sea ice season and/or a change in the timing of melt-out would also explain the 6% reduction in the relative abundance of *Thalassiosira antarctica* compared to Zone 3 (Pike et al., 2009), as the growth season would be curtailed or a later input of meltwater would change

the summer/autumn environment. Thus, Zone 4 is interpreted as reflecting a longer sea-ice season.

5.2.3.5. GC695 Zone 5

5.2.3.5.1. Result

Zone 5 extends between 526 and 322 cm and consists of grey mud interlaminated with diatomaceous ooze (ooze colours: olive, olive grey and light olive brown) and includes occasional layers with a greater concentration of gravel (observed in X-radiographs) (Fig. 5.2 and Fig. 5.3). Zone 5 has an ADA ranging between 298-2606 mvpg and a total *Chs* content of 94-99%. The sampling strategy for analysing temporal changes in diatom assemblage for core GC695 is unsuitable to accurately capture the species comprising the individual laminae within this zone; this is because samples taken at 10-20 cm intervals potentially capture the properties of both grey mud laminae and layers of diatomaceous ooze laminae. Values obtained from the 10-20 cm samples give a wide range of values for species contribution to the overall assemblage. Species are dominated by *Corethron pennatum* (2-18%) *Fragilariopsis curta* (13-26%), *Fragilariopsis kerguelensis* (1-19%), *Thalassiosira antarctica* T2 RS (6-31%), *Thalassiosira antarctica* vegetative (1-19%), *Thalassiosira scotia* RS (4-19%), *Eucampia antarctica* (total) (1-5%), *Fragilariopsis rhombica* (1-6%) and *Nitzschia* spp. (0-16%) (Fig. 5.6).

In order to accurately determine the composition of individual lamina types, a detailed quantitative analysis of diatom assemblages was carried out on a 20 cm section of this unit using toothpick samples, allowing the species assemblage of individual laminations to be analysed. The total abundance of diatoms is greater within the orange/brown laminae than in the grey laminae (Fig. 5.7). Although *Chs* dominate all samples, the species composition of the orange/brown laminae varies. Individual laminae are dominated by *Corethron pennatum*, *Proboscia* spp., *Eucampia antarctica*, *Thalassiosira antarctica*, *Thalassiosira scotia, Porosira glacialis* and *Fragilariopsis curta* (Fig. 5.7). The grey mud laminae contain a more diverse species assemblage (Fig. 5.7).

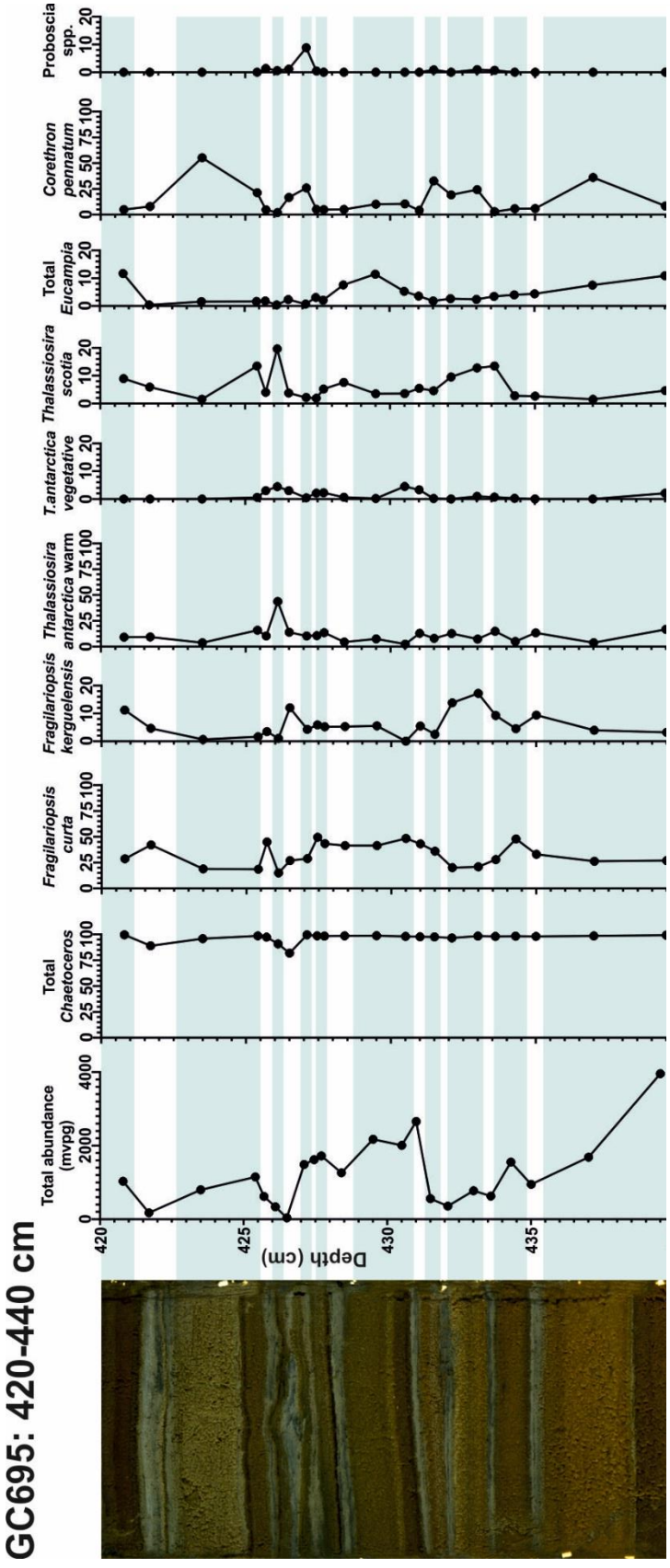

Figure 5.7: Line-scan image and quantitative diatom data for 420-440 cm in core GC695. Absolute diatom abundance and total Chs *data were collected from diatom counts including* Chs. *The percentage contribution data for the species* Fragilariopsis curta, Corethron pennatum, Proboscia spp., Thalassiosira antarctica *T2 RS*, Thalassiosira scotia *RS*, Porosira glacialis, Eucampia antarctica *and* Fragilariosis kerguelensis *were collected from* Chs*-free counts. Green shading represents the data collected for the biogenic laminae. Full quantitative ADA and diatom species data are given in Appendix F.*

5.2.3.5.2. Interpretation

Deposition of sediments in distinct laminae is associated with episodes of high productivity, rapid sedimentation of diatoms and suppressed bioturbation by benthic organisms (Smetacek, 1985; Alldredge and Gotschalk, 1989). Within this zone the highest values of ADA and contents of biogenic opal, TOC and $CaCO_3$ are observed, indicative of enhanced biological productivity. The biogenic laminae are dominated by *Chs*-RS, which are associated with meltwater-induced stratification in the early austral spring, concentrating nutrient delivery in the surface waters and promoting high primary productivity (Leventer, 1991; Leventer et al., 1996; Leventer et al., 2002; Crosta et al., 2005; Maddison et al., 2005; Leventer et al., 2006). The high abundance of *Fragilariopsis curta* (19-50%) throughout the laminated unit supports an interpretation of sea ice (melt) associated productivity (Garrison, 1991; Leventer, 1992; Taylor et al., 1997; Zielinski and Gersonde, 1997). In addition to *Chs*, commonly observed species within the biogenic laminae are *Corethron pennatum, Proboscia* spp. *Eucampia antarctica.*, *Thalassiosira antarctica* T2 RS, *Porosira glacialis* and *Thalassiosira scotia* RS.

Biogenic laminae with high abundance of *Chs*-RS also have a high *Corethron pennatum* component (up to 55%). *C. pennatum* is a species associated with a well-stratified water column as their positive buoyancy allows them to move vertically in the water column to utilise nutrients at depth and thus avoid competition within surface waters (Crawford, 1995; Leventer et al., 2002; Stickley et al., 2005; Alley et al., 2018). Mass export of *C. pennatum* likely occurs when sea ice melt is exhausted, wind stress is enhanced and/or water column mixing causes stratification to break down, and are thus associated with late austral spring/early summer deposition (Leventer et al., 2002; Maddison et al., 2006; Alley et al., 2018). Where *C. pennatum* is present at high relative abundance, the absolute abundance of diatoms is relatively low (e.g. Fig. 5.7: 424 cm; 800 mvpg ADA), compared to that of diatomaceous laminae dominated by other species (e.g. Fig. 5.7: 438 cm; 3955 mvpg ADA). This suggests they are prevalent during periods of overall lower productivity. Like *C. pennatum*, *Proboscia* spp. are adapted for growth beneath a strongly seasonal thermocline, as they are tolerant of low light levels and can adjust their buoyancy (Kemp et al., 2000). Thus, they can move to deeper waters to utilise nutrients at depth and to shallower waters to photosynthesise. A breakdown of the thermocline and enhanced wind stress and water column mixing in the autumn leads to sedimentation of *Proboscia* spp. (Kemp et al., 2000; Leventer et al., 2002; Denis et al., 2006).

The lamination containing peak abundance of *Eucampia antarctica* (~430 cm) contains fewer *Chs*-RS than other orange/brown laminae. This may indicate deposition of *E. antarctica* once stratification has broken down. Within Zone 5, *E. antarctica* is of the symmetrical morphotype

(Table 5.1). This is considered the southern variety, tolerating sea ice (Fryxell, 1989; Fryxell, 1990; Leventer et al., 2002; Allen, 2014). Analysis of modern sediments show that asymmetrical *E. antarctica* are dominant in samples recovered from the Falkland Plateau and Northeast Georgia Rise, whilst the northern Weddell Sea and southern Antarctic Peninsula are characterised by the symmetrical variety (Allen, 2014).

As previously noted, *Thalassiosira antarctica* T2 is associated with relatively warm and open marine environments, with *T. antarctica* T2 RS laminae associated with summer to autumn blooming with an autumn flux to the seafloor (Villareal and Fryxell, 1983; Maddison et al., 2005; Stickley et al., 2005; Buffen et al., 2007; Pike et al., 2009). In contrast to other core zones, Zone 5 contains a higher abundance of *T. antarctica* vegetative cells (Fig. 5.6). The exact mechanisms triggering resting spore formation within *T. antarctica* remains poorly understood, but is suggested to be initiated by environmental stresses at the end of the summer, associated with nutrient depletion, lower temperatures, reduced irradiance and sea ice growth (Hargraves and French, 1983; Maddison et al., 2005; Maddison et al., 2006; Pike et al., 2009). One mechanism that may allow export of vegetative cells is a slower rate of environmental change; for example, a later timing of sea ice growth would allow the population to slowly decrease with reducing temperatures and irradiance and increasing salinity. *Thalassiosira scotia* appears to fill a similar environmental niche to *T. antarctica. Porosira glacialis* often occurs with *T. antarctica* in diatom-rich laminated sediments (Krebs et al., 1987; Zielinski and Gersonde, 1997; Stickley et al., 2005; Maddison et al., 2006). *P. glacialis* blooms in the summer whilst resting spores form in the autumn; this taxon is generally considered a species marking the end of the growing season (Maddison et al., 2006). One biogenic laminae with elevated abundances of *P. glacialis* is observed (Fig. 5.7; 425.5cm), coinciding with a peak in *T. scotia* and a minor increase in *T. antarctica.*

Overall, biogenic laminae with species indicative of spring (*Chs*-RS), late-spring/early-summer (*Corethron pennatum* and *Proboscia* spp.) and summer to autumn (*Thalassiosira antarctica, Thalassiosira scotia* and *Porosira glacialis)* blooms are observed. Terrigenous laminae, interbedded with biogenic laminae, have a lower ADA and percentage of *Chs*-RS, relative to biogenic laminae, and a mixed diatom assemblage (Fig. 5.7). The influx of terrigenous material is thought to be associated with glacial ice melt from icebergs, glaciers (including surface and basal melting) and ice shelves (Leventer et al., 2002; Maddison et al., 2005). Although the sedimentological and diatom evidence indicate that laminations in Zone 5 represent seasonal events of high productivity, similar to deposits observed in other Antarctic regions, these laminations do not resemble the varved seasonal deposits of Palmer Deep and Iceberg Alley (Maddison et al., 2005; Stickley et al., 2005). Generally, these varved sequences

are composed of layers of diatomaceous ooze and terrigenous laminae deposited annually. Within varved diatomaceous oozes, there is typically gradation between diatomaceous and terrigenous laminae, from pure *Chs* ooze through increasingly mixed diatom ooze and then increasingly terrigenous-rich (Maddison et al., 2005; Stickley et al., 2005). This suggests that the laminae present in core GC695 represent part(s) of annual cycles that are not preserved seasonally and/or annually.

5.2.3.6. GC695 Zone 6

5.2.3.6.1. Result

Zone 6 extends between 322 and 240 cm and consists of grey bioturbated mud. Zone 6 has an average ADA of 135 mvpg and a total *Chs* content of 87% (Table 5.1). *Fragilariopsis kerguelensis* 14%; *Fragilariopsis curta* 9%; *Corethron pennatum* 3%, *Thalassiosira antarctica* T2 RS 27%, *Thalassiosira scotia* 10%, *Rhizosolenia* spp. 8% and *Eucampia antarctica* (total) 7% dominate *Chs* free counts (Fig. 5.6).

5.2.3.6.2. Interpretation

Floristically, the key difference between Zone 5 and Zone 6 is the change in ADA, with Zone 6, on average, having a considerably lower ADA (Zone 5: 912 mvpg vs. Zone 6: 135 mvpg) (Table 5.1). Zone 6 additionally has a relative decrease in contributions of *Chs* RS and *Corethron pennatum (*Table 5.1); species associated with the formation of a well-stratified water column, instigated through melting sea and glacial ice in the spring (Crawford, 1995; Kemp et al., 2000; Leventer et al., 2002; Alley et al., 2018). The 10% decrease in the abundance of *Fragilariopsis curta* relative to Zone 5 also supports an overall change in the nature of sea ice melt-out or break up (Cunningham and Leventer, 1998). Open ocean associated species *Fragilariopsis kerguelensis* become slightly more abundant in Zone 6 relative to Zone 5 (3% increase) (Burckle, 1972; Villareal and Fryxell, 1983; Garrison, 1991; Leventer, 1992; Taylor et al., 1997; Cunningham and Leventer, 1998; Zielinski and Gersonde, 1997; Armand et al., 2005; Buffen et al., 2007). The relative decrease in sea ice and meltwater/stratification associated species *Chs*-RS, *F. curta* and *C. pennatum* compared to Zone 5, indicates reduced sea ice melt and meltwater discharge in the spring. Reduced meltwater discharge in the spring could relate to a change in the duration of sea ice cover and the timing and volume of sea ice melt, or reduced springtime meltwater input from glaciers and icebergs related to changes in atmospheric and oceanic temperature (Garrison, 1991;

Leventer, 1992; Taylor et al., 1997; Zielinski and Gersonde, 1997; Cunningham and Leventer, 1998; Armand et al., 2005). Alternatively, this may indicate that increased windiness led to sea ice break up, rather that melting and formation of a stratified water column, that is seeded by species such as *F. curta* (Cunningham and Leventer, 1998). The presence of open water associated species *Thalassiosira antarctica* T2 and *F. kerguelensis* indicates that open water summer conditions persist through deposition of Zone 6.

5.2.3.7. GC695 Zone 7

5.2.3.7.1. Result

Zone 7 extends between 240 and 160 cm and consists of olive grey bioturbated mud. Zone 7 has an average ADA of 66 mvpg and a total *Chs* content of 57% (Table 5.1). *Eucampia* (total) 25%; *Fragilariopsis kerguelensis* 23%, *Rhizosolenia* spp. 12%, *Fragilariopsis curta* 6%, *Thalassiosira antarctica* T2 RS 9% and *Thalassiosira lentiginosa* 4% dominate *Chs* free counts (Fig. 5.6).

5.2.3.7.2. Interpretation

Within Zone 7 there is an increase in *Eucampia antarctica*. This is dominated by the symmetrical morphotype, with a minor increase in the assymmetrical morphotype (Figure 5.6 and Table 5.1). The symmetrical morphotype (*E. antarctica* var. *recta)* is the southern variety, tolerating sea ice, whilst the asymmetrical morphotype (*E. antarctica* var. *antarctica)* is associated with relatively warm sub-polar environments (Fryxell, 1989; Fryxell, 1990; Leventer et al., 2002; Allen, 2014). The overall increase in symmetrical *E. antarctica* suggests an increase in sea ice presence at this time (Leventer et al., 2002; Smith et al., 2007; Peck et al., 2015). The reduction in ADA and in the relative abundance of sea ice and sea ice-melt associated taxa (*Chs, Fragilariopsis curta* and *C. pennatum*), supports environmental conditions with less sea ice-melt related productivity. This may be due to an extended sea ice season and a reduced growing season, particularly in the spring where previously the water column was highly stratified (Zone 5). Alternatively, this may indicate that increased windiness led to sea ice break up, rather that melting and formation of a stratified water column (Cunningham and Leventer, 1998). *Fragilariopsis kerguelensis* is the most abundant diatom species in Southern Ocean sediments and is associated with open ocean environments (Burckle, 1972; Leventer, 1992; Zielinski and Gersonde, 1997). Whilst the increase in the symmetrical morphotype of *E. antarctica* is indicative of a longer sea ice season, this is contradicted by the high proportion of open-water associated *F. kerguelensis.* Potential

scenarios that could lead to the enrichment of both *E. antarctica* and *F. kerguelensis* in Zone 7 include (a) the sample captures both heavier sea ice cover in winter (*E. antarctica*) with warmer open-water conditions in the summer (*F. kerguelensis*). (b) *E. antarctica* and *F. kerguelensis* are heavily silicified species and are preferentially preserved, therefore their relative abundance is elevated when overall valve abundance is low (Allen et al., 2014). Alternatively, (c) the environmental preferences of these species are not fully resolved. In particular, the ratio of symmetrical and assymmetrical *E. antarctica* and its relationship to sea ice extent may be more nuanced than previously understood. Based on the available data, the relationship between *E. antarctica* and ADA (Fig. 5.6), suggests *E. antarctica* is dominant when overall productivity is reduced. Therefore, if not enhanced sea ice extent (as indicated by abundant *F. kerguelensis),* another environmental factor likely caused decreased productivity at this time, for example windiness, or lack of sea and/or glacial ice growth and subsequent melt, proximal to the core site (Cunningham and Leventer, 1998).

5.2.3.8. GC695 Zone 8

5.2.3.8.1. Result

The uppermost Zone 8 extends between 160 and 0 cm and consists of olive grey to grey bioturbated mud. Zone 8 has an average ADA of 194 mvpg and a total *Chs* content of 71% (Table 5.1). *Fragilariopsis curta* 15%, *Fragilariopsis kerguelensis* 28%, *Thalassiosira antarctica* T2 RS 6%, *Fragilariopsis antarctica* T1 RS 3%, *Thalassiosira scotia* 4%, *Rhizosolenia* spp. 7%, *Eucampia antarctica* (total) 6%, *Shionodiscus gracilis* var. *nominate* 4% and *Thalassiosira lentiginosa* 4% dominate *Chs*- free counts (Fig. 5.6). Within the sample analysed at 122 cm (Fig. 5.6) ADA increases to 451 mvpg and the *Chs*-RS total increases to 87%.

5.2.3.8.2. Interpretation

Open-ocean associated species *Fragilariopsis kerguelensis* remain in high abundance within Zone 8 and decreases towards the core top (Fig. 5.6) (Fryxell and Hasle, 1971; Burckle, 1972; Leventer, 1992; Zielinski and Gersonde, 1997; Armand and Zielinski, 2001; Crosta et al., 2005). This is concurrent with an increase in sea ice associated *Thalassiosira antarctica* T1 (Villareal and Fryxell, 1983; Buffen et al., 2007). The ADA additionally increases relative to Zone 7, as does the abundance of *F. curta* and the total *Chs* content. This assemblage indicates enhanced seasonality, with a heavy sea ice cover in the winter and melt-water associated productivity in the spring.

5.2.4. Spatial extent of laminated diatomaceous ooze deposition

The basic characteristics (thickness) of the biogenic laminae and bathymetric context of diatomaceous ooze units within cores GC691, GC695 and GC698 has been presented. This has been supplemented by detailed diatom assemblage data for core GC695 (Fig. 5.6). Although we do not observe thick units of laminated diatomaceous ooze within all cores recovered from AHT, cores GC692, GC690, GC702, GC711, GC697 and GC709 (Fig. 5.1), contain an ~10cm unit of sediment with low magnetic susceptibility at a similar stratigraphic interval (Fig. 5.8). This drop in magnetic susceptibility coincides with an increase in the biogenic content (where measured) of the sediment relative to under and overlying units (Fig. 5.8 & Fig. 5.9; 278-243 cm). Further quantitative diatom assemblage analysis of core GC697 shows that this thin unit (Fig. 5.9b; 278-243 cm) is characterised by an ADA of 444 mvpg and a total *Chs* content of 98% (Table 5.2) *Corethron pennatum* (34%) and *Fragilariopsis curta* (25%) dominate the *Chs* free counts (Fig. 5.9b). The stratigraphic position, diatom species assemblage, and magnetic signature of this unit is comparable with Zone 5 of core GC695 and is thus considered to represent the same period of enhanced productivity.

Zone 4 and Zone 3 are additionally observed in core GC697. Zone 3 represents an initial peak in productivity associated with a seasonally sea ice covered ocean (Fig. 5.8 and Fig. 5.9b). Within core GC695, this unit has an ADA of 76 mvpg and a total *Chs* content of 81%. *Fragilariopsis curta* 12%, *Fragilariopsis kerguelensis* 14%, *Thalassiosira antarctica* T2 RS 25%, *Thalassiosira scotia* RS 24% and *Actinocyclus actinochilus* 5% dominate the *Chs* free counts. Within core GC697, Zone 3 has a similar peak ADA of 71 mvpg and a total *Chs* content of 75% (Fig. 5.9b). As with Zone 3 of GC695, Zone 3 of GC697 is dominated by *F. curta* 19%, *F. kerguelensis* 19%, *T. antarctica* T2 RS 21% and *T. scotia* RS 12% (Fig. 5.9b). Zone 4 is characterised by a drop in ADA, to 12 mvpg in core GC695 and 4 mvpg in core GC697 (Fig. 5.9b), associated with persistent ice cover. As illustrated in Figure 5.8, these units can be traced between other AHT cores based on the stratigraphy of the cores and multi-proxy data obtained.

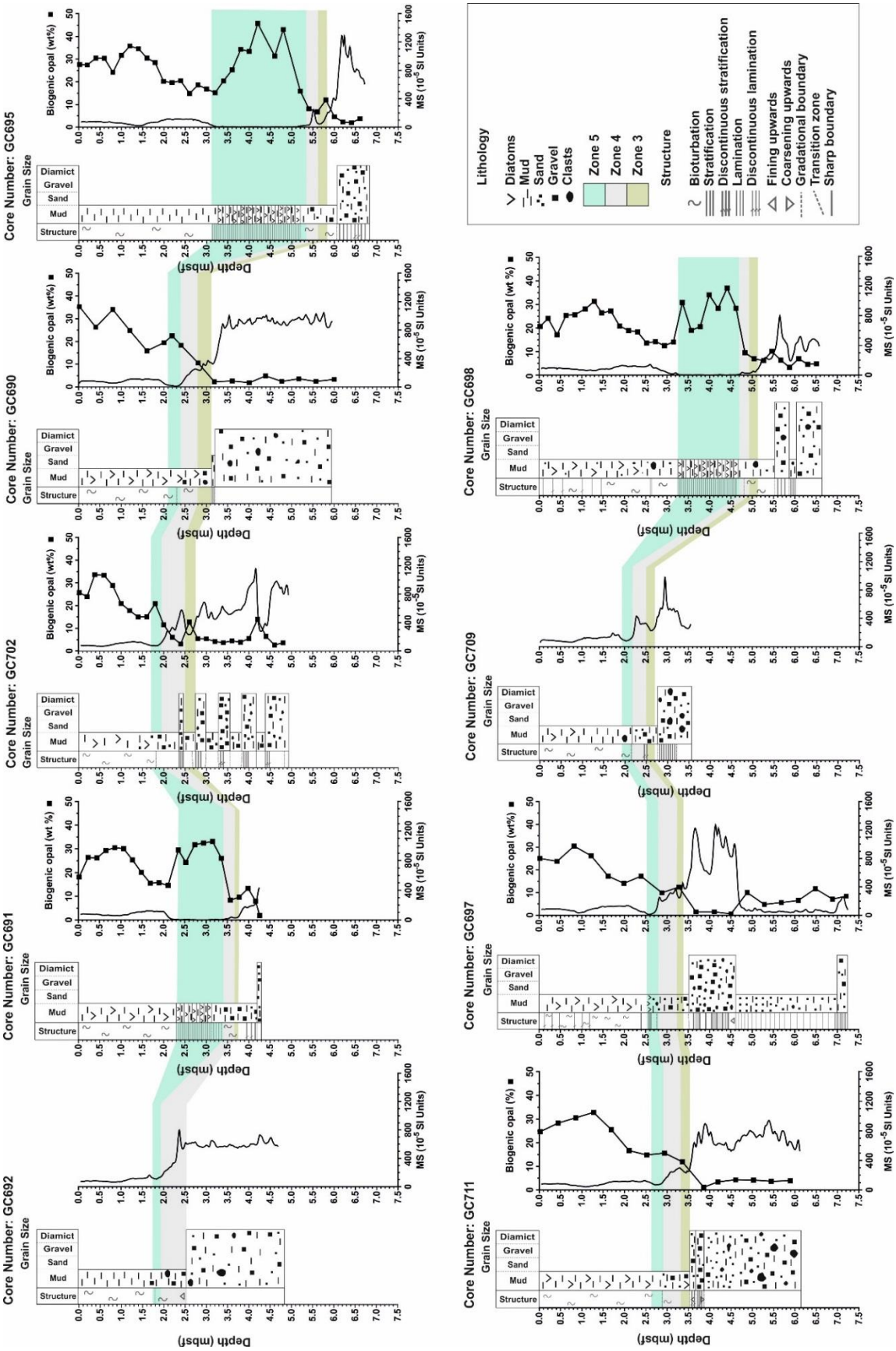

Figure 5.8: Fence diagrams showing simplified core logs and magnetic susceptibility and biogenic opal data for cores GC692, GC691, GC702, GC690, GC695, GC711, GC697, GC709 and GC698. No biogenic opal data is available for core GC692. The green shading indicates the laminated diatomaceous ooze unit (Zone 5) within cores GC691, GC695 and GC698 and the corresponding low MS, high biogenic opal unit in cores GC692, GC702, GC690, GC697 and GC709. Zones 3-4 are also shown.

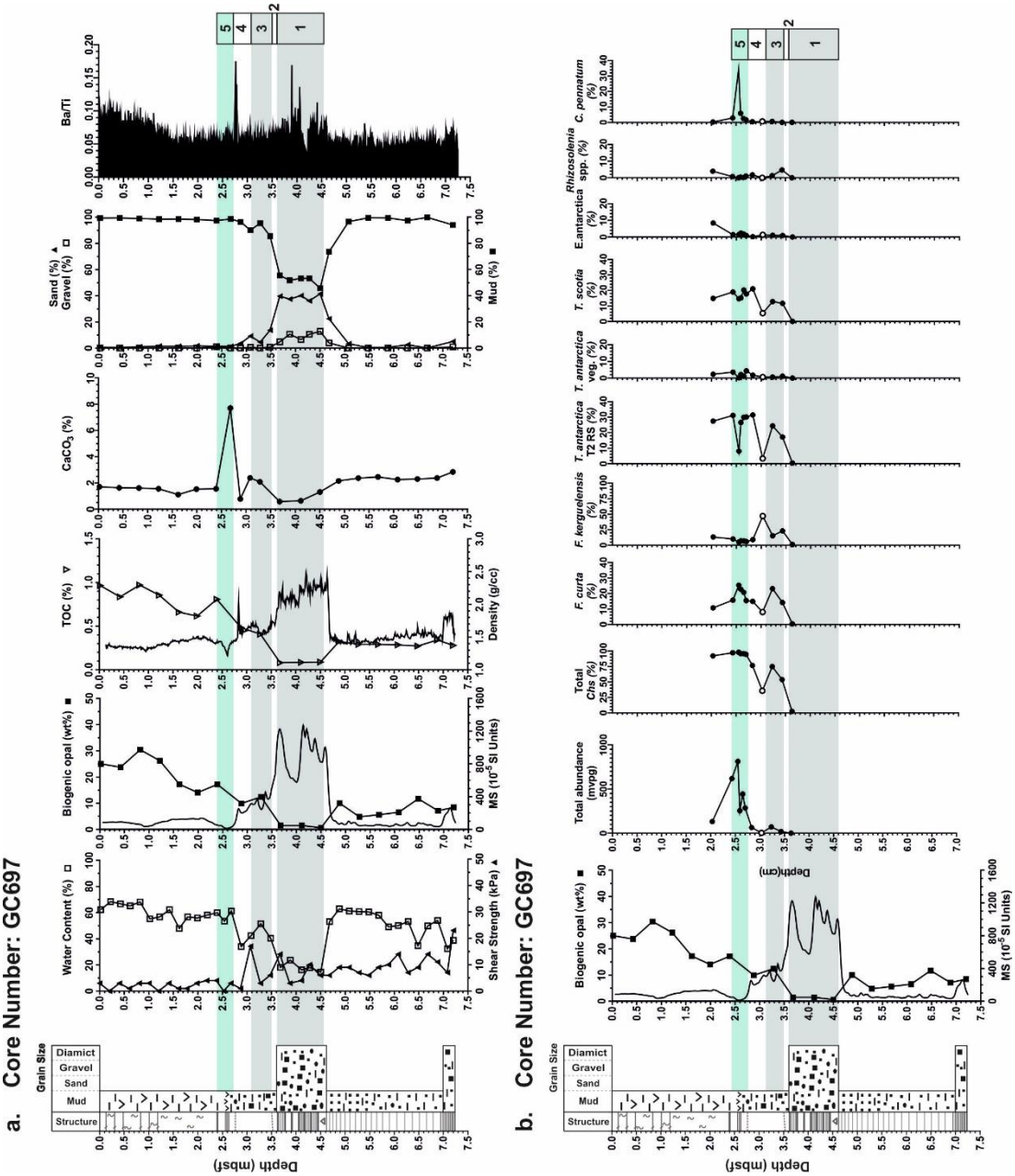

Figure 5.9: (a) Simplified core logs and multi-proxy data for sediment core GC697, including water content (open squares), shear strength (closed triangles), magnetic susceptibility (MS), biogenic opal (closed squares), TOC (open triangles), $CaCO_3$ (closed circles), density, contents of mud (<63µm, closed squares), sand (63 µm-2mm; closed triangles) and gravel (>2 mm; open squares) and Ba/Ti ratios. The green shading indicates the position of Zone 5. Diatom zones (1-4) are also shown on right of panel and as grey/white shading. (b) Quantitative diatom data and sedimentological zones for core GC697. Diatom total abundance and total Chs *data were collected from total diatom counts including* Chs. *The percentage contribution data for the species* Fragilariopsis curta, Fragilariopsis kerguelensis, Thalassiosira antarctica *T2 RS*, Thalassiosira antarctica *(vegetative cells)*, Thalassiosira scotia *RS*, Eucampia *spp.*, Rhizosolenia *spp. and* Corethron pennatum *were collected from* Chs-*free counts.* Samples from which <400 whole valves were counted are indicated (white circles). *Diatom zones (1-5) are also shown on right of panel and as grey/white/green shading. Full quantitative ADA and diatom species data are given in Appendix F.*

Zone	Depth (cm)	No. of samples	Absolute diatom abundance (mypg)		Total *Chaetoceros* subg. *Hyalochaete* (%)		*Corethron pennatum* (%)		*Fragilariopsis curta* (%)		*Fragilariopsis kerguelensis* (%)		*Rhizosolenia* spp. (%)		*Thalassiosira antarctica* (T2) (%)		*Thalassiosira antarctica* vegetative (%)		*Thalassiosira scotia* (%)		*Eucampia antarctica* (total) (%)		*Eucampia antarctica* (symmetrical) (%)		*Eucampia antarctica* (asymmetrical) (%)		*Thalassiosira lentiginosa* (%)	
			Mean	SD	Mean	SD	Mean	SD	Mean	SD	Mean	SD	Mean	SD	Mean	SD	Mean	SD	Mean	SD	Mean	SD	Mean	SD	Mean	SD	Mean	SD
2	370-355	1	0.08	0.00	2	0	0	0	17	0	42	0	0	0	17	0	0	0	0	0	0	0	0	0	0	0	0	0
3	355-313	2	45	25	64	10	0	0	19	4	19	4	3	2	21	4	1	0	12	1	1	0	1	0	0	0	2	1
4	313-278	2	34	30	56	20	1	0	12	3	28	19	1	1	17	14	1	1	13	8	1	1	0	0	0	0	1	0
5	278-243	5	483	210	96	1	9	13	20	4	7	2	0	0	25	9	2	2	17	2	2	1	1	0	0	0	0	0

Table 5.2: Absolute diatom abundance and relative species assemblage data for key environmental indicator diatoms in core GC697 (mean and standard deviation), including number of samples analysed for each diatom zone. Values for Zone 2 (italicised) are from one sample and are therefore not an average.

5.3. Discussion

5.3.1. Stratigraphic and environmental context of laminated diatomaceous ooze deposition

Zones 1 and 2, as defined in core GC695, are interpreted to represent conditions immediately following the retreat of the AHIS grounding line, with the environment transitioning from a grounding line proximal to a grounding line distal setting (Table 5.3). As discussed, the very low ADA and contents of biogenic opal, TOC and $CaCO_3$, as well as the prevalence of heavily silicified taxa within Zone 2 and Zone 1, indicate that diatom deposition is not taking place in situ. Rather, they are likely to have been reworked into glacial diamictons from pre-LGM diatomaceous sediments, or are delivered to the core site by currents. Currents can transport diatoms from reworked material at the grounding line or from beyond the ice shelf in the case of Zone 1, or ice canopy in the case of Zone 2 (Ó Cofaigh et al., 2005; Minzoni et al., 2015). Following deposition of Zone 2 there is evidence of enhanced primary productivity within AHT, with a greater ADA and relative abundance of diatom species associated with seasonal sea ice formation (*Fragilariopsis curta*), spring sea ice melt (*Chs*) and open water summer conditions (*Thalassiosira antarctica* T2 RS) (Fig. 5.10; Zone 3). This signifies the onset of seasonally open marine conditions following the demise of the ice canopy within this region of the trough (Minzoni et al., 2015).

The increase in productivity following grounding line retreat and the loss of the ice canopy is interrupted by a return to an environment with low productivity (Zone 4). Zone 4 is characterised by an assemblage indicative of a shortening of the growth season, with reduced open water associated *Thalassiosira antarctica* T2 RS and a greater number of sea ice associated *Thalassiosira antarctica* T1 RS (Fig. 5.10e). The reduction in sea ice-melt related species (*Chs*-RS and *Corethron pennatum)* additionally supports reduced seasonal sea ice melt over this period. The onset of laminated diatomaceous ooze deposition (Zone 5) is associated with a seasonal cycle of sea ice formation over the austral winter, sea ice melt in the spring, with meltwater and nutrient input, and open-water summer conditions (increased abundance of *Fragilariopsis curta*, *Chs-RS*, *C. pennatum* and *T. antarctica* T2 RS) (Fig. 5.10).

Zone	Description	Interpretation
1	Sediments are stratified diamicton. ADA is 0.02 mvpg with the diatom assemblage dominated by heavily silicified/reworked taxa.	Grounding line proximal environment with presence of an ice shelf.
2	Sediments are grey mud with dispersed gravel. ADA is 0.03 mvpg with the diatom assemblage dominated by heavily silicified/reworked taxa.	Grounding line distal environment with presence of an ice canopy.
3	Sediments are bioturbated olive grey mud with dispersed gravel. ADA is 76 mvpg with the diatom assemblage dominated by *Chs, F. curta, T. antarctica* T2 RS, *T. scotia* RS.	The beginning of a seasonally sea ice covered ocean with elevated primary productivity, with icebergs delivering dispersed sand and gravel to the core site.
4	Sediments are bioturbated dark greenish grey to grey mud with dispersed gravel. ADA is 69 mvpg with the diatom assemblage dominated by *F. kerguelensis*. There is a relative decrease in the abundance of *Chs* and *T. antarctica* T2 RS.	A lengthening of the sea ice season causing the growth season to be curtailed.
5	Sediments are grey mud interlaminated with diatomaceous ooze. ADA is 912 mvpg with the diatom assemblage dominated by *Chs*-RS, *C. pennatum, Proboscia* spp., *T. antarctica* T2 RS, *T. scotia* RS and *P. glacialis.*	Enhanced biological productivity associated with meltwater discharge and nutrient input from sea and glacial ice melt.
6	Sediments are grey bioturbated mud. ADA is 164 mvpg with the diatom assemblage dominated by *Chs, F. kerguelensis, F. curta, C. pennatum, T. antarctica* T2 RS, *T. scotia* RS, *Rhizosolenia* spp. and *E. Antarctica.*	Reduced sea ice melt and meltwater discharge in the spring. Interpreted to be a seasonally open-marine setting.
7	Sediments are olive grey bioturbated mud. ADA is 66 mvpg with the diatom assemblage dominated by *Chs, E. antarctica (symmetrical), F. kerguelensis, Rhizosolenia* spp., *F. curta, T. antarctica* T2 RS.	Reduced primary productivity, preservation of highly silicified taxa. Interpreted to be a seasonally open-marine setting with reduced spring stratification.
8	Sediments are olive grey to grey bioturbated mud. ADA is 194 mvpg with the diatom assemblage dominated by *Chs, F. curta, F. kerguelensis* and *Rhizosolenia* spp.	Enhanced seasonality, with more extensive sea ice over winter and greater spring melt-out associated productivity.

Table 5.3: Summary of diatom zones for GC695 with description of sediments, ADA and assemblage, together with an interpretation of the diatom zone.

Deglacial laminated diatomaceous ooze deposits have been recovered and analysed from several East Antarctic sites (Denis et al., 2006; Maddison et al., 2006; Stickley et al., 2005; Leventer et al., 2006; Maddison et al., 2012; Alley et al., 2018), the Amundsen Sea (Hillenbrand et al., 2010a) and Palmer Deep (Leventer et al., 1996; Domack et al., 2006). These are associated with enhanced meltwater discharge and the formation of a stratified water column, and/or the formation of a calving bay in which meltwater, nutrients and bioavailable iron from melting sea ice, icebergs or glaciers are concentrated (Leventer et al., 1996; Domack et al., 2006; Leventer et al., 2006; Hillenbrand et al., 2010a; Alley et al., 2018). The calving bay re-entrant model is commonly used to explain elevated productivity following the LGM

and preservation of varved to laminated diatomaceous sediments at several locations on the Antarctic continental shelf (Domack et al., 2006; Leventer et al., 2006). Calving bays form when ice retreat within the deepest part of a trough or embayment outpaces ice retreat on the shallow trough margins, creating a bay flanked by ice on three sides. This leads to the focussing of meltwater into the calving bay, stabilising the water column and concentrating nutrients within the surface waters (Leventer et al., 1996; Domack et al., 2006; Leventer et al., 2006). These conditions promote the formation of intense algal blooms.

A reconstruction of palaeo-ice stream systems for the northern AP, indicates the presence of two ice domes constraining ice flow within the AHT during the LGM (Lavoie et al., 2015) (Fig. 2.2). The Hugo and Marr Ice Domes, bordering the AHT to the southwest and southeast, respectively, may have flanked the AHT after the pull back of the AHIS grounding line, thus acting as calving bay margins (Lavoie et al., 2015). Although this hypothesis is suitable for describing an environment within which meltwater, nutrients and bioavailable iron could have been focussed, it does not fully explain the lag between grounding line retreat and the onset of laminated diatomaceous ooze deposition observed in our cores. If a calving bay was the sole driver of enhanced productivity and diatomaceous ooze deposition within AHT, it would be expected to occur at the onset of seasonally open marine conditions (Zone 3); assuming that by this point the calving bay had formed (Fig. 5.10).

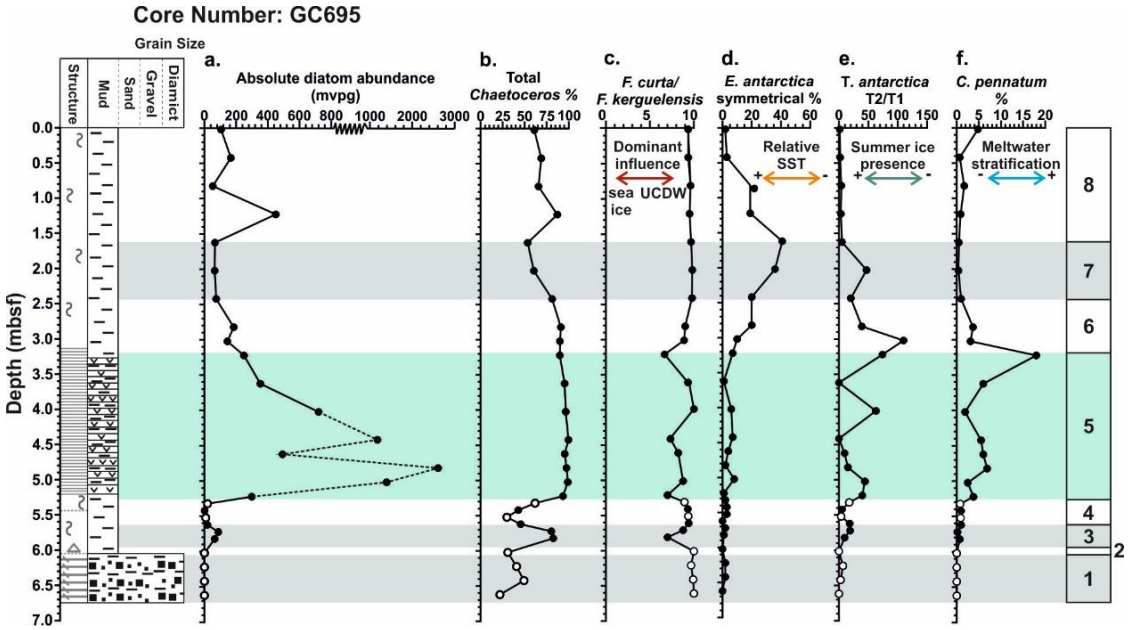

Figure 5.10: Diatom data and palaeoenvironmental interpretations for core GC695. (a) Absolute diatom abundance. (b) Total Chaetoceros*. (c)* F. curta/F. kerguelensis *ratio as a proxy for sea ice vs open water conditions. (d)* E. antarctica *symmetrical as a proxy for SST. (e)* T. antarctica *T2(warm)/T1(cold) ratio as a proxy for summer sea ice presence. (f)* C. pennatum *as a proxy for meltwater induced stratification.*

Within the AHT, an initial rise in productivity follows grounding line retreat and the demise of an ice canopy (Zone 3). If the retreat of the ice stream calving line and the formation of a calving bay, with associated focussing of meltwater, were the sole drivers of enhanced diatom productivity following the LGM, we could expect Zone 3 to represent peak productivity. Instead, deposition of sediments associated with peak post-LGM productivity, comes later, within Zone 5. The diatom assemblage comprising Zone 3 indicates seasonal sea ice formation (*Fragilariopsis curta*), spring sea ice melt (*Chs* and *F. curta*) and open water summer conditions (*Thalassiosira antarctica* T2 RS), at the onset of seasonally open marine conditions. However, relative to this, over Zone 5 deposition, diatom production associated with meltwater input and water column stratification was enhanced (Fig. 5.10). Zone 5 has a far higher abundance of *Chs* (912 vs. 76 mvpg) and relative abundance of *Corethron pennatum* (5% vs 0.5%) and *F. curta* (20% vs. 12%), compared to Zone 3. Therefore, a calving bay model does not solely explain enhanced productivity in AHT. Additional drivers of meltwater input and water column stratification, in addition to the potential formation of a calving bay, were required to enhance productivity of species *F. curta*, *Chs* and *C. pennatum*. Scenarios that could explain the prevalence of meltwater and stratification include sea-level changes, increased atmospheric and SSTs and/or increased upwelling of nutrient-enriched CDW, driving meltwater discharge from sea ice, glaciers and icebergs (Stickley et al., 2005). Radiocarbon dating of this sequence (Ch. 6) allows this interval of slightly elevated diatom productivity event (Zone 3) and the interval of peak productivity (Zone 5) to be compared with records of atmospheric and SST, CDW upwelling, glacial discharge and sea-level rise (e.g., Anderson et al., 2009; Shevenell et al., 2011; Mulvaney et al., 2012; Pike et al., 2013; Etourneau et al., 2013; WAIS Divide Project Members, 2015; Peck et al., 2015; Hillenbrand et al., 2017).

5.3.2. Controls on laminated diatomaceous ooze accumulation

The laminated diatomaceous sediments observed in this study are indicative of seasonal productivity events, with alternating layers of diatomaceous ooze and post-bloom terrigenous sediments. Laminated diatomaceous ooze deposits have been recovered and analysed from several East Antarctic (e.g. Finocchiaro et al., 2005; Denis et al., 2006; Maddison et al., 2006; Stickley et al., 2005; Leventer et al., 2006; Maddison et al., 2012; Alley et al., 2018) and West Antarctic sites (Hillenbrand et al., 2010a) as well as nearby Palmer Deep, on the inner shelf of AHT (Domack et al., 2001; Leventer et al., 2002) (Figure 5.11; Table 5.4). Laminated diatomaceous oozes in these cores fall into three general categories; (1) immediate post glacial varved diatomaceous oozes with highly laminated sediments through most of the Holocene

(Fig. 5.12a), (2) immediate post-glacial laminated (not varved) diatomaceous oozes with highly laminated sediments through most of the Holocene (Fig. 5.12b) and (3) cores contain a discrete unit of post-glacial laminated diatomaceous ooze (Figure 5.12c). In this scheme immediate post-glacial refers to sediments overlying sub-glacial to grounding line-proximal sediments. Suggested controls on the accumulation and preservation of laminated diatomaceous ooze deposits include water depth, basin geometry and duration, stability and prevalence of environmental conditions that promote high levels of productivity e.g. duration of calving bay re-entrant (Stickley et al., 2005; Leventer et al., 2006).

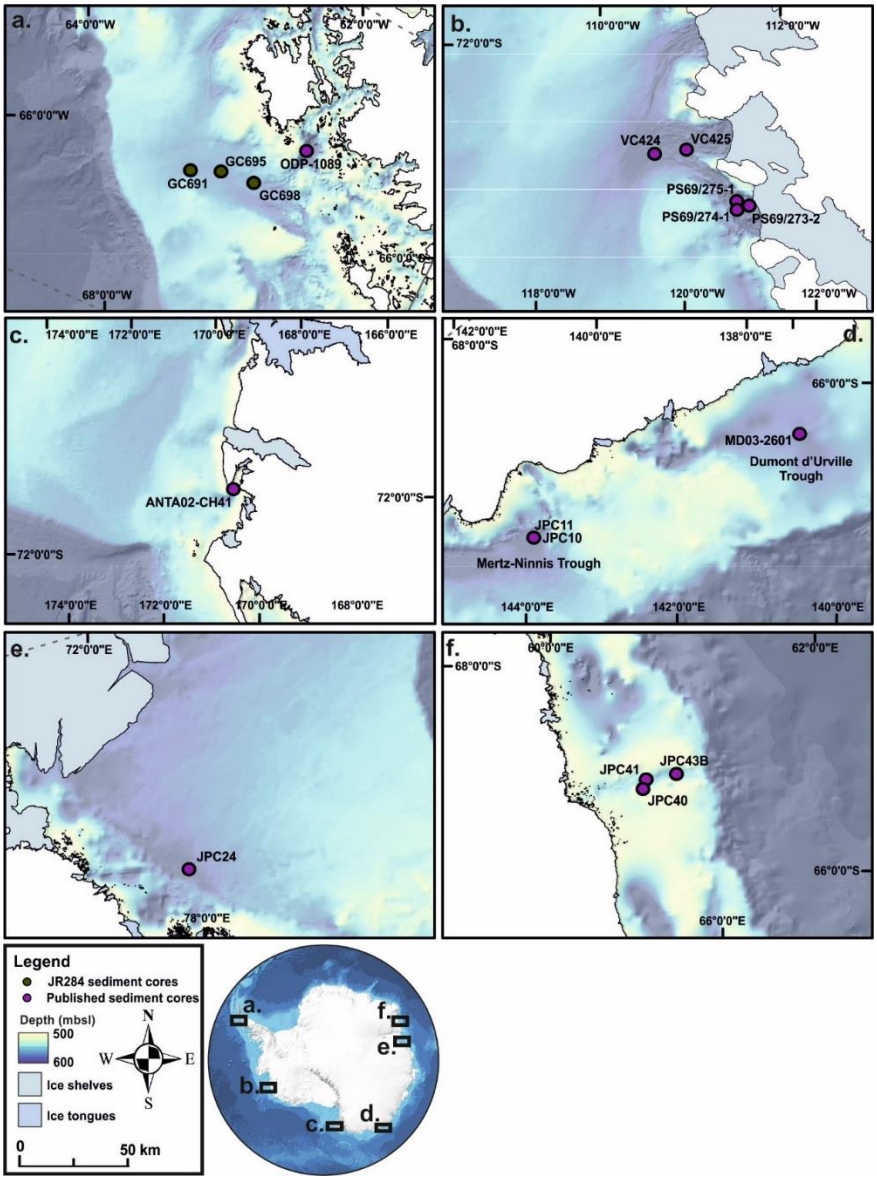

Figure 5.11: Locations of sediment cores containing laminated diatomaceous ooze deposits for (a) AHT (Domack et al., 2001; this study), (b) Amundsen Sea Embayment, WAIS (Hillenbrand et al., 2010a), (c) Cape Hallet Bay (Finocchiaro et al., 2005), (d) Mertz-Ninnis Trough and Dumont d'Urville Trough (Leventer et al., 2006; Crosta et al., 2005; Leventer et al., 2006; Maddison et al., 2006), (e) Svenner Channel (Leventer et al., 2006) and (f) Iceberg Alley and Nielsen Basin (Stickley et al., 2005; Leventer et al., 2006; Alley et al., 2018),

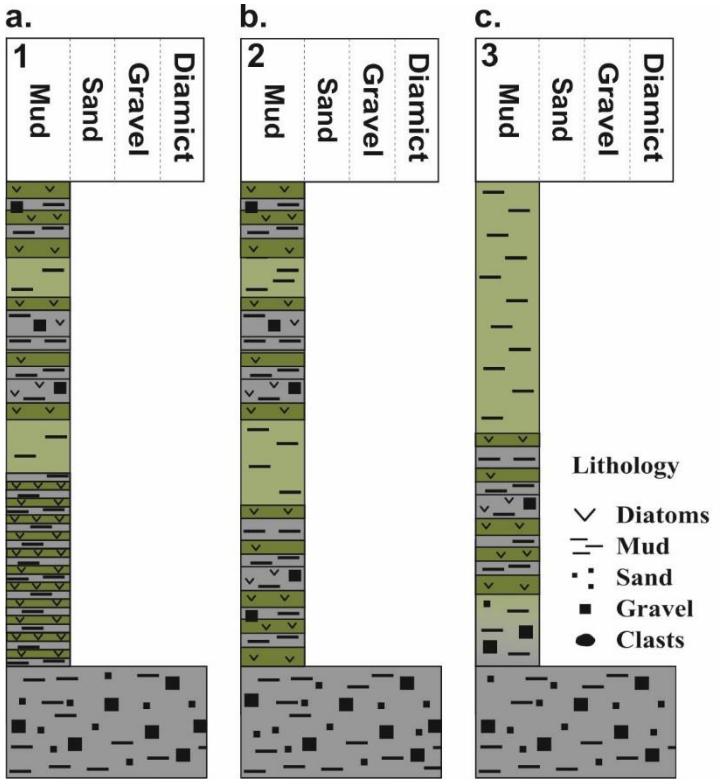

Figure 5.12: Schematic showing the three main types of laminated diatomaceous oozes. (a) Type 1: Immediate post-glacial varved sediments and highly laminated throughout the Holocene. (b) Type 2: Immediate post-glacial laminated but not varved sediments and highly laminated throughout the Holocene. (c) Type 3: Cores contain a discrete unit of post-glacial laminated diatomaceous ooze.

Immediate post-glacial sediments composed of varved diatomaceous ooze (Fig. 5.12a) are seen in cores recovered from Nielsen Basin (JPC40), Svenner Channel (JPC24), Iceberg Alley (JPC43B) and the Palmer Deep (ODP-1098) (Domack et al., 2001; Leventer et al., 2002; Sjunneskog and Taylor, 2002; Taylor and Sjunneskog; 2002; Maddison et al., 2005; Stickley et al., 2005; Leventer et al., 2006; Barbara et al., 2010) (Fig. 5.11). Rhythmic varves are observed at the base of the laminated sequences in these cores, often overlying glaciomarine diamictons or terrigenous sediments deposited in an ice-proximal setting, and are associated with a close proximity to the ice margin with associated meltwater and nutrient input (Leventer et al., 2002). Varves are composed of layers of diatomaceous ooze and terrigenous laminae, representing spring productivity and terrigenous sediment input over the summer; sourced from melting glacial ice (Leventer et al., 2002; Maddison et al., 2005; Stickley et al., 2005; Leventer et al., 2006). There is typically gradation between these layers, from pure *Chs* ooze through increasingly mixed diatom ooze and then increasingly terrigenous-rich (Maddison et al., 2005; Stickley et al., 2005). *Chs*-RS and *Chs*-veg typically dominate the diatomaceous ooze laminae. Sub-dominant species within these varved diatomaceous ooze deposits include *Corethron pennatum, Rhizosolenia* spp., *Fragilariopsis curta, Fragilariopsis cylindrus* and *Thalassiosira antarctica* (Leventer et al., 2002; Taylor and Sjunneskog; 2002; Maddison et al.,

2005; Stickley et al., 2005; Leventer et al., 2006). The terrigenous-rich laminae contain a more diverse diatom assemblage and typically include abundant *T. antarctica* T2 RS (Maddison et al., 2005; Stickley et al., 2005; Leventer et al., 2006; Barbara et al., 2010). The dominance of diatom species with characteristics that aid mass sedimentation enhances the likelihood of forming distinct laminae. These species include highly silicified *Chs*-RS that sink rapidly, as well as *C. pennatum*, which has long spines that enable entanglement and rapid mass export (Alley et al., 2018).

The enhanced productivity and export of diatoms during deglaciation is attributed to a high flux of glacial meltwater and nutrients into a restricted calving bay environment following retreat of grounded ice from the cross-shelf troughs (Domack et al., 2006; Leventer et al., 2006). The thickness of the varved section is therefore considered a function of calving bay duration (Leventer et al., 2006). The geometry of the trough or basin is also considered an important control on varve accumulation and preservation (Stickley et al., 2005; Leventer et al., 2006). Iceberg Alley and Nielsen Basin are relatively narrow (<20 km wide), steep sided (Fig. 5.11f), and the shallow banks of Iceberg Alley are susceptible to remnant grounded ice and/or icebergs. This provides a sheltered setting, promoting focussing of meltwater from sea ice, glaciers and icebergs resulting in water column stratification and enhanced productivity (Stickley et al., 2005; Leventer et al., 2006; Alley et al., 2018). Indeed, the trough geometry of Iceberg Alley creates an environment that favours blooming of meltwater and water column stratification associated diatom species, *Chs*, *Corethron pennatum*, *Fragilariopsis curta*, *Fragilariopsis cylindrus* and *Rhizosolenia* spp. throughout the Holocene, to the modern day (Alley et al., 2018). Palmer Deep core ODP-1098 was recovered from a deep inner-shelf basin with a water depth of 1,012 m (Fig. 5.11a) (Domack et al., 2001). Focussing of sediment promotes high sediment accumulation rates of 0.17-1.02 cm yr^{-1} for Palmer Deep, promoting preservation of seasonal varves (Leventer et al., 2002; Maddison et al., 2005). Svenner Channel core JPC24, contains the thinnest varved unit of 0.22 m (Leventer et al., 2006; Barbara et al., 2010). This thin varved unit is associated with the relatively open oceanographic setting (Fig. 5.11e), allowing current transport to hinder high sediment accumulation rates (Leventer et al., 2006). A relatively short-lived calving bay environment compared to Palmer Deep and the Mac. Robertson Shelf, could have additionally limited varve accumulation in Svenner Channel (Leventer et al., 2006). Varved diatomaceous ooze within Nielsen Basin (JPC40), Svenner Channel (JPC24), Iceberg Alley (JPC43B) and the Palmer Deep (ODP-1098) underlie units of laminated, bioturbated and massive diatomaceous ooze (Fig. 5.12a), and in the case of Palmer Deep core ODP-1098, several turbidites (Domack et al., 2001; Leventer et al., 2002; Sjunneskog and Taylor, 2002; Taylor and Sjunneskog; 2002; Maddison et al., 2005; Stickley

et al., 2005; Leventer et al., 2006; Barbara et al., 2010). The loss of distinct varves up-core is associated with the loss of a calving bay setting and a reduction in glacial discharge, with associated nutrient input, through the Holocene; ultimately reducing biogenic productivity and mass sedimentation events (Leventer et al., 2002; Leventer et al., 2006). The absence of evidence for bioturbation within varved diatomaceous oozes indicates absent or suppressed bioturbation during mass diatom sedimentation events.

Units of laminated, bioturbated and massive diatomaceous ooze comprise the length of cores recovered from Dumont d'Urville Trough (MD03-2601) and Mertz-Ninnis Trough (JPC10 and JPC11). In the case of cores MD03-2601 and JPC10, the glacial to post-glacial transition is not recovered, so it is not possible to rule out immediate post-glacial varve deposition. However, core JPC11, penetrated underlying glaciomarine sediments, comprised of diatomaceous grey, muddy clay with ice rafted debris. Bioturbated and thinly laminated diatomaceous ooze directly overly these glaciomarine sediments and varved sediments were not observed (Fig. 5.11d and Fig. 5.12b). *Chs* dominate biogenic laminae, whilst terrigenous laminae are characterised by a more diverse species assemblage (Leventer et al., 2006). Despite being recovered from a relatively deep setting, the relatively open geometry of Mertz-Ninnis Trough may have hindered calving bay formation and created a more open oceanographic setting, inhibiting the deposition of seasonal laminae (varves) (Leventer et al., 2006).

Cores GC691, GC695 and GC698 (this study; Fig. 5.11a) contain laminations of alternating biogenic and terrigenous laminae; rhythmic annual varves are not observed, and the deposition of laminations does not persist through the Holocene (Fig. 5.12c). These discrete laminated units contain a diatom assemblage indicative of a seasonal species succession, such as that observed with the annual varves deposited at the base of the Palmer Deep, Iceberg Alley, Svenner Channel and Nielsen Basin laminated sequences (Domack et al., 2001; Leventer et al., 2002; Sjunneskog and Taylor, 2002; Taylor and Sjunneskog; 2002; Maddison et al., 2005; Stickley et al., 2005; Leventer et al., 2006; Barbara et al., 2010). This includes abundant *Fragilariopsis curta*, *Chs*, *Corethron pennatum* and *Thalassiosira antarctica* T2 RS and is interpreted to represent similar environmental conditions; enhanced flux of meltwater and nutrients from sea and glacial ice. The presence of a discrete unit of laminated diatomaceous ooze in these cores, with a lack of laminations through the overlying Holocene diatomaceous muds, may be the result of the geometry of AHT, which is relatively wide (24-40 km) and shallow (400-800 m) compared to sites containing continuously/discontinuously laminated sediments throughout the Holocene. Relatively open oceanographic conditions may favour

diatom assemblages to be advected by currents on the continental shelf during deposition, or to be re-mobilised post-deposition (Scherer et al., 1994). It is possible that only during deposition of Zone 5, were diatom export rates high enough to form distinct laminae and supress bioturbation by benthic fauna. A similar discrete laminated unit of *C. pennatum, F. curta* and *Chs*-RS dominated laminated diatomaceous ooze is present in Cape Hallet Bay core ANTA02-CH41 (Fig. 5.11c; water depth 461 m) and in cores recovered from Amundsen Sea (Fig. 5.11b; water depth >1,000 m) (Finocchiaro et al., 2005; Hillenbrand et al., 2010a). As with cores analysed for this study, laminations in core ANTA02-CH41 and within those recovered from the Amundsen Sea, relate to a period of enhanced primary productivity, associated with glacial meltwater input and the formation of a well-stratified water column (Finocchiaro et al., 2005; Hillenbrand et al., 2010a). Interestingly, despite being recovered from relatively deep settings, cores recovered from the Amundsen Sea contain relatively thin units of bioturbated, laminated and stratified, *C. pennatum, F. curta* and *Chs*-RS dominated, diatomaceous ooze (Hillenbrand et al., 2010a). This potentially relates to regional variability in glacial meltwater availability and/or variability in the length of the growing season.

5.3.3. Bathymetric control on laminated diatomaceous ooze accumulation

As shown in the previous section, controls on the accumulation and preservation of laminated diatomaceous ooze deposits include water depth, basin geometry and duration, stability and prevalence of environmental conditions that promote high levels of productivity e.g. duration of calving bay re-entrant (Stickley et al., 2005; Leventer et al., 2006). These controls have been used to interpret the thickness and distribution of laminated diatomaceous ooze within previously published cores (Leventer et al., 2006). This study has a unique benefit of utilising several cores from one region that is extensively surveyed, and can thus be used to further investigate the spatial extent of diatom bloom production and the controls on laminated diatomaceous ooze deposition, accumulation and preservation.

Through carrying out quantitative diatom analysis for cores GC695 and GC697, cores that do and do not contain thick (> 100 cm) units of laminated diatomaceous ooze can be compared. Results of this study indicate that thin (<30 cm) units of *Chs*-RS and *Corethron pennatum*-dominated sediments within core GC697 occur at the same stratigraphic interval as the unit of *Chs*-RS and *C. pennatum* dominated laminated diatomaceous ooze within core GC695 (Figure 5.8). These units are thus both considered diatom Zone 5, representing peak productivity during a period of enhanced meltwater input. The results of the multi-proxy analysis of all cores (Ch. 4) can be used to trace Zone 5 along AHT (e.g. Fig. 5.8). Thin homogenous units

(of Zone 5) are observed in cores GC692, GC690, GC702, GC711, GC697 and GC709, whilst thick units of laminated diatomaceous ooze are found only in cores GC691, GC695 and GC698 (Fig 5.8). These two core types differ in their bathymetric context, with core sites GC691, GC695 and GC698 recovered from bathymetric low points compared with the exposed position of most other sites (Fig 5.5). Seafloor bathymetry is therefore considered a key control on ooze accumulation. Specifically, bathymetric depressions could act as a focussing point for any current-mobilised diatoms that have been exported to the seafloor.

Based on this inference, diatom blooms forming the laminations of Zone 5 potentially covered an area with an along trough expanse of 50 km (between core sites GC698 and GC691). The observation of wide-scale diatom blooming within the AHT following the last deglaciation of the AHIS, preserved as thick (100 cm) laminated or thin (<30 cm) homogenous *Chs*-RS and *Corethron pennatum*-dominated diatomaceous ooze units, emphasises that it is possible to underestimate the scale of surface productivity depending on the bathymetric setting of a chosen core site. The spatial distribution and thickness of ooze deposits on the seabed does not necessarily directly reflect productivity within the immediate surface waters.

Therefore, in addition to water depth, basin geometry, stability/duration of favourable environmental conditions (e.g., calving bay), seafloor bathymetry plays an important role in laminated diatomaceous ooze accumulation. The discontinuity of *Chs*-RS and *Corethron pennatum*-dominated diatomaceous ooze thickness across the AHT, indicates that ooze thickness is not always a function of the scale and duration of surface productivity and associated environmental conditions. This is an important inference when sediment cores are used to assess the relationship between deglaciation and primary productivity during past deglacial periods, and when these inferred palaeoenvironmental conditions are used as an analogue for future environmental change.

5.4. Conclusions

- Quantitative ADA and assemblage data indicates that the AHT trough experienced a number of environmental changes, including a period of enhanced biological productivity associated with deposition of laminated diatomaceous ooze following grounding line retreat after the LGM.
- Deposition of laminated diatomaceous ooze is associated with meltwater discharge and nutrient input from sea and glacial ice melt. This is indicated by the prevalence of

sea ice and sea ice-melt associated diatom species *Fragilariopsis curta, Chs* and *Corethron pennatum.*

- Grounding line retreat within AHT and the formation of a calving bay were not solely responsible for the enhanced productivity and formation of laminated diatomaceous ooze units within AHT, as laminated diatomaceous ooze units do not directly overly sub-glacial to grounding-line proximal sediments in these cores. Additional drivers of meltwater input and water column stratification, in addition to the formation of a calving bay, were required to enhance productivity of species *Fragilariopsis curta, Chs* and *Corethron pennatum*. Radiocarbon dating of this sequence (next Chapter) will allow this episode of peak productivity (Zone 5; laminated diatomaceous ooze) to be compared with published records of sea level, atmospheric and SSTs, CDW upwelling, and glacial discharge.
- The use of multiple sediment cores and extensive bathymetric mapping of the AHT, demonstrates that seafloor bathymetry, in addition to water depth, basin geometry and duration, stability and prevalence of environmental conditions, plays an important role in laminated diatomaceous ooze accumulation. The presence of thick (100 cm) laminated or thin (<30 cm) homogenous *Chs*-RS and *Corethron pennatum*-dominated diatomaceous ooze units emphasises that it is possible to underestimate the scale of surface productivity depending on the bathymetric setting of a chosen core site. This is an important inference when sediment cores are used to assess the relationship between deglaciation and primary productivity during past deglacial periods, and when these inferred palaeoenvironmental conditions are used as an analogue for future environmental change.
- The next chapter will present new chronological data, used to constrain the timing of grounding line retreat together with the timing of subsequent productivity events and deposition of the oozes.

Author	Region	Core no.	Longitude	Latitude	Depth (mbsl)	Onset of laminae deposition (Cal yr BP)	Underlying sediment	Lamination style	Diatom assemblage
Finocchiaro et al, 2005	Cape Hallett Bay in, western Ross Sea, West Antarctica	ANTA02-CH41	170.1500	-72.2917	416	>10,070 + 50 (not calibrated)	Not recovered	Sediments consist of a 1 m unit of laminated diatomaceous ooze. Laminae are differentiated by distinct colour changes. The laminated unit is overlain by a 1 m unit of massive mud with irregular laminae and an upper 2.07 m unit of muddy sand.	Diatom ooze laminae are dominated by Chs-RS, C. pennatum and F. curta. The overlying muddy sand is dominated by *Ch*-RS and a higher percentage of *F.curta* relative to the laminated unit.
Stickley et al, 2005; Leventer et al, 2006	Iceberg Alley, Mac.Robertson Shelf, East Antarctica	JPC43B	63.1229	-66.9324	465	>11,450 + 300	Not recovered	At least 4.8 m of varved sediments overly glacial sediments. Varves consist of interbedded diatomaceous ooze and terrigenous-rich laminae. Varved sediments are overlain by 19.13 m of laminated and bioturbated diatomaceous ooze.	Varved sediments are dominated by *Chs*- Rs and vegetative cells. Other common species are *C. criophilium* , *Rhizosolenia* spp. and *F.curta*. Terrigenous laminae contain a more diverse diatom assemblage, including abundant *T. antarctica* .
Alley et al, 2018	Iceberg Alley, Mac.Robertson Shelf, East Antarctica	JPC41	62.9897	-67.1305	573	>1,600	Not recovered	Core continuously laminated over 21 m. Lamiae are differentiated by distinct colour changes.	Laminated sediments are dominated by *F. curta, Chaetoceros Ehrnberg* subg., *Hylochaete Gran* vegetative cells and resting spores, *C. pennatum* and *Rhizosolenia* spp.
This study	Anvers-Hugo Trough, western Antarctic Pensinsula	GC691	-65.4915	-64.2873	604	11,200 + 1,300	Grey mud with dispersed gravel	A 1.11 m laminated diatomaceous ooze unit overlies glaciomarine sediments. 2.09m of bioturbated diatomaceous mud overlies the laminated unit and extends to the core top.	Biogenic laminae are dominated by *Chs* -RS, *C. pennatum* , *Proboscia* spp., *T antarctica, T. scotia* and *P. glacialis* . Terrigenous laminae have a lower absolute diatom abundance, a lower percentage of *Chs* -RS and a mixed diatom assemblage
This study	Anvers-Hugo Trough, western Antarctic Pensinsula	GC698	-65.3303	-64.6323	607	11,475 + 434	Grey mud with dispersed gravel	A 1.36 m laminated diatomaceous ooze unit overlies glaciomarine sediments. 3.13 m of bioturbated diatomaceous mud overlies the laminated unit and extends to the core top.	Idem GC691
This study	Anvers-Hugo Trough, western Antarctic Pensinsula	GC695	-65.3130	-64.4738	629	11,300 + 250	Grey mud with dispersed gravel	A 2.23 m laminated diatomaceous ooze unit overlies glaciomarine sediments. 3.23 m of bioturbated diatomaceous mud overlies the laminated unit and extends to the core top.	Idem GC691
Denis et al, 2006; Crosta et al, 2005	Dumont d'Urville Trough, Adelie Land, East Antarctica	MD03-2601	138.5572	-66.0512	746	>9,555	Not recovered	Sediments consist of 40.24 m of laminated diatomaceous ooze interbedded with units of massive mud.	Diatom ooze laminae are dominated by *F. curta, Chs* -RS, *C. pennatum, Rhizosolenia spp., Phaeoceros spp* . and *F. rhombica. T* errigenous laminae contain species present in diatom ooze laminae, with a higher percentage of *T. antarctica* , *F. kerguelensis* ,
Leventer et al, 2006; Mackintosh et al, 2011	Nielsen Basin, Mac.Robertson Shelf, East Antarctica	JPC40	63.1229	-67.1765	750	14,000	Dark greenish grey silty clay and granule rich sand	Immediate post-glacial sediments are varved for 0.5 m. Varved sediments are overlain by 21.08 m of laminated and bioturbated diatomaceous ooze.	
Leventer et al, 2006; Barbara et al, 2010	Svenner Channel, Prydz Bay, East Antarctica	JPC24	76.7093	-68.6943	816	11,069 + 70 (extrapolated)	Greenish grey sandy and silty clay with ice rafter debris	Immediate post-glacial sediments are varved for 0.22 cm. Varved sediments are overlain by 15.58 m of laminated and bioturbated diatomaceous ooze.	*Chs* , *F. curta* , *F. cylindrus* and *T. antarctica* dominate postglacial sediments. *Chs-rs* are in highest abundance within varved sediments.
Leventer et al, 2006	Mertz-Ninnis Trough, East Antarctica	JPC11	143.0861	-66.5722	850	10,400 (not calibrated)	Diatomaceous grey, muddy clay with ice rafted debris	Post-glacial sediments consist 22.53 m of bioturbated and thinly laminated diatomaceous ooze.	Laminations alternate between *Chaetoceros* spp. dominated layers and layers with a diverse diatoms assemblage.

Table 5.4: Summary table for cores containing units of laminated diatomaceous ooze, including the author, geographic region, core number, location (longitude and latitude), water depth, date for the onset of laminated diatomaceous ooze deposition, underlying sediment type, diatomaceous lamination style and diatom assemblage.

Author	Region	Core no.	Longitude	Latitude	Depth (mbsl)	Onset of laminae deposition (Cal yr BP)	Underlying sediment	Lamination style	Diatom assemblage
Maddison et al, 2006, Leventer et al, 2001	Mertz-Ninnis Trough, East Antarctica	JPC10	143.0861	-66.5722	850	>13,550 + 50	Not recovered	Sediments consist 21.35 m of laminated diatomaceous ooze, with minor amounts of bioturbation	Diatom ooze laminae are dominated by *Chs*-RS, *C. pennatum* and *Rhizosolenia* spp. Terrigenous laminae contain a more diverse diatom assemblage, including abundant *P. glacialis*.
Maddison et al, 2005; Domack et al, 2001; Leventer et al, 2002; Sjunneskog and Taylor, 2002; Taylor and Sjunneskog 2002.	Palmer Deep, western Antarctic Peninsula	ODP core 178-1098A & 178-1098C	-64.4167	-64.9167	1012	13,180	Diamict	Immediate post-glacial sediments are varved for 4.44 m. Varves consist of interbedded diatomaceous ooze and terrigenous-rich laminae. Varved sediments are overlain by units of laminated diatomaceous ooze, massive muddy diatom ooze interbedded turbitdites.	Diatom ooze laminae are dominated by *Chs*-RS, with present *Chs*-veg, *T. antarctica*, *C. bouvet*, *O. weissflogii*, *Fragilariopsis* spp. and *C. criophilum*. Terrigenous laminae contain a more diverse assemblage including *C. criophilum*, *C. bouvet*, *O*. weissflogii, *T. antarctica* and *Fragilariopsis* spp.
Hillenbrand et al, 2010	Western Amundsen Sea Embayment, West Antarctica	VC424	-115.1983	-73.4467	1073	14,103	Bioturbated mud, sandy mud and muddy sand (with diatoms)	79 cm diatomaceous ooze unit, with bioturbation, lamination and stratification. The diatomaceous ooze unit is overlain by 198 cm of bioturbated and stratified mud and silty clay (with diatoms).	Diatom ooze is dominated by *C. pennatum*, *F. curta* and *Chs* and includes *Chaetoceros dichaeta*, *Proboscia inermis* and *Pseudo-nitzschia lineola*
Hillenbrand et al, 2010	Western Amundsen Sea Embayment, West Antarctica	VC425	-115.4867	-73.7033	1020	13,420	Bioturbated mud, sandy mud and muddy sand (with diatoms)	3 cm diatomaceous ooze unit, with bioturbation, lamination and stratification. The diatomaceous ooze unit is overlain by 221 cm of bioturbated and stratified mud and silty clay (with diatoms).	Diatom ooze is dominated by *C. pennatum*, *F. curta* and *Chs*.
Hillenbrand et al, 2010	Western Amundsen Sea Embayment, West Antarctica	PS69/273-2	-117.8433	-73.9617	1352	12,659	Bioturbated mud, sandy mud and muddy sand (with diatoms)	56 cm diatomaceous ooze unit, with bioturbation, lamination and stratification. The diatomaceous ooze unit is overlain by 163 cm of bioturbated and stratified mud and silty clay (with diatoms).	Diatom ooze is dominated by *C. pennatum*, *F. curta* and *Chs*.
Hillenbrand et al, 2010	Western Amundsen Sea Embayment, West Antarctica	PS69/274-1	-117.7750	-73.8567	1452	12,681	Bioturbated mud, sandy mud and muddy sand (with diatoms)	42 cm diatomaceous ooze unit, with bioturbation, lamination and stratification. The diatomaceous ooze unit is overlain by 196 cm of bioturbated and stratified mud and silty clay (with diatoms).	Diatom ooze is dominated by *C. pennatum*, *F. curta* and *Chs*.
Hillenbrand et al, 2010	Western Amundsen Sea Embayment, West Antarctica	PS69/275-1	-117.5483	-73.8883	1518	11,956	Bioturbated mud, sandy mud and muddy sand (with diatoms)	16 cm diatomaceous ooze unit, with bioturbation, lamination and stratification. The diatomaceous ooze unit is overlain by 191 cm of bioturbated and stratified mud and silty clay (with diatoms).	Diatom ooze is dominated by *C. pennatum*, *F. curta* and *Chs*.

Table 5.4 (continued): Summary table for cores containing units of laminated diatomaceous ooze, including the author, geographic region, core number, location (longitude and latitude), water depth, date for the onset of laminated diatomaceous ooze deposition, underlying sediment type, diatomaceous lamination style and diatom assemblage.

Chapter 6

6. Deglacial chronology of Anvers-Hugo Trough

Abstract

Palaeo-ice stream reconstructions provide an opportunity to extend the timescales over which we understand deglaciation and the mechanisms that control ice sheet retreat. An important aspect of these reconstructions is accurately constraining the timing and rate of grounding line retreat. This allows potential drivers, including the relative importance of sea-level rise, atmospheric and ocean forcing, together with trough geometry and bathymetry, to be identified. In comparison to other well-dated palaeo-ice stream troughs, the deglacial chronology of AHT is poorly constrained. This reflects a lack of core sites, as well as limitations associated with dating the AIO fraction of sediments. This study utilises an extensive network of cores recovered from Anvers-Hugo Trough and twenty-seven new radiocarbon dates, obtained from calcareous (micro-) fossils, the AIO fraction of sediments and Ramped PyrOx ^{14}C dating, to build on this deglacial chronology. It aims to date the deglaciation of the trough, as well as environmental changes following grounding line retreat, in particular focussing on the timing of laminated diatomaceous ooze deposition. This chapter also considers the influence of GZWs on ice stream retreat including an assessment of the time-period over which these features are likely to have formed. The new dates indicate that the Anvers-Hugo Ice Stream had retreated across the outer and middle shelf at a rate of 127 m yr^{-1}. Over this period two GZWs, including one compound-GZW were deposited, likely on centennial timescales. Grounded ice retreated from the middle shelf to Palmer Deep on the inner shelf from 15.84 to 12.85 cal. kyr BP and occurred at a rate of 25 m yr^{-1}. The presence of pinning points and the rugged bedrock topography of the inner shelf part of AHT appears to have slowed down ice stream retreat. Seasonally open marine conditions in AHT were established as early as 14.40 cal. kyr BP, driven by oceanic warming, associated with an influx of CDW onto the AP shelf. Between 11.27 to 9.29 cal. kyr BP, approximately 4.64 kyr after grounded ice retreat, thick laminated diatomaceous ooze was deposited at mid-shelf sites in AHT during a period of high diatom productivity. We suggest that the retreat of AHIS and the creation of a calving bay was not the sole driver this highly productive environment. Instead, it is argued that high atmospheric and sea surface temperatures and intensified upwelling of CDW delivered warm, nutrient-rich waters to AHT, which facilitated enhanced meltwater-driven productivity.

6.1. Introduction

This chapter builds on the detailed sedimentological and diatom assemblage data presented in Chapters 4 and 5 respectively. It presents new radiocarbon age-data for cores recovered from AHT with the dual aim of constraining: (i) the timing of grounded ice retreat following the LGM, and (ii) the timing of key palaeoenvironmental changes following deglaciation. The latter includes the deposition of laminated diatomaceous oozes, i.e. packages of sediments deposited during an episode of elevated biological productivity following grounded ice-stream retreat from AHT (Ch. 5). The new age-date is also used to investigate the dominant controls on ice sheet retreat in this region including the relative importance of sea-level rise, atmospheric and ocean forcing, together with trough geometry and bathymetry. This chapter also considers the influence of GZWs on ice stream retreat including an assessment of the time-period over which these features are likely to have formed. First, the overall dating strategy and ^{14}C data is outlined.

6.2. Results

6.2.1. ^{14}C data and dating approach

A total of twenty-seven new radiocarbon ages were acquired for this thesis (seven = carbonate (benthic and calcareous foraminifera), thirteen = AIO and seven = Ramped PyrOx ^{14}C; Table 6.1 and 6.2 and Fig. 6.1-6.3). All ages are given as uncorrected ^{14}C years or cal. yrs B.P., quoted as the mid-point of the 2σ range (Table 6.1 and Fig. 6.3). For traceability, uncorrected/calibrated ages are quoted in full and are not rounded. In order to assess differences (and the magnitude of the error(s)) in the three dating methods employed in this thesis, a number of steps were undertaken. First, the LCO, which gives some indication about the reliability of using the AIO fraction for dating was assessed (qualitatively) by dating surface sediments at two sites (BC696 and BC699). Substantial deviation from a modern surface age indicates significant input of fossil carbon and low confidence in using the AIO fraction for establishing reliable chronologies. Second, the reliability of using AIO-derived ages was tested through paired AIO-foraminifera dating in two cores. Finally, the result of the Ramped PyrOx ^{14}C dating is compared with both AIO and foraminifera-derived ages to provide independent assessment of both dating approaches as well as a qualitative test of the apparent reliability of the Ramped PyrOx method. Note that reliability in the context of this discussion is in part quantitative (e.g., paired-dating) and part qualitative, whereby stratigraphic context and sediment type is taken into consideration (e.g., glacier proximal

terrigenous sediments are more likely to yield anomalously old AIO ages relative to organic-rich sediments deposited in a seasonally open marine environment).

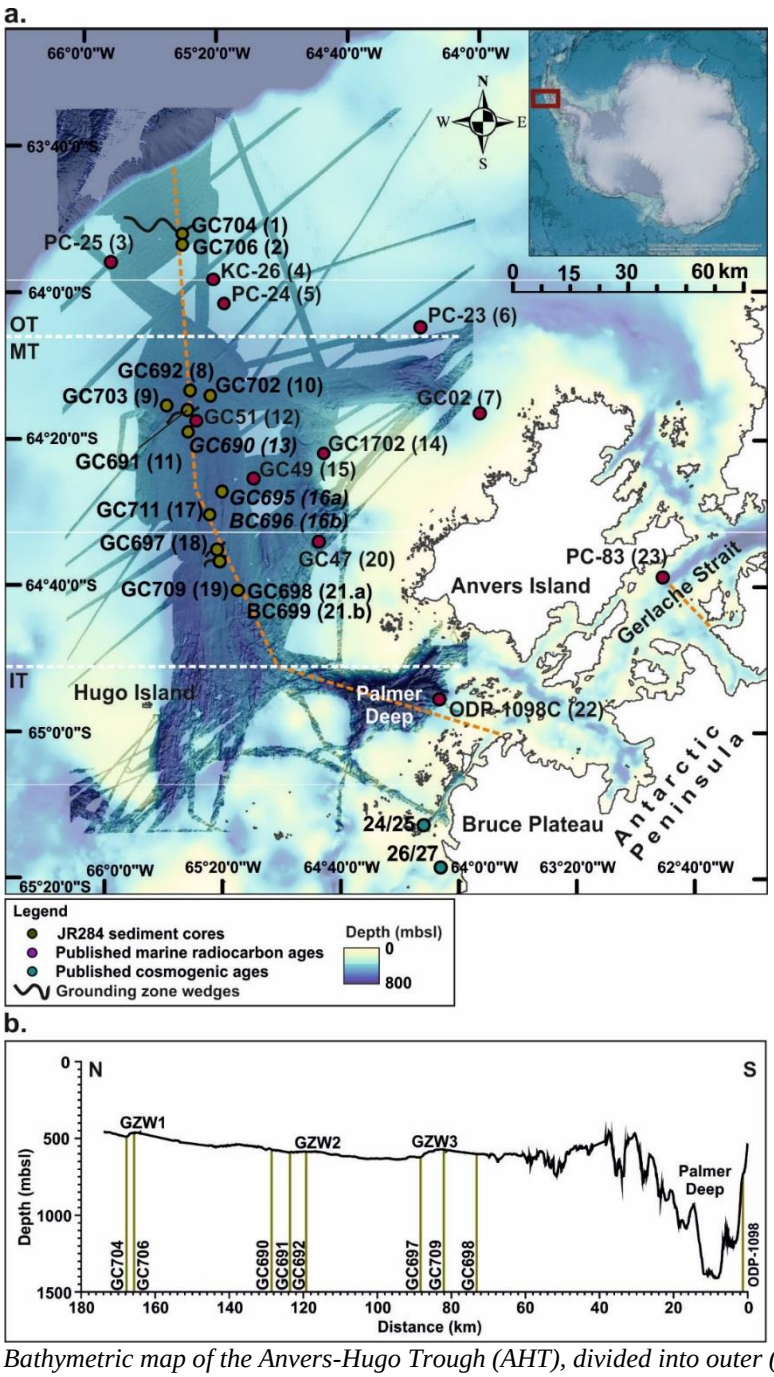

Figure 6.1: (a) Bathymetric map of the Anvers-Hugo Trough (AHT), divided into outer (OT), mid (MT) and inner-trough (IT) regions. Inset shows location of the study area in the wider Antarctic context. Cores discussed in this chapter are labelled with an ID number (in brackets) (Harden et al., 1992; Pudsey et al., 1994; Nishimura et al., 1999; Domack et al., 2001; Yoon et al., 2002; Heroy and Anderson, 2005, 2007; Ó Cofaigh et al., 2014). (b) Bathymetric cross section (Fig. 6.1a; dashed orange line) of AHT trough with GZWs 1-3 and core locations labelled.

Marine radiocarbon ages

Core	^{14}C Lab code	Cruise	Study	Latitude	Longitude	Water depth (mbsl)	Depth Interval (cm)	Uncorrected age (yrs BP)	Reported uncertainty	Marine reservoir (yrs)	+/-	Core top age	LCO	Mean calibrated age (yrs BP)	2σ error range	δ^{13}C (‰)	Material dated	Sediment dated	Biogenic opal content (%)	ID
JR284 Dates																				
GC690	4GC690307F	JR284	This study	-64.337167	-65.489500	584	307-308	13910	50	1230	100			15049	442	0.0	F (P & B)	SD: Top		13
GC690	DB1584-2, GC690	JR284	This study	-64.337167	-65.489500	584	313-314	13030	180	1230	100			13688	863	-27.6	RP	SD: Top		13
GC691	11GC691265AIO	JR284	This study	-64.287333	-65.491500	604	265-266	9520	50	1230	100			9292	493	-	AIO	LDO: Mid	31	11
GC691	5GC691285F	JR284	This study	-64.287333	-65.491500	604	285-286	11030	40	1230	100			11191	183	0.5	F (P)	LDO: Base		11
GC691	12GC691292.5AIO	JR284	This study	-64.287333	-65.491500	604	292.5-293.5	11140	40	1230	100			11462	725	-23.4	AIO	LDO: Base	33	11
GC691	DB1575-2, GC691D	JR284	This study	-64.287333	-65.491500	604	327-328	11770	120	1230	100			11197.5	989	-26.0	RP	mbGM: Top		11
GC695	695_161-162_O	JR284	This study	-64.473833	-65.313000	629	161-162	8250	30	1230	100			7883	440	-23	AIO	mbGM	30	
GC695	695_240-241_O	JR284	This study	-64.473833	-65.313000	629	240-241	11420	30	1230	100	2080	850	10648	250	-23.8	AIO	mbGM	20	
GC695	1GC695324AIO	JR284	This study	-64.473833	-65.313000	629	324-325	11790	40	1230	100	2080	850	11096	262	-24.5	AIO	LDO: Top	15	16
GC695	2GC695372AIO	JR284	This study	-64.473833	-65.313000	629	372-373	10860	40	1230	100			10968.5	507	-24.2	AIO	LDO: Mid	34	16
GC695	3GC695460.5AIO	JR284	This study	-64.473833	-65.313000	629	460.5-461.5	11060	40	1230	100			11345	737	-21.1	AIO	LDO: Mid	31	16
GC695	6GC695541F	JR284	This study	-64.473833	-65.313000	629	541-542	11100	40	1230	100			11270	250	-11.2	F (P)	mbGM: Mid		16
GC695	2GC695541AIO	JR284	This study	-64.473833	-65.313000	629	541-542	13690	30	1230	100	2080	850	13450.5	251	-24.9	AIO	mbGM: Mid	8	16
GC695	DB1580-1, GC695	JR284	This study	-64.473833	-65.313000	629	580-581	12360	190	1230	100			13010	765	-26.2	RP	mbGM: Mid		16
BC696	696_0-1_O	JR284	This study	-64.473833	-65.313000	629	0	2080	30	1230	100			-	-	-26.6	AIO	mbGM	28	
GC697	DB1572-2, GC697	JR284	This study	-64.605000	-65.343333	583	281-282	11080	140	1230	100			11279.5	1097	-26.8	RP	mbGM: Top		18
GC697	7GC697343.5F	JR284	This study	-64.605000	-65.343333	583	343.5-344.5	13580	40	1230	100			14389	548	-0.2	F (P & B)	SD: Top		18
GC698	13GC698365.5AIO	JR284	This study	-64.700000	-65.233333	607	365.5-366.5	10570	40	1230	100	2320	1090	9308	275	-20.0	AIO	LDO: Mid	21	20
GC698	14GC698389AIO	JR284	This study	-64.700000	-65.233333	607	389-399	10420	40	1230	100			10457	504	-21.0	AIO	LDO: Mid	33	20
GC698	8GC698445F	JR284	This study	-64.700000	-65.233333	607	445-446	11220	30	1230	100			11475	434	0.1	F (B)	LDO: Base		20
GC698	3GC698445AIO	JR284	This study	-64.700000	-65.233333	607	445-446	11390	50	1230	100			11769	958	-22.8	AIO	LDO: Base	28	20
BC699	1BC699AIO	JR284	This study	-64.700000	-65.233333	605	Surface	2320	30	1230	100			-	-	-24.9	AIO	bM: Top	21	21
GC704	DB1582-2, GC704	JR284	This study	-63.886833	-65.511333	475	93-94	12700	180	1230	100			13336	886	-26.0	RP	GSM: Top		1
GC706	DB1576-1, GC706	JR284	This study	-63.910833	-65.513833	453	32-33	11550	190	1230	100			11971	1282	-28.5	RP	IT		2
GC709	DB1581-1, GC709	JR284	This study	-64.632333	-65.330333	556	232-233	10440	140	1230	100			10555	874	-27.0	RP	mbGM: Mid		19
GC709	9GC709284.5F	JR284	This study	-64.632333	-65.330333	556	284.5-285.5	14410	40	1230	100			15843	348	0.6	F (P)	SD: Top		19
GC711	10GC711346.5F	JR284	This study	-64.527333	-65.381333	614	346.5-347.5	14260	40	1230	100			15569	434	0.3	F (P)	SD: Top		17
Published dates																				
PC-23		NBP-0201	Heroy and Anderson 2007	-64.098445	-64.277570	533	306	11170	81	1230	100			11514	814	1.3	S	SD		6
PC-24		NBP-0201	Heroy and Anderson 2007	-64.046476	-65.297234	557	190	14020	110	1230	100			15198	1162	-0.1	F (P & B)	SD		5
PC-25		NBP-0201	Heroy and Anderson 2007	-63.949026	-65.883094	438	20-30	14450	120	1230	100			15811	940	0.2	F (P & B)	IT		3
KC-26		NBP-0201	Heroy and Anderson 2007	-63.991068	-65.355262	530	248-252	14880	200	1230	100			16488	1306	0.0	F (P & B)	SD		4
GC-02		KARP 1998/1999 99/00	Yoon et al. 2002	-64.291822	-63.962335	400	70	12840	85	1230	100	3000	1770	11336	576	0.0	AIO	mbGM: Top		7
GC49		D172	Pudsey et al. 1994	-64.443000	-65.148000	547	290	13110	120	1230	100	3200	1970	11469	772	0.0	AIO	mbGM: Top		15
GC51		D172	Pudsey et al. 1994	-64.313000	-65.450000	575	210	12730	130	1230	100	1500	270	13077	553	0.0	AIO	mbGM: Top		12
GC1702		TH96 RV Hakurei-Maru	Nishimura et al. 1999	-64.387146	-64.779050	522	195-198	14320	50	1230	100	2430	1200	13864	304	-25.1	AIO	mbGM: Mid		14
ODP-1098C	OS-24758	ODP Leg 178 Cruise 98-02	Domack et al. 2001	-64.786142	-60.556385	1012	4192-4194	12250	60	1230	100	1260	30	12852	330	-21.8	AIO	LDO: Mid		22
PC-83		Deep Freeze 1986	Harden et al. 1992	-64.671912	-62.996757	393	70-85	10240	250	1230	100	2760	1530	8423.5	1499	-22.2	AIO	mbMG		23

Table 6.1: Site information and uncorrected and calibrated AMS ^{14}C dates for the Anvers-Hugo Trough. Including sample depth, sampled material/method (AIO, foraminifera, shell and Ramped PyrOx), biogenic opal content of sediment and sediment unit dated (with position in unit): SD: stratified diamicton, GSM: mud alternating with gravel and sand, mbMG: bioturbated to massive mud with dispersed gravel, bM: bioturbated mud, LDO: laminated to stratified diatomaceous ooze, IT: iceberg turbate. Foraminifera dates are corrected for the marine reservoir effect (1,230±100 yrs (Ó Cofaigh et al., 2014)). AIO dates are corrected using the seafloor surface sediment ages of 2,320±30 or 2,080±30 yrs obtained from BC699 and BC696, respectively, when a sample has a biogenic opal content of less than 21%. When samples have a biogenic opal content of more than 21%, dates are corrected using the marine reservoir effect only (1,230±100 yrs). All dates are calibrated in Calib v.7.0.4, using the Marine13 calibration curve. Reported ages are the midpoint between the 2σ standard deviation.

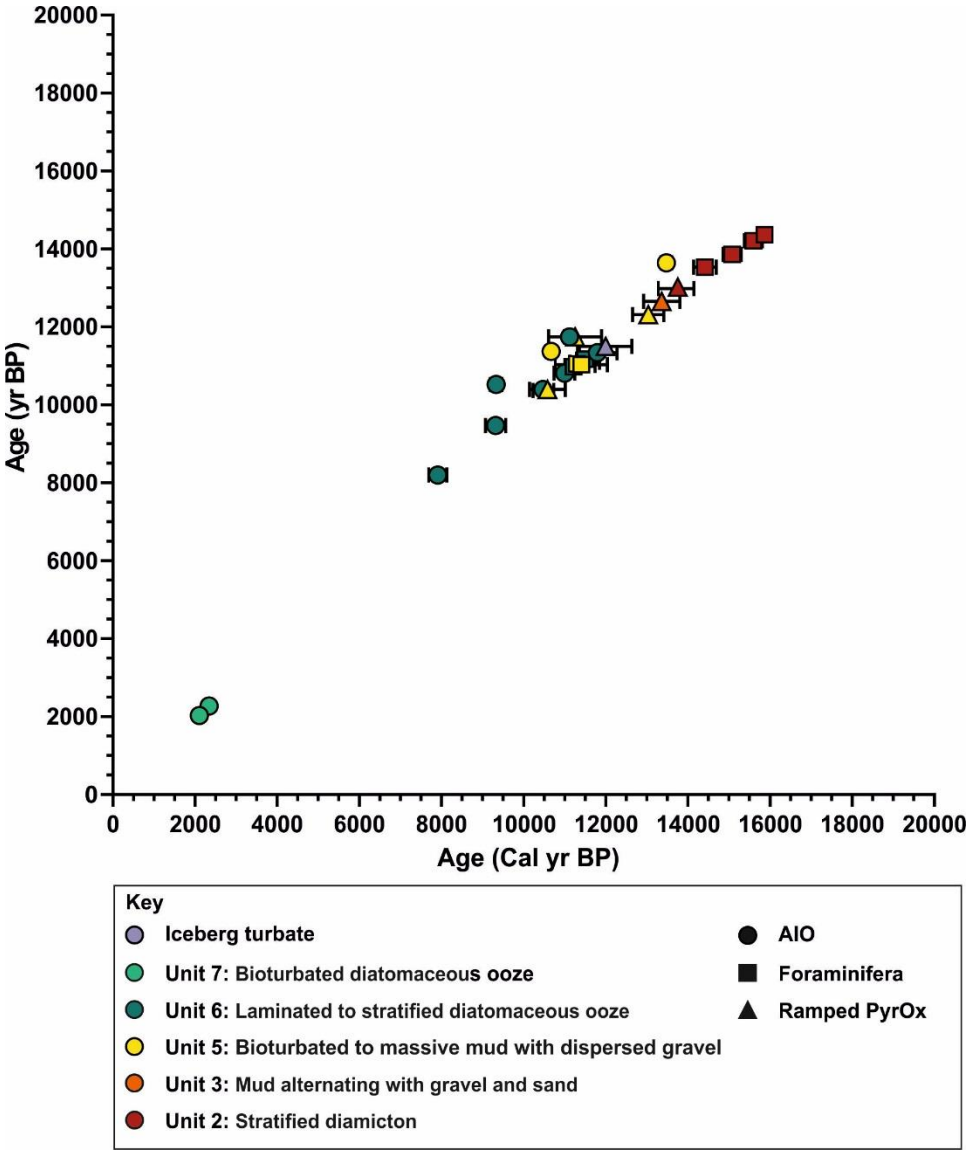

Figure 6.2: Reported (uncorrected) ^{14}C ages, versus corrected and calibrated ^{14}C ages for new ages obtained for this study, showing distribution of ages. Error bars represent the total 2σ standard deviation for calibrated ^{14}C ages. Marker shape indicates the dating method used and marker colour indicates the sediment type dated.

6.2.2. Local contamination offset in Anvers-Hugo Trough

Seafloor surface AIO ^{14}C ages were obtained from BC696 and BC699 (Fig. 6.1). Both ages (2,320±30 yr BP; BC699) and (2,080±30 yr BP; BC696) are older than the MRE (1,230±100 yrs; Ó Cofaigh et al., 2014). Whilst clearly reflecting some degree of contamination with fossil carbon, the fact that the two ages are relatively uniform (separated by only ~300 years) and up to 1,100 years older that the MRE, indicates that the LCO in AHT is not as severe as some other coastal areas of APIS (e.g., Larsen A/B where surfaces ages in excess of ~9,000 years have been obtained). Whilst not ideal, this situation suggests that the AIO fraction might prove

useful for establishing chronologies in this region, as demonstrated by the Palmer Deep sediment cores (Domack et al., 2001).

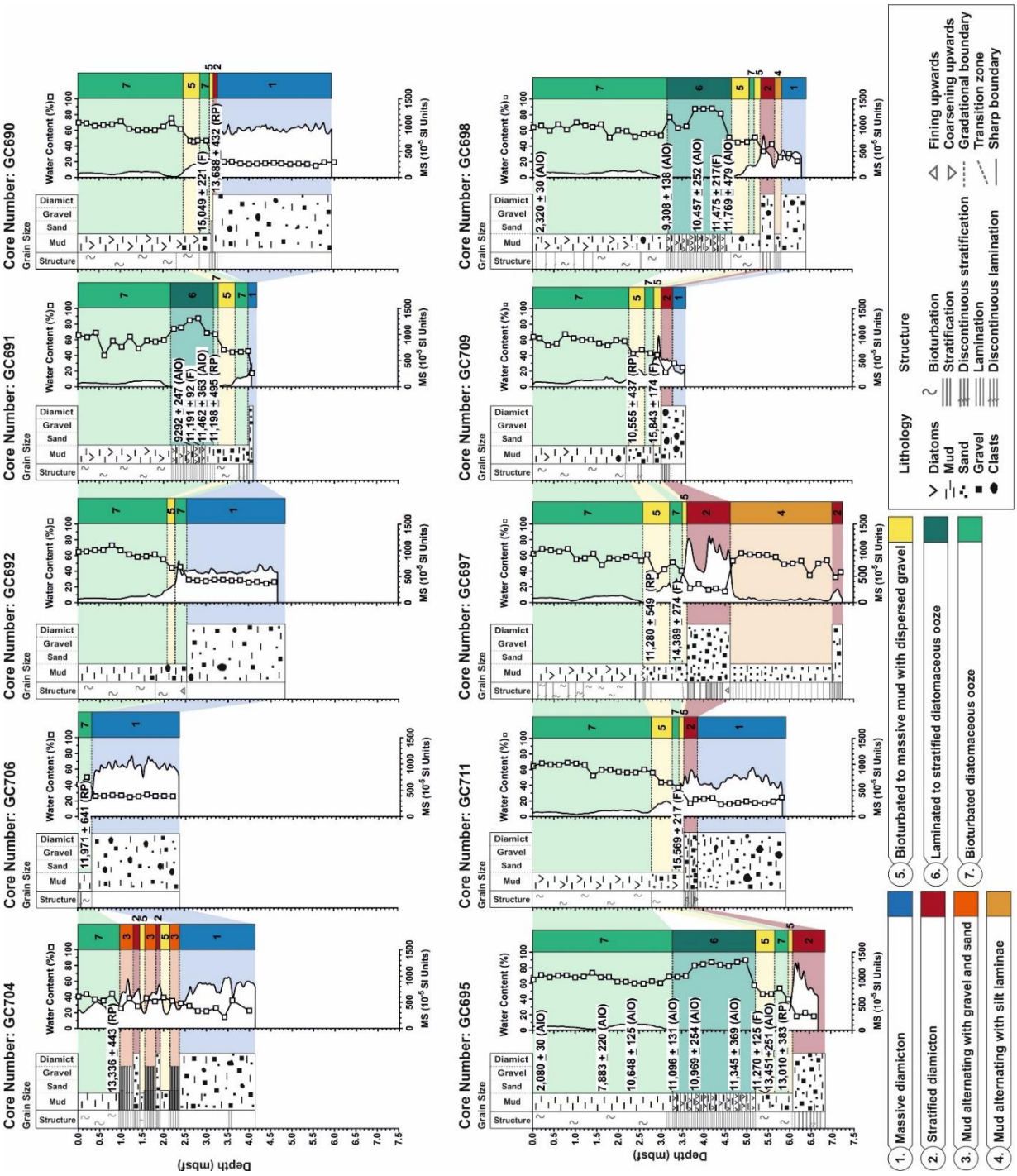

Figure 6.3: Fence diagrams summarising the spatial distribution of lithological units within Anvers-Hugo Trough, with radiocarbon ages (cal. yr BP) (AIO, foraminifera (F), and Ramped PyrOx (RP)), magnetic susceptibility values and water content (open squares) for each core. The top and bottom row form one along trough transect, with GC704 (top-left) recovered from the outermost shelf and core GC698 (bottom-right) recovered from the innermost shelf.

6.2.3. Paired AIO-foraminifera ^{14}C ages

As noted in Chapter 3, downcore AIO ages are typically corrected by subtracting surface AIO ages, and this assumes that the level of contamination remains constant through time. In many instances, this approach is not verified by independent dating methods, which is one of the reasons why AIO-derived chronologies are traditionally considered unreliable (see Smith et al. (2014) for further discussion). To test this assumption, paired calcareous foraminifera-AIO dating was performed on cores GC698 (445-446 cm) and GC695 (541-542 cm), at horizons where foraminifera were present.

In core GC698, the two uncorrected ^{14}C ages (AIO = 11,390±50 and foraminifera = 11,220±30 ^{14}C years) are in close agreement and differ by ~170 years (Fig. 6.3 and 6.4). However, this could be as little as ~90 years, if the full analytical error is taken into account (Table 6.1; Fig. 6.4; A-C). Their similarity implies minimal input of fossil carbon during the time of deposition and generally contradicts the assumption that AIO ages are inherently unreliable. Importantly, the paired samples were recovered from laminated diatomaceous ooze (Unit 6, see Chapter 4) with higher biogenic content (28% biogenic opal content, 0.99% TOC content) than the dated surface sediment (21% biogenic opal content, 0.79% TOC content). The similarity in ages is attributed to the combination of the relatively high biogenic content and low terrigenous content and is consistent with previous work that suggested that reliable AIO dates could be obtained from biogenic-rich sediments (Andrews et al., 1999; Hillenbrand et al., 2010a). Consequently, and following Hillenbrand et al. (2010a), all AIO ages obtained from diatomaceous oozes are corrected using the MRE (i.e., with no LCO correction), under the assumption that the diatomaceous oozes were largely unaffected by reworked fossil carbon (Table 6.1 and Figure 6.4C).

In core GC695 (541-542 cm), the uncorrected AIO age is 13,690±30 whilst the foraminifera-derived age is 11,100±40 ^{14}C yrs (Fig. 6.4; D-F). The offset (2.59 kyrs) indicates a higher proportion of terrestrially derived fossil carbon, relative to modern organic detritus within this stratigraphic horizon. Using the surface age of 2,080±30 yr BP to correct the downcore AIO sample, yields a calibrated age of 13.45±0.13 cal. kyr BP (Fig. 6.4E), whilst the calibrated foraminifera sample is 11.27±.13 cal. kyr BP (using MRE of 1,230±100 yrs) (Fig. 6.4D). Whilst the difference between the calibrated ages is slightly smaller (2.18 kyr versus 2.29 kyr), the persistent offset likely reflects the heterogeneous nature of Antarctic shelf sediments and highlights the difficulty in relying entirely on dating the AIO fraction. This issue appears to be a consequence of the low biogenic content of the sample (8%), which is the lowest of all the

dated AIO samples (Table 6.1), and potentially provides a crude indication of the reliability of AIO ages (see Hillenbrand et al., 2010b; Smith et al., 2014). It should also be noted that the sample itself was taken from bioturbated muds directly overlying glacier proximal sediments, where old AIO are often observed due to significant inputs of reworked fossil carbon (Heroy and Anderson, 2005). In this case, the foraminifera sample is considered to be the most reliable and reflects the true age of this interval.

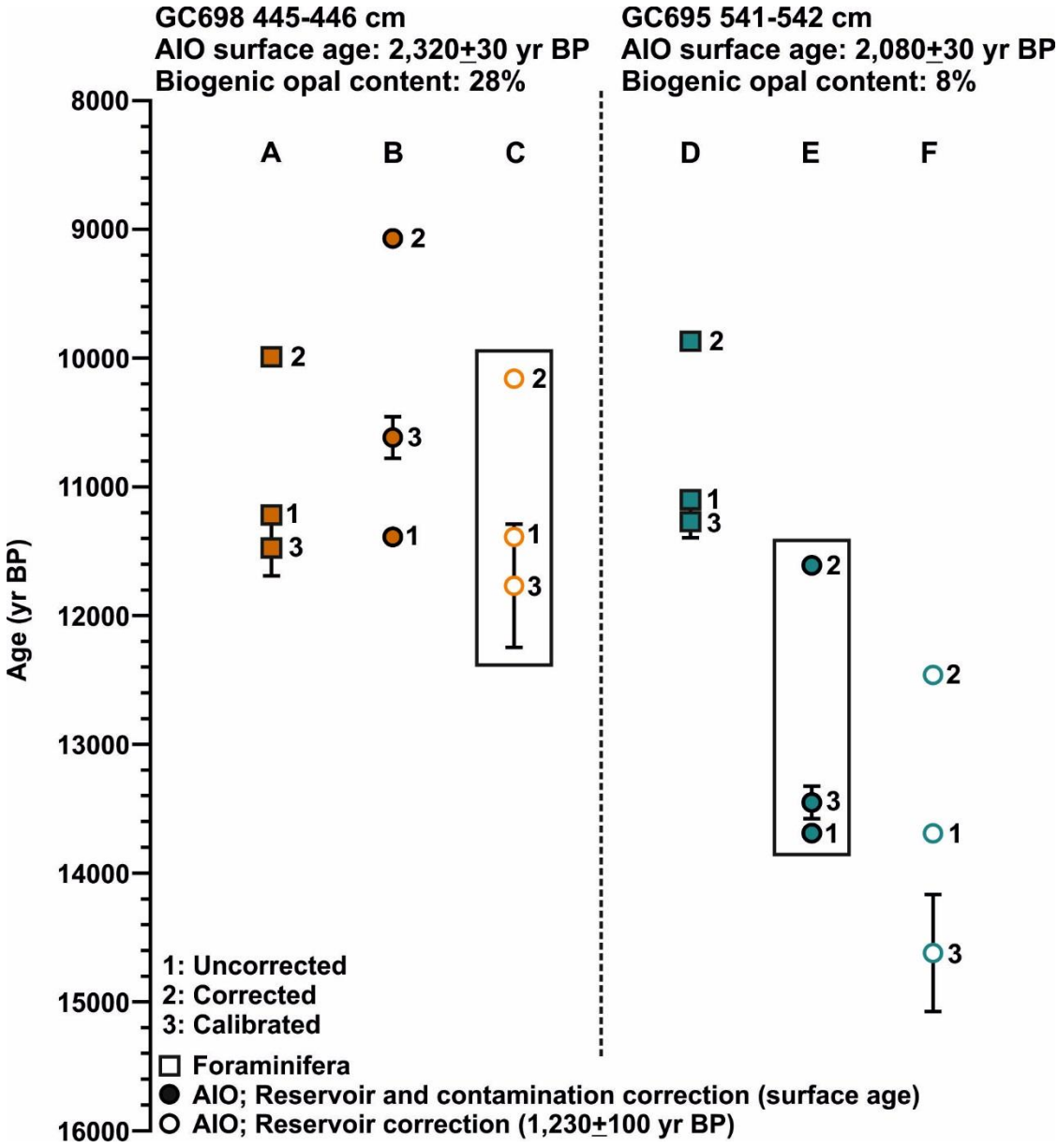

Figure 6.4: Uncorrected (1), corrected (2) and calibrated (3) ^{14}C ages for two paired samples from cores GC698 (orange) (445-446 cm) and GC695 (blue) (541-542 cm). Foraminifera ages from these samples are plotted as squares and are corrected using the marine reservoir effect (MRE) (A and D). AIO samples are plotted as circles (B, C, E and F). AIO samples corrected using the MRE and local contamination offset (LCO) are plotted as full circles (B and E), whilst AIO samples corrected using the MRE only, are plotted as hollow circles (C and F). All dates are calibrated in Calib v.7.0.4, using the Marine13 calibration curve. For AIO ages, the black box indicates the accepted correction used for that sample.

6.2.4. Ramped PyrOx ^{14}C ages

Ramped PyrOx ^{14}C dating was applied where calcareous foraminifera were absent and where sediments had low biogenic/organic content and would typically yield unreliable AIO ages (Table 6.2). Each sample is subject to five heating steps that generally yield younger (low/ambient temperature) to older (high temperature) age splits (splits 1-5, Table 6.2). Split 1 is routinely assumed to represent the true age of the sample. Two samples, from cores GC690 (313-314 cm) and GC704 (93-94 cm), did not contain enough young organic carbon to be captured in a normal Ramped PyrOx aliquot (~10-15 µmol CO_2). A composite Ramped PyrOx technique was applied to these samples, where the Ramped PyrOx method was applied to portions of the same sediment sample twice. CO_2 obtained from the first split over these two runs was combined to produce ~10-15 µmol CO_2 for ^{14}C dating ('comp' in Table 6.2) (after Subt et al., 2017). The first CO_2 split from the sample recovered from core GC704, was dated to 26.40±0.42 kyr BP, significantly older than the date of the second split; 12.45±0.40 kyr BP. This is assumed to be anomalous and is attributed to sampling error (B. Rosenheim pers. comm). The date of the second split is therefore reported for this horizon (Table. 6.2). More generally, the dates of the first and second CO_2 splits (Table 6.2) are typically separated by less than 2 kyr, although in some cases (GC690, GC691 and GC697) the age of the first split is older than the second split. In this situation, the youngest split is used (Table 6.1 and Table 6.2).

Viewed together, the Ramped PyrOx ages typically occur in stratigraphic order (within error) relative to AIO and foraminifera-derived ages (Fig. 6.3). Exceptions to this include the basal Ramped PyrOx age from GC695, which is younger than the overlying AIO age and the basal Ramped PyrOx age of GC690 relative to the overlying, and older foraminifera age (Table 6.1 and Fig. 6.3). The apparent older AIO age in GC695 has already been discussed in relation to the corresponding foraminifera-derived age from the same depth interval, and has been attributed to increased input of fossil carbon. Given that the foraminifera age is younger than the underlying RP age gives us some confidence that the RP age is more reliable than the AIO age, although this assessment is largely qualitative. The minor age reversal in core GC690, where the uncorrected Ramped PyrOx ^{14}C age (313-314 cm) is ~900 years younger than the overlying foraminifera date (307-308 cm), is not easily reconciled. Previous studies also observed that low temperature Ramped PyrOx ages could be younger than carbonate ^{14}C ages from the same stratigraphic interval (Subt et al., 2016; Subt et al., 2017). The disparity might reflect bioturbation, introducing younger sediments to a particular stratigraphic interval or reworking of older foraminifera (Domack et al., 1999; Subt et al., 2017). Within the units of

laminated diatomaceous ooze, age reversals are observed in cores GC691 and GC695. This consists of an AIO age that is older than the underlying Ramped PyrOx age in core GC691 and the underlying foraminifera data in core GC695 (Fig. 6.3). However, these reversals are minimal and are within the analytical error.

Core	Sample depth (cm)	Split	Temperature interval (°C)	CO_2 analysed (µmol)	$\delta^{13}C$ (per mil)	Fraction modern	±	Age (yrs BP)	±
GC697	281-282	1	ambient-311	9.3	-26.8	0.2518	0.0020	11080	180
GC697	281-282	2	311-368	11.5	-25.9	0.2536	0.0012	11020	140
GC697	281-282	3	368-451	19.2	-26.2	0.2218	0.0009	12110	100
GC697	281-282	4	451-562	30.5	-25.4	0.1997	0.0008	12950	80
GC697	281-282	5	562-813	27.9	-25.9	0.1495	0.0009	15300	110
GC691	327-328	1	ambient-322	9.8	-26.0	0.2313	0.0029	11770	200
GC691	327-328	2	322-436	14.4	-25.6	0.2550	0.0014	10970	120
GC691	327-328	3	436-490	20.5	-25.1	0.2375	0.0012	11550	90
GC691	327-328	4	490-541	25.0	-24.7	0.2232	0.0010	12050	80
GC691	327-328	5	541-823	34.0	-25.8	0.1886	0.0008	13410	80
GC706	32-33	1	ambient-302	9.3	-28.5	0.2376	0.0020	11550	190
GC706	32-33	2	302-397	22.3	-27.5	0.2368	0.0009	11570	80
GC706	32-33	4	464-539	21.9	-26.8	0.1910	0.0010	13320	110
GC706	32-33	5	539-844	33.1	-27.0	0.1466	0.0009	15450	100
GC695	580-581	1	ambient-293	10.4	-26.2	0.2151	0.0018	12360	190
GC695	580-581	2	293-381	21.7	-26.5	0.1820	0.0009	13710	110
GC695	580-581	3	381-444	19.4	-26.0	0.1606	0.0009	14730	140
GC695	580-581	4	444-506	36.3	-25.1	0.1567	0.0009	14910	90
GC695	580-581	5	506-814	41.3	-25.9	0.1318	0.0008	16310	100
GC709	232-233	1	ambient-294	10.3	-27.0	0.2724	0.0015	10440	140
GC709	232-233	2	294-380	22.0	-26.2	0.2658	0.0010	10640	80
GC709	232-233	3	380-439	22.0	-25.4	0.2241	0.0009	12020	90
GC709	232-233	4	439-505	22.6	-24.9	0.2075	0.0009	12640	100
GC709	232-233	5	505-779	35.9	-25.2	0.1745	0.0008	14040	80
GC704	93-94	1 (comp)	ambient-326	10.6	-27.9	0.0376	0.0020	27070	1320
GC704	93-94	2	326-416	11.1	-26.0	0.2065	0.0010	12700	180
GC704	93-94	3	416-506	10.8	-24.6	0.1528	0.0010	15170	260
GC704	93-94	4	506-597	9.8	-25.1	0.1082	0.0009	18040	410
GC704	93-94	5	597-829	9.5	-24.8	0.2585	0.0018	10860	170
GC690	313-314	1 (comp)	ambient-278	9.0	-27.6	0.1817	0.0023	13750	270
GC690	313-314	2	278-345	11.5	-26.7	0.1981	0.0010	13030	180
GC690	313-314	3	345-416	16.0	-26.1	0.1662	0.0012	14460	170
GC690	313-314	4	416-513	25.9	-25.1	0.1315	0.0008	16340	140
GC690	313-314	5	513-832	23.5	-25.3	0.0836	0.0008	20040	240

Table 6.2: Sample information for Ramped PyrOx AMS ^{14}C dates for the Anvers-Hugo Trough, including core, sample depth, CO_2 split (or aliquot) number, temperature interval over which the CO_2 split was obtained (°C), $\delta^{13}C$ (per mil), fraction modern and reported age (^{14}C yr BP). Grey shading indicates ages that are accepted as representing the true timing of sediment deposition. Where samples did not contain enough young organic carbon to be captured in a normal Ramped PyrOx aliquot (~10-15 µmol CO_2), a composite Ramped PyrOx technique was applied (comp in table).

6.3. Interpretation

The new age data demonstrates two key things. First, paired foraminifera-AIO dating suggests that samples taken from diatomaceous sediment are more likely to yield reliable AIO ages compared to samples taken from diatom-/organic-poor sediments (Fig. 6.4). Secondly, the Ramped PyrOx ^{14}C method achieves consistent results, negating some of the problems associated with dating organic-poor sediment that contain unknown quantities of fossil carbon. In general however, and in the absence of further work on the Ramped PyrOx ^{14}C method, ^{14}C ages derived from calcareous (micro-)fossils, are still considered to produce the most reliable chronologies for constraining the retreat of grounded ice. As such, these ages are preferentially selected (below) to establish the timing of grounded ice retreat across AHT (Fig. 6.5).

6.3.1. Grounding line retreat across Anvers-Hugo Trough

Outer shelf cores GC704 and GC706 do not help constrain initial retreat of grounded ice from the shelf edge due to the lack of datable carbonate as well as complex/unreliable sediment stratigraphies (gravelly sandy muds/iceberg turbate respectively). Instead, previously published ages (cores KC26, PC-24; Heroy and Anderson, 2007) (Table 6.1, Fig. 6.1; ID 4 and 5) offer the best constraint on the timing of deglaciation of the outer shelf, suggesting that grounded ice began its retreat sometime after ~16.48 cal. kyr BP (Fig. 6.5; ID. 4/KC26) (Heroy and Anderson, 2007). The retreat of grounded ice across the mid-shelf is well constrained by cores GC711, GC709 and GC690 and together indicate that the grounding line had retreated across the outer and mid shelf as early as 15.84 cal. kyr BP (Fig. 6.5; ID 19/GC709). Ages of 15.57 cal. kyr BP from GC711 (Fig. 6.5; ID 17) and 15.05 cal. kyr BP from GC690 (Fig. 6.5; ID 13) are consistent with this interpretation. On the inner shelf, previously reported AIO age data from rhythmically interbedded diatomaceous ooze and pebbly mud, directly overlying subglacial till (Site 1098, Palmer Deep (Fig 6.5; ID 22), indicate that grounded ice had retreated from an inner shelf position by 12.85 cal. kyr BP, and possibly as early as 13.18 cal. kyr BP if the published age-model is correct (Domack et al., 2001). An early deglaciation of the inner shelf is also consistent with nearby surface exposure ages which suggest that grounded ice had withdrawn past Uruguay Island (Fig. 6.1; ID 24 and 25) by 10.1 ka, thinned to <160 m altitude at the Berthelot Islands (Fig. 6.1; ID 26 and 27) by 8.7 ka, and was at Primavera, within 5 km of present-day limits, by 6.5 ka (Fig. 6.8a; ID 32-35, 63) (Bentley et al., 2011). Whilst not on the same ice flow-path, a near coastal site (PC-83) in Gerlache Straight indicates that this area was also ice free by 8.42±0.75 cal. kyr BP (Fig. 6.1 and Fig. 6.5; ID 23) (Harden et al., 1992).

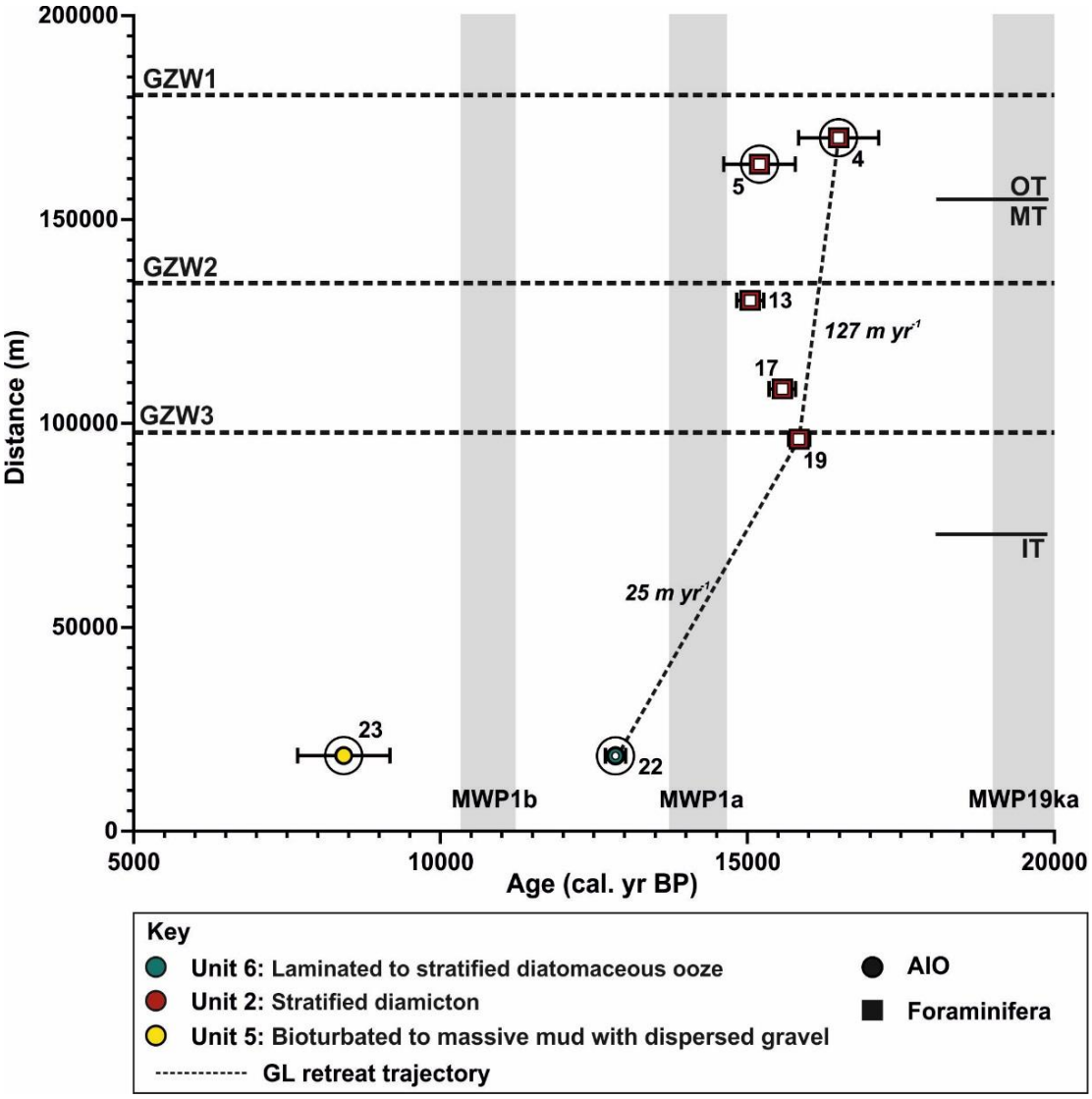

Figure 6.5: Calibrated AMS ^{14}C ages that constrain retreat of grounded ice within Anvers-Hugo Trough, for JR284 and previously published cores, versus distance along palaeo-ice stream trough. For cores off the main trough axis (Fig. 6.1; orange dashed line) cores were projected onto the centre line at the same latitude in order to calculate distance. Colour of symbols indicates the sediment type dated and symbol shape indicates material dated. Open symbols represent the most reliable minimum dates for grounding line retreat. Grey shading highlights the timing of MWP1a, MWP1b and MWP19ka and numbers correlate with core ID.

The overall pattern of deglaciation, with initial ice retreat from the shelf edge sometime after 16.49 cal. kyr BP, and retreat of ice from the mid and inner-shelf areas as early as 15.84 cal. kyr BP and 12.85 cal. kyr BP respectively, differs from previous reconstructions (Heroy and Anderson, 2005; Livingstone et al., 2012; Ó Cofaigh et al., 2014). Specifically, the data generated in this thesis suggests that the mid-shelf deglaciated much earlier than previously thought (cf. Livingstone et al., 2012). Past reconstructions have suggested that the grounding line did not retreat beyond the mid-shelf until 11.3 cal. kyr BP (PC-23 and GC-02 from Heroy and Anderson, (2005) and Yoon et al., (2002) respectively). In addition, because previous

studies suggested a later deglaciation of the mid-shelf, this posed problems for an apparent early deglaciation of the inner shelf at 12.85 cal. kyr BP (Palmer Deep; Domack et al. 2001). However, the new deglacial ages presented here help to reconcile this issue. Based on the revised retreat chronology, calculated retreat rate across the outer and mid-shelf is 127 m yr^{-1}, slowing to 25 m yr^{-1} from mid to inner shelf (Fig. 6.5). Faster retreat across the outer and mid shelf is in some ways counterintuitive, as this part of the shelf is characterised by several large GZWs (Fig. 6.1) which are assumed to mark still-stands during retreat. However, whilst the current chronology does not permit accurate dating of each individual wedge, it does provide a maximum and bounding window for the formation of two of the wedge complexes. GZWs 2 and compound-GZW 3 on the mid-shelf, were deposited between 16.49 cal. kyr BP (date from core KC-26) and 15.84 cal. kyr. BP (date from core GC709), indicating that they formed over a period of ~650 years.

6.3.2. Post glacial changes and the onset of seasonally open marine sedimentation

Directly following grounding line retreat and before the onset of enhanced productivity associated with deposition of laminated diatomaceous ooze, AHT experienced a brief period of seasonally open marine conditions followed by the development of persistent sea ice (Ch. 5). This time-interval is characterised by the deposition of a 12-34 cm thick layer of olive-green, bioturbated diatomaceous ooze with dispersed gravel, indicative of seasonally open marine conditions. It directly overlies subglacial or grounding line proximal sediments in several cores (GC690, GC695, GC711, GC697, GC709, GC698, GC692 and GC691) (Fig. 6.3 and Fig. 6.6; Zone 3). Two dates obtained from this facies (cores GC695 and GC697) constrain this phase of seasonally open water conditions to between 13.01 cal. kyr BP (GC695, ID 16; Ramped PyrOx) and 14.40 cal. kyr BP (GC697, ID 18; foraminifera) (Fig. 6.3, Fig. 6.6; Zone 3 and Fig. 6.7). The transition back to grey bioturbated mud with dispersed gravel in several cores (GC692, GC691, GC690, GC695, GC711, GC697, GC709 and GC698; Fig. 6.3, Fig. 6.6; Zone 4) is associated with a lengthening of the sea ice season. This is inferred from the reduction in spring meltwater and open-water summer associated diatoms (Ch. 5). As with the previous seasonally open marine unit, there is limited chronological constraints on this period of persistent sea ice cover, as the onset of the deposition of the upper grey bioturbated mud with dispersed gravel unit is not dated. However, lengthened sea ice conditions likely ceased around 11.27 cal. kyr BP as indicated from dates obtained from cores GC695 (foraminifera; 11.27 cal. kyr BP; Fig. 6.3 and 6.6) and GC697 (Ramped PyrOx; 11.28 cal. kyr BP; Fig. 6.3).

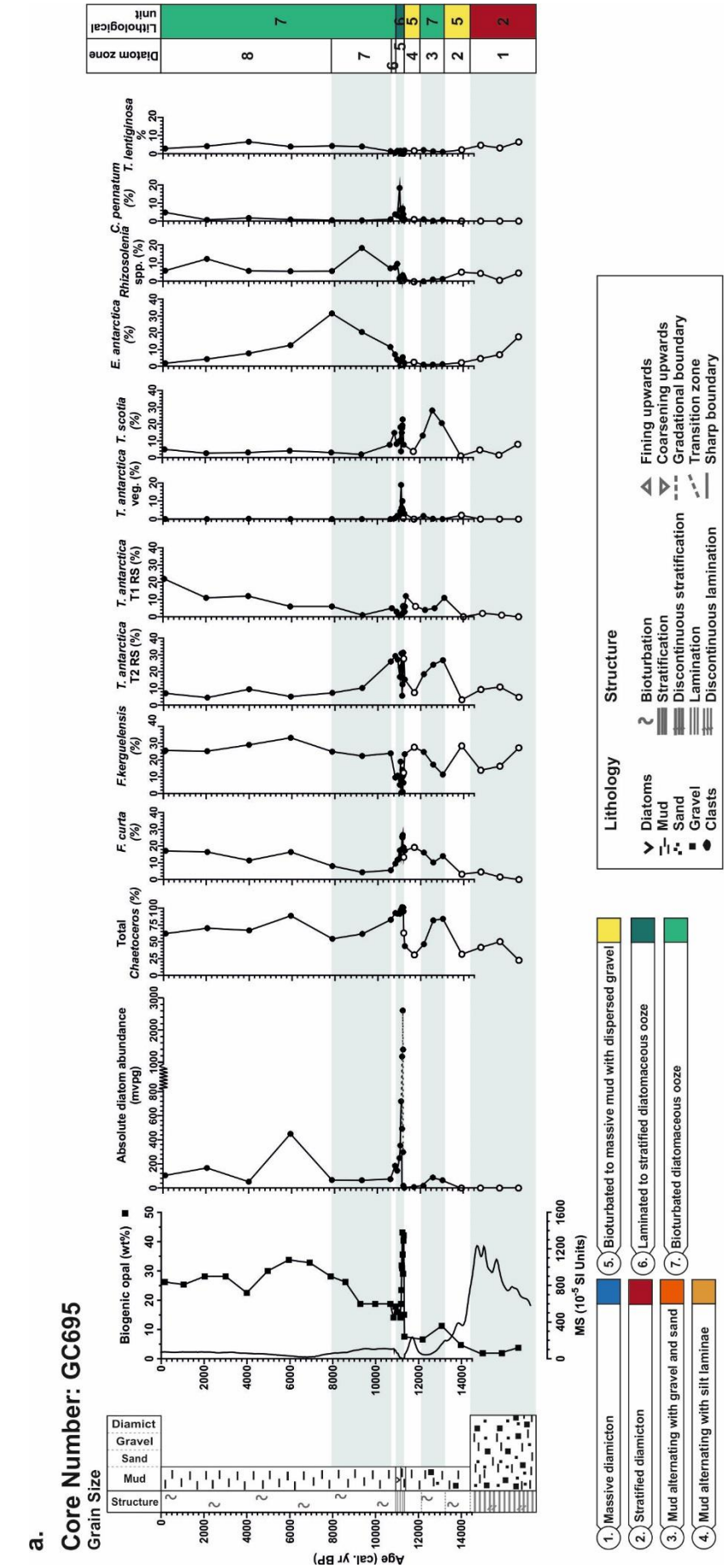
a.
Core Number: GC695
Grain Size
Diamict
Gravel
Sand
Mud
Structure
Age (cal. yr BP)
Biogenic opal (wt%)
Absolute diatom abundance (mvpg)
Total Chaetoceros (%)
F. curta (%)
F.kerguelensis (%)
T. antarctica T2 RS (%)
T. antarctica T1 RS (%)
T. antarctica veg. (%)
T. scotia (%)
E. antarctica (%)
Rhizosolenia spp. (%)
C. pennatum (%)
T. lentiginosa %
Diatom zone
Lithological unit
MS (10^{-5} SI Units)
Lithology
Diatoms
Mud
Sand
Gravel
Clasts
Structure
Bioturbation
Stratification
Discontinuous stratification
Lamination
Discontinuous lamination
Fining upwards
Coarsening upwards
Gradational boundary
Transition zone
Sharp boundary
1. Massive diamicton
2. Stratified diamicton
3. Mud alternating with gravel and sand
4. Mud alternating with silt laminae
5. Bioturbated to massive mud with dispersed gravel
6. Laminated to stratified diatomaceous ooze
7. Bioturbated diatomaceous ooze

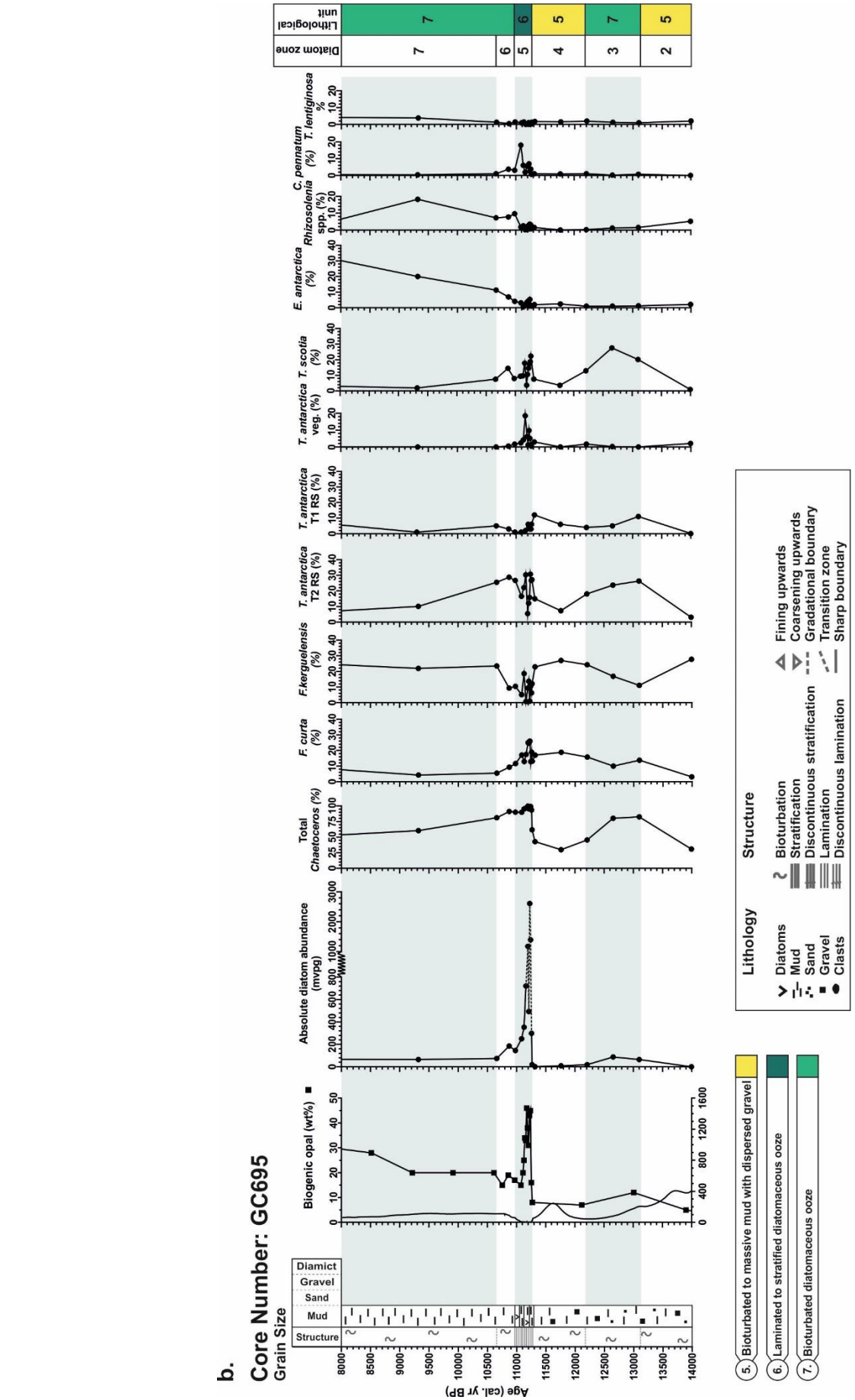

Figure 6.6: (a) Core log, biogenic opal content, magnetic susceptibility and quantitative diatom data against age (cal. yr BP) for core GC695. Absolute diatom abundance, and total Chaetoceros subg. Hyalochaete (Chs) *data were collected from total diatom counts including Chs. The relative abundance data for the species* Fragilariopsis curta, Fragilariopsis kerguelensis, Thalassiosira antarctica *T2 RS*, Thalassiosira antarctica *T1 RS*, Thalassiosira antarctica *(veg)*, Thalassiosira scotia, Eucampia *spp.*, Rhizosolenia *spp.*, Corethron pennatum *and* Thalassiosira lentiginosa *were collected from* Chs*-free counts. Samples from which <400 whole valves were counted are indicated (white circles). Diatom and sedimentological zones for core GC695 are indicated. (b) As (a) over the period 14,000 to 8,000 cal. yr BP.*

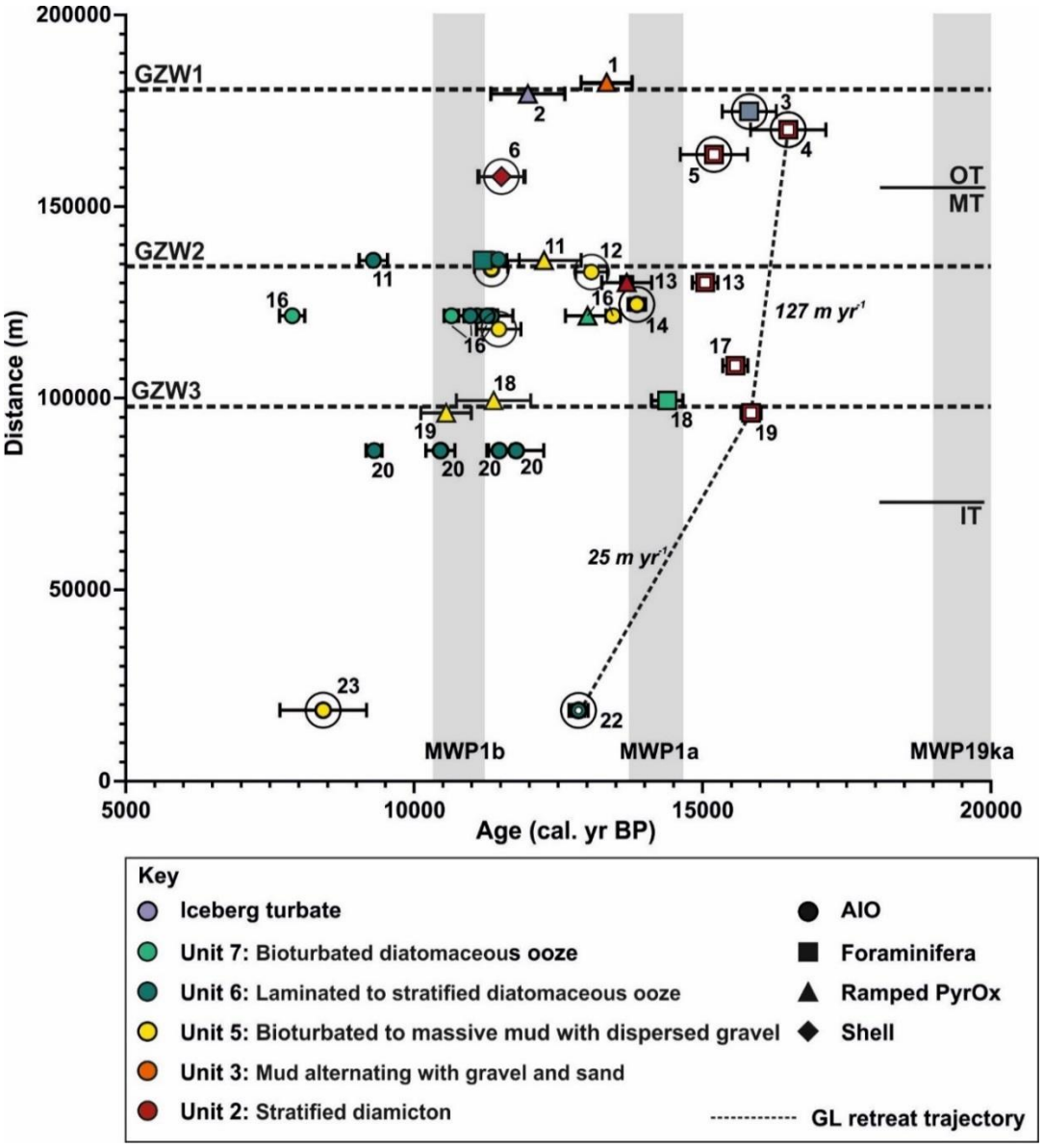

Figure 6.7: Calibrated AMS ^{14}C ages for JR284 and previously published cores versus distance along palaeo-ice stream trough. For cores off the main trough axis (Fig. 6.1; orange dashed line) cores were projected onto the centre line at the same latitude, in order to calculate their distance along the trough. Colour of symbols indicates the different sediment types dated. Shape of symbols indicates material dated. Open symbols represent the most reliable minimum dates for grounding line retreat. Grey shading highlights the timing of MWP1a, MWP1b and MWP19ka and numbers correlate with core ID.

An additional Ramped PyrOx age from this unit in core GC709 was dated to 10.56 cal. kyr BP (Fig. 6.3 and fig. 6.7; ID 19). However, this falls within the time period during which the laminated diatomaceous oozes were deposited, suggesting that this event was time-transgressive or that the Ramped PyrOx date is unreliable. The onset of laminated diatomaceous ooze deposition, and peak post-glacial productivity in AHT is dated to 11.77±0.48 (AIO), 11.27±0.13 (foraminifera) and 11.20±0.49 cal. kyr BP (Ramped PyrOx) (dates from GC698, GC695 and GC691, respectively). The age-data indicates near-synchronous deposition after ~11.27 cal. kyr BP, extending to 9.29 cal. kyr BP (Fig. 6.7). A

sample that was dated from the bioturbated diatomaceous ooze unit, overlying laminated diatomaceous oozes in core GC695 (10.64±0.25 cal. kyr BP), indicates deposition of laminated diatomaceous ooze might have been even more rapid at this core site, and could have occurred in <600 years (Fig. 6.6; Zone 5 and Fig. 6.7; ID 16).

Following deposition of laminated diatomaceous ooze, the ADA of sediments decreases, as does the contributions of *Chs*-RS and *Corethron pennatum*, species associated with the formation of a well-stratified water column, instigated through melting sea ice in the spring (Crawford, 1995; Kemp et al., 2000; Leventer et al., 2002; Alley et al., 2018). This transition occurs over Zone 6 and Zone 7 (Fig. 6.6). Our new age data together with quantitative diatom assemblage analysis indicates a decrease in productivity after ~10.95 cal. kyr BP (Fig. 6.6). At this time, highly silicified sea ice-associated *Eucampia antarctica* (symmetrical) become abundant. *Fragilariopsis kerguelensis* is additionally dominant in this zone, which is typically associated with open-ocean settings. This contradiction may indicate that the environmental preferences of symmetrical and asymmetrical *E. antarctica* are not fully resolved, or that reduced diatom productivity, may have led to preferential preservation of highly silicified *E. antarctica* and *F. kerguelensis* within the sediments. Samples analysed over this zone could have captured both heavier sea ice cover in winter (*E. antarctica*) with open-water conditions in the summer (*F. kerguelensis*). Therefore, if not enhanced sea ice duration (as indicated by abundant *F. kerguelensis)*, another environmental factor likely caused decreased productivity at this time, for example windiness and/or reduced sea ice melt-out proximal to the core site (Cunningham and Leventer, 1998). This would additionally explain the relatively low abundance of sea ice and melt-out-associated *Fragilariopsis curta* and *Chs*.

From ~8.00 cal. kyr BP, sea ice and melt-out associated taxa *Fragilariopsis curta* and *Thalassiosira antarctica* T1, increase in abundance. The overall ADA additionally increases, as does the total *Chs* content. This indicates enhanced seasonality, with a heavy sea ice cover in the winter and melt-water associated productivity in the spring. However, it should be noted that the sample resolution is low over this interval so variability in absolute diatom abundance and species assemblage may not be fully resolved. In the late Holocene (Fig. 6.6; uppermost sample GC695) there is an increase in *C. pennatum,* indicating an influx of meltwater and the formation of a well-stratified water column.

6.4. Discussion

6.4.1. Deglaciation of AHT: A regional perspective

The new chronological data enable us to place the retreat of the AHIS within the context of ice sheet retreat across the WAP shelf following the LGM. It also enables us to assess whether this part of the APIS contributed to meltwater pulses (MWPs) during deglaciation. The timing of grounded ice retreat within AHT is largely consistent with onset of deglaciation across much of the WAP shelf (Fig. 6.8) and also appears to support the idea of a north-south trend during deglaciation of the WAP, whereby grounded ice in the north retreated earlier than ice in the south (Heroy and Anderson, 2005; Livingstone et al., 2012; Ó Cofaigh et al., 2014). Prior to 20.00 cal. kyr BP, the APIS was grounded at, or close to, the continental shelf edge around most of its margin (Ó Cofaigh et al., 2014). Grounding line retreat was underway in the northern Lafond Trough, east of Bransfield Basin by 17.531±0.416 cal. kyr BP (Fig. 6.8), similar to the outer-shelf of Smith Trough, where grounding line retreat was underway by 17.5095±0.5475 cal. kyr BP (Fig. 6.8) (Banfield and Anderson, 1995; Heroy and Anderson, 2007; Ó Cofaigh et al., 2014). This was followed by ice retreat from the outer parts of AHT commencing after 16.488±0.653 cal. kyr BP. Within the more southern Marguerite Trough and Biscoe Strait, grounding line retreat was initiated by 14.0915±0.5005 and 13.194±0.325 cal. kyr BP, respectively (Fig. 6.8) (Pope and Anderson, 1992; Heroy and Anderson, 2007). Southernmost Charcot Trough and Rothschild Trough also deglaciated around this time (13.5135±0.2405 and 14.5545±0.5055 cal. kyr BP, respectively (Graham and Smith, 2012) (Fig. 6.8).

An Antarctic source for MWP1a and 1b (Fig. 6.8) has been suggested on the basis of both viscoelastic Earth models (e.g., Bassett et al., 2005, 2007) and limited geological data from the margins of the WAIS (Heroy and Anderson, 2007; Weber et al., 2014). Heroy and Anderson (2007) argued that the timing of deglacial steps of the APIS are roughly concomitant with MWP1a (14.65-13.70 cal. kyr BP or 12.50-11.80 ^{14}C kyr BP) and possibly 1b (10.35-11.20 cal. kyr BP or 9.20-9.80 ^{14}C BP) (Fairbanks, 1989), but that the earliest APIS retreat occurred later (~1000 years) than the 19 ka MWP (22.00-19.00 cal. kyr BP; Yokoyama et al., 2000). Deglaciation of AHT started early enough to contribute to MWP1a, preceding MWP1a by >1,000 yrs (Fig. 6.5). However, APIS volume at the LGM is estimated to be only 2.9 m sea-level equivalent (Denton and Hughes, 2002; Huybrechts, 2002; Heroy and Anderson, 2007), and contribution from AHT to MWP1a would only have been a fraction of this. Similarly, MWP1b (coeval with deposition of the laminated diatomaceous ooze deposits within AHT; Fig. 6.7) occurred when the majority of the AHT had already deglaciated, with

the exception of near-coastal ice which might have continued thinning into the early Holocene, based on cosmogenic dating of glacial erratics from nearby coastal islands (Bentley et al., 2011). Thus on present data it seems unlikely that deglaciation of AHT contributed to MWPs 1a and 1b, although it is possible that the rapid increases in sea-level at MWP1b helped to force deglaciation of the mid-inner shelf, promoting enhanced productivity through the injection of meltwater.

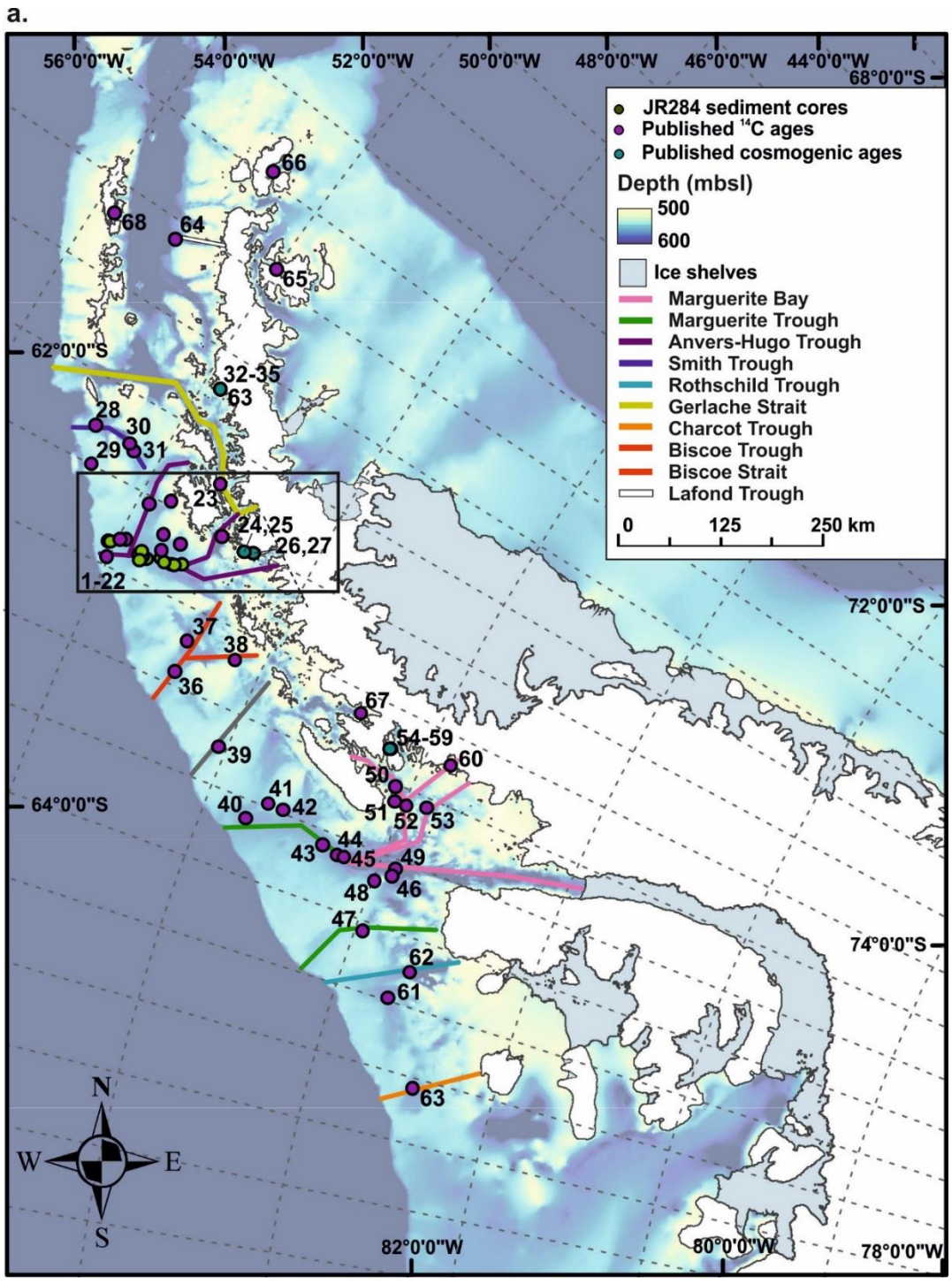

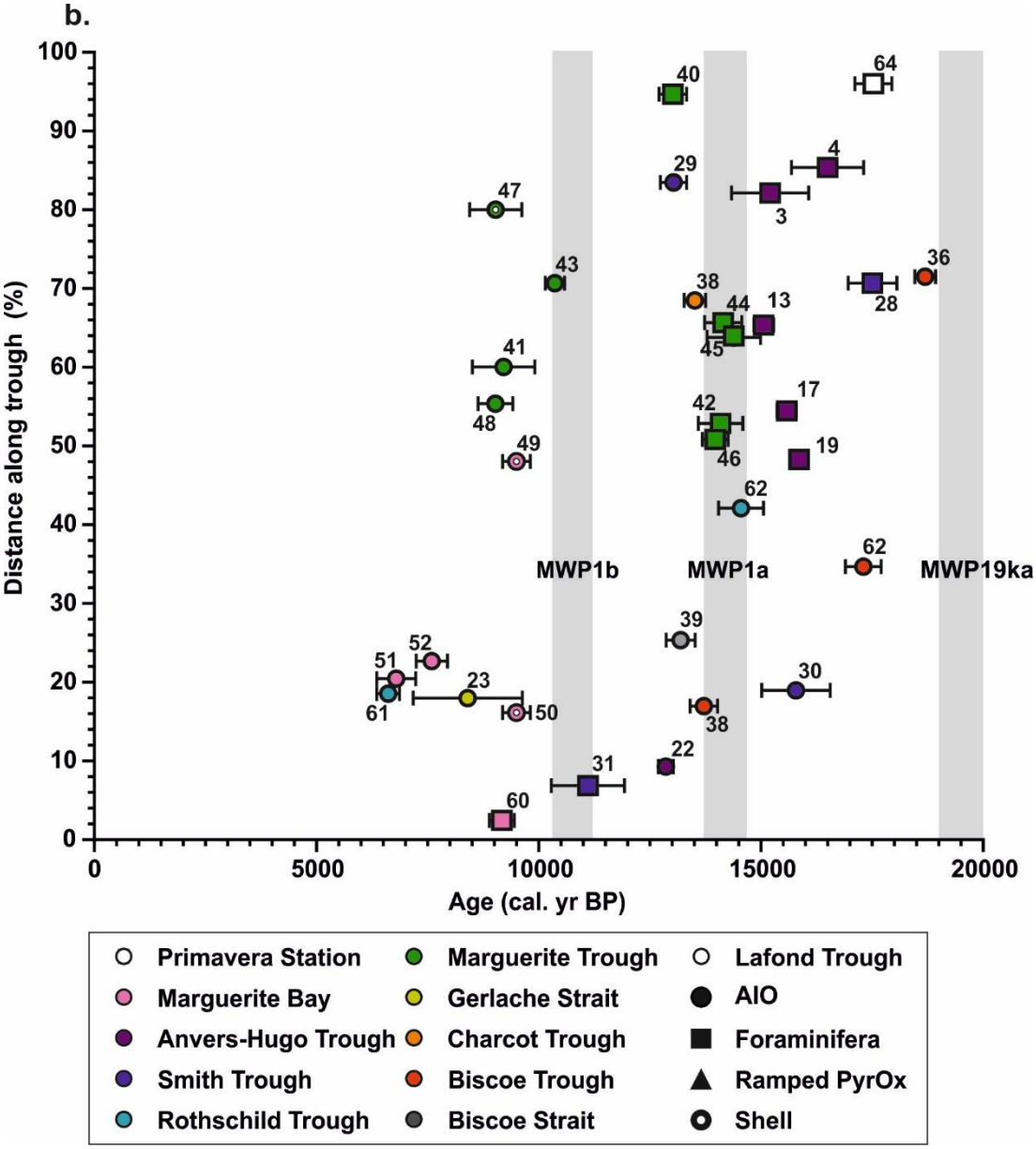

Figure 6.8: (a) Map of the Antarctic Peninsula with the location of discussed palaeo-ice stream troughs and sample/core locations. For a detailed map of core sites bordered by the black box see Fig. 6.1. (b) Minimum ages for grounded ice retreat from core sites shown in (a) versus distance along palaeo-ice stream trough (%) (Lavoie et al., 2015). Point colour indicates the location of each core site, whilst the shape represents material dated (AIO, foraminifera, shell or Ramped PyrOx). Sample ID corresponds with map location and in text discussion. Grey shading indicates the timing of MWP1a, MWP1b and MWP19ka (Fairbanks, 1989; Yokoyama et al., 2000; Deschamps et al., 2012).

6.4.2. Drivers of grounding line retreat

Deglaciation of the APIS following the LGM, and AIS more generally has been attributed to both global (sea level) and more regional drivers, such as increasing atmospheric oceanic temperatures, and it is likely that it was the interplay between these variables that drove grounding line retreat in AHT. Thus initial post-LGM retreat of AHT was likely caused by

raising global sea-level associated with deglaciation of Northern Hemisphere ice sheets after ~21 kyr (Fig. 6.9m) (Denton et al., 1991). Coeval with raising global sea-level, ice core records indicate that warming of West Antarctica began around 20 kyr (WAIS Divide Project Members, 2013), attributed to orbital forcing as well as potential bi-polar see-saw effects (Blunier et al., 1998; Steig and Alley, 2002; Anderson et al., 2009; Weber et al., 2011; WAIS Divide Project Members, 2013). A southward shift of the SHWW in parallel with well-documented shifts of the intertropical convergence zone (Schneider et al., 2014) has been inferred in numerous reconstructions (Anderson et al., 2009; Kaiser and Lamy, 2005; Buizert et al., 2018). This is thought to have driven enhanced Southern Ocean upwelling, a rise in atmospheric CO_2 (Anderson et al., 2009) and further warming of Antarctica until ~14.5 ka (Pedro et al., 2016; WAIS Divide Project Members, 2015). It is also possible that a more southerly position of the SHWW helped to drive greater volumes of warmer CDW onto the WAP shelf, and along AHT. Unfortunately, proxy reconstructions for CDW upwelling onto the WAP and West Antarctic (Pacific sector) shelf are largely limited to the Late Glacial/Holocene (Fig. 6.9) (Shevenell et al., 2011; Peck et al., 2015; Hillenbrand et al., 2017). Thus, it is likely that the initial retreat of the APIS in AHT was driven by a combination of raising global sea level and atmospheric temperatures, and possibly increased presence of CDW on the continental shelf. In addition, several studies have highlighted the important role that bathymetry, and particularly a retrograde seabed, has on ice stream retreat both for modern (Schoof, 2007; Gudmundsson, 2013) as well as palaeo ice streams (Jamieson et al., 2012; Smith et al., 2011; 2014). In this context, bathymetry might help explain the apparent, although crudely constrained change from fast grounding line retreat from outer to mid shelf (127 m yr^{-1}; Fig. 6.10) to slower retreat across the mid to inner shelf (25 m yr^{-1}; Fig. 6.10). In cross profile (Fig. 6.10) this slowdown in grounding line retreat appears to coincide with a much rougher topography extending westwards from Anvers Island and north of Hugo Island; a setting that provides bathymetric pinning points for the ice stream (6.1a). A slowdown in grounding line retreat over the inner-shelf additionally accounts for the deposition of an expanded sub-ice shelf sediment unit in core GC697 (Section 4.4.4). In this respect, the mid-inner shelf of AHT differs slightly from other palaeo ice stream troughs that tend to deepen gradually from the mid shelf landward. AHT by contrast deepens to the mid-shelf before shallowing to a more neutral rougher seabed before diving down again into Palmer Deep and then up again to the modern coastline (Fig. 6.10).

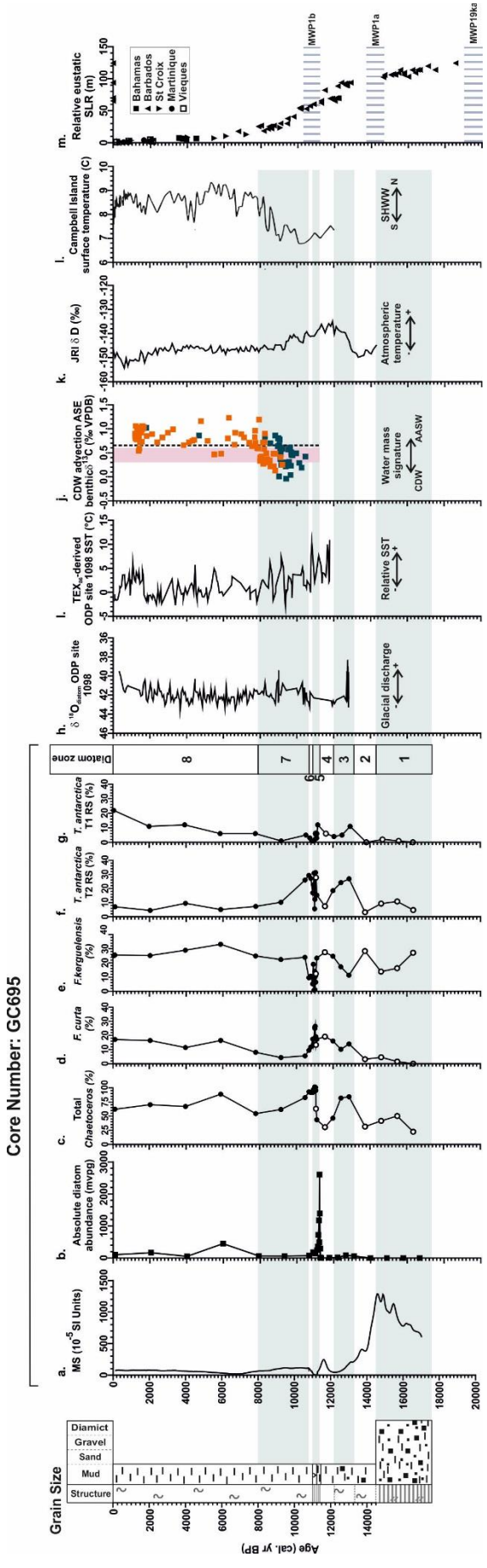

Figure 6.9: GC695 core log, magnetic susceptibility (MS; a) and quantitative diatom data against age (cal. yr BP); (b) Absolute diatom abundance, (c) % Total Chs *(d)* Fragilariopsis curta *(e) %* Fragilariopsis kerguelensis *(f) %* Thalassiosira antarctica *T2 (h) $\delta^{18}O_{diatom}$ as a proxy for glacial discharge from ODP Site 1098 (Pike et al., 2013). (i) TEX$_{86}$-derived SST record from ODP Site 1098 (Shevenell et al., 2011). (j) $\delta^{13}C$ values of benthic foraminifera from the Amundsen Sea PS75/160-PS75/167 record, as a proxy for CDW upwelling (Hillenbrand et al., 2017). $\delta^{13}C$ values of modern benthic foraminifera (black dashed lines) and $\delta^{13}C$ dissolved organic carbon ranges typical for CDW (pink box) are given. (k) Deuterium (δD) isotope ratio in the JRI Ice Core as proxy for air temperature (Mulvaney et al., 2012). (l) Atmospheric surface temperature for Campbell Island, SW Pacific, as a proxy for the position of the Southern Hemisphere westerly winds (SHWW) (McGlone et al., 2015). (m) Relative sea-level curves based on coral records (Fairbanks et al., 1989).*

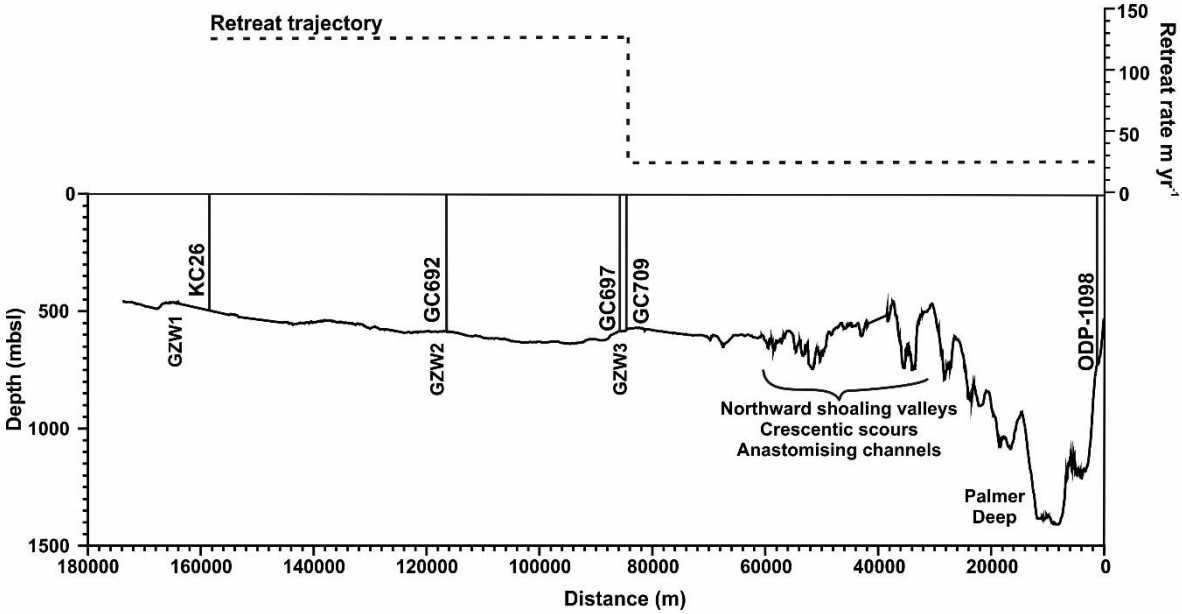

Figure 6.10: Calculated grounding-line retreat rates for AHIS and bathymetric trough profile. This incorporates data from this study (GC692, GC697 and GC709), Heroy and Anderson (2007; KC26) and Domack et al. (2001; ODP-Site 1098). GZWs (1-3) are discussed in the text.

6.4.3. Role of GZWs in regulating grounding line retreat in AHT

Marine ice sheets that rest on a retrograde bed are thought to be inherently unstable (e.g., MISI; Schoof, 2007). However, this instability can be negated, or at least temporarily halted, by increased lateral drag on the ice stream margins (e.g., during trough narrowing) and/or due to the presence of pinning points which can cause temporary still stands or slow-downs in grounding line retreat (Jamieson et al., 2012; 2014). This may explain the position of GZW 2, which is located at a trough constriction caused by the bathymetric highs to the west and east of AHT (Fig. 6.1). Several GZWs were deposited within the AHT during the last deglaciation of the trough, suggesting that grounding line retreat paused on at least three occasions (Fig. 6.1). Indeed, a major aim of this work was to establish the duration of these still-stands through targeted sediment coring on the stoss and lee sides of each GZW. Unfortunately, the new chronological information does not provide detailed data with which to constrain their formation. The only firm conclusion that can be drawn is that GZWs 2 and compound-GZW 3 on the mid-shelf must have been deposited over a period of ~650 years from 16.49 cal. kyr BP (date from core KC-26) to 15.84 cal. kyr. BP (date from core GC709). Whilst crude, this does imply that the wedges formed over hundreds of years rather than thousands. GZW development on centennial scale (~120 yrs) has also been estimated for GZWs in the eastern Amundsen Sea (Graham et al., 2010; Jakobsson et al., 2012), although depending on the sediment flux utilised in this calculation, these wedges may have formed over 2,000 years (Jakobsson et al., 2012). In contrast, a compound-GZW, comprised of seven stacked GZWs,

marks the position of a still-stand of the Bindschadler Ice Stream during its post-LGM retreat from the Whales Deep Basin, Ross Sea. This compound GZW is estimated to have formed over 3,700 yrs (Whales Deep, Ross Sea; Bart et al., 2017). It should be noted that this wedge is substantially larger (140 m thickness; ~543 km^3 volume) than those identified in this study (e.g., GZWs 1, 2 and compound-GZW 3 have a thickness of 25, 33, 26 (3a), 30 (3b) and 53 (3c) m respectively). The difference in formation duration may account for the difference in GZW size, assuming that rate of sediment delivery to the grounding line is comparable for these different troughs.

6.4.4. Deglaciation as a driver of biological productivity

The presence of laminated diatomaceous oozes within AHT have been associated with a period of enhanced productivity following deglaciation (Ch. 5). Similar deposits in Palmer Deep and at sites on the East Antarctic shelf have previously been associated with the formation of a calving bay, into which meltwater, nutrients and bioavailable iron from melting sea ice, icebergs or glaciers can be concentrated (Ch. 5). These conditions enhance biological productivity and promote the rapid deposition of laminated oozes (Leventer et al., 1996; Domack et al., 2006; Leventer et al., 2006). New radiocarbon ages from these deposits in AHT indicate the onset of laminated diatomaceous ooze deposition after 11.77±0.48 (AIO), 11.27±0.13 (foraminifera) and 11.20+0.49 cal. kyr BP (Ramped PyrOx) (dates from GC698, GC695 and GC691, respectively). This new age-date indicates near-synchronous deposition of the oozes in AHT, occurring after ~11.27 cal. kyr BP (foraminifera age). Assuming grounding line retreat across the outer and mid-shelf by 15.84±0.17 cal. kyr BP, deposition of the laminated diatomaceous oozes lagged grounding line retreat by as much as 4,600 yrs (Fig. 6.12). This conflicts with the prevailing model that suggests enhanced productivity and laminated diatomaceous ooze deposition as a result of calving bay formation, established immediately after grounding line retreat (Domack et al., 2001; Leventer et al, 2006). However, if this were the case we would expect to see deposition of the laminated oozes immediately above the glacier-proximal sediments. This observation implies that additional drivers, other than a favourable physiographic setting, are required to trigger this episode of peak productivity.

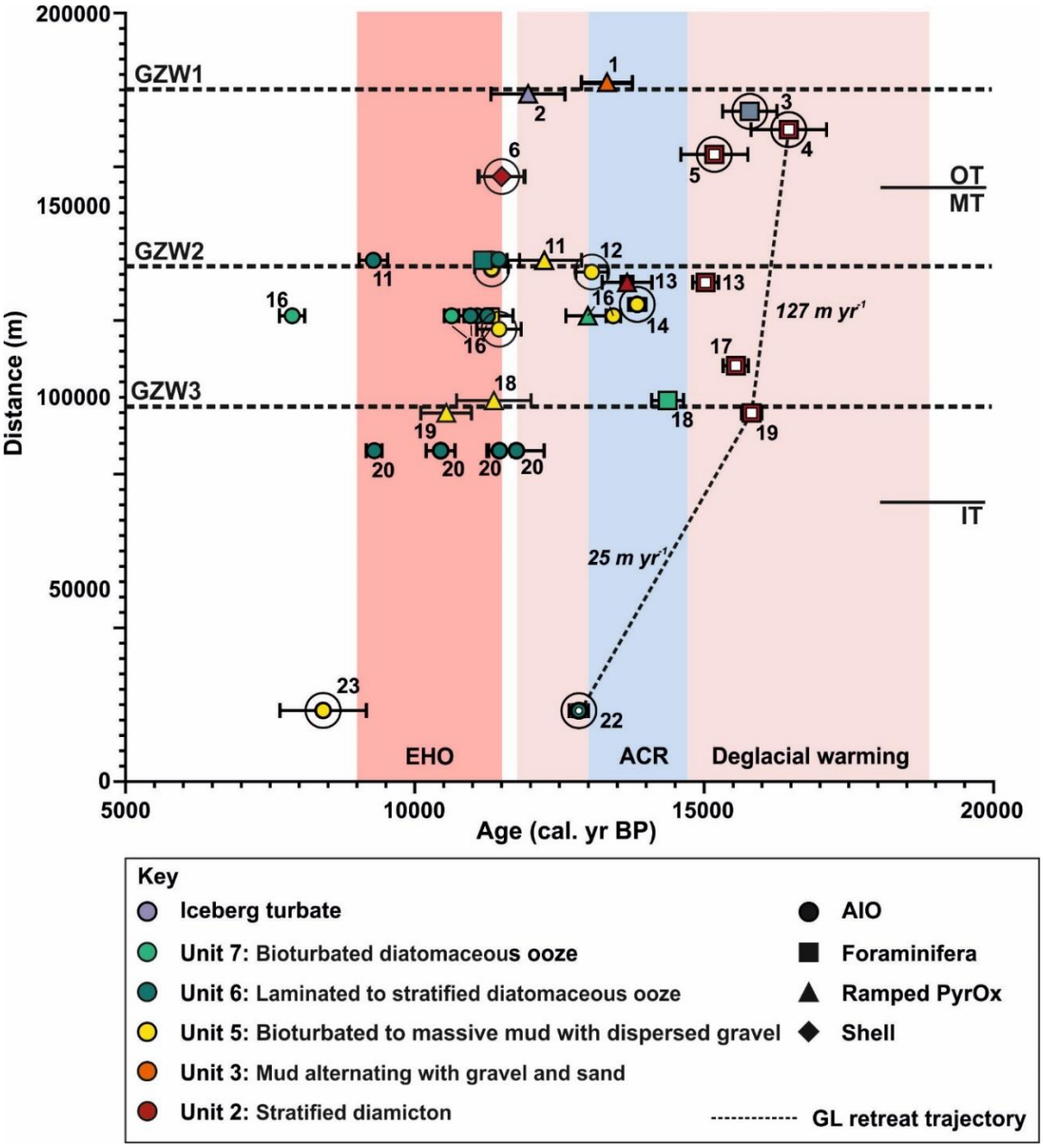

Figure 6.11: Calibrated AMS ^{14}C ages for new and previously published cores from AHT vs. distance along palaeo-ice stream trough. Point colour indicates sediment unit dated, for previously published cores this is inferred from sediment description. Point shape indicates material dated. Red and blue shading is indicative of deglacial atmospheric warming (light red (Pedro et al., 2016)), the Antarctic Cold Reversal (ACR) (blue; 14.7-13.0 kyr BP (Pedro et al., 2016)) and the early Holocene optimum (EHO) (dark red; 11.5-9.0 kyr BP (Masson et al., 2000)).

The initial onset of seasonally open marine conditions on the mid-inner shelf (Zone 3) is dated to between 14.40 and 13.01 cal. kyr BP (Fig. 6.3, 6.12b). This occurs after the initial phase of atmospheric warming following the LGM (WAIS Divide Project Members, 2013) but is broadly coincident with the Antarctic Cold Reversal (ACR), a prominent phase of atmospheric cooling observed in several Antarctic ice core records (Fig. 6.11) (~14.7-13.0 kyr BP; Pedro et al., 2016). Nearby Palmer Deep was deglaciated prior to ~13.18 cal. kyr BP, with the onset

of open marine conditions occurring shortly after this at ~ 12.85 cal. kyr BP (Fig. 6.12; ID 22) (Domack et al., 2001). In Palmer Deep, this is associated with increases in ADA (dominated by *Thalassiosira antarctica;* Taylor and Sjunneskog, 2002), iceberg rafting (Domack et al., 2001), and a low $\delta^{18}O_{diatom}$ signature (Pike et al., 2013). The latter indicates increased glacial discharge, thought to be associated with enhanced frontal melting of ice shelf/glacial ice between 13.0 and 12.1 kyr BP (Pike et al., 2013). In addition, Taylor and Sjunneskog (2002) also document significant increases of *Coscinodiscus* spp. during this early deglacial phase (~13.18-11.01 cal. kyr BP). They suggest this is indicative of an influx of warm, northern surface water, which they hypothesise occurred either in pulses or as the result of rising postglacial sea levels. Together, these results suggest that the enhanced biological productivity in AHT between 14.40 and 13.01 cal. kyr BP, and possibly extending to ~12 cal. kyr BP (Taylor and Sjunneskog, 2002; Pike et al., 2013) was a response to increased upwelling of CDW, opposed to variations in atmospheric temperature.

Following this initial phase of seasonally open marine conditions, the new core data suggests that these conditions were interrupted by a period of persistent sea-ice cover, marked by the deposition of a grey mud unit (Zone 4) (Fig. 6.3, 6.6; and Fig. 6.12c). Dates from this unit (cores GC695 and GC697) indicate deposition occurred sometime prior to ~11.27 cal. kyr BP (Fig. 6.6; Zone 4 and Fig. 6.11; ID 16 and 18), although the onset of deposition is not well-constrained by the new ^{14}C data. Roughly coeval with this, the $\delta^{18}O_{diatom}$ record from Palmer Deep indicates a reduction in glacial discharge between 12.1 and 11.5 kyr BP (Fig. 6.9h) (Pike et al., 2013). Reduced discharge is thought to have been driven by atmospheric and/or oceanic cooling (Pike et al., 2013), although there is currently a dearth of proxy records covering this time interval. Reduced advection of CDW could explain a decrease in glacial discharge, which would also supress meltwater-driven productivity. Alternatively, atmospheric cooling and increased sea ice extent might also explain this period of reduced productivity, although atmospheric temperature records from the JRI ice core indicate relatively warm conditions at this time (Fig. 6.9k) (Mulvaney et al., 2012).

After 11.27 cal. kyr BP, laminated diatomaceous oozes were deposited within AHT, which is attributed to a period of enhanced meltwater discharge and nutrient input from sea and glacial ice melt (Fig. 6.12d). These environmental conditions appear to have persisted until 9.29 cal. kyr BP, although a date from the overlying unit in core GC695 (~10.64 cal. kyr BP, 240-241cm) implies deposition of the oozes was far more rapid (within ~600 yrs) (Fig. 6.6; Zone 5). Enhanced productivity after 11.27 and until 9.29 cal. kyr BP coincides with the onset of the early Holocene climatic optimum (Fig. 6.11) (~11.50 and 9.00 kyr; Masson et al., 2000).

The JRI ice core record indicates that temperatures were 1.3±0.3°C warmer than present day (Mulvaney et al., 2012), although this signal is rather muted in the WAIS Divide Ice Core (WAIS Divide project Members, 2013; Cuffey et al., 2016). A TEX86-based reconstruction from Palmer Deep indicates high SSTs between 11.80 and 9.00 kyr BP (Fig. 6.9i) (Shevenell et al., 2011; Etourneau et al., 2013) whilst the $\delta^{18}O_{diatom}$ data from Palmer Deep indicates increased glacial discharge between 11.50 and 9.00 kyr BP (Fig. 6.9h) (Pike et al., 2013). Atmospheric and oceanic variability during this time is thought to have been driven by latitudinal shifts in the SHWW (McGlone et al., 2010; Shevenell et al., 2011). Pollen records from the Magellan Strait and Patagonia, southern Chile, indicate a southerly shift of the SHWW between ~12.20 and 9.20 cal. kyr BP (McCulloch and Davies, 2001; Mayr et al., 2007). Similarly, a pollen record from Campbell Island south of New Zealand in combination with a SST reconstruction from a core located east of New Zealand's south island additionally indicates a southerly migration of the SHWW between 12.50 and 9.20 cal. kyr BP (Fig. 6.9l) (McGlone et al., 2010). A southward shift of the SHWW probably brought warmer winds to the WAP region and also drove increased upwelling of CDW; delivering relatively warm water and nutrients to the AHT, further promoting productivity (Martinson, 2008; Anderson et al., 2009; Bentley et al., 2009; McGlone et al., 2010; Shevenell et al., 2011; Peck et al., 2015; Hillenbrand et al., 2017). Support for intensified CDW advection along the Pacific margin of Antarctica during the early Holocene comes from a multi-proxy analysis of sediment cores recovered from Pine Island Bay in eastern Amundsen Sea Embayment (Fig. 6.9j) (Hillenbrand et al., 2017). This study demonstrated that enhanced CDW upwelling between ~10.40 and 7.50 cal. kyrs BP led to the deglaciation of Pine Island Bay, and likely retreat/collapse of an ice shelf (Hillenbrand et al., 2017). From ~7.0 cal. yr BP, Peck et al. (2015) suggest a decreasing influence of CDW and greater sea-ice formation in Marguerite Bay, linked to a northward shift in the SHWW.

Deposition of thick laminated diatomaceous oozes within AHT is therefore explained in terms of increased atmospheric/ocean temperatures rather than simply the establishment of favourable physiographic conditions (e.g., calving bay). Warmer ocean/atmosphere temperatures would have set up a system whereby the sea ice season was reduced in duration with melting and the formation of a well-stratified water column in spring, with open water conditions lasting from summer to autumn. In this scenario, melting sea ice introduced nutrients, including bioavailable iron, to the surface waters promoted diatom blooms (cf. Sedwick and DiTullio, 1997; Measures, 1999; Sambrotto et al., 2003; Stickley et al., 2005). We also note that deposition of the laminated diatomaceous oozes is coeval with MWP1b (Fig.

6.7), which possibly intensified deglaciation of mid-inner shelf areas and further enhanced the meltwater-driven productivity.

Whilst not the primary focus of this PhD, environmental changes following deglaciation and into the Holocene can be inferred from core GC695 which is well constrained by ^{14}C data (Fig. 6.6). It should be noted however, that the sampling resolution for diatom analyses and therefore the level of detail, is relatively low above the laminated diatomaceous ooze unit. Following deposition of laminated diatomaceous oozes, the ADA of sediments decreases, as does the contributions of *Chs*, *Fragilariopsis curta* and *Corethron pennatum*, species associated with the formation of a well-stratified water column, instigated through melting sea ice in the spring (Fig. 6.6) (Crawford, 1995; Kemp et al., 2000; Leventer et al., 2002; Alley et al., 2018). This suggests an overall reduction in meltwater discharge or sea ice melt-related stratification after ~10.95 cal. kyr BP (Fig. 6.12e), relative to the period 11.27-10.95 cal. kyr BP. After ~10.95 cal. kyr BP sediments are characterised by an increase in the contribution of *Eucampia* antarctica, dominated by the 'southern' sea-ice associated variety (Fig. 6.6; Zone 7), which peaks at ~9.25 cal. kyr BP. Whilst the symmetrical variety of *E. antarctica* is indicative of increased sea ice presence, this is contradicted by a relatively high abundance of open ocean-associated *Fragilariopsis kerguelensis*. As mentioned, these contradictions may indicate that the environmental preferences of symmetrical and asymmetrical *E. antarctica* are not fully resolved, or that reduced diatom productivity may have led to preferential preservation of highly silicified *E. antarctica* and *F. kerguelensis* within the sediments. Alternatively, samples analysed over Zone 7 could have captured both heavier sea ice cover in winter (*E. antarctica*) and open-water conditions in the summer (*F. kerguelensis*). Therefore, if not enhanced sea ice duration (as indicated by abundant *F. kerguelensis)*, another environmental factor likely caused decreased productivity, for example windiness and/or reduced sea ice-melt proximal to the core site (Cunningham and Leventer, 1998). This would explain the reduction in species associated with melting sea ice and water column stratification. Over Zone 7, there is a northward shift of the SHWW (Fig. 6.9j and l). A northward shift of the SHWW could have reduced the upwelling of warm, nutrient-rich CDW to AHT at this time, leading to reduced diatom productivity (Martinson, 2008; Anderson et al., 2009; Bentley et al., 2009; McGlone et al., 2010; Shevenell et al., 2011; Peck et al., 2015; Hillenbrand et al., 2017).

Reduced productivity/ADA, with a seasonally open water diatom assemblage, is additionally observed in Palmer Deep between 11.7 and 8.7 cal. kyr BP (Sjunneskog and Taylor, 2002). Although instigated earlier (11.7 cal. kyr BP in Palmer Deep and 10.95 cal.

kyr BP in AHT), this might represent the same event. Reduced ADA at Palmer Deep between 11.7 and 8.7 cal. kyr BP has been associated with the opening of the connection between Gerlache and Bransfield Strait, with an increase in terrigenous sediment input (Domack et al., 2001; Sjunneskog and Taylor, 2002; Taylor and Sjunneskog, 2002). Opening of the Gerlache and Bransfield Strait could have changed surface current direction and strength in the Palmer Deep region, reducing meltwater/stratification and associated productivity of 'bloom species' (*Fragilariopsis curta* and *Chs*) (Domack et al., 2001; Sjunneskog and Taylor, 2002). In addition, the glaciers that fed into AHT and Palmer Deep could have retreated to a point at which they terminated on land at this time; this would have additionally reduced meltwater input to the AP continental shelf (Sjunneskog and Taylor, 2002).

In core GC695 *Fragilariopsis curta* and *T. antarctica* T1 generally increase in abundance after ~9.00 cal. kyr BP, indicative of greater sea ice presence (Fig. 6.6 and 6.12f). The SST record from Palmer Deep (Shevenell et al., 2011) shows an overall cooling of ~3–4 °C throughout the Holocene, with the lowest SSTs occurring between 2.7 and 1.7 kyr (Fig. 6.9i). The TEX-based SST record from Etourneau et al. (2013), indicates a cooling trend from 7.0 to 3.8 cal. kyr BP, followed by an increase in variability from 3.8 cal. kyr BP and a general shift to cooler conditions (Etourneau et al., 2013). The $\delta^{18}O_{diatom}$ data from Palmer Deep indicates a strong reduction and stabilisation of glacial discharge after 9.00 cal. kyr BP and until 5.00 cal. kyr BP (Fig. 6.9h) (Pike et al., 2013). Between 5.0 and 3.6 cal. kyr BP a variable $\delta^{18}O_{diatom}$ record reflects fluctuations in glacial discharge and shifts in sea surface temperature, associated with the movement of the inter-tropical convergence zone, increased ENSO activity, a shift in the position of the SHWW and changes to associated CDW upwelling (Pike et al., 2015). Between 3.6 and 0.36 kyr BP, Palmer Deep experienced enhanced glacial ice discharge (Pike et al., 2015). During the same time (from ~4.2 cal. kyr BP), Marguerite Bay experienced reduced glacial meltwater discharge, increased sea ice cover and relatively low SSTs (Peck et al., 2015). A multi-proxy marine record from Marguerite Bay and Neny Fjord indicates cooling from 6.9-4.2 cal. kyr BP, reflected in an increased abundance of ice-tolerant diatom species and a decreased flux of phytodetritus to the sea floor (Allen et al., 2010; Peck et al., 2015). Diatom abundance and species assemblage records from the Palmer Deep and Lallemend Fjord show that these regions experienced cool neoglacial conditions with more extensive sea ice from 3.7 and 3.9 cal. kyr BP, respectively (Shevenell et al., 1996; Domack et al., 2001; Taylor et al., 2001; Sjunneskog and Taylor, 2002; Taylor and Sjunneskog, 2002; Etourneau et al., 2013).

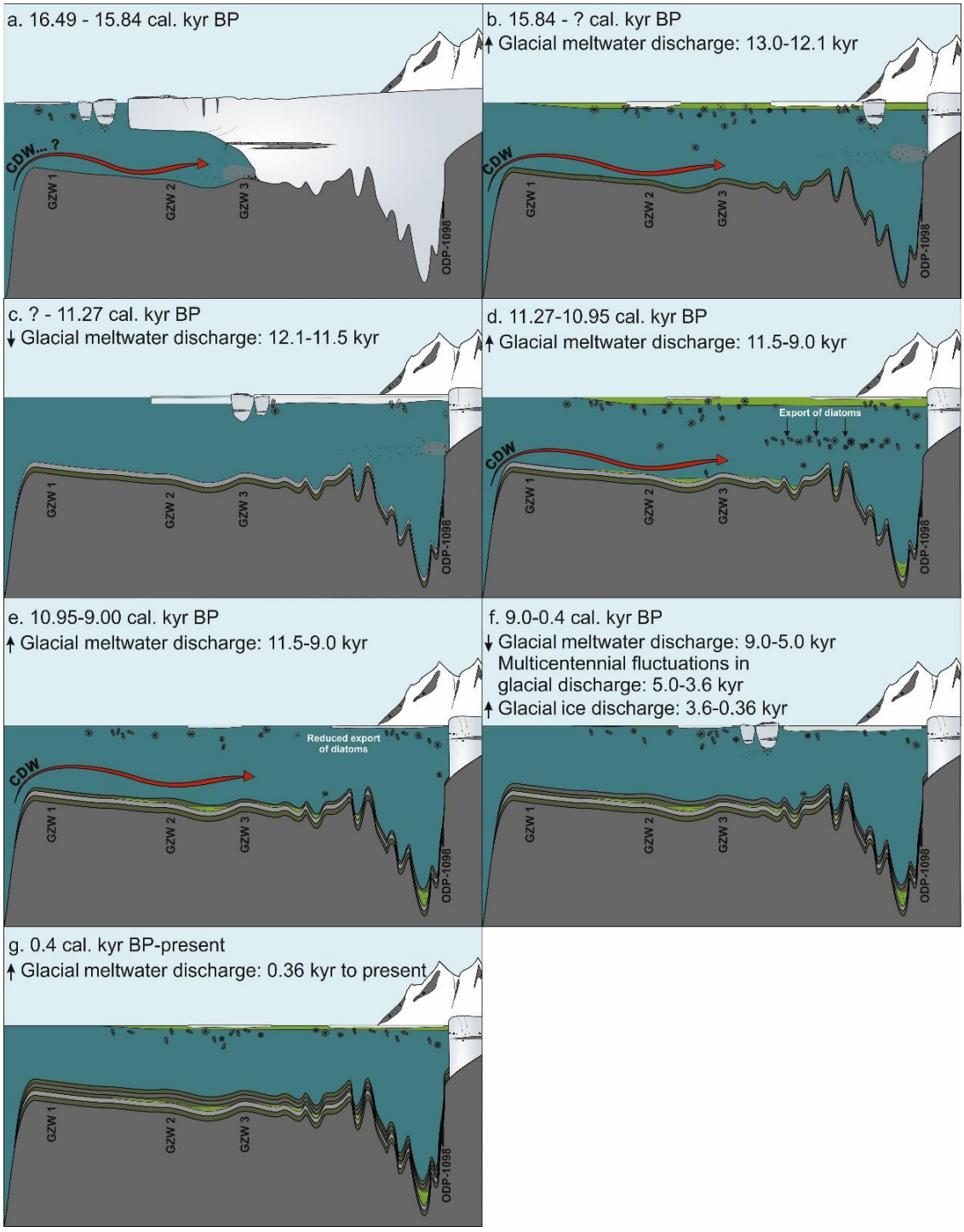

Figure 6.12: Schematic diagram (not to scale) of changes in environmental conditions in AHT during post-LGM deglaciation, inferred from core GC695. This includes information on relative glacial discharge (Pike et al., 2013). (a) Grounded ice retreat from outer and mid-shelf and formation of GZWs. (b) Grounded ice retreat from middle to inner shelf (north of Palmer Deep) and seasonally open marine conditions in AHT. (c) Development of persistent sea-ice cover. (d) Maximum in diatom productivity between 11.27 and 10.95 cal. kyr BP. (e) Reduced diatom productivity between 10.95 and 9.25. (f) Reduced CDW presence and increasing sea ice associated taxa between 9.0 and 0.4 cal. kyr BP. (g) Increased meltwater discharge and associated taxa after 0.4 cal. kyr BP.

In the late Holocene (after ~0.4 cal. kyr BP) (Fig. 6.6; uppermost sample GC695), there is an increase in *Corethron pennatum*, indicating an influx of meltwater and the formation of a well-stratified water column (Fig. 6.12g). Late-Holocene warming is inferred from the Palmer Deep TEX-based SST record from Etourneau et al. (2013), with SSTs reaching 2.9°C (average) between 1.6 and 0.5 kyr BP (Shevenell et al., 2011). The JRI ice core also shows warming during the past 500 years (Fig. 6.10h) (Mulvaney et al., 2012), which is broadly coincident with a trend to increasing glacial discharge observed in the Palmer Deep record (Fig. 6.10e) (Pike et al., 2013). Overall, the chronological and diatom records obtained for this study are in close agreement with Holocene marine palaeoenvironmental reconstructions from other AP regions.

6.5. Conclusions

- From 16.49 to cal. 15.84 cal. kyr BP, the AHIS had retreated across the outer and middle shelf at a rate of 127 m yr^{-1}. Over this period two GZWs, including one compound-GZW were deposited, likely on centennial timescales.
- Grounded ice retreat in AHT occurred early enough to contribute to MWP1a, although its contribution would have been minimal. Deglaciation of the outer and mid-shelf section of AHT preceded MWP1a by >1000 yrs.
- Grounded ice retreated from the middle shelf to Palmer Deep on the inner shelf from 15.84 to 12.85 cal. kyr BP and occurred at a rate of 25 m yr^{-1}. The presence of pinning points and the rugged bedrock topography of the inner shelf part of AHT appears to have slowed down ice stream retreat.
- Seasonally open marine conditions in AHT were established as early as 14.40 cal. kyr BP and appear to have persisted throughout the ACR. It appears that the initial onset of open marine conditions was driven by oceanic warming, associated with an influx of CDW onto the AP shelf.
- The development of a more persistent sea-ice cover in AHT initiated prior to 11.27 cal. kyr BP is linked to a reduction in meltwater and open-water associated diatoms in cores GC695 and GC697. This is in agreement with a period of reduced meltwater discharge from coastal ice between 12.1 and 11.5 kyr BP (Pike et al., 2013).
- Between 11.27 to 9.29 cal. kyr BP, approximately 4.64 kyr after grounded ice retreat, thick laminated diatomaceous ooze was deposited at mid-shelf sites in AHT during a period of high diatom productivity. We suggest that the retreat of AHIS and the creation of a calving bay was not the sole driver this highly productive environment. Instead, it is argued that high atmospheric and sea surface temperatures and intensified

upwelling of CDW delivered warm, nutrient-rich waters to AHT, which facilitated enhanced meltwater-driven productivity.

- Following laminated diatomaceous ooze deposition, a reduction in meltwater discharge or sea ice melt-related stratification is inferred from the diatom assemblage and a reduction in ADA. The dominance of *Fragilariopsis kerguelensis* and *Eucampia antarctica* (symmetrical) indicates heavier sea ice cover in winter (E. antarctica) and open-water conditions in the summer (F. kerguelensis). These species are highly silicified and thus may be preferentially preserved with diatom abundances are low. A reduction in meltwater discharge or sea ice melt-related stratification could relate to cooler atmospheric temperatures or reduced CDW upwelling associated with a northward shift of the SHWW. In addition, glacial ice that fed into AHT could have retreated to a position where it terminated on land, reducing glacial meltwater input into AHT (Sjunneskog and Taylor, 2002).
- Relatively cold conditions with enhanced sea ice extent persisted to ~0.4 cal. kyr BP. Cooling and increased climate variability during the late Holocene (after 4.2 cal. yr BP) has been attributed to the increasing influence of the ENSO and waning of the SHWW on AP climate (Etourneau et al., 2013; Pike et al., 2013).
- In the late Holocene (after ~0.4 cal. kyr BP), the diatom species assemblage indicates an influx of meltwater and the formation of a well-stratified water column. This is consistent with SST and atmospheric temperature records that indicate a period of warming over the last 500 years (Mulvaney et al., 2012; Pike et al., 2013).

Chapter 7

7. Concluding remarks

7.1. Thesis summary

The overarching aim of this study was to expand our understanding of the deglacial and palaeoenvironmental history of the AHT, utilising extensive new marine geological and geophysical data sets collected during cruise JR284 on RRS *James Clark Ross*. Detailed bathymetric data and sediment core analysis, including visual core description, X-radiographs, quantitative assessment of ADA and diatom species assemblage, radiocarbon dating and a multi-proxy approach (water content, shear strength, grain size distribution, magnetic susceptibility, density, contents of biogenic opal, TOC and $CaCO_3$), were used to address three key questions:

I. What controls the variability in sediments at a retreating ice stream grounding line? (Chapter 4)
II. What are the palaeoenvironmental conditions of the AHT during and after deglaciation? (Chapter 5)
III. What are the timings of environmental change(s) within AHT? (Chapter 6)

7.1.1. Controls on the variability of sediments deposited at the grounding line of a retreating ice stream

The grounding line of ice streams remain poorly understood due to the lack of modern grounding line observations and a reliance on conceptual models that may not necessarily reflect the variability in grounding line processes and environments that exist in natural settings. Correctly identifying the environment within which transitional sediments are deposited is particularly important when sediments are targeted for radiocarbon dating, or when a link between the rate and style of ice stream retreat and the nature of the grounding line or ice margin environment (e.g. presence of absence of an ice shelf), is deemed important. Understanding the full range of processes and the controls on sediment variability in the transitional environment, is essential if we are to utilise the geological record to accurately reconstruct the palaeo-ice stream retreat and build reliable analogues between these and modern day ice streams and marine terminating glaciers. In order to investigate the variability in transitional sediments deposited by a retreating grounding line, Chapter 4 utilised multi-

proxy analysis on an extensive network of sediment cores that captured the last deglaciation of AHT.

Detailed sedimentological analyses of cores recovered from AHT revealed that sediments can be divided into six broad depositional environments; subglacial, grounding line, grounding line proximal, grounding line distal, calving line and seasonally open marine. Sedimentological information was used to identify sediment 'end-members' which are representative of key processes and modes of sedimentation in these depositional environments. Within cores recovered from AHT, transitional sedimentary units are found to be deposited systematically, varying with marine processes, grounding line retreat rate, ice margin type and bathymetric and across trough position. These observations provided an insight into the rate and style of grounding line retreat within AHT.

The AHIS is interpreted to have retreated episodically. The thickness of transitional units along the AHT are highly variable, but appear to correlate with the location of GZWs. Thicker transitional sediments are found seawards of GZWs, deposited during still-stands. Minor oscillations of the grounding line during these still-stands and/or varying sediment flux are reflected in interbedded coarser and finer units. During fast ice stream retreat (e.g. between the GZWs), the sediment source is constantly retreating so there is insufficient time for thick deposits to accumulate. The geometry of the ice stream margin, and specifically whether it has a fringing ice shelf, exerts a significant control on the depositional processes that operate at the grounding line and beyond, as well as on the rate of grounding line retreat (Pollard et al., 2015; DeConto and Pollard, 2016). The majority of stratified diamictons, deposited at the AHIS grounding line, are characterised by low biogenic content and a clay mineral assemblage that is comparable to underlying sub-glacial sediments. Because of this, they are interpreted to have been deposited in a sub-ice shelf environment. The most expanded 'sub-ice shelf sediments' coincides with a narrowing of the AHT between Anvers and Hugo Islands; a setting that would provide ice shelf pinning points and shelter from wind, waves and currents. These conditions favour ice shelf formation and stability (Powell, 1984). Additional factors influencing the style and distribution of transitional sediment facies include a variety of marine processes. Fast currents can prevent fine sediments from being deposited and can winnow fine sediments from deposited material. The well-sorted nature of sediments recovered from the outer-continental shelf are indicative of high bottom current activity at the shelf edge. On the mid to inner-shelf, deposition of silty laminae (plumites) suggest deposition in a quiescent (sub-ice shelf cavity) and potentially more grounding line distal environment. This additionally highlights the importance of grounding line proximity, as current velocity is likely

to be enhanced near the grounding line as the accommodation space in the ice-shelf cavity is reduced. Cores recovered from relatively shallow trough regions and perpendicular to the main trough axis highlight the role of icebergs for delivering and redistributing sediments. The availability of extensive bathymetric data is helpful for providing context for cores containing sediments indicative of iceberg turbation. Cores recovered perpendicular to the trough axis may have been influenced by ice within the main trough and ice draining from other source regions (e.g. ice domes). However, further work is required to fully understand if there are key differences between trough flank/trough axis sedimentation. In addition, more needs to be understood about the deglacial history of Antarctic Peninsula ice domes.

7.1.2. Palaeoenvironmental conditions of the AHT over and following deglaciation

Chapter 5 utilised the sediment core analysis carried out in Chapter 4 along with new quantitative ADA and diatom species assemblage data. The main aim of this chapter was to investigate the palaeoenvironmental conditions in AHT during deglaciation and assess the link between deglaciation and primary productivity. Chapter 4 identified a post-glacial unit of laminated diatomaceous ooze, deposited above the glacial sediments; interpreted to have been deposited during a period of high-productivity following grounding line retreat. To explore these sediments in more detail, the factors controlling production and preservation of laminated diatomaceous ooze deposits in this region were investigated and discussed in the context of similar deposits found elsewhere around Antarctica.

Quantitative ADA and assemblage data indicated that the AHT trough experienced a number of environmental changes following grounding line retreat and the demise of an ice canopy. This includes an increase in productivity at the initial onset of seasonally open marine conditions, the return to an environment with low productivity associated with sea ice expansion and then the onset of environmental conditions that led to deposition of laminated diatomaceous ooze. Deposition of laminated diatomaceous ooze is associated with meltwater discharge and nutrient input from sea ice and glacial ice melt. This is indicated by the prevalence of sea ice and sea ice-melt associated diatom species *Fragilariopsis curta, Chs* and *Corethron pennatum.* Grounding line retreat within AHT and the formation of a calving bay were not solely responsible for the enhanced productivity and formation of laminated diatomaceous ooze units within AHT. Laminated diatomaceous ooze units do not directly overly sub-glacial to grounding-line proximal sediments in these cores and the onset of open-marine conditions within AHT did not coincide with peak productivity. Additional drivers of meltwater input and water column stratification, in addition to the formation of a calving bay,

were required to enhance productivity of species *F. curta*, *Chs* and *C. pennatum*. This provides an important insight into the consequences of deglaciation on marine productivity, which may be important for our understanding of future Antarctic environmental change. The use of multiple sediment cores and extensive bathymetric mapping of AHT, demonstrated that seafloor bathymetry, in addition to water depth, basin geometry and duration, stability and prevalence of environmental conditions, played an important role in laminated diatomaceous ooze accumulation. The discontinuity of *Chs*-RS and *C. pennatum*-dominated diatomaceous ooze thickness across the AHT indicates that thickness is not always a function of the scale and duration of environmental conditions. The presence of thick (100 cm) laminated or thin (<30 cm) homogenous *Chs*-RS and *C. pennatum*-dominated diatomaceous ooze units, emphasises that it is possible to underestimate the scale of surface productivity depending on the bathymetric setting of a chosen core site. This is an important inference when sediment cores are used to assess the relationship between deglaciation and primary productivity during past deglacial periods, and when these inferred palaeoenvironmental conditions are used as an analogue for future environmental change.

7.1.3. Deglacial chronology of Anvers-Hugo Trough

The deglacial chronology of AHT was previously poorly constrained. Available chronological data suggested that deglaciation following the LGM started at ~16.4 cal. yr BP (Heroy and Anderson, 2007), with deglaciation of the inner shelf by ~13.18 and ~8.40 cal. kyr BP, for the Palmer Deep and the Gerlache Strait, respectively (Harden et al., 1992; Domack et al., 2001, 2006). In a compilation of deglacial ages by Livingstone et al. (2012), deglaciation of the mid-shelf occurred by ~11.2 cal. kyr BP (Livingstone et al., 2012), although this was incompatible with earlier deglaciation of the inner shelf, prior to ~13.18 cal. kyr BP. These issues resulted from a lack of core sites, the grouping of transitional sediment facies and, as a result, radiocarbon dating sediments deposited at an unknown time after grounding line retreat, as well as reliance on AIO dating without adequate investigation into its reliability. Furthermore, the lack of a concise deglacial chronology for AHT made it difficult to understand the link between deglaciation of the trough and the establishment of seasonally open marine conditions with enhanced productivity at Palmer Deep, including if and when a calving bay was established.

Timing of environmental changes are constrained in Chapter 6 with new radiocarbon dates from AHT sediment cores. These dates were be used to (i) constrain the timing of grounded ice retreat following the LGM, and (ii) constrain the timing of key palaeoenvironmental

changes following deglaciation. The latter includes the deposition of laminated diatomaceous oozes. Twenty-seven new radiocarbon ages were obtained from benthic and calcareous foraminifera, AIO and Ramped PyrOx ^{14}C dating. An initial review of the age data demonstrated, that the LCO in the mid-inner part of AHT is relatively small giving us some confidence that the AIO dating method can be applied in this area. Paired foraminifera-AIO dating also suggested that samples taken from diatomaceous sediment are more likely to yield reliable AIO ages compared to samples taken from diatom-/organic-poor sediments. Finally, the Ramped PyrOx ^{14}C method achieves consistent results, negating some of the problems associated with dating organic-poor sediment that contain unknown quantities of fossil carbon.

These dates were used to show that grounded ice had retreated from the outer to mid-shelf section of AHT by 15.84 cal. kyr BP. Over this period, two GZWs, including one compound-GZW, were formed on centennial timescales. Onset of deglaciation of AHT was likely initiated by raising global sea level associated with deglaciation of Northern Hemisphere ice sheets after ~21 kyr. Retreat also coincided with post-LGM atmospheric warming and upwelling of CDW onto the AP continental shelf. Grounded ice retreat in AHT occurred early enough to contribute to MWP1a, although its contribution would have been minimal. Deglaciation of the outer and mid-shelf section of AHT preceded MWP1a by >1,000 yrs.

Seasonally open marine conditions in AHT appear to have persisted throughout the ACR, possibly due to the presence of CDW on the AP shelf (e.g. Sjunneskog and Taylor, 2002). The development of a more persistent sea-ice cover in AHT initiated prior to 11.27 cal. kyr BP is interpreted from a reduction in meltwater and open-water associated diatoms. This roughly coincides with reduced meltwater discharge into Palmer Deep at this time (Pike et al., 2013). Between 11.20 and 10.95 (GC695) or 9.29 (GC691 and GC698) cal. kyr BP, some ~ 4.64 kyr after grounded ice retreat, thick laminated diatomaceous ooze was deposited at mid-shelf sites in AHT, during a period of high diatom productivity. It was tentatively noted that deposition of the laminated diatomaceous oozes is coeval with MWP1b, which possibly contributed to the final deglaciation of inner shelf areas leading to a pulse of meltwater into the system.

Following laminated diatomaceous ooze deposition, a reduction in meltwater discharge or sea ice melt-related stratification is inferred from the diatom assemblage and a reduction in ADA. The dominance of *Fragilariopsis kerguelensis* and *Eucampia antarctica* (symmetrical) indicates heavier sea ice cover in winter (*E. antarctica*) and open-water conditions in the summer (*F. kerguelensis*). These species are highly silicified and thus may be preferentially preserved with diatom abundances are low. A reduction in meltwater discharge or sea ice melt-related stratification, as inferred from the relatively low ADA and abundance of melt-water

associated species, could relate to wind-forced sea ice break-up, cooler atmospheric temperatures or reduced CDW upwelling associated with a northward shift of the SHWW. In addition, glacial ice that fed into AHT could have retreated to a position where it terminated on land, reducing glacial meltwater input into AHT (Sjunneskog and Taylor, 2002). *Fragilariopsis curta* and *Thalassiosira antarctica* T1 generally increase in abundance after ~9.00 cal. kyr BP, indicative of greater sea ice presence and spring melt. This coincides with a $\delta^{18}O_{diatom}$ increase from ~9.0 kyr BP, associated with a slowdown in glacial discharge (Pike et al., 2013). This is linked to reduced CDW influx onto the continental shelf, associated with a northward shift in the SHWW (Peck et al., 2015). Relatively cold conditions with enhanced sea ice extent persisted within AHT until ~0.4 cal. kyr BP. These cold conditions are consistent with cooling SSTs through the Holocene, which reached a minimum at 2.7 and 1.7 kyr (Shevenell et al., 2011). In the late Holocene (after ~0.4 cal. kyr BP), the diatom species assemblage data from AHT indicates an influx of meltwater and the formation of a well-stratified water column. This is consistent with SST and atmospheric temperature records that indicate a period of warming over the last 500 years (Mulvaney et al., 2012; Pike et al., 2013).

7.2. Limitations and perspectives for future research

7.2.1. Establishing the presence of a fringing ice shelf

Two key criteria were used to establish the presence of a fringing ice shelf, within grounding line proximal sediments, during deglaciation. These were low siliceous and calcareous microfossil content and a clay mineral assemblage that was comparable to underlying subglacial sediments; this assumes that a higher proportion of exotic lithologies are deposited at a tidewater margin and that biological productivity is supressed beneath an ice shelf. Previous studies have used the presence of 'pelletized muds' to identify ice shelf presence (Domack and Harris, 1998; Domack et al., 1999), however, these muds are regionally patchy and not always found in sub-ice-shelf sediments (e.g., Kilfeather et al., 2011; Smith et al., 2017; this study). Furthermore, currents can transport sediment and biogenic material into the sub-ice shelf cavity, complicating the criteria set out in this investigation (Hemer and Harris, 2003; Hemer et al., 2007; Post et al., 2014). In a grounding line distal setting, ice shelf presence was inferred on the basis of largely terrigenous, finely laminated (clay/silt) sediments that lack a coarse grain-size fraction (>sand). The lack of coarse debris has been used as an indication of deposition in a grounding line-distal, sub-ice shelf setting, as it is assumed that the majority of coarse debris is melted out proximal to the grounding line (Powell et al., 1996; Domack and Harris, 1998; Smith et al., 2017). However, several studies have demonstrated that coarse sediments can be distributed throughout the ice shelf, both englacial and supraglacially (Evans

and Ó Cofaigh, 2003; Nicholls et al., 2012), which enables coarse-grained material to be deposited distally to the grounding line. Furthermore, this study has identified that spatial and temporal variations in ocean currents, basal melt rates, retreat rate and evolution of the shape/size of the ice shelf cavity will all influence sedimentation and the ice shelf 'signature' preserved in the geological record. These complications ultimately arise from the small number of observations in modern sub-ice shelf environments. This highlights the need for observations beneath a greater range of modern ice shelves, subject to different environments and processes, in order to expand our understanding of key criteria that can be used to identify ice shelves in palaeo-records.

7.2.2. Incomplete deglacial chronology

One of the strengths of this study was the implementation of a well-developed sampling strategy for ^{14}C dating, guided by detailed sedimentological information (e.g., Heroy and Anderson, 2005; Hillenbrand et al., 2010a, b; 2012; Smith et al., 2011; 2014) and the application of multiple dating methods that targeted different sediment/material types. Based on this data it was possible to establish the timing and rate of grounding line retreat across AHT and accurately date the deposition of laminated diatomaceous oozes. In addition, this thesis demonstrated that the deposition of laminated diatomaceous oozes lagged grounding line retreat by as much as 4.64 kyrs. However, despite generating a substantial amount of new chronological data, there are a number of cases where additional dating would be beneficial. For instance, there remains limited chronological control for deglaciation of the outer and innermost parts of shelf as well as a lack of age-data with which to constrain the timing and formation of GZWs. The deglaciation of proposed ice domes is also poorly constrained, whilst specific palaeoenvironmental changes are not dated in all cores.

Our current data indicates that GZWs 2 and compound-GZW 3 were deposited over a relatively short period of time (~650 years). To constrain the formation of individual wedges requires additional cores, including the use of other coring technologies (e.g., vibrocoring, MeBo, Rock-Drill 2) that are able to penetrate through and sample key sub-bottom reflectors. Further gaps in dating exist for the interval between grounding line retreat and the onset of laminated diatomaceous ooze deposition. This means that certain palaeoenvironmental changes, including the onset of open marine conditions and subsequent lengthening of the sea ice season, are not well constrained in all cores. Based on the relatively high terrigenous component of these sediments, and in the in the absence of calcareous (micro-)fossils to date, application of Ramped PyrOx dating is recommended.

Published data indicate that grounded ice had retreated to Palmer Deep by 13.10 cal. kyr BP, although thinning of ice in the hinterland continued into the early Holocene (Bentley et al., 2011). However, there is currently limited (direct) information about ice sheet retreat across the innermost part of the shelf (between the Palmer Deep and the current coastline); although inferences about ice sheet thinning have been made from proxy records (e.g., $\delta^{18}O_{diatom}$ data; Pike et al., 2013). Likewise, ice domes, which are thought to have flanked the AHT during the LGM (Domack et al., 2006; Lavoie et al., 2015), may have played an important role in controlling the pattern of deglaciation and represent an important source of meltwater to drive productivity. In both instances, additional sediment cores and dating from the inner shelf and proposed locations of ice domes, would provide a more complete picture of deglaciation and allow further investigations into the potential connection between deglaciation and enhanced productivity.

7.2.3. Modern day spatial distribution of *Thalassiosira scotia*

The lack of information regarding the modern distribution of *T. scotia* means that it remains challenging to use the presence/absence of this species to infer palaeoenvironmental conditions. In this study it appears to occupy a similar environmental niche to *T. antarctica* T2, although there are some subtle differences in their distribution that would be beneficial to explore. This would aid reconstructions of palaeoenvironmental conditions where these species are dominant, especially due to their association with the last deglaciation of AHT and, potentially, the wider WAP region. One method for addressing this knowledge gap could be through investigating the spatial distribution of this species in modern surface sediments, so to link its distribution with modern environmental conditions. Such studies have previously been successfully applied to other diatom species, including *T. antarctica* and *E. antarctica,* and the results are subsequently used to infer palaeoenvironmental conditions (e.g. Zielinski and Gersonde, 1996; Buffen et al., 2007; Allen et al., 2014).

7.2.4. Assessing the role of CDW on ice sheet retreat and initial onset of open-marine conditions in AHT

Grounded ice had begun its retreat from the outer AHT prior to 16.49 cal. kyr BP, reaching the mid-shelf area as early as 15.84 cal. kyr BP and the inner shelf (Palmer Deep) after 13.18 cal. kyr BP. It is likely that atmospheric warming following the LGM together with Northern Hemisphere sea-level rise drove initial retreat. Multi-proxy records from Palmer Deep, including SST reconstructions (Shevenell et al., 2011; Etourneau et al., 2013), benthic foraminiferal assemblage data (Ishman and Sperling, 2002) and stable carbon and oxygen

isotope data on benthic foraminifera (Shevenell and Kennett, 2002) indicate that CDW played a dominant role in deglaciation of the inner shelf (after 13 kyr) as well as subsequent variations in productivity/the environment of WAP throughout the Holocene. Variations in glacier melting, likely driven by warm CDW, are also inferred from $\delta^{18}O_{diatom}$ data (Pike et al., 2013). It has also been speculated in this thesis and elsewhere that incursion of warm CDW were also important in driving the initial ice retreat (after ~17 kyr) but there is currently a dearth of proxy records which cover the early deglacial phase (~17-13 cal. kyr BP). This situation largely reflects the fact that the shelf was covered by grounded ice, thereby preventing accumulation of sediment archives, but also a more general lack of suitable proxies with which to reconstruct CDW variability. Hillenbrand et al. (2017) recently demonstrated the utility of Mg/Ca analysis on benthic and planktic foraminifera to reconstruct bottom water temperatures, although this study was limited due to the lack of a suitable temperature calibration. Whilst application of this approach to cores from AHT is desirable, it is important to point out that to do so requires foraminifera-rich sediments which may only be present in inner shelf basins such as Palmer Deep. Other indirect approaches to reconstruct CDW (e.g., TEX86-L, $\delta^{18}O_{diatom}$) could be applied to cores from the mid-shelf, potentially providing information on CDW variability from 15.84 kyrs-onwards. Alternatively, it might be possible to refine ice sheet models which include warm-water forcing (e.g., Pollard and DeConto, 2009) to better understand its role in forcing initial ice retreat. Future work should focus on this problem firstly by assessing the suitability of these proxies for sediments in AHT (based on the presence/absence of foraminifera and utility of biomarkers) and secondly by incorporating models/and or offshore records (e.g., Lamy et al., 2015; Ullermann et al., 2016).

Appendices

Appendix A

Cluster analysis of ITRAX Si/Ti data over laminated diatomaceous ooze unit in core GC695

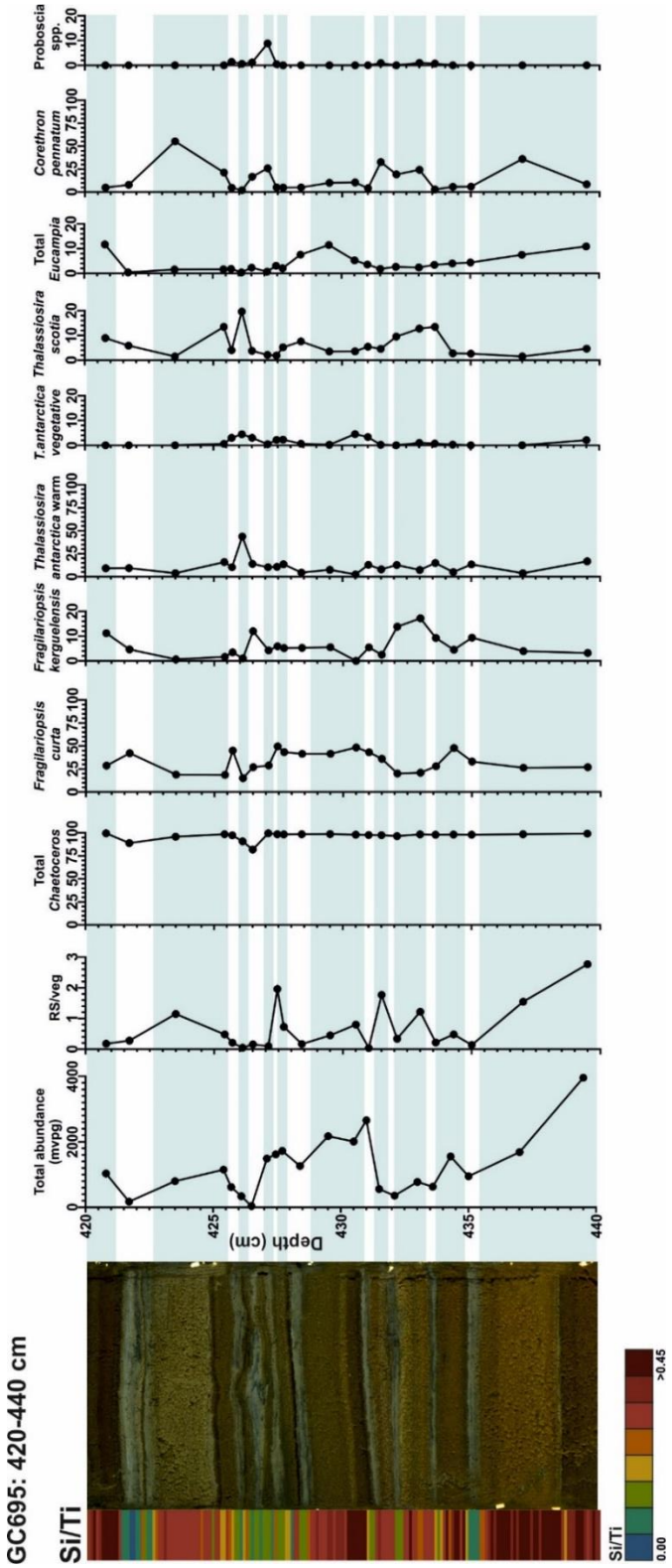

Cluster analysis of ITRAX Si/Ti data for cores GC691. GC695, GC711, GC697 and GC698

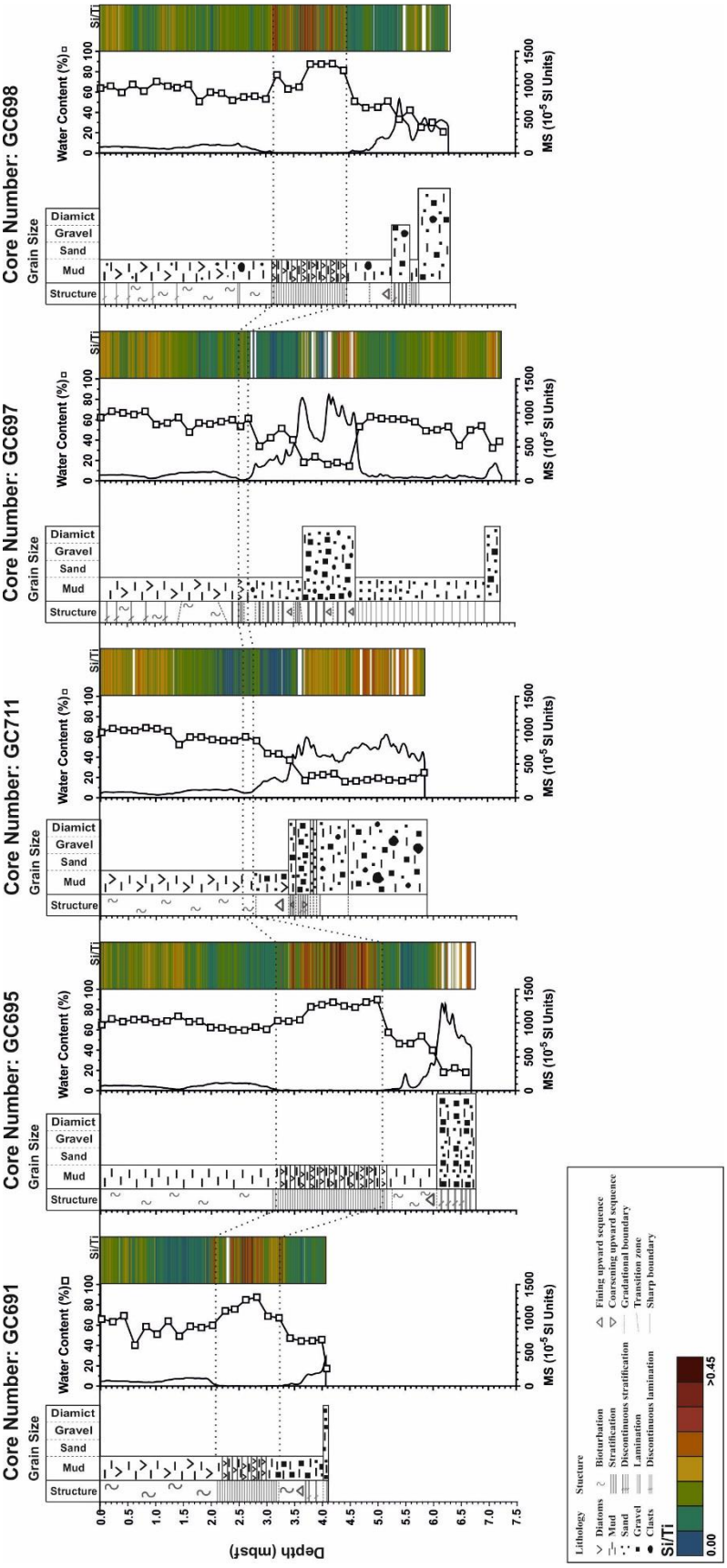

Dashed line indicates diatom zone 5

Appendix B: Light microscopy images of Anvers-Hugo Trough diatoms

Appendix B: i

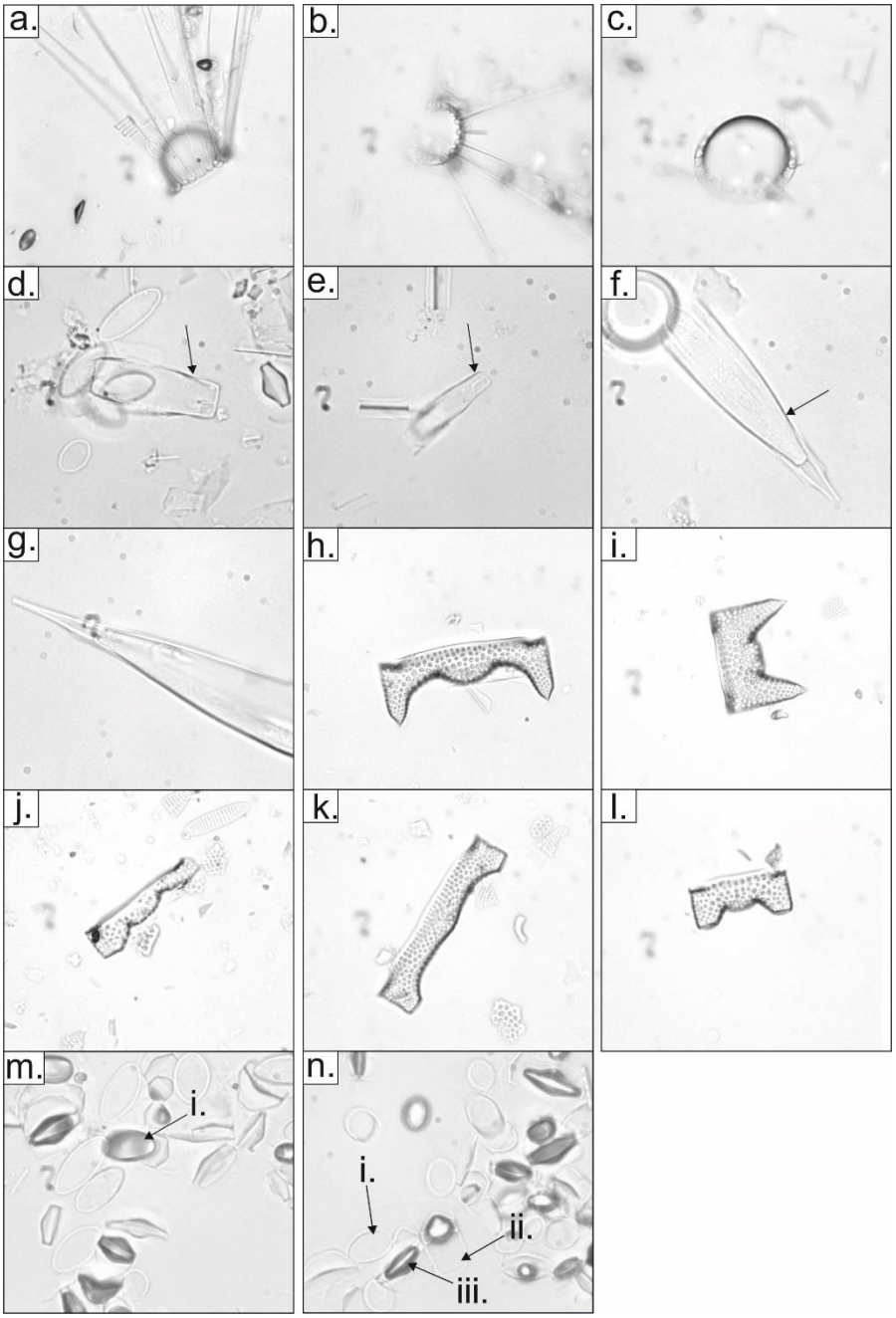

Appendix B (i): Light microscope images from JR284 sediment core GC695. a-c: Corethron pennatum *(a-b, 442 cm, magnification of ×400) (c, 452 cm, magnification of ×400). d-e:* Proboscia *spp. (427.1 cm, magnification of ×1000). f-g:* Rhizosolenia *spp. (42 cm, magnification of ×1000). h-l:* Eucampia antarctica *(h-i, symmetrical, pointed, 202 cm, magnification of ×400) (j, asymmetrical, flattened, 162 cm, magnification of ×400) (k-l, symmetrical, flattened, 202 cm, magnification of ×400). m-n:* Chaetoceros subg. Hyalochaete *(442 cm, magnification of ×1000) (m.i:* Chaetoceros subg. Hyalochaete, *resting spore); n.i & iii:* Chaetoceros subg. Hyalochaete, *resting spore; n.ii:* Chaetoceros subg. Hyalochaete, *vegetative cell).*

Appendix B: ii

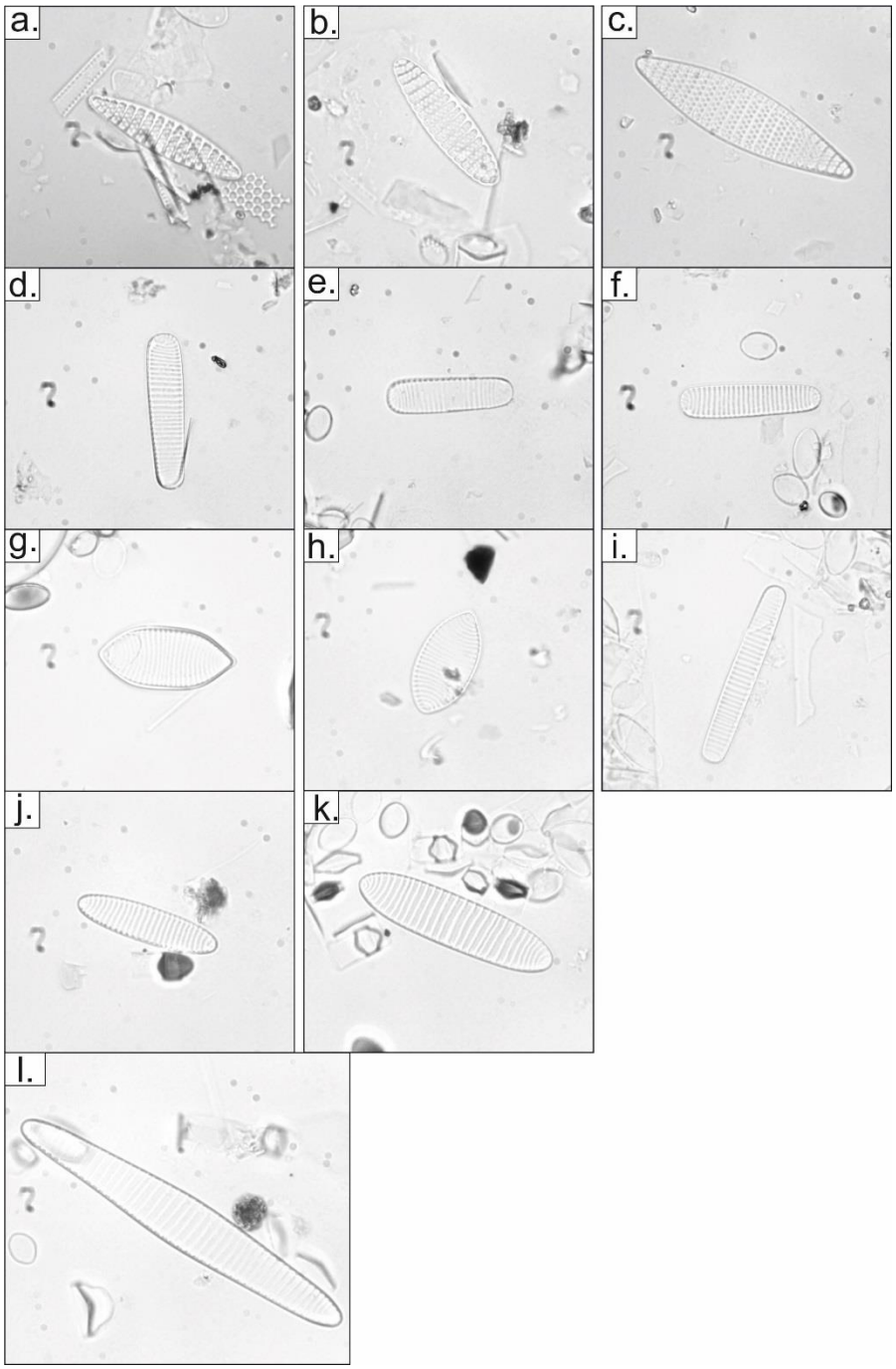

Appendix B (ii): Light microscope images from JR284 sediment core GC695. a-c: Fragilariopsis kerguelensis *(a, 42 cm, magnification of ×1000) (b, 442 cm, magnification of ×1000) (c, 452 cm, magnification of ×1000). d-f:* Fragilariopsis curta *(d, 442 cm, magnification of ×1000) (e-f, 427.1 cm, magnification of ×1000). g-h:* Fragilariopsis rhombica *(g, 442 cm, magnification of ×1000) (h, 427.1 cm, magnification of ×1000). i:* Fragilariopsis vanheurckii *(427.1 cm, magnification of ×1000). j-k:* Fragilariopsis ritscheri *(442 cm, magnification of ×1000). l:* Fragilariopsis obliquecostata *(442 cm, magnification of ×1000).*

Appendix B: iii

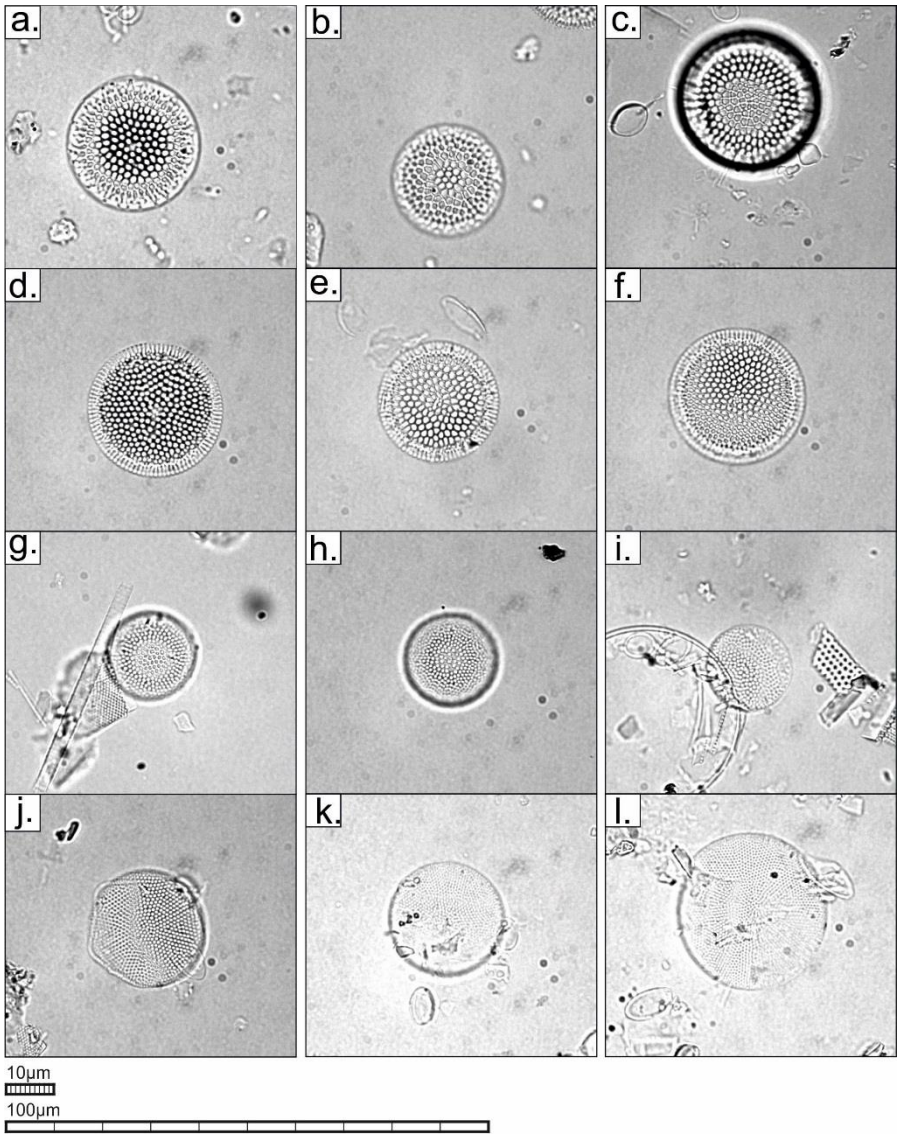

Appendix B (iii): Light microscope images from JR284 sediment core GC695, magnification of ×1000. a-c: Thalassiosira scotia *resting spore (2 cm). d-f:* Thalassiosira antarctica *T2 (warm) resting spore (2 cm). g-i* Thalassiosira antarctica *T1 (cold) resting spore (2 cm),* Thalassiosira antarctica *vegetative cell (259 cm).*

Appendix B: iv

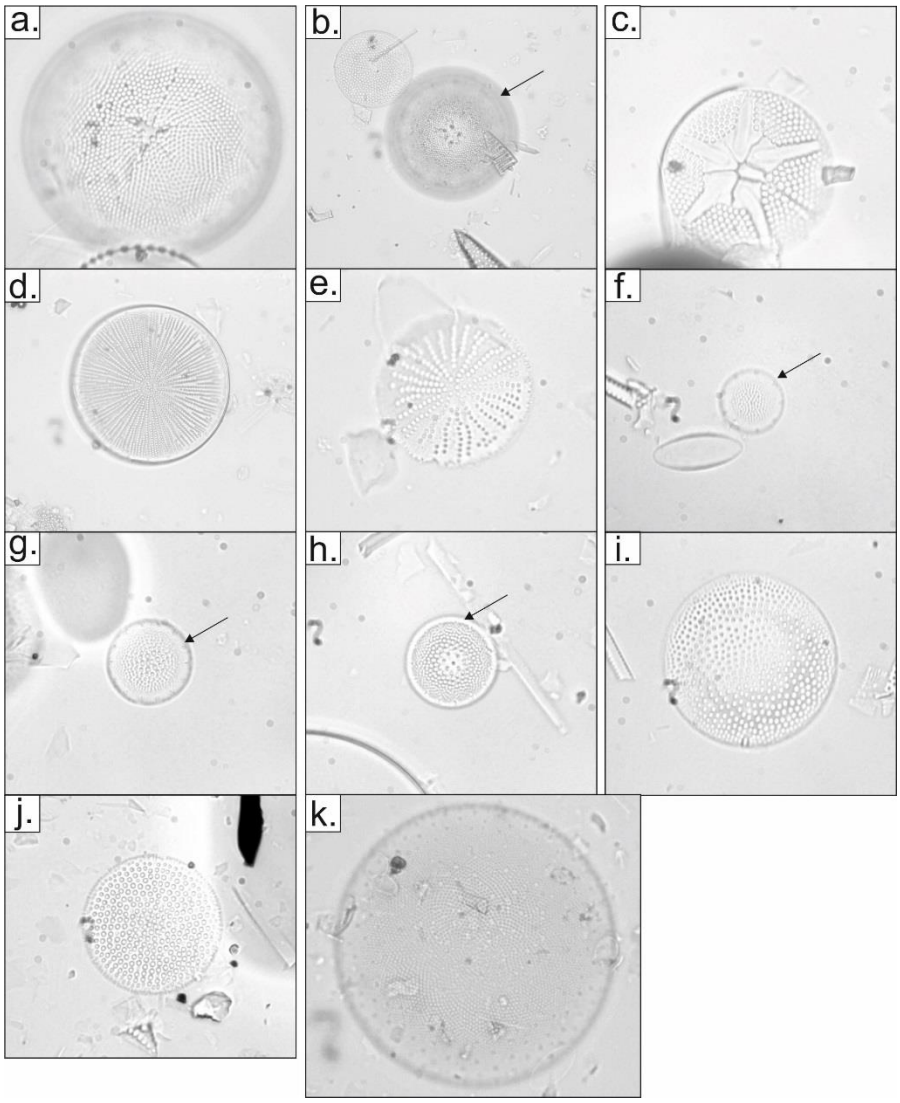

Appendix B (iv): Light microscope images from JR284 sediment core GC695.a-b: Stellarima microtrias *(a, 42cm, magnification of ×1000) (b, 162 cm, magnification of ×400). c:* Asteromphalus *spp. (442 cm, magnification of ×1000). d-e:* Actinocyclus actinochilus *(d, 442 cm, magnification of ×400) (e, 42 cm, magnification of ×1000). f.* Shionodiscus gracilis *var. expecta (42 cm, magnification of ×1000). g-h:* Shionodiscus gracilis *var. nominate (42 cm, magnification of ×1000). i-j:* Thalassiosira lentiginosa *(42 cm, magnification of ×1000). k:* Porosira glacialis *(452 cm, magnification of ×400).*

Appendix B: v

Appendix B (v): Light microscope field-of-view images from core GC695 (2cm, magnification of ×1000). a: Light microscope image including Thalassiosira scotia and Chaetoceros subg. Hyalochaete, *resting spore's*. b: Light microscope image including Thalassiosira antarctica *vegetative cell.*

Appendix B: vi

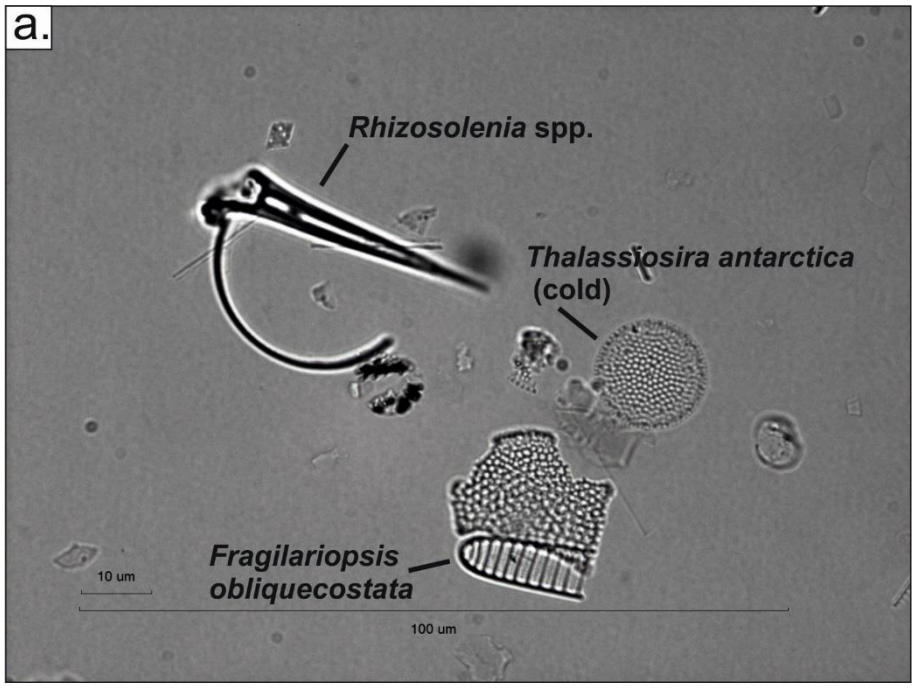

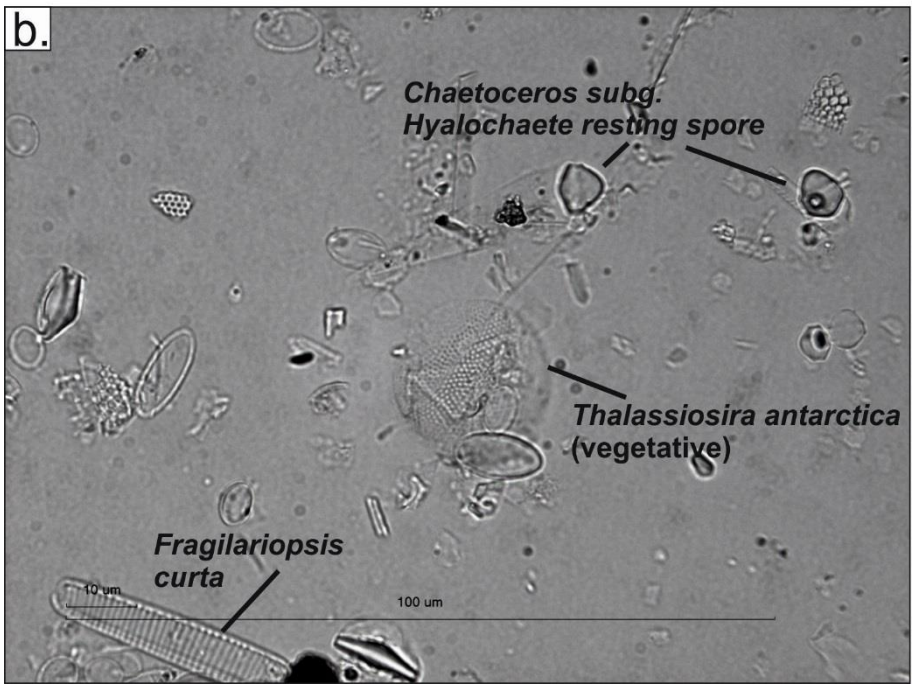

Appendix B (vi): Light microscope field-of-view images from core GC695 (2cm, magnification of ×1000). a: Light microscope image including Rhizosolenia *spp.,* Thalassiosira antarctica *T1 (cold) resting spore and a fragment of* Fragilariopsis obliquecostata. b: *Light microscope image including* Thalassiosira antarctica *vegetative cell,* Chaetoceros subg. Hyalochaete, *resting spore's and* Fragilariopsis curta.

Appendix B: vii

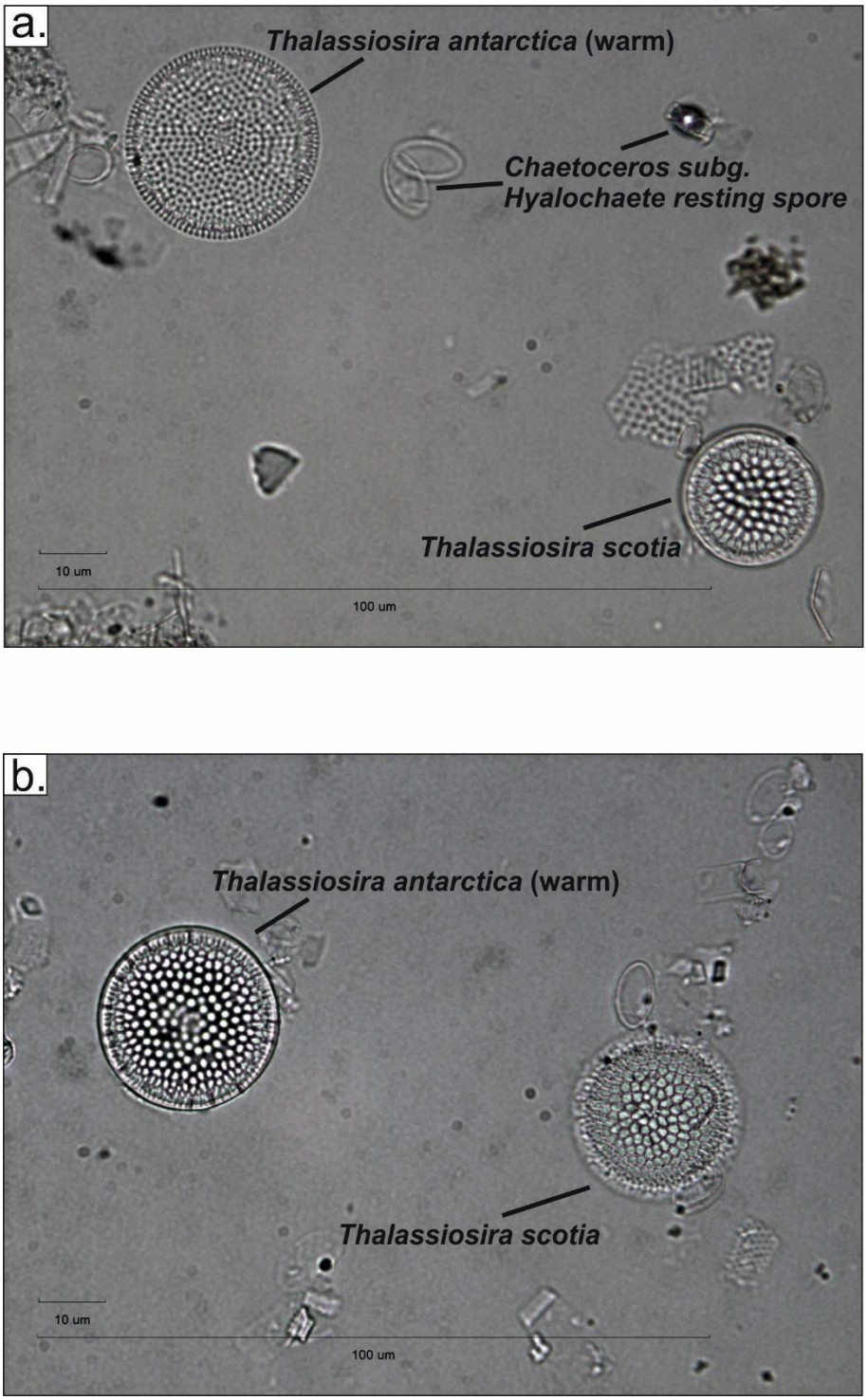

Appendix B (vii): Light microscope field-of-view images from core GC695 (2cm, magnification of ×1000). a: Light microscope image including a Thalassiosira scotia *resting spore,* Thalassiosira antarctica *T2 (warm) resting spore and* Chaetoceros subg. Hyalochaete, *resting spore's. b: Light microscope image including a* Thalassiosira scotia *resting spore and* Thalassiosira antarctica *T2 (warm) resting spore.*

Appendix C: Lithological unit depths and cross-plot (Fig. 4.7) data

Core	Unit	Depth	Water content (%)	Shear strength (kPa)	Biogenic opal (wt%)
GC690	7	0-245	65	0	13
GC690	5	245-283	54	2	8
GC690	7	283-315	47		
GC690	5	315-319	21	3	2
GC690	1	319-604.5	18	16	1
GC691	7	0-209	58	0	23
GC691	6	209-320	78	1	30
GC691	7	320-329	67	3	26
GC691	5	329-368	46	8	9
GC691	7	368-402	45	3	11
GC691	2	402-409.5	17	1	2
GC692	1	0-186	28	16	
GC692	7	186-227	45	1	
GC692	5	227-245	50	6	
GC692	7	245-473.5	64	1	
GC695	7	0-323	66	1	25
GC695	6	323-546	76	5	31
GC695	5	546-565	46	10	7
GC695	7	565-598	54	3	12
GC695	5	598-607	40	11	5
GC695	2	607-675	20	3	3
GC697	7	0-259	60	2	11
GC697	5	259-321	46	7	3
GC697	7	321-349	46	5	6
GC697	5	349-360			
GC697	2	360-460	18	7	1
GC697	4	460-694	54	9	4
GC697	2	694-722	36	15	4
GC698	7	0-313	61	1	21
GC698	6	313-459.5	78	2	28
GC698	5	459.5-507	47	7	8
GC698	7	507-519			
GC698	5	519-536	51	6	10
GC698	2	536-561	38	6	5
GC698	4	561-574			
GC698	1	574-634	26	11	6

Core	Unit	Depth	Water content (%)	Shear strength (kPa)	Biogenic opal (wt%)
GC702	7	0-180	63	0	24
GC702	5	180-235	48	5	9
GC702	2	235-245	18	17	3
GC702	7	245-264	51	1	13
GC702	2	264-269			
GC702	5	269-295	55	6	5
GC702	2	295-320	40	4	5
GC702	5	320-343	17	10	4
GC702	2	343-383	29	4	4
GC702	5	383-416	21	34	6
GC702	7	416-438	48	9	14
GC702	5	438-481	30	17	4
GC703	7	0-66	59	0	20
GC703	5	122-134			
GC703	2	134-178	27	17	5
GC703	2	192-229	23	14	4
GC703	1	229-392	21	19	4
GC703	5	278-192	43	2	6
GC703	1	66-122	26	14	5
GC704	7	0-94	40	3	5
GC704	2	129-144	28	3	
GC704	5	144-156			
GC704	3	156-183.5	36	2	4
GC704	2	183.5-193.5			
GC704	5	193.5-208	39	0	3
GC704	3	208-239.5	35	0	
GC704	1	239.5-414.5	25	10	4
GC704	3	94-129	32	2	4
GC706	7	0-34	45	2	
GC706	1	34-237	26	16	
GC709	7	0-223	59	2	
GC709	5	229-261	45	5	
GC709	7	261-281	43	3	
GC709	5	281-300	41	6	
GC709	2	300-327	19	29	
GC709	1	327-358	28	20	
GC711	7	0-284	62	2	13
GC711	5	284-324	43	8	6
GC711	7	324-344	37		
GC711	5	344-352			
GC711	2	352-388	20	7	1
GC711	1	388-588	20	24	2

Appendix D: Images of JR284 sediment cores

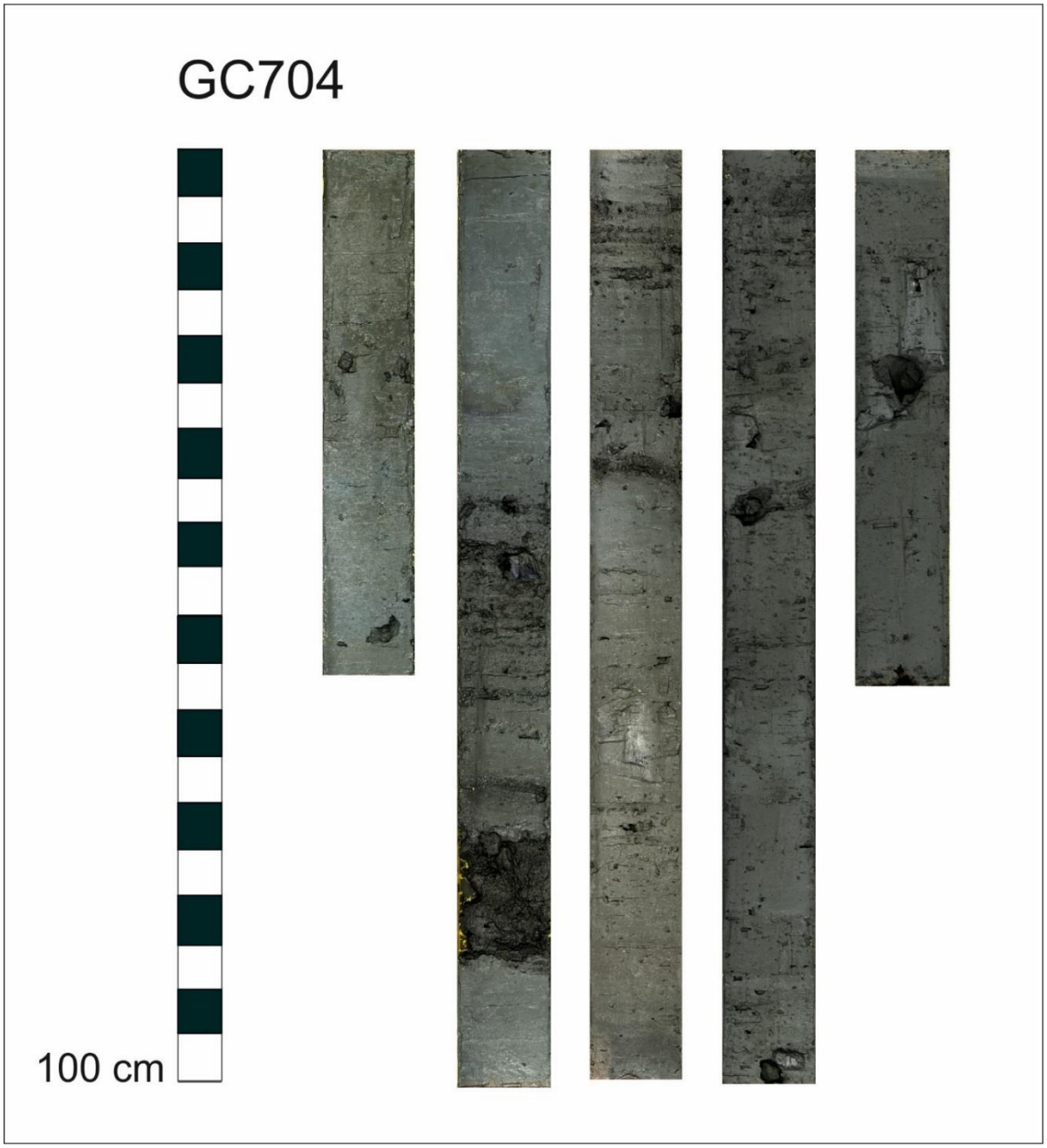


GC706
100 cm

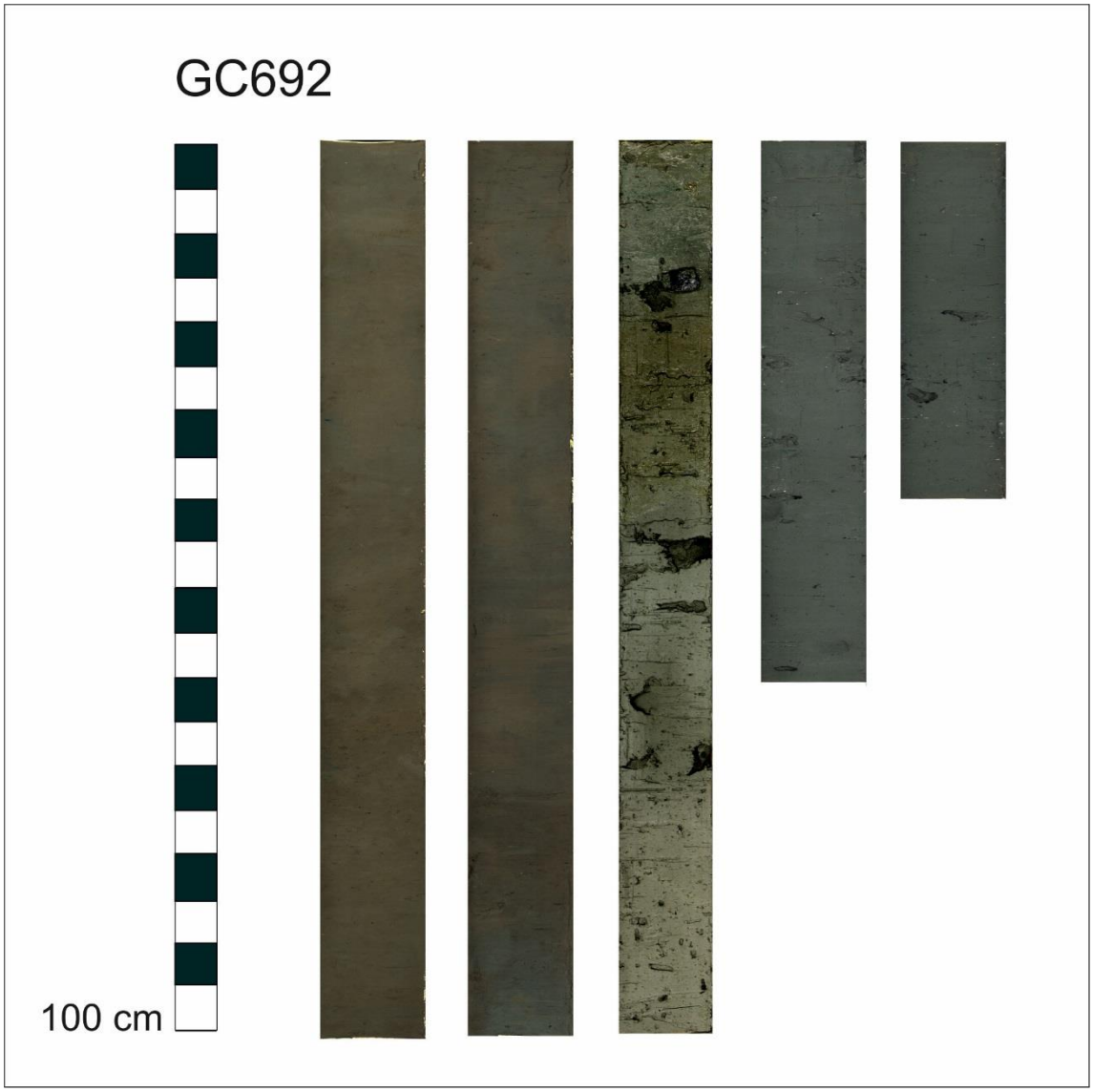
GC692
100 cm

- 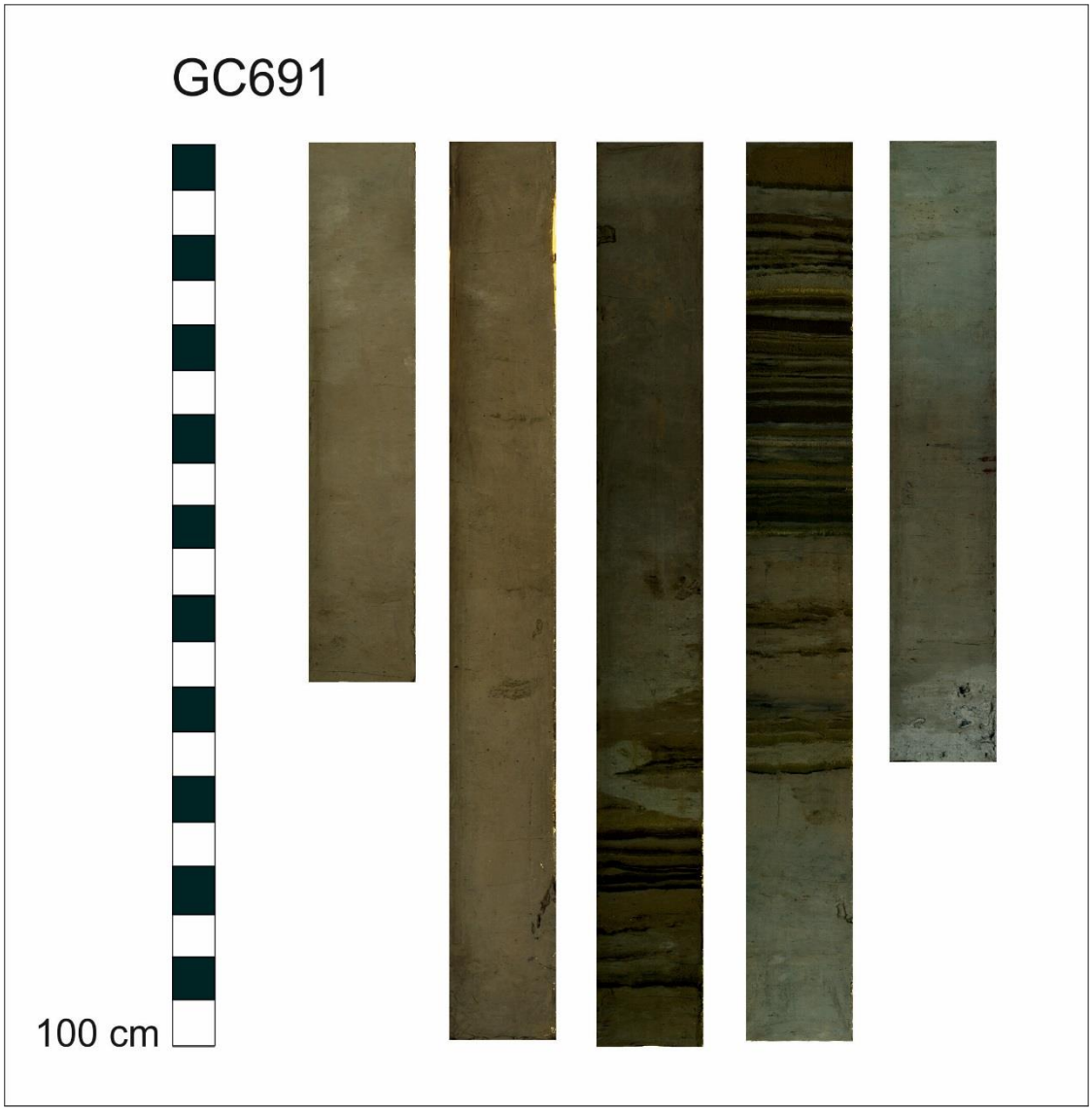
GC691
100 cm

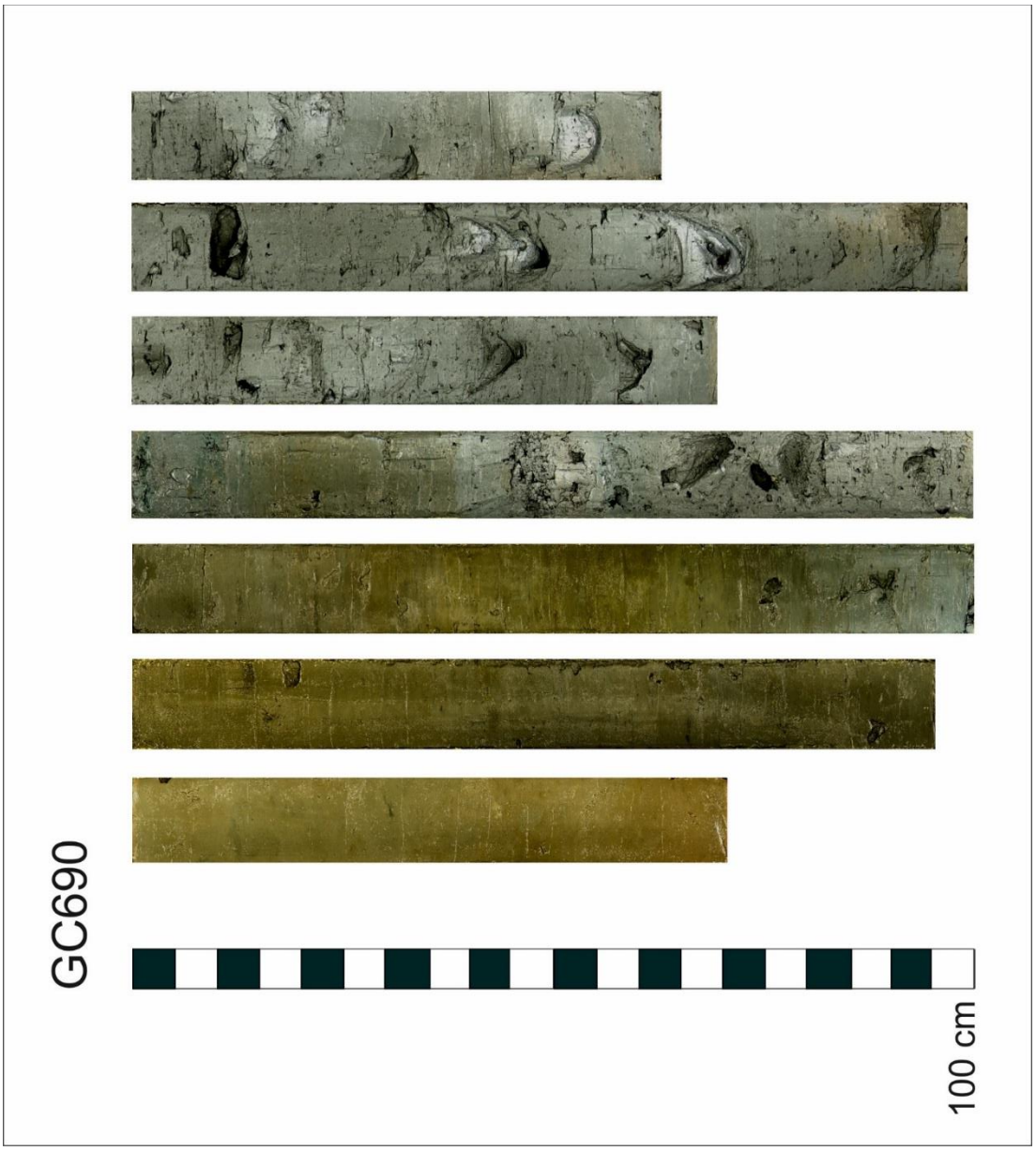
GC690
100 cm

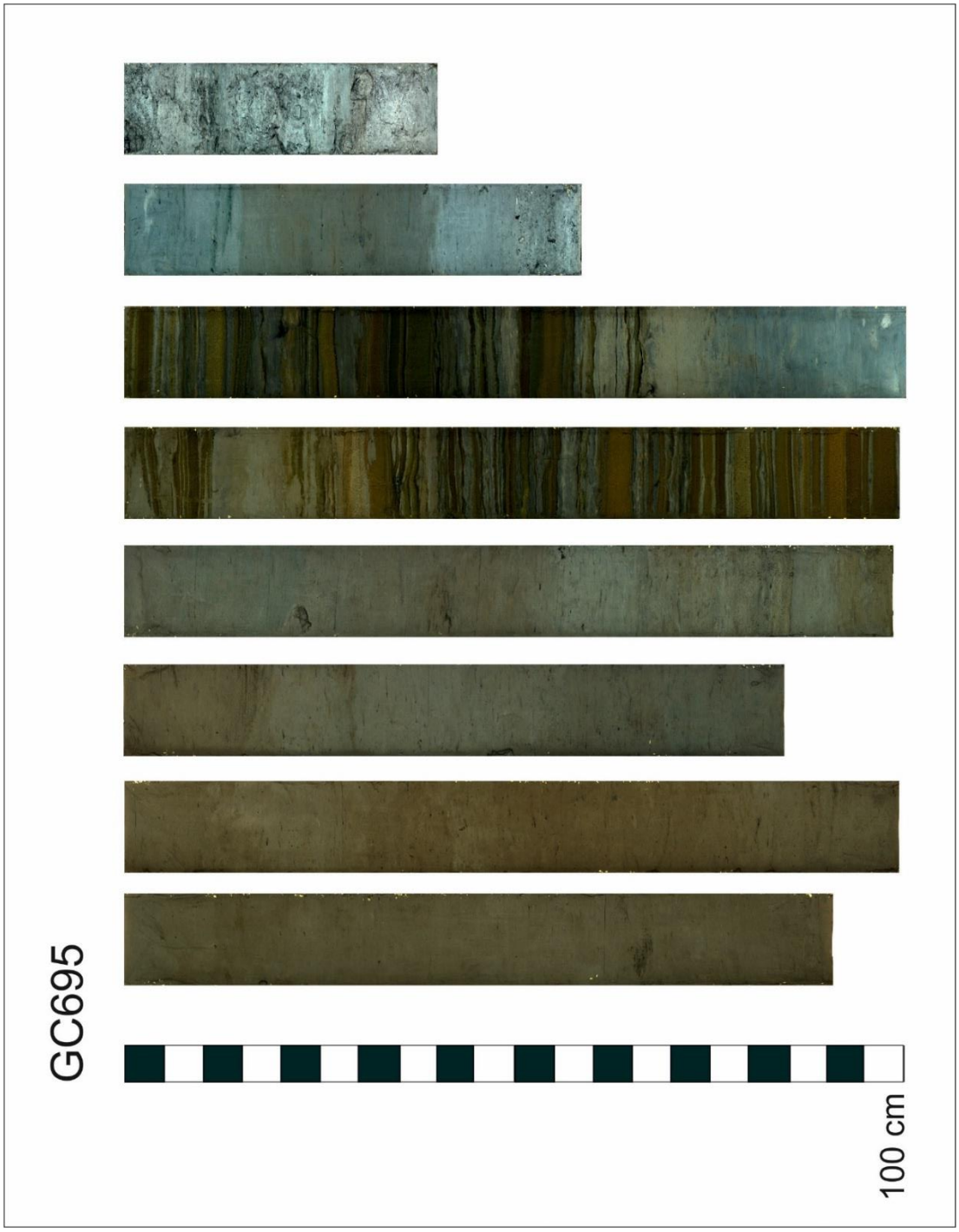
GC695
100 cm

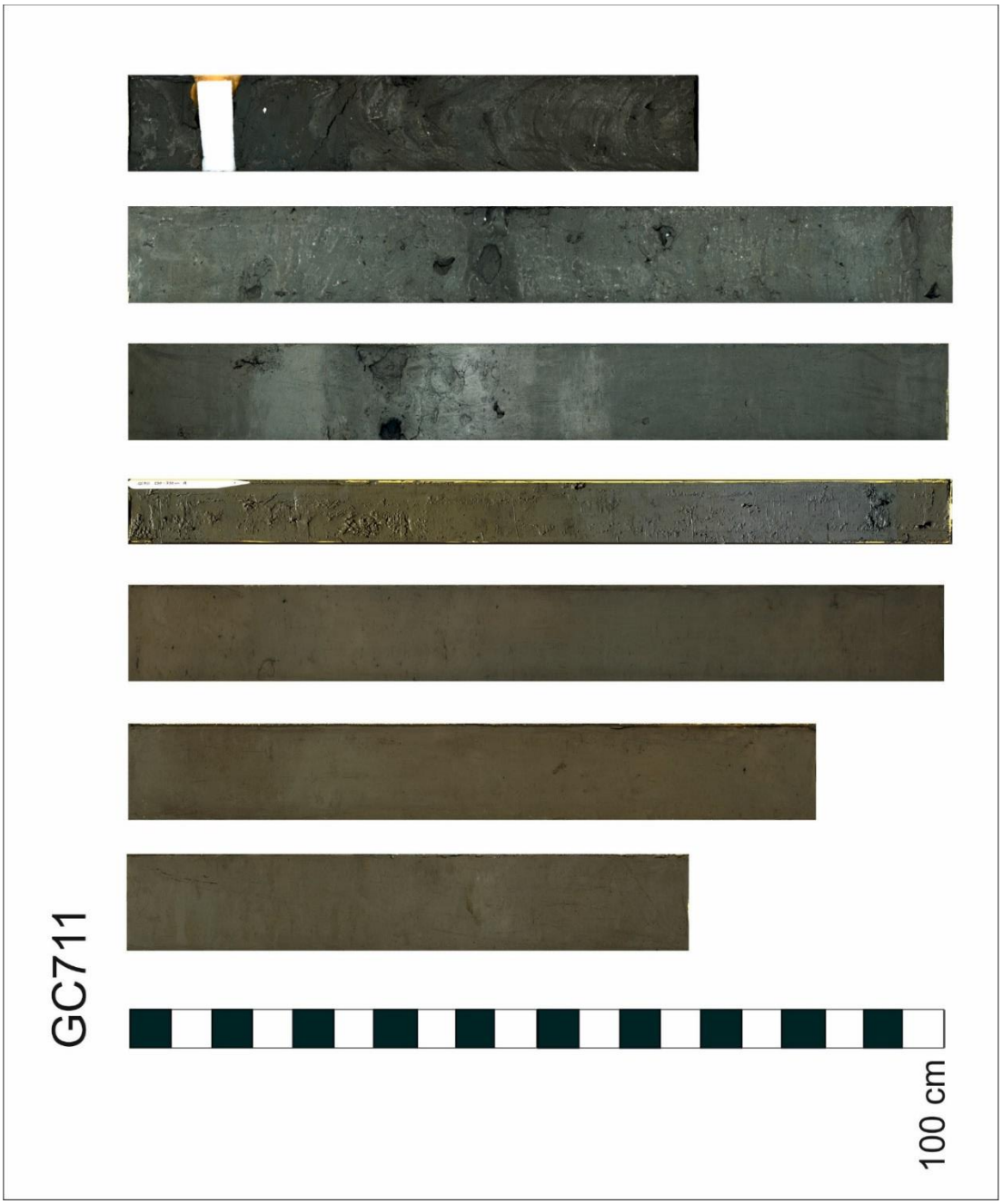
GC711
100 cm

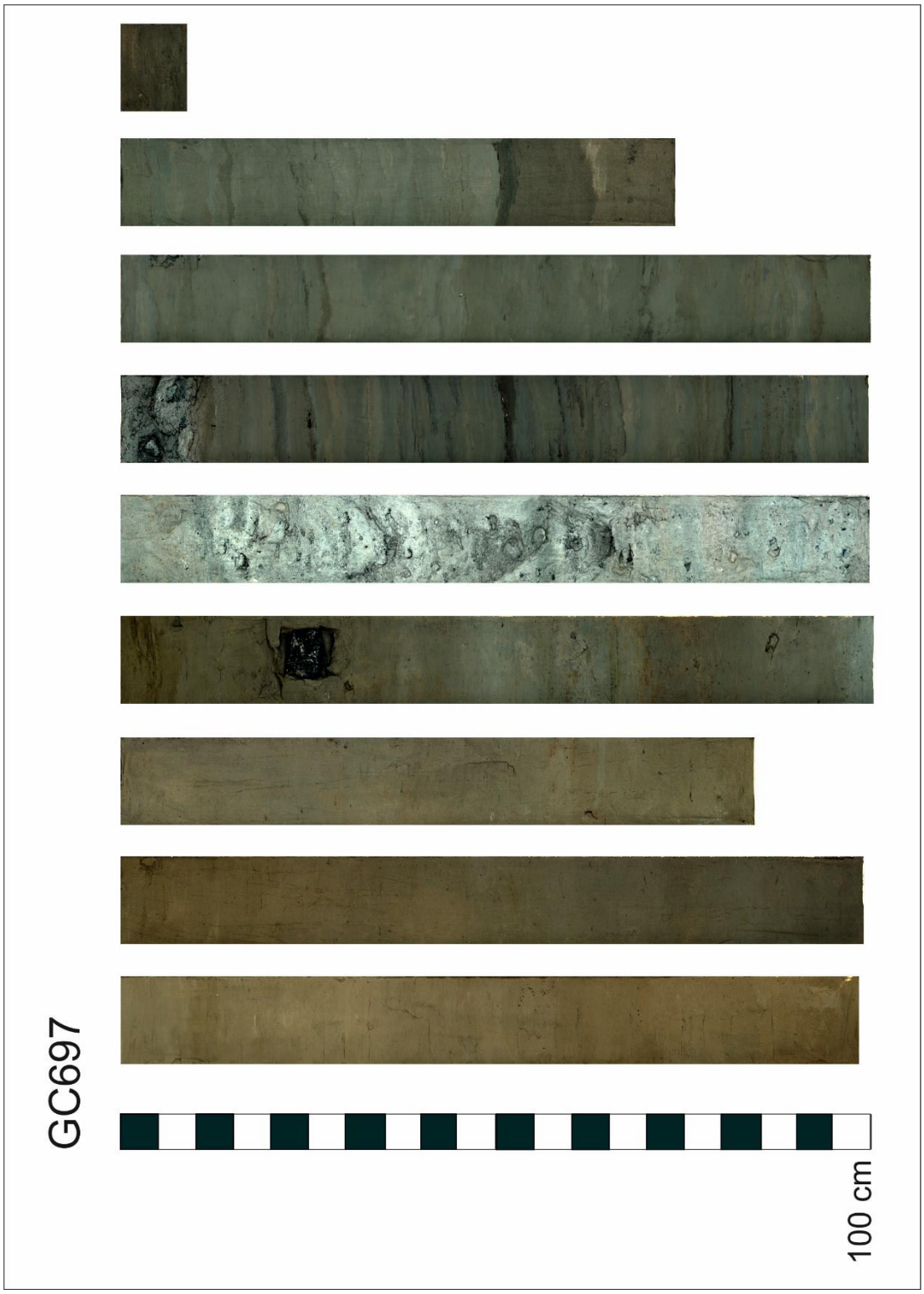
GC697
100 cm


GC709
100 cm

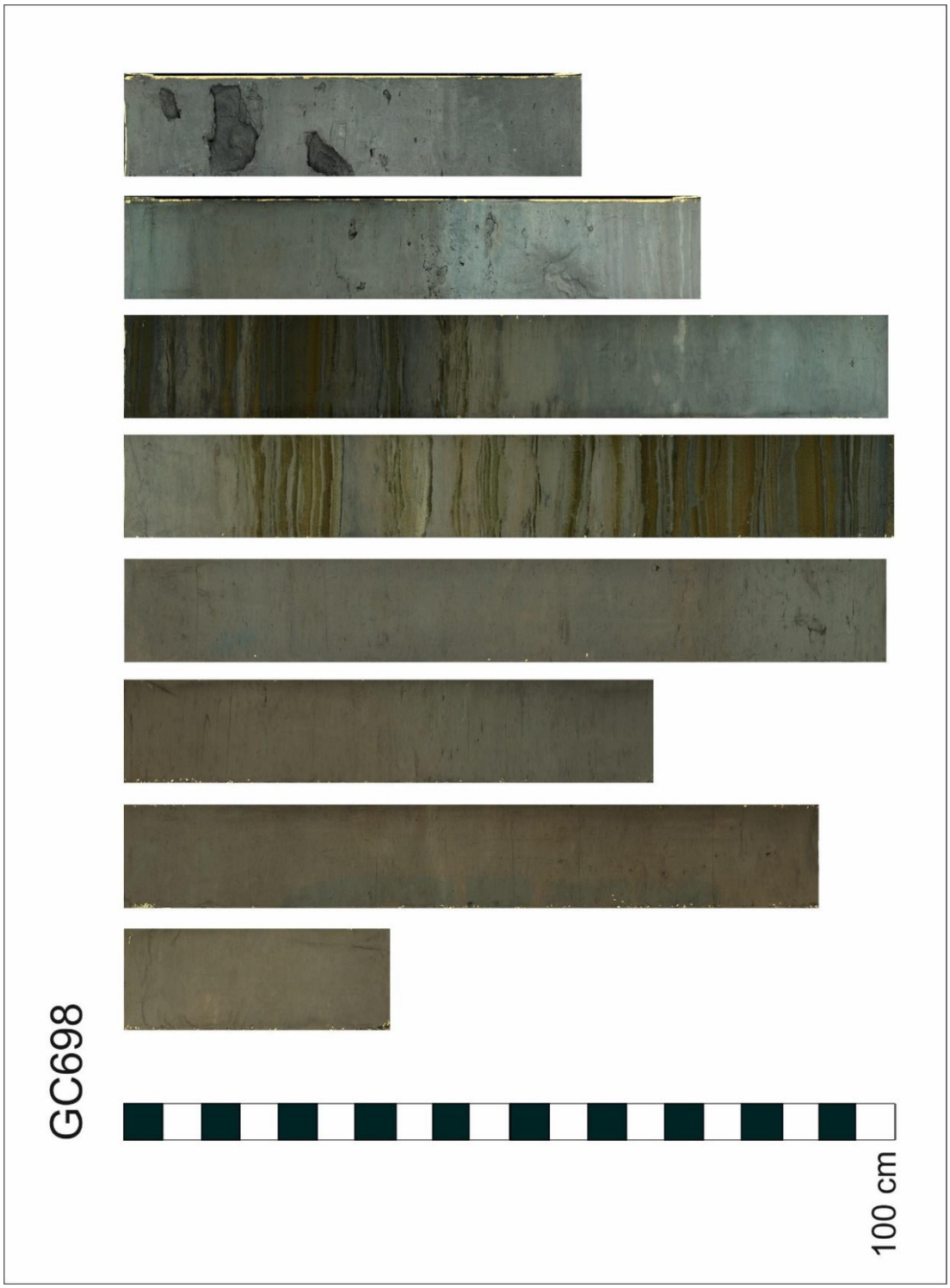
GC698
100 cm

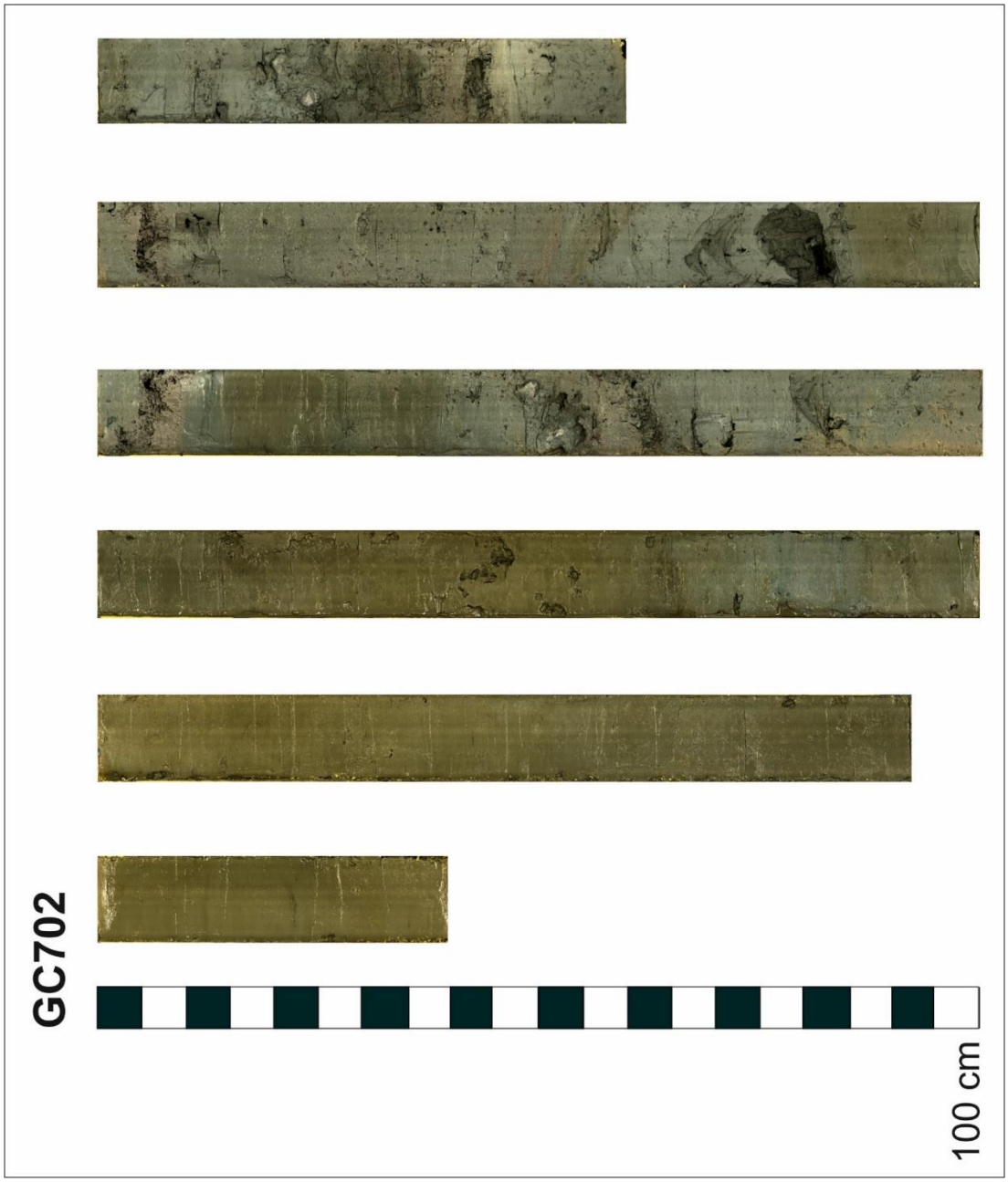
GC702
100 cm


GC703
100 cm

Appendix E: X-radiographs of transitional sediments within JR284 sediment cores

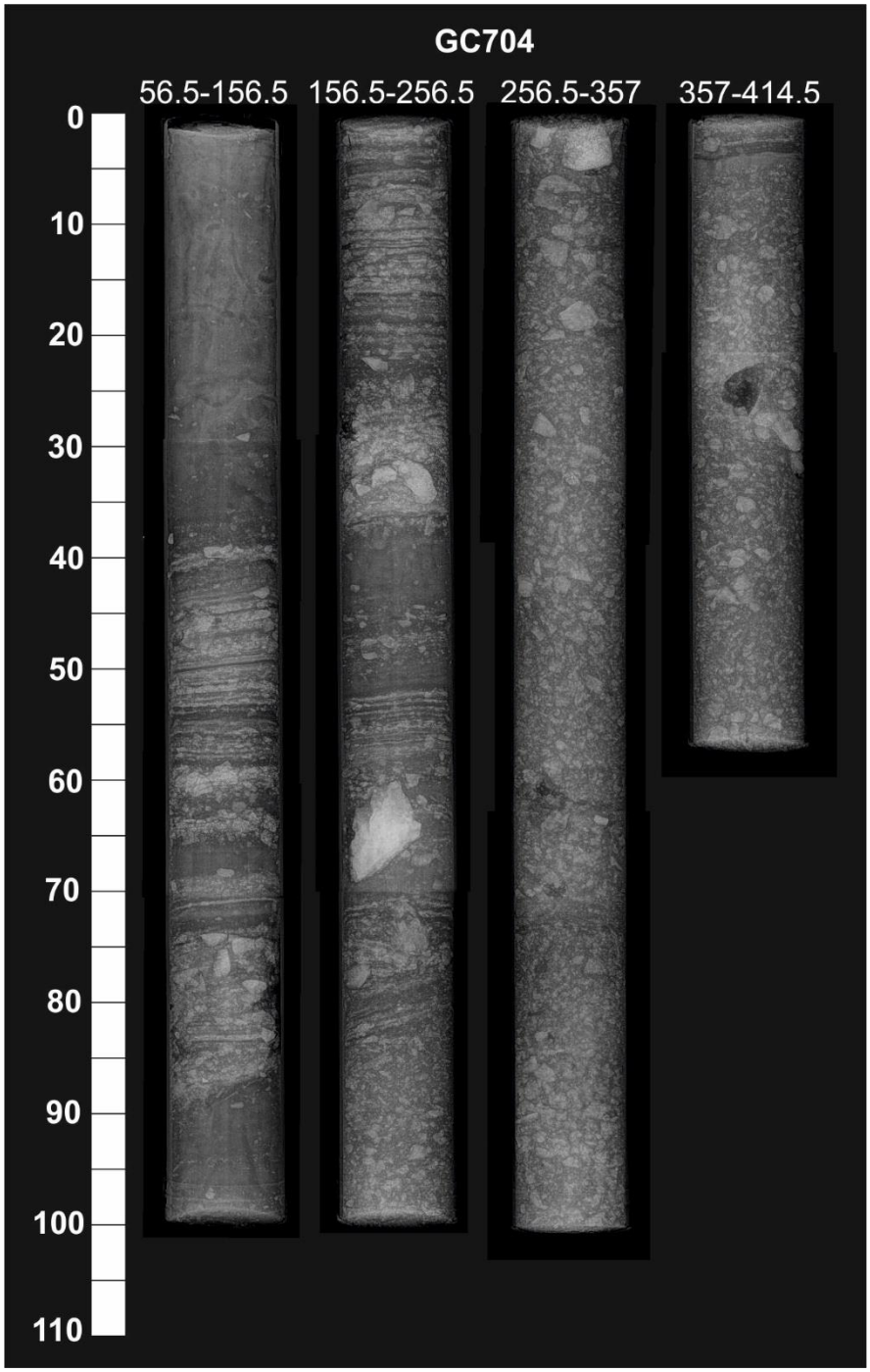

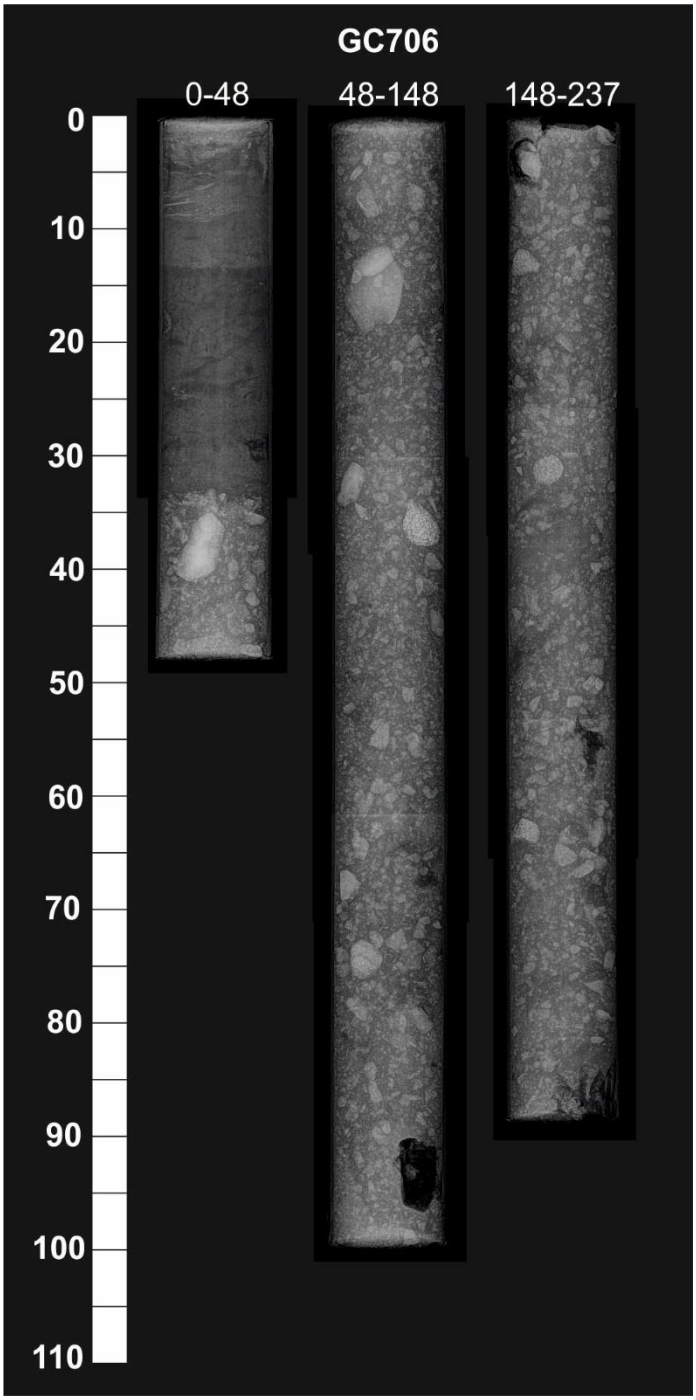
GC706
0-48
48-148
148-237
0
10
20
30
40
50
60
70
80
90
100
110

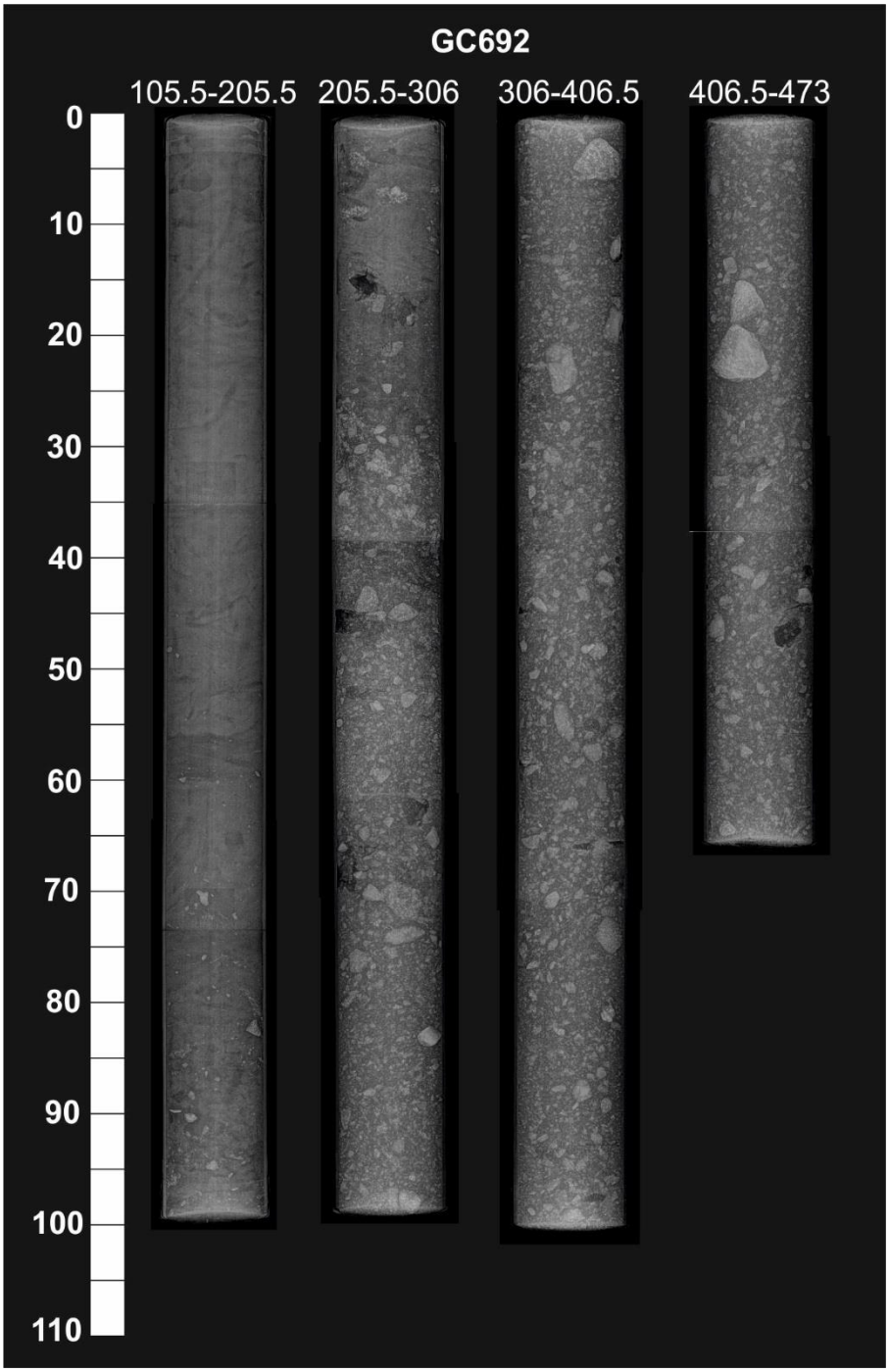
GC692
105.5-205.5
205.5-306
306-406.5
406.5-473
0
10
20
30
40
50
60
70
80
90
100
110

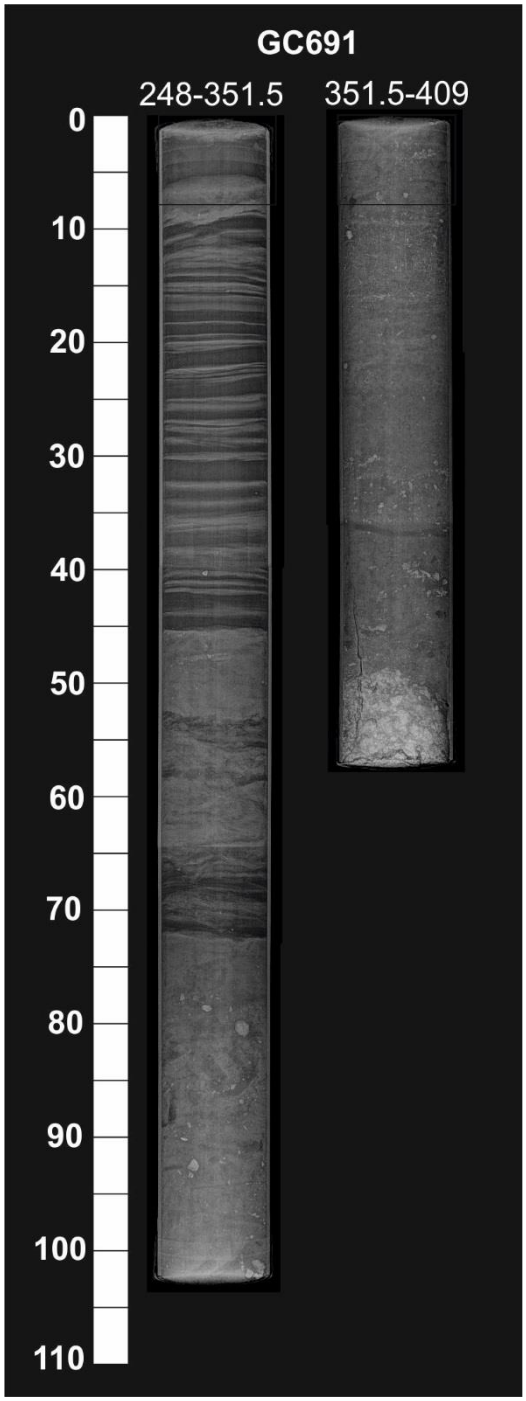
GC691
248-351.5
351.5-409
0
10
20
30
40
50
60
70
80
90
100
110

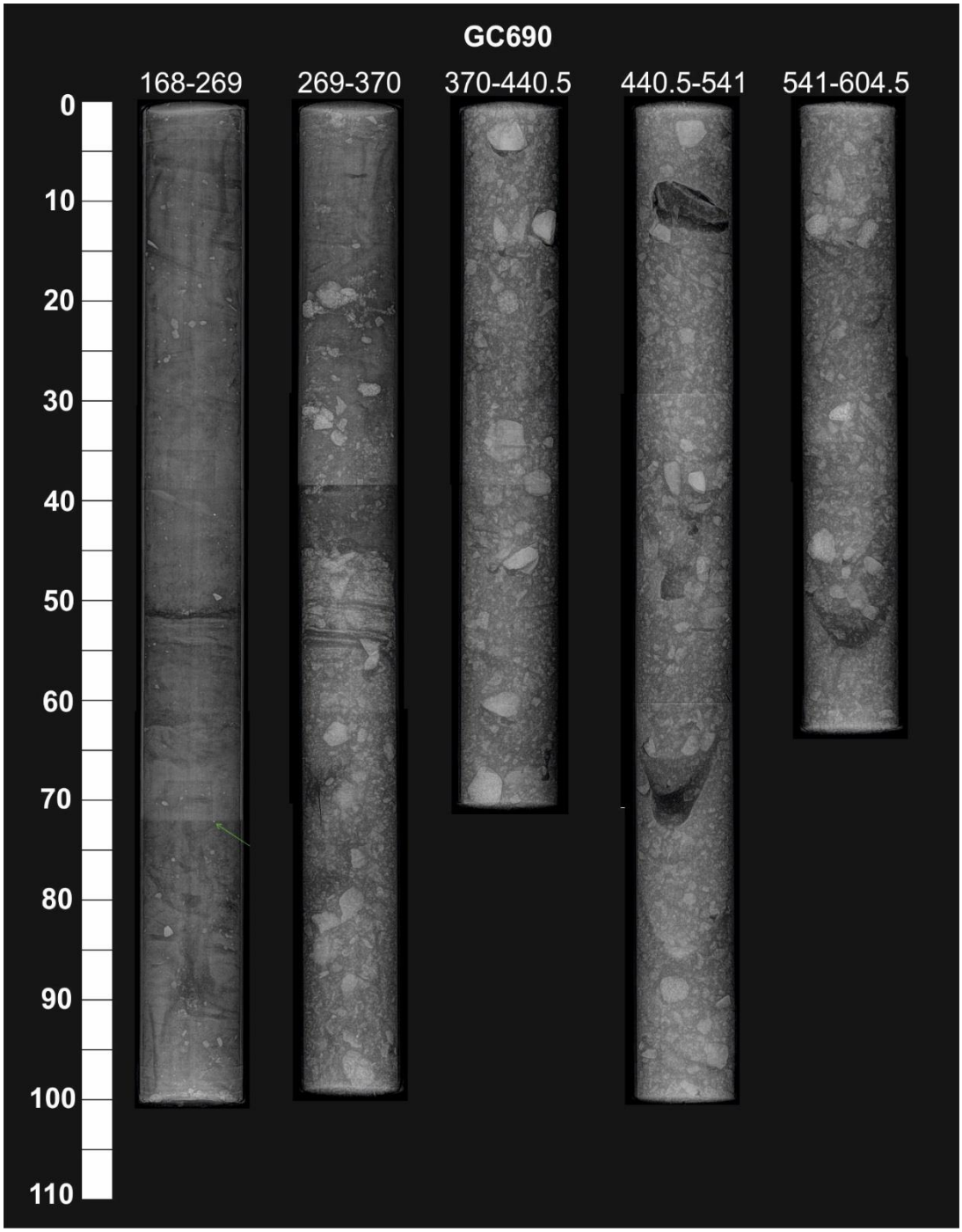
GC690
168-269
269-370
370-440.5
440.5-541
541-604.5
0
10
20
30
40
50
60
70
80
90
100
110

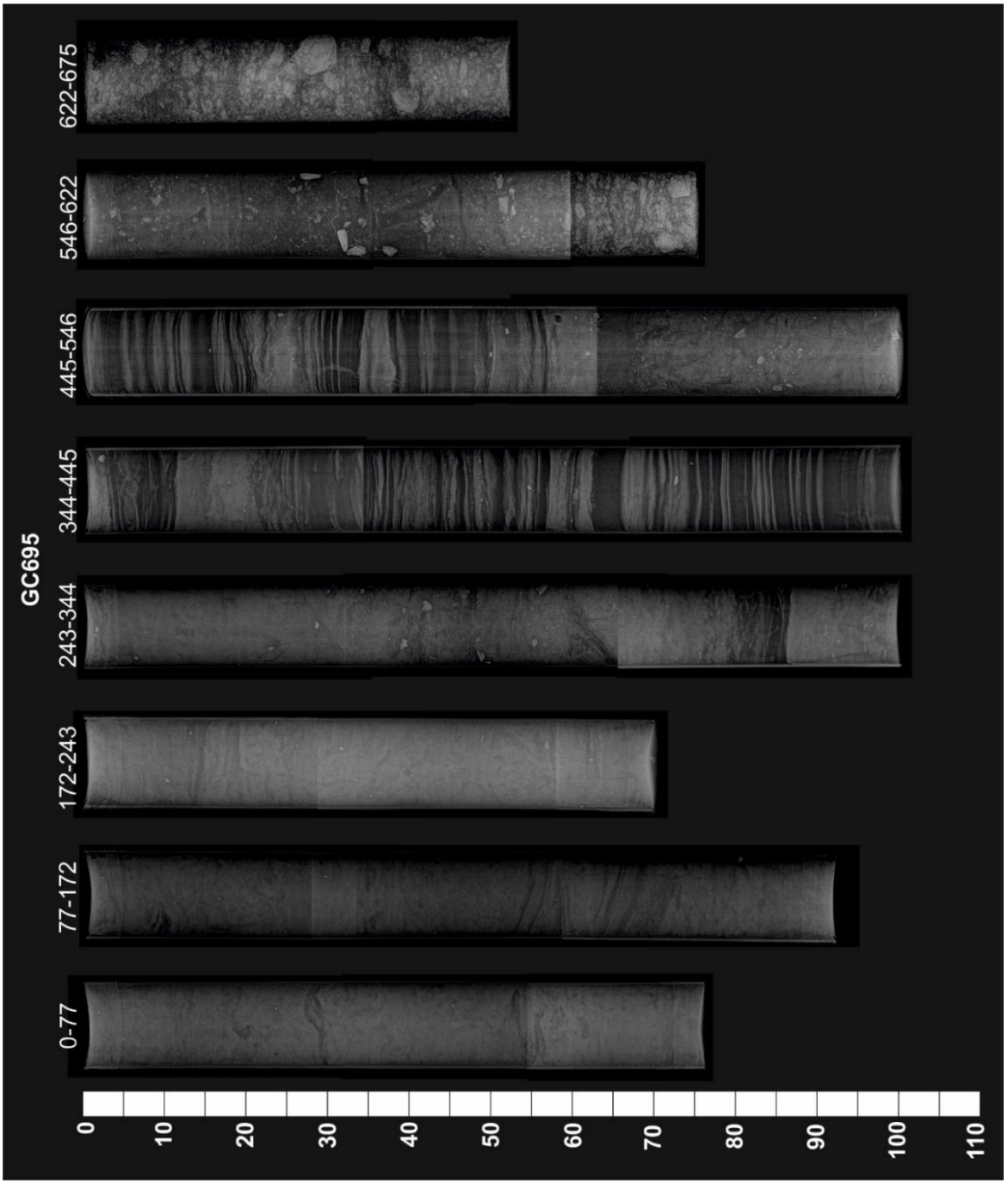
GC695
0-77
77-172
172-243
243-344
344-445
445-546
546-622
622-675
0
10
20
30
40
50
60
70
80
90
100
110

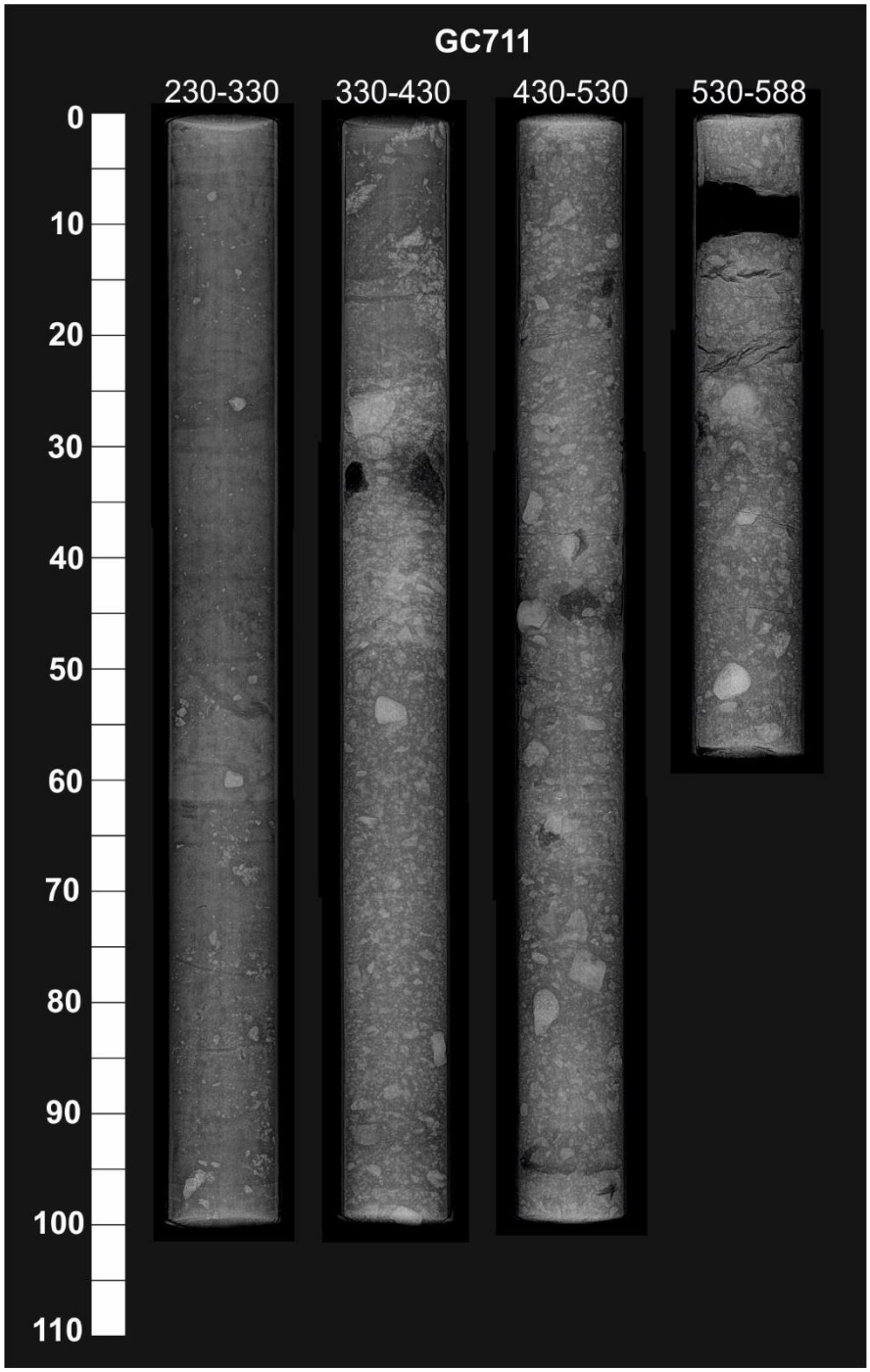
GC711
230-330
330-430
430-530
530-588
0
10
20
30
40
50
60
70
80
90
100
110

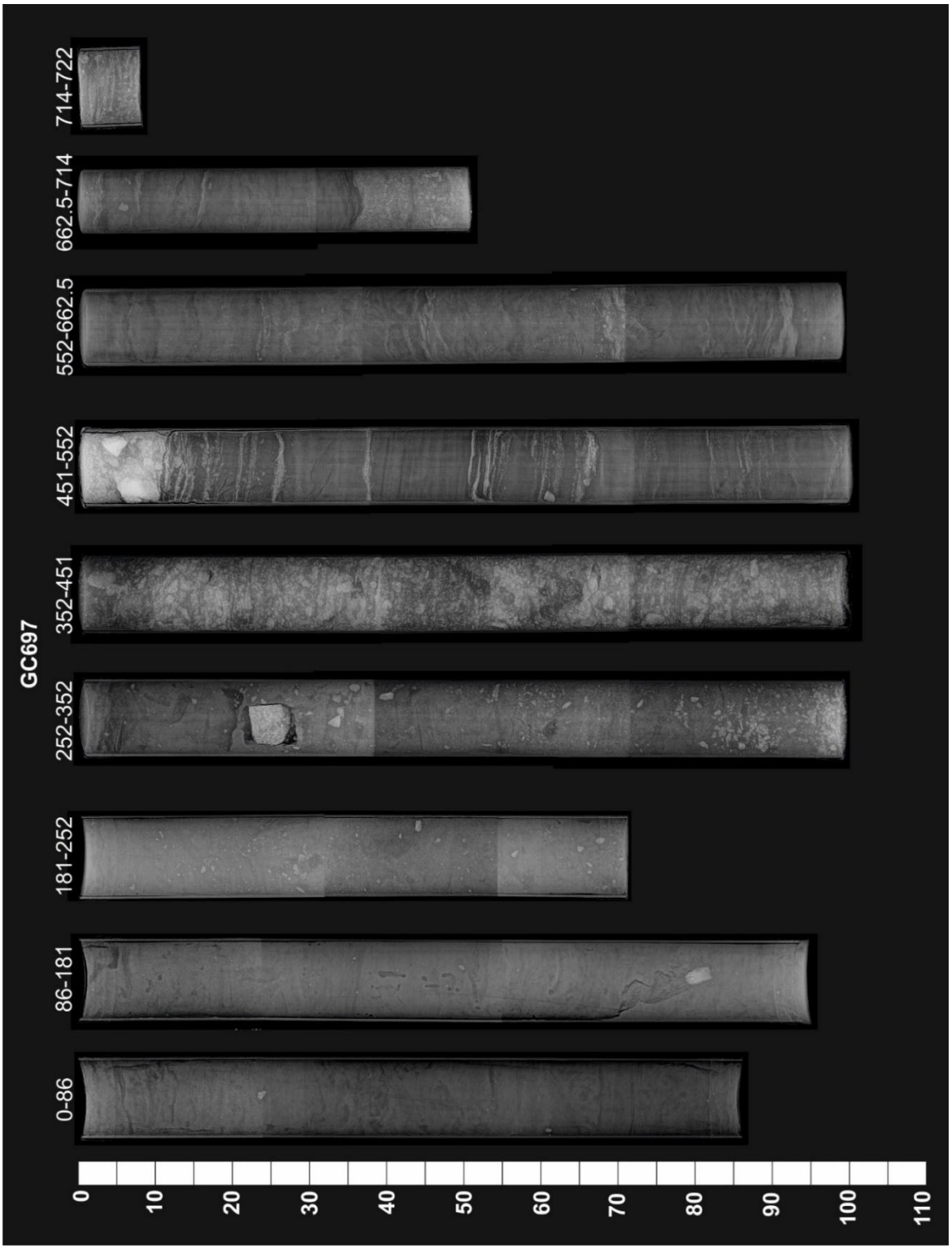
GC697
0-86
86-181
181-252
252-352
352-451
451-552
552-662.5
662.5-714
714-722
0
10
20
30
40
50
60
70
80
90
100
110

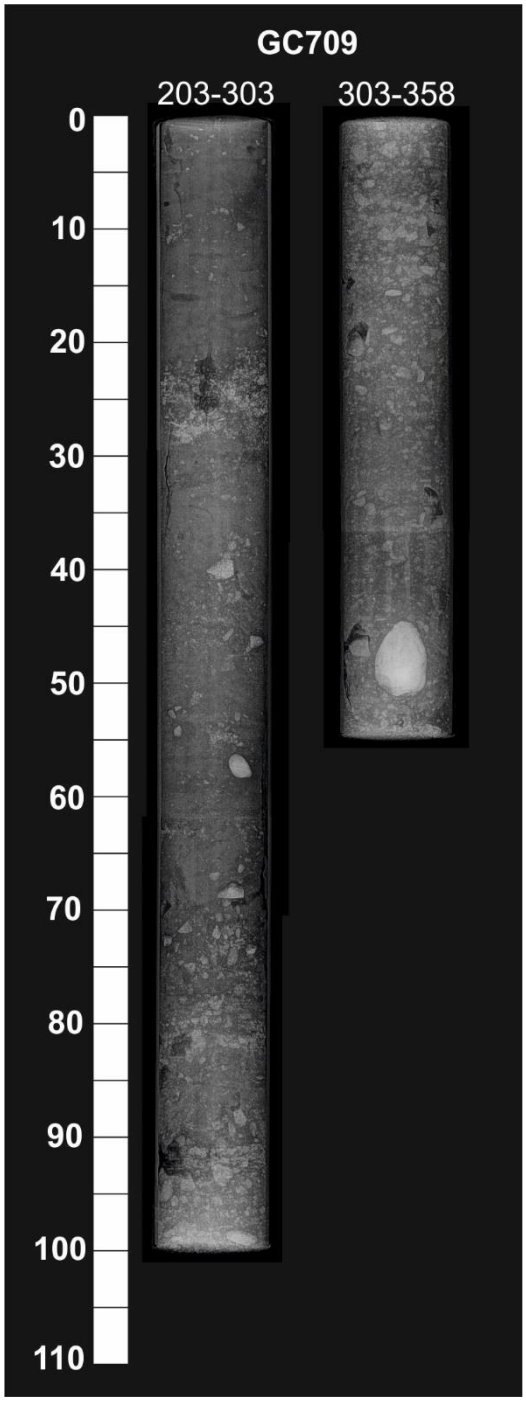
GC709
203-303
303-358
0
10
20
30
40
50
60
70
80
90
100
110

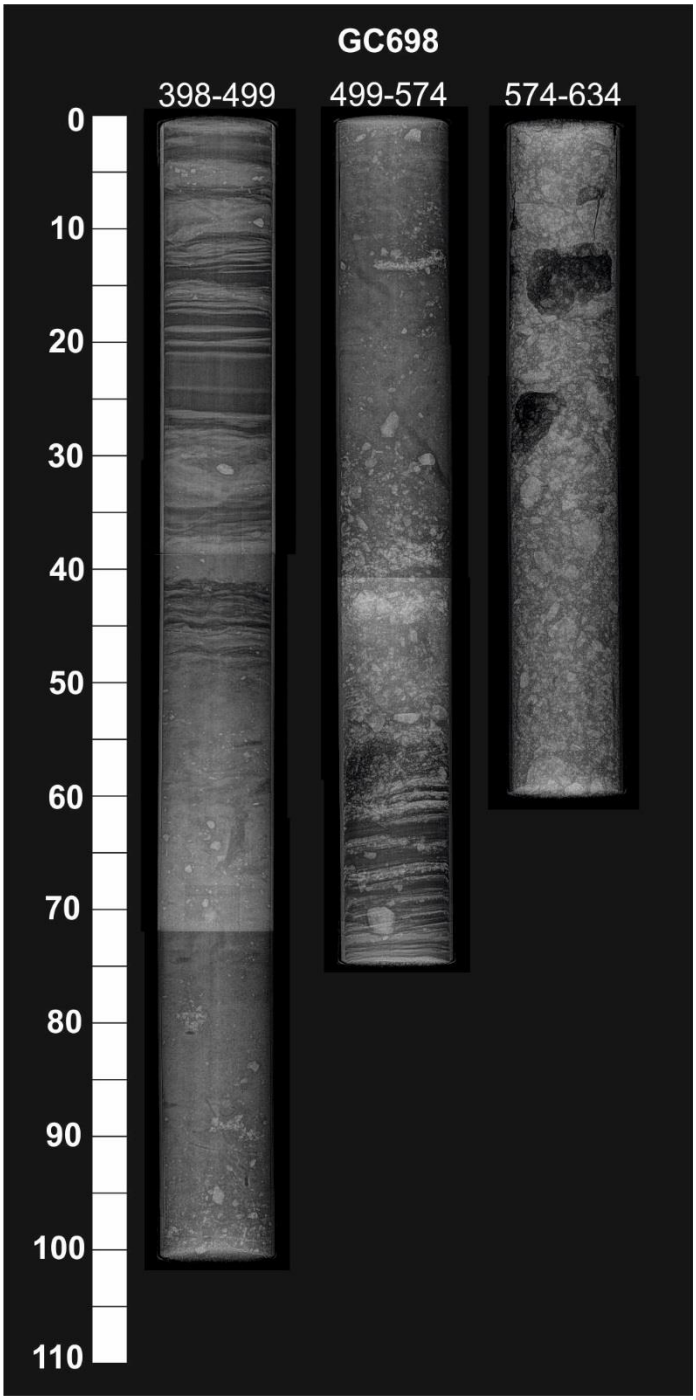
GC698
398-499
499-574
574-634
0
10
20
30
40
50
60
70
80
90
100
110

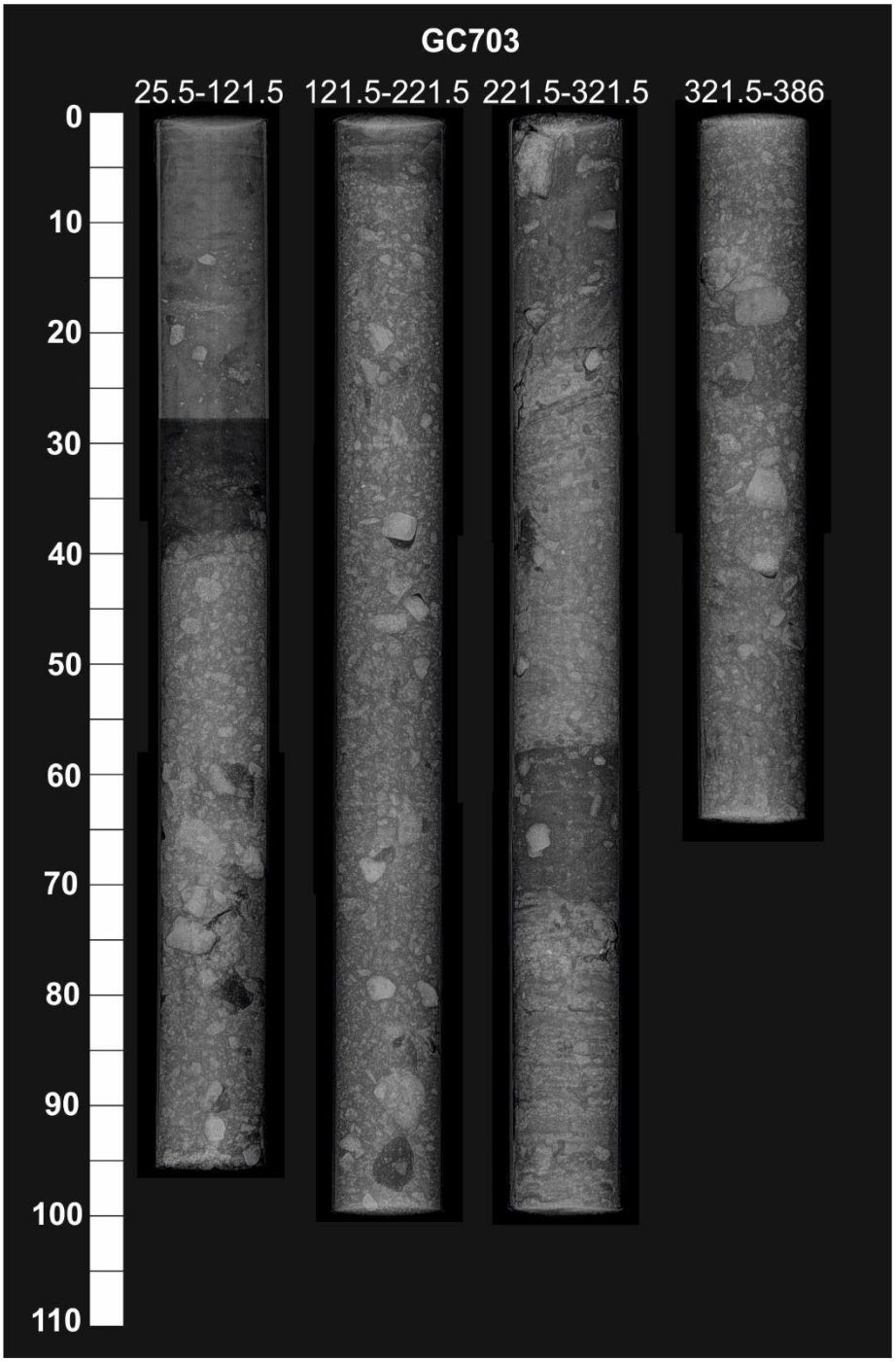
GC703
25.5-121.5
121.5-221.5
221.5-321.5
321.5-386
0
10
20
30
40
50
60
70
80
90
100
110

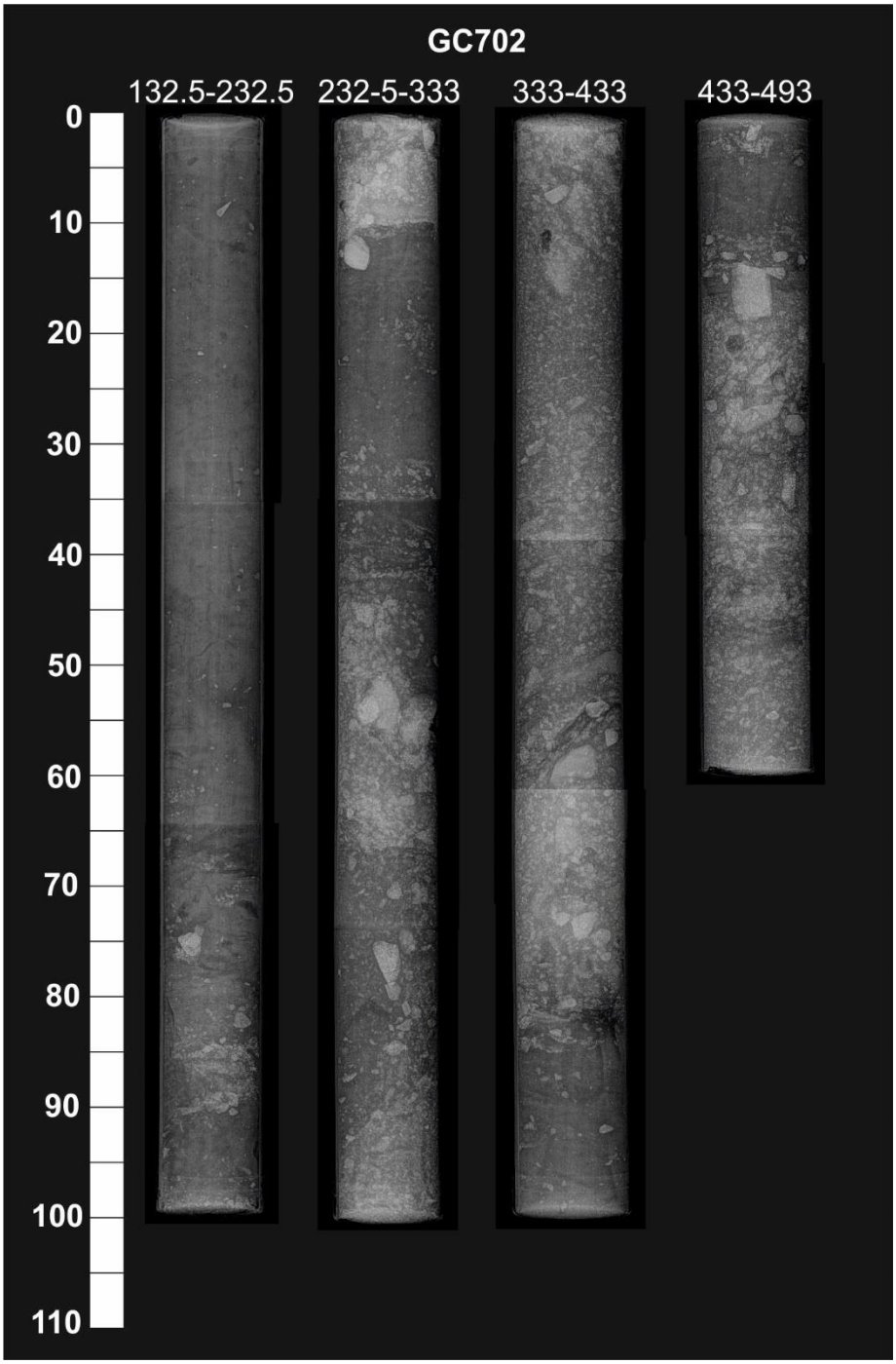
GC702
132.5-232.5
232-5-333
333-433
433-493
0
10
20
30
40
50
60
70
80
90
100
110

Appendix F

GC695 diatom counts, whole core, including *Chs*

Core	GC695	GC695	GC695	GC695	GC695	GC695	GC695	GC695	GC695	GC695	GC695	GC695	GC695	GC695	GC695	GC695	GC695	GC695	GC695	GC695	GC695	GC695	GC695	GC695	GC695	GC695	GC695	GC695	GC695	GC695
Depth	2	42	82	122	162	202	242	282	302	322	362	402	442	462	482	502	522	532	542	552	562	572	582	602	622	642	662			
	C	C	C	C	C	C	C	C	C	C	C	C	C	C	C	C	C	C	C	C	C	C	C	C	C	C	C	C	C	C
TAXA	#	#	#	#	#	#	#	#	#	#	#	#	#	#	#	#	#	#	#	#	#	#	#	#	#	#	#	#	#	#
Actinocyclus actinochilus		3	10	9	2	3	1	2		1	1						1	19	17	34	23	10	6	6	1	3				
Asteromphalus spp.		1	1				1				1								1	2	1	1					1			
Chaetoceros-Hyalochaete (total)		239	314	291	353	238	264	365	380	381	405	409	422	413	403	411	394	298	180	124	210	418	336	30	9	65	14			
Cocconeis spp.			1			1	1		2	1																				
Corethron pennatum		10	2	2	1	2	1	1	2		8	1		2			1	1	2	3	2									
Coscinodiscus spp.		1																												
Eucampia Sym Pointy					1	1																								
Eucampia Sym Flat		2	1	8	3	22	10	6			2							2	2	3						2	2			
Eucampia Asym Pointy						1																								
Eucampia Asym Flat						6																								
Eucampia General		1	6	10	3	50	24	5			1				1				2	5	1		2	2	1	7	9			
Fragilariopsis curta		32	14	3	5	7	7	6	2	8	10	3	2		4	1	7	24	41	48	36	6	12	3	1	2				
Fragilariopsis cylindrus		1	2					2	1		1			1		1		5	5	3		1	3							
Fragilariopsis kerguelensis		42	29	35	12	35	32	12	8	6	1	3			2			1	21	49	89	65	15	4	27	3	21	17		
Fragilariopsis obliquecostata			2	4	1	1	2	1																	1		1			
Fragilariopsis peragallii																			5	3		3		5						
Fragilariopsis rhombica		1	2	5	2	1	2		1	1	1				1			2	1	3	2					1				
Fragilariopsis ritscheri		3	2	5	2	5	6		2	2		1					1	4	3	8	4	3	1	1		1				
Fragilariopsis separanda		3		2		2												1		1						1	1			
Fragilariopsis sublinearis					2		1			1	1							1	1	4	2			1						
Fragilariopsis vanheurckii		1		2		1			1	2							3	5	24	21	4	1	2							
Navicula spp.		1				1		1									1	1		2	1									
Nitzschia spp.			1														1													
Odontella weissflogii		6	4	3		4	4	1	3	2	1							2		4							3			
Porosira glacialis		1	1		1	2	1	1				2					1	2		1	2		1							
Proboscia spp.			3	4		1	3		1					1					1											
Rhizosolenia spp.		5	24	11	4	13	40	8	5	1		1						5				1		5	1	1	3			
Stellarima microtrias (rs and veg)			2	3	1	4	2										4	1	3	2			1		1					
Thalassiosira antarctica warm		6	5	16	3	17	12	23	9	7	4	1	2			3	5	3	43	38	21	48	26	16	3	2	14	3		
Thalassiosira antarctica cold		12	1			3		2										1	1	7	6	2	2	2	2		2	1		
Thalassiosira gracilis var. expecta		6	2					1		1	1									3	4	1	2			1				
Thalassiosira gracilis var. nominate			11	6	6	8	3	2		2	4	1								6	1	4		1	7		2			
Thalassiosira lentiginosa		6	4	14		7	6	1				1						3		5	4	6	1		2	1	4	4		
Thalassiosira oliverana						1															1									
Thalassiosira ritscheri																					1	2								
Thalassiosira tumida		2	1	3	1	3	4	3				2					1			7	5	1	3			3	1			
Thalassiothrix/Trichotoxon			3				3	1			0.5								0.5	1.5				1						
Unidentified centrics						2		1												1		2								
Unidentified pennates			3																											
Thalassiosira antarctica vegetative												1							1		7									
Thalassiosira scotia		6	4	7	3	4	5	4	3	6	6	2	5		4	1		5	42	18	10	30	29	17	1	1	2	5		
Total diatoms counted		391	455	443	405	446	436	449	417	423	445.5	425	423	423	432	413	415	421	481.5	420.5	416	462	520	407	97	22	132	64		
Transects		0.62	0.45	1.39	0.15	1.09	1.11	1	0.37	0.5	0.29	0.2	0.1	0.06	0.15	0.027	0.05	0.23	4	1.43	8	4	1	1.073	10	10	10	10		
Weight (g)		0.02	0.0203	0.0202	0.0201	0.0204	0.0202	0.0203	0.0204	0.0196	0.0206	0.0202	0.0197	0.0201	0.0196	0.0197	0.02	0.0206	0.0197	0.997	0.0203	0.0205	0.0199	0.0196	1.001	1.006	0.996	0.995		
Total abundnace (mvpg)		105.8425	167.1891	52.99596	450.8924	67.32609	65.27056	74.243	185.4425	144.8837	250.3155	353.1122	720.7412	1177.33	493.2211	2606.305	1393.007	298.2581	20.51045	0.990011	8.598298	18.91182	87.71128	64.95967	0.032527	0.007341	0.044486	0.02159		
Total Chaetoceros		239	314	291	353	238	264	365	380	381	401	405	409	422	413	403	411	394	298	180	124	210	418	336	30	9	65	14		
RS/veg		0.071749	0.009646	0.028269	0.06006	0.067265	0.035294	0.00551	0.016043	0.005277	0.09863	0.046512	0.132964	0.674603	0.00978	0.759825	0.164306	0.088398	0.003367	0.005587	0.00813	0.039604	0.060914	0.05	0.111111	0	0.015625	0		

GC695 diatom counts, whole core, excluding *Chs*

Core	GC695	GC695	GC695	GC695	GC695	GC695	GC695	GC695	GC695	GC695	GC695	GC695	GC695	GC695	GC695	GC695	GC695	GC695	GC695	GC695	GC695	GC695	GC695	GC695	GC695	GC695
Depth	2	42	82	122	162	202	242	282	302	322	362	402	442	462	482	502	522	532	542	552	562	572	582	622	642	662
	CF	CF	CF	CF	CF	CF	CF	CF	CF	CF	CF	CF	CF	CF	CF	CF	CF	CF	CF	CF	CF	CF	CF	CF	CF	CF
TAXA	#	#	#	#	#	#	#	#	#	#	#	#	#	#	#	#	#	#	#	#	#	#	#	#	#	#
Actinocyclus actinochilus	20	24	24	7	6	5	5	25	12	8	5	2	1	17	5	1	17	32	29	37	37	21	23	1	3	
Asteromphalus spp.	2	2	1	1	1	1					1		1						1	2	1	2				1
Cocconeis spp.	3	5	2	1	3	2	1	2	4	3	2					1	1		1							
Corethron pennatum	21	4	9	4	2	2	4	15	13	81	24	8	24	29	33	11	17	3	4	3	4	1	3			
Coscinodiscus spp.	1																									
Diploneis spp.			1																							
Eucampia Sym Pointy				1	2	4	2	1															1			
Eucampia Sym Flat	2	3	19	18	39	32	18	19	10	7	1	6	7	4	2	8	1	2	3	3		2			2	2
Eucampia Asym Pointy					1	1																				
Eucampia Asym Flat				8	7	2	2																			
Eucampia General	6	20	21	25	84	54	23	8	7	7	1	3	9	16	4	15	6	2	5	5	4	2	4	1	7	9
Fragilariopsis curta	73	87	59	68	34	20	22	38	48	77	52	73	109	118	125	56	84	51	69	62	64	40	56	1	2	
Fragilariopsis cylindrus	3	5	1	2			2	4	1	6		6	17	13	16	2	8	5	11	5	1	1	6			
Fragilariopsis kerguelensis	109	134	150	137	105	102	94	38	43	23	75	3	41	66	5	45	28	47	93	89	98	68	45	3	21	17
Fragilariopsis obliquecostata	3	7	9	2	1	3	3	2	1		2		3	9	2		4	2			1		6		1	
Fragilariopsis peragallii	1	1	1																7	3		4	1			
Fragilariopsis rhombica	5	12	6	8	2	3	2	2	9	7	9		25	5	5	3	2	3	2	3	3	2	3		1	
Fragilariopsis ritscheri	10	14	12	9	7	15	2	7	4	8	12	8	4	11	9	6	9	5	6	8	4	5	8		1	
Fragilariopsis separanda	5	7	11	9	5	1					2		1	1	1	1		2		1					1	1
Fragilariopsis sublinearis		1	1	2		1	1	1	1	3	1	4	7	1	13	5	2	2	1	5	4		2			
Fragilariopsis vanheurckii	6	4	5	1	1	1	1	4	5	12	17		10	8	10	9	7	7	32	29	9	7	13			
Navicula spp.	1	3		2	1	2	1		6	2	3		4	5		1	5	1	1	3	1					
Nitzschia spp.		1							2		2	7	71	3	7	2	7									
Odontella weissflogii	17	7	8	4	7	11	12	6	13	11	4	1		7	1	3	2	4	3	4	1	4				3
Pleurosigma sp.																							1			
Porosira glacialis	2	3	1	2	3	1	3	2	6	4	5	9		7	14	4	1	4		1	2		2			
Porosira pseudodenticulata	1												1	1	3		1									
Proboscia spp.	2	6	7		2	5		5	11	11	9		1	1	6		3		2				4			
Rhizosolenia spp.	26	67	31	24	25	85	29	32	40	8	10	1	2	12	3	15	14	3	6		1	5	6	1	1	3
Stellarima microtrias (rs and veg)	3	10	11	3	6	3	1	1	3		2				2	1		4	2	3	3	1	3	1		
Synedra/Synedropsis spp.				1			2	1		3	1			1	1											
Thalassiosira antarctica warm	30	24	49	21	31	47	102	117	110	74	89	126	24	58	76	133	119	106	61	24	73	95	107	2	14	3
Thalassiosira antarctica cold	22	11	12	6	6	1	5	3	1	1		2		6	5	3	3	6	12	6	4	5	11		2	1
Thalassiosira gracilis var. expecta	14	7	2	2		2	4		2	10	1		1	2	2	1			4	4	2	3		1		
Thalassiosira gracilis var. nominate	8	34	18	15	11	13	6	6	7	15	2		1	6			2	1	8	2	6	7	5		2	
Thalassiosira lentiginosa	12	22	34	16	18	18	5	2	6	4	6		1	5	2		1	5	7	5	8	5	4	1	4	4
Thalassiosira oliverana	1		1		1															1						
Thalassiosira ritscheri																				1	2					
Thalassiosira tumida	3	3	5	6	4	12	14	6	5	7	6	3	1	11		6	4			7	10	2	7		3	1
Thalassiothrix/Trichotoxon	1		1		0.5	6	1.5		3.5	2	2.5	3.5	3.5	0.5	1	3	1	1.5	1.5	1		1.5	1.5			
Unidentified centrics	1				2	1	2								8	1	4	1	2		2	6	2			
Thalassiosira antarctica vegetative			1					2	7	11	17	77	27	6	47	22	6	2	2		7	1				
Thalassiosira scotia	21	14	16	17	13	9	30	59	33	42	39	74	16	51	70	75	84	87	31	12	52	111	82	1	2	5
Chaetoceros bulbosea										2			22		1											
Pseudogomphonema kamtschaticum													1		2		4	1								
Total diatoms counted	435	542	529	422	430.5	465	399.5	408	413.5	449	402.5	416.5	435.5	480.5	481	433	447	389.5	406.5	330	404	401.5	406.5	22	132	64

GC695 diatom counts, laminated diatomaceous ooze (420-440 cm), including *Chs*

Core	GC695	GC695	GC695	GC695	GC695	GC695	GC695	GC695	GC695	GC695	GC695	GC695	GC695	GC695	GC695	GC695	GC695	GC695	GC695	GC695	GC695	GC695	GC695
Depth	420.7	421.7	423.7	425.2	425.8	426.4	426.8	427.1	427.8	427.9	428.1	428.8	430	430.4	431.1	431.8	432.5	433.1	433.7	434.6	436.9	438.4	
U-channel sample	1	2	3	4	5	6	7	8	10	9	11	12	13	14	15	16	17	18	19	20	21	22	
	C	C	C	C	C	C	C	C	C	C	C	C	C	C	C	C	C	C	C	C	C	C	
TAXA	#	#	#	#	#	#	#	#	#	#	#	#	#	#	#	#	#	#	#	#	#	#	
Actinocyclus actinochilus		1					2													1	1		
Chaetoceros-Hyalochaete (total)	430	358	412	405	401	374	401	439	429	412	406	416	418	424	485	411	418	436	403	406	408	419	
Corethron pennatum	1	2	10	1			16		1			1	1			1		1		1	1		
Eucampia Sym Flat											1												
Eucampia General			6				3			2											1		
Fragilariopsis curta	1	15			5	4	13	1	4		4	2	3	6	9	5		5	4	2	1		
Fragilariopsis cylindrus		3		1		1	1			2			3		1					2		2	
Fragilariopsis kerguelensis		1			2		9					1		2		1			2	1			
Fragilariopsis rhombica					1		2			1						2		1					
Fragilariopsis ritscheri							1																
Fragilariopsis sublinearis			1				1																
Fragilariopsis vanheurckii					1	1	2					1									2	1	
Navicula spp.		1		1	1		1									1	1		1				
Odontella weissflogii							2			1													
Porosira glacialis							1						1					1					
Porosira pseudodenticulata		1																					
Proboscia spp.							2																
Rhizosolenia spp.		1					3								1								
Synedra/Synedropsis spp.																	1						
Thalassiosira antarctica warm		4	1		1	15	19			1				1		2	3	1		1			
Thalassiosira antarctica cold				2																			
Thalassiosira gracilis var. expecta															1								
Thalassiosira lentiginosa		1									1												
Thalassiosira ritscheri			1																				
Thalassiosira tumida		3																					
Thalassiothrix/Trichotoxon		3					0.5																
Unidentified pennates		3																					
Thalassiosira antarctica vegetative						7	7	1	1					1									
Thalassiosira scotia		5				10	3									3	2						
Total diatoms counted	432	402	430	411	412	412	489.5	441	435	419	412	421	426	434	497	426	425	445	410	414	414	422	
Transects	0.07	0.38	0.09	0.06	0.11	0.2	2	0.05	0.045	0.041	0.055	0.032	0.036	0.027	0.15	0.2	0.09	0.12	0.045	0.073	0.041	0.018	
Weight (g)	0.02	0.0202	0.02	0.02	0.0203	0.0204	0.02	0.0199	0.02	0.0199	0.0199	0.0203	0.0188	0.0203	0.0199	0.02	0.0204	0.0198	0.0197	0.02	0.0201	0.0199	
Total abundnace (mvpg)	1035.764	175.7909	801.8648	1149.65	619.318	338.9552	41.07692	1487.718	1622.378	1723.782	1263.533	2175.411	2112.781	2657.879	558.8783	357.4825	777.0008	628.6643	1552.424	951.8153	1686.264	3954.504	
Total Chaetoceros	430	358	412	405	401	374	401	439	429	412	406	416	418	424	485	411	418	436	403	406	408	419	
RS/veg	0.181319	0.278571	1.145833	0.483516	0.21148	0.053521	0.162319	0.100251	1.958621	0.731092	0.166667	0.454545	0.801724	0.039216	1.771429	0.338762	1.223404	0.224719	0.47619	0.140449	1.55	2.774775	

GC695 diatom counts, laminated diatomaceous ooze (420-440 cm), excluding Chs

Core	GC695	GC695	GC695	GC695	GC695	GC695	GC695	GC695	GC695	GC695	GC695	GC695	GC695	GC695	GC695	GC695	GC695	GC695	GC695	GC695	GC695	GC695	GC695	GC695	GC695
Depth	420.7	421.7	423.7	425.2	421.7	426.4	426.8	427.1	427.8	427.9	428.1	428.8	430	430.4	431.1	431.8	432.5	433.1	433.7	434.6	436.9	438.4			
U-channel sample	1	2	3	4	5	6	7	8	10	9	11	12	13	14	15	16	17	18	19	20	21	22			
	CF	CF	CF	CF	CF	CF	CF	CF	CF	CF	CF	CF	CF	CF	CF	CF	CF	CF	CF	CF	CF	CF			
TAXA	#	#	#	#	#	#	#	#	#	#	#	#	#	#	#	#	#	#	#	#	#	#			
Achnanthes spp.																				1					
Actinocyclus actinochilus	8	19	8	6	7	8	18	9	5	11	22	7	3	14	8	10	4	12	12	18	8	20			
Asteromphalus spp.															1	1		2							
Azpeitia tabularis																		1							
Cocconeis spp.				1				1		3									1						
Corethron pennatum	20	39	248	105	24	10	71	109	22	24	24	46	44	18	142	81	99	13	23	27	163	37			
Coscinodiscus spp.					1									2			1								
Eucampia Sym Pointy	2													1											
Eucampia Sym Flat	8	1	2	3	4		2	1	2	1	5	7	19	5	2	4	1	9	1	4	4	11			
Eucampia General	37	1	5	5	5	2	8	2	11	9	31	45	3	9	6	7	9	6	15	16	30	36			
Fragilariopsis curta	115	208	85	91	222	74	114	121	209	208	196	188	203	181	157	84	85	121	191	151	119	117			
Fragilariopsis cylindrus	20	8	2	12	3	10	5	9	10	7	8	15	55	6	5	2	5	8	36	6	15	7			
Fragilariopsis kerguelensis	45	23	3	8	17	5	51	18	25	25	25	25		23	11	58	70	40	18	43	18	14			
Fragilariopsis obliquecostata	1									9		2	1	6	5	6	1	4							
Fragilariopsis peragallii																				1					
Fragilariopsis rhombica		1	5	3	4	2	14	19	5	2	9	2	2	5	3	10	13	16	1	4	3	2			
Fragilariopsis ritscheri	7	4	6	6	17	2	11	11	15	4	14	5	1	1		10	1	6	3	8	6	1			
Fragilariopsis separanda					1		2					1													
Fragilariopsis sublinearis	23	2	7	3	7	2	7	1	6	9	5	4	3	5	3	1	2	2	2	3	7	8			
Fragilariopsis vanheurckii	5	8	8	2	70	17	5	8	25	39	4	5	9	4	15	2	2	13	13	12	32	18			
Navicula spp.	3	11	4	9	5	9	3	3	3	3	2	1	3	4	2	2	4	5	7	2	1	2			
Nitzschia spp.										1			10												
Odontella weissflogii					4		4		1	8	1	3		7	1	2		4		3		1			
Paralia spp.			4																						
Porosira glacialis	12	11		43	5	12	4		5	4	9	6	5	9	6	6	2	7	2	13	6	20			
Porosira pseudodenticulata	4			15		2				1	6	3	1	2	1				1	5	1	1			
Proboscia spp.					7	3	5	37	2				14		4		4	3							
Pseudo-nitzschia turgiduloides															1										
Rhizosolenia spp.	1	1	1				4	4	1	1	3			4		6	1	1	1	2					
Stellarima microtrias (rs and veg)	1	1			1		1	1	2	1	1	3	3	2		2	1	2	1	4		1			
Synedra/Synedropsis spp.		3	1								2			1			2					1			
Thalassiosira antarctica warm	37	46	17	78	51	215	59	43	45	65	21	34	10	54	35	53	30	64	20	61	17	72			
Thalassiosira antarctica cold	3	29	5	10							6	4							22	22	6	21			
Thalassiosira gracilis var. expecta	1	1	4	1	1		2		1	2	4	2	1	4	1		2	1	4	2		3			
Thalassiosira gracilis var. nominate							3			3				1	2	3	1	1							
Thalassiosira lentiginosa	4	9	2	6			1	3	2	3	6	10	1	2	1	2	3	5	2	5		1			
Thalassiosira oliverana															1					1					
Thalassiosira ritscheri		14	2	3				1			3	4				11	2	13	2	5	1	1			
Thalassiosira tumida	5	14	18	7	1	1	2	3	6	1	24	13	2	12	3	13	5	10	7	10	7	5			
Thalassiothrix/Trichotoxon	1.5	3.5	1	4	1		3	2.5	2	0.5	2.5	1.5	1	0.5	1	2	3	2.5	1	6	0.5	3			
Unidentified centrics		1	1	1														1	1						
Unidentified pennates	2	4	2																						
Thalassiosira antarctica vegetative				3	15	22	13	2	9	11	3	1	19	14	1		4	3	1			9			
Thalassiosira scotia	36	29	7	66	20	97	16	9	8	25	36	16	6	23	20	40	52	58	11	12	7	20			
Chaetoceros dicheata																1	2			9					
Denticulopsis		1																							
Total diatoms counted	401.5	492.5	448	491	493	493	428	418.5	422	480.5	472.5	453.5	419	419.5	438	419	411	433.5	399	456	451.5	432			

GC697 diatom counts, including *Chs*

Core	GC697	GC697	GC697	GC697	GC697	GC697	GC697	GC697	GC697	GC697	GC697
Depth	203	243	255	259	265	270	283	303	323	343	363
	C	C	C	C	C	C	C	C	C	C	C
TAXA	#	#	#	#	#	#	#	#	#	#	#
Actinocyclus actinochilus							5	15	1	9	
Asteromphalus spp.								3	2		
Chaetoceros-Hyalochaete (total)	377	409	418	395	441	397	327	83	319	249	11
Cocconeis spp.	1						2	1	2	1	1
Corethron pennatum			4	1	1	1	1	1			
Eucampia Sym Pointy										1	
Eucampia Sym Flat	1				1			1		1	
Eucampia General	3							1	1		
Fragilariopsis curta	3		3	5	3	2	16	12	16	35	2
Fragilariopsis cylindrus			1			1	1	2	1		
Fragilariopsis kerguelensis	6	2				2	11	70	17	54	5
Fragilariopsis obliquecostata										1	
Fragilariopsis peragallii								1	1		
Fragilariopsis rhombica						1	1	1	2	6	
Fragilariopsis ritscheri						1		2	3	4	
Fragilariopsis vanheurckii	1					3		6	8	5	
Fragilariopsis spp.											
Navicula spp.							1	1		3	
Nitzschia spp.				2							
Odontella weissflogii	1						1	1	1		
Porosira glacialis						1			1	1	
Porosira pseudodenticulata								1			
Proboscia spp.							1		2	2	
Rhizosolenia spp.	1			1			2		2	11	
Stellarima microtrias (rs and veg)					1			1	2		
Synedra/Synedropsis spp.									1		
Thalassiosira antarctica warm	6	7		5	5	6	26	5	29	36	2
Thalassiosira antarctica cold							1			6	
Thalassiosira gracilis var. expecta									1	4	
Thalassiosira gracilis var. nominate							1	7		2	2
Thalassiosira lentiginosa	1							1		5	
Thalassiosira ritscheri					2						
Thalassiosira tumida	1			1				5	1	1	
Thalassiothrix/Trichotoxon	1	0.5					2	1	0.5	2.5	
Unidentified centrics									1	2	
Unidentified pennates								1		1	
Thalassiosira antarctica vegetative	1			1			4	1	1	2	
Thalassiosira scotia	5	1		1	6	4	22	8	11	18	
Total diatoms counted	409	420.5	426	412	460	419	426	232	426.5	462.5	23
Transects	0.514	0.11	0.11	0.31	0.2	0.281818	1.09	10	1	4	10
Weight (g)	0.0196	0.02	0.016	0.0175	0.0174	0.0175	0.0204	0.0203	0.0203	0.0197	0.1
Total abundnace (mvpg)	131.669	619.9017	812.4603	254.9193	443.6942	285.1755	64.30698	3.836164	70.52258	19.70111	0.077203
Total Chaetoceros	377	409	418	395	441	397	327	83	319	249	11
RS/veg	0.005333	0.108401	0.208092	0.005089	0.099751	0.064343	0.072131	0.064103	0.135231	0.214634	0

GC697 diatom counts, excluding *Chs*

Core	GC697	GC697	GC697	GC697	GC697	GC697	GC697	GC697	GC697	GC697
Depth	203	243	255	259	265	270	283	303	323	343
	CF	CF	CF	CF	CF	CF	CF	CF	CF	CF
TAXA	#	#	#	#	#	#	#	#	#	#
Achnanthes spp.			1							
Actinocyclus actinochilus	8	13	4	12	16	7	22	15	11	12
Chaetoceros - Hyalochaete (total)				2						
Chaetoceros - Phaeoceros			1							1
Cocconeis spp.	4	2			1		2	1	3	
Corethron pennatum	1	12	157	29	10	8	2	1	3	
Coscinodiscus spp.						2				
Diploneis spp.			1							
Eucampia Sym Pointy			2	2	1					1
Eucampia Sym Flat	19	1	2	3	4	1		1	2	2
Eucampia General	17	5	3	7	2	3	1	1	3	1
Fragilariopsis curta	46	66	116	112	84	74	66	12	108	57
Fragilariopsis cylindrus	4	2	3	4		3	4	2	4	2
Fragilariopsis kerguelensis	57	42	23	35	28	28	40	70	71	93
Fragilariopsis obliquecostata				3	4	1			3	4
Fragilariopsis peragallii							1	1	1	
Fragilariopsis rhombica	1	1	5	5	2	6	5	1	7	8
Fragilariopsis ritscheri	1	1	2	5	1	16	1	2	6	13
Fragilariopsis sublinearis	1	5	4	3	5	11	2		1	1
Fragilariopsis vanheurckii	8	6	10	11	8	41	13	6	17	13
Navicula spp.			4	2	1	2	2	1	5	3
Nitzschia spp.				8	2	2	1		1	
Odontella weissflogii	8	6	4	9	5	3	3	1	8	
Porosira glacialis	2	5		6	8	3	1		1	1
Porosira pseudodenticulata								1		
Proboscia spp.	2	2			2		2		2	4
Rhizosolenia spp.	17	3		2	1	5	8		6	19
Stellarima microtrias (rs and veg)	4	2			1	1	3	1	2	
Synedra/Synedropsis spp.			1		1	4			1	
Thalassiosira antarctica warm	118	131	37	131	121	144	139	5	114	69
Thalassiosira antarctica cold		3	1			1	4		2	17
Thalassiosira gracilis var. expecta	4	2	1				1		1	5
Thalassiosira gracilis var. nominate	6	5		6			4	7	3	5
Thalassiosira lentiginosa	6	3		2	1	2	2	1	8	11
Thalassiosira ritscheri			3		2					
Thalassiosira tumida	12	2	4	6	3	1	4	5	2	3
Thalassiosira spp.										
Thalassiothrix/Trichotoxon	1.5	5.5	1	2	3	4	4.5	1	1.5	2.5
Unidentified centrics	8						3		4	2
Unidentified pennates								1	1	1
Thalassiosira antarctica vegetative	10	15	1	11	5	21	8	1	3	5
Thalassiosira scotia	64	80	67	75	82	85	93	8	60	47
Total diatoms counted	429.5	420.5	458	493	404	479	441.5	149	466.5	402.5

Reference List

Abelmann, A., Gersonde, R., 1991. Biosiliceous particle flux in the Southern Ocean. Marine Chemistry 35, 503-536.

Alldredge, A.L., Gotschalk, C.C., 1989. Direct observations of the mass flocculation of diatom blooms: characteristics, settling velocities and formation of diatom aggregates. Deep Sea Research Part A. Oceanographic Research Papers 36, 159-171.

Allen, C.S., 2003. Late Quaternary palaeoceanography of the Scotia Sea, Southwest Atlantic: Evidence from the Diatom Record. School of Earth. Ocean and Planetary Science. Cardiff, Cardiff University, PhD: 218.

Allen, C.S., Oakes-Fretwell, L., Anderson, J.B., Hodgson, D.A., 2010. A record of Holocene glacial and oceanographic variability in Neny Fjord, Antarctic Peninsula. The Holocene 20, 551-564.

Allen, C.S., 2014. Proxy development: a new facet of morphological diversity in the marine diatom Eucampia antarctica (Castracane) Mangin. Journal of Micropalaeontology 33, 131-142.

Alley, K., Patacca, K., Pike, J., Dunbar, R., Leventer, A., 2018. Iceberg Alley, East Antarctic Margin: Continuously laminated diatomaceous sediments from the late Holocene. Marine Micropaleontology 140, 56-68.

Alley, R.B., Blankenship, D.D., Rooney, S.T., Bentley, C.R., 1989. Sedimentation beneath ice shelves — the view from ice stream B. Marine Geology 85, 101-120.

Alley, R.B., Dupont, T.K., Parizek, B.R., Anandakrishnan, S., Lawson, D.E., Larson, G.J., Evenson, E.B., 2006. Outburst flooding and the initiation of ice-stream surges in response to climatic cooling: A hypothesis. Geomorphology 75, 76-89.

Alverson, A.J., Kang, S.-H., Theriot, E.C., 2006. CELL WALL MORPHOLOGY AND SYSTEMATIC IMPORTANCE OF THALASSIOSIRA RITSCHERI (HUSTEDT) HASLE, WITH A DESCRIPTION OF SHIONODISCUS GEN. NOV. Diatom Research 21, 251-262.

Amblas, D., Urgeles, R., Canals, M., Calafat, A.M., Rebesco, M., Camerlenghi, A., Estrada, F., De Batist, M., Hughes-Clarke, J.E., 2006. Relationship between continental rise development and palaeo-ice sheet dynamics, Northern Antarctic Peninsula Pacific margin. Quaternary Science Reviews 25, 933-944.

Anandakrishnan, S., Catania, G.A., Alley, R.B., Horgan, H.J., 2007. Discovery of Till Deposition at the Grounding Line of Whillans Ice Stream. Science 315, 1835-1838.

Anderson, J.B., 1999. Antarctic Marine Geology. Cambridge University Press, Cambridge.

Anderson, J., 2005: Processed Multibeam Sonar Data (version 2) near the Antarctic Peninsula acquired during Nathaniel B. Palmer expedition NBP0201 (2002), Interdisciplinary Earth Data Alliance (IEDA).

Anderson, R.F., Ali, S., Bradtmiller, L.I., Nielsen, S.H.H., Fleisher, M.Q., Anderson, B.E., Burckle, L.H., 2009. Wind-Driven Upwelling in the Southern Ocean and the Deglacial Rise in Atmospheric CO_2. Science 323, 1443-1448.

Andrews, J.T., Domack, E.W., Cunningham, W.L., Leventer, A., Licht, K.J., Jull, A.J.T., DeMaster, D.J., Jennings, A.E., 1999. Problems and Possible Solutions Concerning Radiocarbon Dating of Surface Marine Sediments, Ross Sea, Antarctica. Quaternary Research 52, 206-216.

Armand, L.K., Zielinski, U., 2001. Diatom species of the genus Rhizosolenia from Southern Ocean sediments: Distribution and taxonomic notes. Diatom Research 16, 259-294.

Armand, L.K., Crosta, X., Romero, O., Pichon, J.-J., 2005. The biogeography of major diatom taxa in Southern Ocean sediments: 1. Sea ice related species. Palaeogeography, Palaeoclimatology, Palaeoecology 223, 93-126.

Armand, L.K., Cornet-Barthaux, V., Mosseri, J., Quéguiner, B., 2008. Late summer diatom biomass and community structure on and around the naturally iron-fertilised Kerguelen Plateau in the Southern Ocean. Deep Sea Research Part II: Topical Studies in Oceanography 55, 653-676.

Arndt, J.E., Schenke, H.W., Jakobsson, M., Nitsche, F., Buys, G., Goleby, B., Rebesco, M., Bohoyo, F., Hong, J.K., Black, J., Greku, R., Udintsev, G., Barrios, F., Reynoso-Peralta, W., Morishita, T., Wigley, R., 2013. The International Bathymetric Chart of the Southern Ocean (IBCSO) Version 1.0 - A new bathymetric compilation covering circum-Antarctic waters. Geophysical Research Letters 40, 3111-3117.

Banfield, L.A., Anderson, J.B. 1995. Seismic facies investigation of the Late Quaternary glacial history of Bransfield Basin, Antarctica. In: Cooper, A.K., Barker, P.F., Brancolini, G. (Eds.), Geology and Seismic Stratigraphy of the Antarctic Margin. American Geophysical Union, Washington DC, Antarctic Research Series, 68, 123-140.

Barbara, L., Crosta, X., Massé, G., Ther, O., 2010. Deglacial environments in eastern Prydz Bay, East Antarctica. Quaternary Science Reviews 29, 2731-2740.

Bart, P.J., Krogmeier, B.J., Bart, M.P., Tulaczyk, S., 2017. The paradox of a long grounding during West Antarctic Ice Sheet retreat in Ross Sea. Scientific Reports 7, 1262.

Bart, P.J., DeCesare, M., Rosenheim, B.E., Majewski, W., McGlannan, A., 2018. A centuries-long delay between a paleo-ice-shelf collapse and grounding-line retreat in the Whales Deep Basin, eastern Ross Sea, Antarctica. Scientific Reports 8.

Bassett, S.E., Milne, G.A., Mitrovica, J.X., Clark, P.U., 2005. Ice Sheet and Solid Earth Influences on Far-Field Sea-Level Histories. Science 309, 925-928.

Bassett, S.E., Milne, G.A., Bentley, M.J., Huybrechts, P., 2007. Modelling Antarctic sea-level data to explore the possibility of a dominant Antarctic contribution to meltwater pulse IA. Quaternary Science Reviews 26, 2113-2127.

Batchelor, C.L., Dowdeswell, J.A., 2015. Ice-sheet grounding-zone wedges (GZWs) on high-latitude continental margins. Marine Geology 363, 65-92.

Bentley, M.J., Hodgson, D.A., Smith, J.A., Cofaigh, C.Ó., Domack, E.W., Larter, R.D., Roberts, S.J., Brachfeld, S., Leventer, A., Hjort, C., Hillenbrand, C.-D., Evans, J., 2009. Mechanisms of Holocene palaeoenvironmental change in the Antarctic Peninsula region. The Holocene 19, 51-69.

Bentley, M.J., Johnson, J.S., Hodgson, D.A., Dunai, T., Freeman, S.P.H.T., Ó Cofaigh, C., 2011. Rapid deglaciation of Marguerite Bay, western Antarctic Peninsula in the Early Holocene. Quaternary Science Reviews 30, 3338-3349.

Blunier, T., Chappellaz, J., Schwander, J., Dällenbach, A., Stauffer, B., Stocker, T.F., Raynaud, D., Jouzel, J., Clausen, H.B., Hammer, C.U., Johnsen, S.J., 1998. Asynchrony of Antarctic and Greenland climate change during the last glacial period. Nature 394, 739-743.

Boulton, G.S., 1996. Theory of glacial erosion, transport and deposition as a consequence of subglacial sediment deformation. Journal of Glaciology 42, 43-62.

British Antarctic Survey, 1981a. British Antarctic Territory geological map, Sheet 3, BAS 500g Series, 1:500,000, British Antarctic Survey, Cambridge.

British Antarctic Survey, 1981a. British Antarctic Territory geological map, Sheet 4, BAS 500g Series, 1:500,000, British Antarctic Survey, Cambridge.

Bronselaer, B., Winton, M., Griffies, S.M., Hurlin, W.J., Rodgers, K.B., Sergienko, O.V., Stouffer, R.J., Russell, J.L., 2018. Change in future climate due to Antarctic meltwater. Nature 564, 53-58.

Buffen, A., Leventer, A., Rubin, A., Hutchins, T., 2007. Diatom assemblages in surface sediments of the northwestern Weddell Sea, Antarctic Peninsula. Marine Micropaleontology 62, 7-30.

Buizert, C., Sigl, M., Severi, M., Markle, B.R., Wettstein, J.J., McConnell, J.R., Pedro, J.B., Sodemann, H., Goto-Azuma, K., Kawamura, K., Fujita, S., Motoyama, H., Hirabayashi, M., Uemura, R., Stenni, B., Parrenin, F., He, F., Fudge, T.J., Steig, E.J., 2018. Abrupt ice-age shifts in southern westerly winds and Antarctic climate forced from the north. Nature 563, 681-685.

Burckle, L.H., 1972. Diatom evidence bearing on the Holocene in the South Atlantic. Quaternary Research 2, 323-326.

Burton-Johnson, A., Riley, T.R., 2015. Autochthonous v. accreted terrane development of continental margins: a revised in situ tectonic history of the Antarctic Peninsula. Journal of the Geological Society 172, 822.

Canals, M., Urgeles, R., Calafat, A.M., 2000. Deep sea-floor evidence of past ice streams off the Antarctic Peninsula. Geology 28, 31-34.

Christianson, K. A., Holschuh, N., Paden, J. D., Sprick, J., Peters, L. E., Anandakrishnan, S., Alley, R. B., 2017. A varied subglacial landscape under Thwaites Glacier, West Antarctica. American Geophysical Union, Fall Meeting 2017, abstract.

Clark, C.D., 1993. Mega-scale glacial lineations and cross-cutting ice-flow landforms. Earth Surface Processes and Landforms 18, 1-29.

Convey, P., Stevens, M.I., Hodgson, D.A., Smellie, J.L., Hillenbrand, C.-D., Barnes, D.K.A., Clarke, A., Pugh, P.J.A., Linse, K., Cary, S.C., 2009. Exploring biological constraints on the glacial history of Antarctica. Quaternary Science Reviews 28, 3035-3048.

Cook, A.J., Holland, P.R., Meredith, M.P., Murray, T., Luckman, A., Vaughan, D.G., 2016. Ocean forcing of glacier retreat in the western Antarctic Peninsula. Science 353, 283-286.

Cooper, A.P.R., 1997. Historical observations of Prince Gustav Ice Shelf. Polar Record 33, 285-294.

Crawford, R.M., 1995. The role of sex in the sedimentation of a marine diatom bloom. Limnology and Oceanography 40, 200-204.

Crosta, X., Romero, O., Armand, L.K., Pichon, J.-J., 2005. The biogeography of major diatom taxa in Southern Ocean sediments: 2. Open ocean related species. Palaeogeography, Palaeoclimatology, Palaeoecology 223, 66-92.

Croudace, I.W., Rothwell, R.G., 2015. Micro-XRF Studies of Sediment Cores: Applications of a non-destructive tool for the environmental sciences. Springer Netherlands.

Cuffey, K.M., Clow, G.D., Steig, E.J., Buizert, C., Fudge, T.J., Koutnik, M., Waddington, E.D., Alley, R.B., Severinghaus, J.P., 2016. Deglacial temperature history of West Antarctica. Proceedings of the National Academy of Sciences 113, 14249-14254.

Cunningham, W.L., Leventer, A., 1998. Diatom assemblages in surface sediments of the Ross Sea: relationship to present oceanographic conditions. Antarctic Science 10, 134-146.

DeConto, R.M., Pollard, D., 2016. Contribution of Antarctica to past and future sea-level rise. Nature 531, 591.

Denis, D., Crosta, X., Zaragosi, S., Romero, O., Martin, B., Mas, V., 2006. Seasonal and subseasonal climate changes recorded in laminated diatom ooze sediments, Adélie Land, East Antarctica. The Holocene 16, 1137-1147.

Denton, G.H., Prentice, M.L., Burckle, L.H., 1991. Cainozoic history of the Antarctic ice sheet. In: Ingey, R.J. (Eds.), Geology of Antarctica. Oxford: Oxford University Press, 365-433.

Denton, G.H., Hughes, T.J., 2002. Reconstructing the Antarctic Ice Sheet at the Last Glacial Maximum. Quaternary Science Reviews 21, 193-202.

Deschamps, P., Durand, N., Bard, E., Hamelin, B., Camoin, G., Thomas, A.L., Henderson, G.M., Okuno, J.i., Yokoyama, Y., 2012. Ice-sheet collapse and sea-level rise at the Bølling warming 14,600 years ago. Nature 483, 559.

Dinniman, M.S., Klinck, J.M., Smith Jr, W.O., 2011. A model study of Circumpolar Deep Water on the West Antarctic Peninsula and Ross Sea continental shelves. Deep Sea Research Part II: Topical Studies in Oceanography 58, 1508-1523.

Dinniman, M.S., Klinck, J.M., Hofmann, E.E., 2012. Sensitivity of Circumpolar Deep Water Transport and Ice Shelf Basal Melt along the West Antarctic Peninsula to Changes in the Winds. Journal of Climate 25, 4799-4816.

Doake, C.S.M., Vaughan, D.G., 1991. Rapid disintegration of the Wordie Ice Shelf in response to atmospheric warming. Nature 350, 328-330.

Domack, E.W., Williams, C.R., 1990. Fine Structure and Suspended Sediment Transport in Three Antarctic Fjords, Contributions to Antarctic Research I. American Geophysical Union 50, 71-89.

Domack, E.W., Harris, P.T., 1998. A new depositional model for ice shelves, based upon sediment cores from the Ross Sea and the Mac. Robertson shelf, Antarctica. Annals of Glaciology 27, 281-284.

Domack, E., O'Brien, P., Harris, P., Santis, L., Raker, B., 1998. Late Quaternary sediment facies in Prydz Bay, East Antarctica and their relationship to glacial advance onto the continental shelf. Antarctic Science 10, 236-246.

Domack, E.W., Jacobson, E.A., Shipp, S., Anderson, J.B., 1999. Late Pleistocene–Holocene retreat of the West Antarctic Ice-Sheet system in the Ross Sea: Part 2—Sedimentologic and stratigraphic signature. Geological Society of America Bulletin 111, 1517-1536.

Domack, E., Leventer, A., Dunbar, R., Taylor, F., Brachfeld, S., Sjunneskog, C., 2001. Chronology of the Palmer Deep site, Antarctic Peninsula: a Holocene palaeoenvironmental reference for the circum-Antarctic. The Holocene 11, 1-9.

Domack, E. W., Burnett, A., Leventer, A., 2003. Environmental Setting of the Antarctic Peninsula. In: Domack, E., Leventer, A., Burnet, A., Bindschadler, R., Convey, P., Kirby, M. (Eds.), Antarctic Peninsula Climate Variability: Historical and Paleoenvironmental Perspectives.

Domack, E., 2005. Processed Multibeam Sonar Data (version 2) near the Antarctic Peninsula acquired during Nathaniel B. Palmer expedition NBP0107 (2001), Interdisciplinary Earth Data Alliance (IEDA).

Domack, E., Amblàs, D., Gilbert, R., Brachfeld, S., Camerlenghi, A., Rebesco, M., Canals, M., Urgeles, R., 2006. Subglacial morphology and glacial evolution of the Palmer deep outlet system, Antarctic Peninsula. Geomorphology 75, 125-142.

Domack, E.W., Powell, R., 2018. Chapter 7 - Modern Glaciomarine Environments and Sediments: An Antarctic Perspective, In: Menzies, J., van der Meer, J.J.M. (Eds.), Past Glacial Environments (Second Edition). Elsevier, 181-272.

Dowdeswell, J.A., Ottesen, D., Forwick, M., 2016. Grounding-zone wedges on the western Svalbard shelf. Geological Society, London, Memoirs 46, 233-234.

Drewry, D.J., Cooper, A.P.R., 1981. Processes and Models of Antarctic Glaciomarine Sedimentation. Annals of Glaciology 2, 117-122.

Ehrmann, W.U., Melles, M., Kuhn, G., Grobe, H., 1992. Significance of clay mineral assemblages in the Antarctic Ocean. Marine Geology 107, 249-273.

Etourneau, J., Collins, L.G., Willmott, V., Kim, J.H., Barbara, L., Leventer, A., Schouten, S., Sinninghe Damsté, J.S., Bianchini, A., Klein, V., Crosta, X., Massé, G., 2013. Holocene climate variations in the western Antarctic Peninsula: evidence for sea ice extent predominantly controlled by changes in insolation and ENSO variability. Climate of the Past 9, 1431-1446.

Evans, J., Pudsey, C.J., 2002. Sedimentation associated with Antarctic Peninsula ice shelves: implications for palaeoenvironmental reconstructions of glacimarine sediments. Journal of the Geological Society 159, 233-237.

Evans, J., Cofaigh, C.Ó., 2003. Supraglacial debris along the front of the Larsen-A Ice Shelf, Antarctic Peninsula. Antarctic Science 15, 503-506.

Evans, J., Dowdeswell, J.A., Cofaigh, C.Ó., 2004. Late Quaternary submarine bedforms and ice-sheet flow in Gerlache Strait and on the adjacent continental shelf, Antarctic Peninsula. Journal of Quaternary Science 19, 397-407.

Evans, J., Pudsey, C.J., Ó Cofaigh, C., Morris, P., Domack, E., 2005. Late Quaternary glacial history, flow dynamics and sedimentation along the eastern margin of the Antarctic Peninsula Ice Sheet. Quaternary Science Reviews 24, 741-774.

Eyles, C.H., Eyles, N., Miall, A.D., 1985. Models of glaciomarine sedimentation and their application to the interpretation of ancient glacial sequences. Palaeogeography, Palaeoclimatology, Palaeoecology 51, 15-84.

Fairbanks, R.G., 1989. A 17,000-year glacio-eustatic sea level record: influence of glacial melting rates on the Younger Dryas event and deep-ocean circulation. Nature 342, 637-642.

Finocchiaro, F., Langone, L., Colizza, E., Fontolan, G., Giglio, F., Tuzzi, E., 2005. Record of the early Holocene warming in a laminated sediment core from Cape Hallett Bay (Northern Victoria Land, Antarctica). Global and Planetary Change 45, 193-206.

Fryxell, G.A., Hasle, G.R., 1971. Corethron criophilum Castracane: its distribution and structure. In: Llano, G.A., Wallen, I.E. (Eds.), Biology of the Antarctic Seas, vol IV. American Geophysical Union, Washington DC, Antarctic Research Series 17, 335–346.

Fryxell, G.A., 1989. Marine phytoplankton at the Weddell Sea ice edge: Seasonal changes at the specific level. Polar Biology 10, 1-18.

Fryxell, G.A., 1990. Planktonic marine diatom winter stages. Antarctic alternatives to resting spores. K.J. Kocilek (Ed.), Proceedings of the 11th Diatom Symposium, San Francisco, California, 437-448.

Fryxell, G.A., 1994. Planktonic marine diatom winter stages: Antarctic alternatives to resting spores. Memoirs of the California Academy of Sciences 17, 437-448.

Garrison, D.L., 1991. Antarctic Sea Ice Biota. Integrative and Comparative Biology 31, 17-34.

Golledge, N.R., Levy, R.H., McKay, R.M., Fogwill, C.J., White, D.A., Graham, A.G.C., Smith, J.A., Hillenbrand, C.-D., Licht, K.J., Denton, G.H., Ackert, R.P., Maas, S.M., Hall, B.L., 2013. Glaciology and geological signature of the Last Glacial Maximum Antarctic ice sheet. Quaternary Science Reviews 78, 225-247.

Golledge, N.R., Keller, E.D., Gomez, N., Naughten, K.A., Bernales, J., Trusel, L.D., Edwards, T.L., 2019. Global environmental consequences of twenty-first-century ice-sheet melt. Nature 566, 65-72.

Graham, A.G.C., Larter, R.D., Gohl, K., Hillenbrand, C.-D., Smith, J.A., Kuhn, G., 2009. Bedform signature of a West Antarctic palaeo-ice stream reveals a multi-temporal record of flow and substrate control. Quaternary Science Reviews 28, 2774-2793.

Graham, A.G.C., Larter, R.D., Gohl, K., Dowdeswell, J.A., Hillenbrand, C.D., Smith, J.A., Evans, J., Kuhn, G., Deen, T., 2010. Flow and retreat of the Late Quaternary Pine Island-Thwaites palaeo-ice stream, West Antarctica. Journal of Geophysical Research: Earth Surface 115.

Graham, A.G.C., Smith, J.A., 2012. Palaeoglaciology of the Alexander Island ice cap, western Antarctic Peninsula, reconstructed from marine geophysical and core data. Quaternary Science Reviews 35, 63-81.

Gudmundsson, G.H., 2013. Ice-shelf buttressing and the stability of marine ice sheets. The Cryosphere 7, 647-655.

Harden, S.L., DeMaster, D.J., Nittrouer, C.A., 1992. Developing sediment geochronologies for high-latitude continental shelf deposits: a radiochemical approach. Marine Geology 103, 69-97.

Hargraves, P.E., French, F.W., 1983. Diatom resting spores: significance and strategies. In: Fryxell, G. (Ed.), Survival Strategies of the Algae. Cambridge University Press, New York, 49–68.

Hemer, M.A., Harris, P.T., 2003. Sediment core from beneath the Amery Ice Shelf, East Antarctica, suggests mid-Holocene ice-shelf retreat. Geology 31, 127-130.

Hemer, M.A., Post, A.L., O'Brien, P.E., Craven, M., Truswell, E.M., Roberts, D., Harris, P.T., 2007. Sedimentological signatures of the sub-Amery Ice Shelf circulation. Antarctic Science 19, 497-506.

Hendry, K.R., Meredith, M.P., Ducklow, H.W., 2018. The marine system of the West Antarctic Peninsula: status and strategy for progress. Philosophical Transactions of the Royal Society A: Mathematical, Physical and Engineering Sciences 376.

Henley, S.F., Schofield, O.M., Hendry, K.R., Schloss, I.R., Steinberg, D.K., Moffat, C., Peck, L.S., Costa, D.P., Bakker, D.C.E., Hughes, C., Rozema, P.D., Ducklow, H.W., Abele, D., Stefels, J., Van Leeuwe, M.A., Brussaard, C.P.D., Buma, A.G.J., Kohut, J., Sahade, R., Friedlaender, A.S., Stammerjohn, S.E., Venables, H.J., Meredith, M.P., 2019. Variability and change in the west Antarctic Peninsula marine system: Research priorities and opportunities. Progress in Oceanography 173, 208-237.

Heroy, D.C., Anderson, J.B., 2005. Ice-sheet extent of the Antarctic Peninsula region during the Last Glacial Maximum (LGM)—Insights from glacial geomorphology. Geological Society of America Bulletin 117, 1497-1512.

Heroy, D.C., Anderson, J.B., 2007. Radiocarbon constraints on Antarctic Peninsula Ice Sheet retreat following the Last Glacial Maximum (LGM). Quaternary Science Reviews 26, 3286-3297.

Hillenbrand, C.-D., Ehrmann, W., 2001. Distribution of clay minerals in drift sediments on the continental rise west of the Antarctic Peninsula, ODP Leg 178, Sites 1095 and 1096. In: Barker, P.F., Camerlenghi, A., Acton, G.D., and Ramsay, A.T.S. (Eds.), Proc. ODP, Sci. Results, 178.

Hillenbrand, C.-D., Baesler, A., Grobe, H., 2005. The sedimentary record of the last glaciation in the western Bellingshausen Sea (West Antarctica): Implications for the interpretation of diamictons in a polar-marine setting. Marine Geology 216, 191-204.

Hillenbrand, C.-D., Ehrmann, W., Larter, R.D., Benetti, S., Dowdeswell, J.A., Ó Cofaigh, C., Graham, A.G.C., Grobe, H., 2009. Clay mineral provenance of sediments in the southern Bellingshausen Sea reveals drainage changes of the West Antarctic Ice Sheet during the Late Quaternary. Marine Geology 265, 1-18.

Hillenbrand, C.-D., Smith, J.A., Kuhn, G., Esper, O., Gersonde, R., Larter, R.D., Maher, B., Moreton, S.G., Shimmield, T.M., Korte, M., 2010a. Age assignment of a diatomaceous ooze deposited in the western Amundsen Sea Embayment after the Last Glacial Maximum. Journal of Quaternary Science 25, 280-295.

Hillenbrand, C.-D., Larter, R.D., Dowdeswell, J.A., Ehrmann, W., Ó Cofaigh, C., Benetti, S., Graham, A.G.C., Grobe, H., 2010b. The sedimentary legacy of a palaeo-ice stream on the shelf of the southern Bellingshausen Sea: Clues to West Antarctic glacial history during the Late Quaternary. Quaternary Science Reviews 29, 2741-2763.

Hillenbrand, C.-D., Melles, M., Kuhn, G., Larter, R.D., 2012. Marine geological constraints for the grounding-line position of the Antarctic Ice Sheet on the southern Weddell Sea shelf at the Last Glacial Maximum. Quaternary Science Reviews 32, 25-47.

Hillenbrand, C.-D., Smith, J.A., Hodell, D.A., Greaves, M., Poole, C.R., Kender, S., Williams, M., Andersen, T.J., Jernas, P.E., Elderfield, H., Klages, J.P., Roberts, S.J., Gohl, K., Larter, R.D., Kuhn, G., 2017. West Antarctic Ice Sheet retreat driven by Holocene warm water incursions. Nature 547, 43.

Hofmann, E.E., Klinck, J.M., Lascara, C.M., Smith, D.A., 1996. Water Mass Distribution and Circulation West of the Antarctic Peninsula And Including Bransfield Strait, Foundations for Ecological Research West of the Antarctic Peninsula. American Geophysical Union, 61-80.

Hofmann, E.E., Klinck, J.M., 1998. Thermohaline Variability of the Waters Overlying The West Antarctic Peninsula Continental Shelf, In: Jacobs, S.S., Weiss, R.F. (Eds.), Ocean, Ice, and Atmosphere: Interactions at the Antarctic Continental Margin. American Geophysical Union, Antarctic Research Series, 67–81.

Howat, I.M., Domack, E.W., 2003. Reconstructions of western Ross Sea palaeo-ice-stream grounding zones from high-resolution acoustic stratigraphy. Boreas 32, 56-75.

Humbert, A., Braun, M., 2008. The Wilkins Ice Shelf, Antarctica: break-up along failure zones. Journal of Glaciology 54, 943-944

Huybrechts, P., 2002. Sea-level changes at the LGM from ice-dynamic reconstructions of the Greenland and Antarctic ice sheets during the glacial cycles. Quaternary Science Reviews 21, 203-231.

Ishman, S.E., Sperling, M.R., 2002. Benthic foraminiferal record of Holocene deep-water evolution in the Palmer Deep, western Antarctic Peninsula. Geology 30, 435-438.

Jacobs, S.S., 2006. Observations of change in the Southern Ocean. Philosophical Transactions of the Royal Society A: Mathematical, Physical and Engineering Sciences 364, 1657-1681.

Jacobs, S.S., Jenkins, A., Giulivi, C.F., Dutrieux, P., 2011. Stronger ocean circulation and increased melting under Pine Island Glacier ice shelf. Nature Geoscience 4, 519-523.

Jakobsson, M., Anderson, J.B., Nitsche, F.O., Gyllencreutz, R., Kirshner, A.E., Kirchner, N., O'Regan, M., Mohammad, R., Eriksson, B., 2012. Ice sheet retreat dynamics inferred from glacial morphology of the central Pine Island Bay Trough, West Antarctica. Quaternary Science Reviews 38, 1-10.

Jamieson, S.S.R., Vieli, A., Livingstone, S.J., Cofaigh, C.O., Stokes, C., Hillenbrand, C.-D., Dowdeswell, J.A., 2012. Ice-stream stability on a reverse bed slope. Nature Geoscience 5, 799-802.

Jamieson, S.S.R., Vieli, A., Cofaigh, C.Ó., Stokes, C.R., Livingstone, S.J., Hillenbrand, C.-D., 2014. Understanding controls on rapid ice-stream retreat during the last deglaciation of Marguerite Bay, Antarctica, using a numerical model. Journal of Geophysical Research: Earth Surface 119, 247-263.

Johansen, J.R., Fryxell, G.A., 1985. The genus Thalassiosira (Bacillariophyceae): studies on species occurring south of the Antarctic Convergence Zone. Phycologia 24, 155-179.

Kaiser, J., Lamy, F., Hebbeln, D., 2005. A 70-kyr sea surface temperature record off southern Chile (Ocean Drilling Program Site 1233). Paleoceanography 20.

Kemp, A.E.S., Pike, J., Pearce, R.B., Lange, C.B., 2000. The "Fall dump" — a new perspective on the role of a "shade flora" in the annual cycle of diatom production and export flux. Deep Sea Research Part II: Topical Studies in Oceanography 47, 2129-2154.

Kilfeather, A.A., Ó Cofaigh, C., Lloyd, J.M., Dowdeswell, J.A., Xu, S., Moreton, S.G., 2011. Ice-stream retreat and ice-shelf history in Marguerite Trough, Antarctic Peninsula: Sedimentological and foraminiferal signatures. Geological Society of America Bulletin 123, 997-1015.

Kim, H., Ducklow, H.W., Abele, D., Ruiz Barlett, E.M., Buma, A.G.J., Meredith, M.P., Rozema, P.D., Schofield, O.M., Venables, H.J., Schloss, I.R., 2018. Inter-decadal variability of phytoplankton biomass along the coastal West Antarctic Peninsula. Philosophical Transactions of the Royal Society A: Mathematical, Physical and Engineering Sciences 376.

Klinck, J.M., Hofmann, E.E., Beardsley, R.C., Salihoglu, B., Howard, S., 2004. Water-mass properties and circulation on the west Antarctic Peninsula Continental Shelf in Austral Fall and Winter 2001. Deep Sea Research Part II: Topical Studies in Oceanography 51, 1925-1946.

Krebs, W.N., Lipps, J.H., Burckle, L.H., 1987. Ice diatom floras, Arthur Harbor, Antarctica. Polar Biology 7, 163-171.

Kurtz, D.D., Anderson, J.B., 1979. Recognition and sedimentologic description of Recent debris flow deposits from the Ross and Weddell seas, Antarctica. Journal of Sedimentary Research 49, 1159-1169.

Lamy, F., Arz, H. W., Kilian, R., Lange, C. B., Lembke-Jene, L., Wengler, M., Kaiser, J., Baeza-Urrea, O., Hall, I. R., Harada, N., Tiedemann, R., 2015. Glacial reduction and millennial-scale variations in Drake Passage throughflow. Proceedings of the National Academy of Sciences 112, 13496-13501.

Larter, R.D., Barker, P.F., 1989. Seismic stratigraphy of the Antarctic Peninsula Pacific margin: A record of Pliocene-Pleistocene ice volume and paleoclimate. Geology 17, 731-734.

Larter, R.D., Hogan, K.A., Hillenbrand, C.-D., Smith, J.A., Batchelor, C.L., Cartigny, M., Tate, A.J., Kirkham, J.D., Roseby, Z.A., Kuhn, G., Graham, A.G.C., Dowdeswell,

J.A., 2019. Subglacial hydrological control on flow of an Antarctic Peninsula palaeo-ice stream. The Cryosphere 13, 1583-1596.

Lavoie, C., Domack, E.W., Pettit, E.C., Scambos, T.A., Larter, R.D., Schenke, H.W., Yoo, K.C., Gutt, J., Wellner, J., Canals, M., Anderson, J.B., Amblas, D., 2015. Configuration of the Northern Antarctic Peninsula Ice Sheet at LGM based on a new synthesis of seabed imagery. The Cryosphere 9, 613-629.

Le Brocq, A.M., Ross, N., Griggs, J.A., Bingham, R.G., Corr, H.F.J., Ferraccioli, F., Jenkins, A., Jordan, T.A., Payne, A.J., Rippin, D.M., Siegert, M.J., 2013. Evidence from ice shelves for channelized meltwater flow beneath the Antarctic Ice Sheet. Nature Geoscience 6, 945.

Leventer, A., 1991. Sediment trap diatom assemblages from the northern Antarctic Peninsula region. Deep Sea Research Part A. Oceanographic Research Papers 38, 1127-1143.

Leventer, A., 1992. Modern distribution of diatoms in sediments from the George V Coast, Antarctica. Marine Micropaleontology 19, 315-332.

Leventer, A., Domack, E.W., Ishman, S.E., Brachfeld, S., McClennen, C.E., Manley, P., 1996. Productivity cycles of 200–300 years in the Antarctic Peninsula region: Understanding linkages among the sun, atmosphere, oceans, sea ice, and biota. Geological Society of America Bulletin 108, 1626-1644.

Leventer, A., 1998. The Fate of Antarctic "Sea Ice Diatoms" and Their Use as Paleoenvironmental Indicators, In: Lizotte, M.P., Arrigo, K.R. (Eds.), Antarctic Sea Ice: Biological Processes, Interactions and Variability.

Leventer, A., Domack, E., Barkoukis, A., McAndrews, B., Murray, J., 2002. Laminations from the Palmer Deep: A diatom-based interpretation. Paleoceanography 17.

Leventer, A., Domack, E., A Dunbar, R., A Pike, J., Stickley, C., Maddison, E., Brachfeld, S., Manley, P., McClennen, C., 2006. Marine sediment record from the East Antarctic margin reveals dynamics of ice sheet recession. GSA Today 16, 4-10.

Licht, K.J., Cunningham, W.L., Andrews, J.T., Domack, E.W., Jennings, A.E., 1998. Establishing chronologies from acid-insoluble organic 14C dates on Antarctic (Ross Sea) and Arctic (North Atlantic) marine sediments. 17, 14.

Licht, K.J., Dunbar, N.W., Andrews, J.T., Jennings, A.E., 1999. Distinguishing subglacial till and glacial marine diamictons in the western Ross Sea, Antarctica: Implications for a last glacial maximum grounding line. Geological Society of America Bulletin 111, 91-103.

Livingstone, S.J., Ó Cofaigh, C., Stokes, C.R., Hillenbrand, C.-D., Vieli, A., Jamieson, S.S.R., 2012. Antarctic palaeo-ice streams. Earth-Science Reviews 111, 90-128.

Löwemark, L., Chen, H.F., Yang, T.N., Kylander, M., Yu, E.F., Hsu, Y.W., Lee, T.Q., Song, S.R., Jarvis, S., 2011. Normalizing XRF-scanner data: A cautionary note on the interpretation of high-resolution records from organic-rich lakes. Journal of Asian Earth Sciences 40, 1250-1256.

MacAyeal, D. R., 1985. Evolution of Tidally Triggered Meltwater Plumes Below Ice Shelves. In: Jacobs, S.S. (Ed.), Oceanology of the Antarctic Continental Shelf.

Maddison, E.J., Pike, J., Leventer, A., Domack, E.W., 2005. Deglacial seasonal and sub-seasonal diatom record from Palmer Deep, Antarctica. Journal of Quaternary Science 20, 435-446.

Maddison, E.J., Pike, J., Leventer, A., Dunbar, R., Brachfeld, S., Domack, E.W., Manley, P., McClennen, C., 2006. Post-glacial seasonal diatom record of the Mertz Glacier Polynya, East Antarctica. Marine Micropaleontology 60, 66-88.

Maddison, E.J., Pike, J., Dunbar, R., 2012. Seasonally laminated diatom-rich sediments from Dumont d'Urville Trough, East Antarctic Margin: Late-Holocene Neoglacial sea-ice conditions. The Holocene 22, 857-875.

Marshall, G.J., Orr, A., Lipzig, N.P.M.v., King, J.C., 2006. The Impact of a Changing Southern Hemisphere Annular Mode on Antarctic Peninsula Summer Temperatures. Journal of Climate 19, 5388-5404.

Martin, P.J., Peel, D.A., 1978. The Spatial Distribution of 10 m Temperatures in the Antarctic Peninsula. Journal of Glaciology 20, 311-317.

Martinson, D.G., Stammerjohn, S.E., Iannuzzi, R.A., Smith, R.C., Vernet, M., 2008. Western Antarctic Peninsula physical oceanography and spatio–temporal variability. Deep Sea Research Part II: Topical Studies in Oceanography 55, 1964-1987.

Masson, V., Vimeux, F., Jouzel, J., Morgan, V., Delmotte, M., Ciais, P., Hammer, C., Johnsen, S., Lipenkov, V.Y., Mosley-Thompson, E., Petit, J.-R., Steig, E.J., Stievenard, M., Vaikmae, R., 2000. Holocene Climate Variability in Antarctica Based on 11 Ice-Core Isotopic Records. Quaternary Research 54, 348-358.

Mayr, C., Wille, M., Haberzettl, T., Fey, M., Janssen, S., Lücke, A., Ohlendorf, C., Oliva, G., Schäbitz, F., Schleser, G.H., Zolitschka, B., 2007. Holocene variability of the Southern Hemisphere westerlies in Argentinean Patagonia (52°S). Quaternary Science Reviews 26, 579-584.

McCulloch, R.D., Davies, S.J., 2001. Late-glacial and Holocene palaeoenvironmental change in the central Strait of Magellan, southern Patagonia. Palaeogeography, Palaeoclimatology, Palaeoecology 173, 143-173.

McGlone, M.S., Turney, C.S.M., Wilmshurst, J.M., Renwick, J., Pahnke, K., 2010. Divergent trends in land and ocean temperature in the Southern Ocean over the past 18,000 years. Nature Geoscience 3, 622.

McKay, R.M., Golledge, N.R., Maas, S., Naish, T., Levy, R., Dunbar, G., Kuhn, G., 2016. Antarctic marine ice-sheet retreat in the Ross Sea during the early Holocene. Geology 44, 7-10.

Measures, C.I., 1999. The role of entrained sediments in sea ice in the distribution of aluminium and iron in the surface waters of the Arctic Ocean. Marine Chemistry 68, 59-70.

Meredith, M.P., King, J.C., 2005. Rapid climate change in the ocean west of the Antarctic Peninsula during the second half of the 20th century. Geophysical Research Letters 32.

Meredith, M.P., Brandon, M.A., Wallace, M.I., Clarke, A., Leng, M.J., Renfrew, I.A., van Lipzig, N.P.M., King, J.C., 2008. Variability in the freshwater balance of northern Marguerite Bay, Antarctic Peninsula: Results from δ18O. Deep Sea Research Part II: Topical Studies in Oceanography 55, 309-322.

Meredith, M.P., Stammerjohn, S,E., Venables, H.J., Ducklow, H.W., Martinson, D.G., Ianuzzi, R.A., Leng, M.J., van Wessem, J. M., Reijmer, C.H., Barrand, N.E., 2017. Changing distributions of sea ice melt and meteoric water west of the Antarctic Peninsula. Deep Sea Research Part II: Topical Studies in Oceanography 139, 40-57.

Meredith, M.P., Falk, U., Bers Anna, V., Mackensen, A., Schloss Irene, R., Ruiz Barlett, E., Jerosch, K., Silva Busso, A., Abele, D., 2018. Anatomy of a glacial meltwater discharge event in an Antarctic cove. Philosophical Transactions of the Royal Society A: Mathematical, Physical and Engineering Sciences 376.

Minzoni, R.T., Anderson, J.B., Fernandez, R., Wellner, J.S., 2015. Marine record of Holocene climate, ocean, and cryosphere interactions: Herbert Sound, James Ross Island, Antarctica. Quaternary Science Reviews 129, 239-259.

Moffat, C., Beardsley, R.C., Owens, B., van Lipzig, N., 2008. A first description of the Antarctic Peninsula Coastal Current. Deep Sea Research Part II: Topical Studies in Oceanography 55, 277-293.

Moffat, C., Meredith, M., 2018. Shelf–ocean exchange and hydrography west of the Antarctic Peninsula: a review. Philosophical Transactions of the Royal Society A: Mathematical, Physical and Engineering Sciences 376.

Montes-Hugo, M., Doney, S.C., Ducklow, H.W., Fraser, W., Martinson, D., Stammerjohn, S.E., Schofield, O., 2009. Recent Changes in Phytoplankton Communities Associated with Rapid Regional Climate Change Along the Western Antarctic Peninsula. Science 323, 1470-1473.

Mortlock, R.A., Froelich, P.N., 1989. A simple method for the rapid determination of biogenic opal in pelagic marine sediments. Deep Sea Research Part A. Oceanographic Research Papers 36, 1415-1426.

Müller, P.J., Schneider, R., 1993. An automated leaching method for the determination of opal in sediments and particulate matter. Deep Sea Research Part I: Oceanographic Research Papers 40, 425-444.

Mulvaney, R., Abram, N.J., Hindmarsh, R.C.A., Arrowsmith, C., Fleet, L., Triest, J., Sime, L.C., Alemany, O., Foord, S., 2012. Recent Antarctic Peninsula warming relative to Holocene climate and ice-shelf history. Nature 489, 141-144.

Nicholls, K.W., Corr, H.F.J., Makinson, K., Pudsey, C.J., 2012. Rock debris in an Antarctic ice shelf. Annals of Glaciology 53, 235-240.

Nishimura, A., Tanahashi, M., Tokuhashi, S., Oda, H., Nakasone, T., 1999. Marine sediment cores from the continental shelf around Anvers Island, Antarctic Peninsula region. Polar geoscience 12, 215-226.

Ó Cofaigh, C., Pudsey, C.J., Dowdeswell, J.A., Morris, P., 2002. Evolution of subglacial bedforms along a paleo-ice stream, Antarctic Peninsula continental shelf. Geophysical Research Letters 29, 41-44.

Ó Cofaigh, C., Dowdeswell, J.A., Allen, C.S., Hiemstra, J.F., Pudsey, C.J., Evans, J., J.A. Evans, D., 2005. Flow dynamics and till genesis associated with a marine-based Antarctic palaeo-ice stream. Quaternary Science Reviews 24, 709-740.

Ó Cofaigh, C., Davies, B.J., Livingstone, S.J., Smith, J.A., Johnson, J.S., Hocking, E.P., Hodgson, D.A., Anderson, J.B., Bentley, M.J., Canals, M., Domack, E., Dowdeswell, J.A., Evans, J., Glasser, N.F., Hillenbrand, C.-D., Larter, R.D., Roberts, S.J., Simms, A.R., 2014. Reconstruction of ice-sheet changes in the Antarctic Peninsula since the Last Glacial Maximum. Quaternary Science Reviews 100, 87-110.

Ohkouchi, N., Eglinton, T.I., Hayes, J.M., 2003. Radiocarbon Dating of Individual Fatty Acids as a Tool for Refining Antarctic Margin Sediment Chronologies. Radiocarbon 45, 17-24.

Orsi, A.H., Whitworth, T., Nowlin, W.D., 1995. On the meridional extent and fronts of the Antarctic Circumpolar Current. Deep Sea Research Part I: Oceanographic Research Papers 42, 641-673.

Paolo, F.S., Fricker, H.A., Padman, L., 2015. Volume loss from Antarctic ice shelves is accelerating. Science 348, 327-331.

Paolo, F.S., Padman, L., Fricker, H.A., Adusumilli, S., Howard, S., Siegfried, M.R., 2018. Response of Pacific-sector Antarctic ice shelves to the El Niño/Southern Oscillation. Nature Geoscience 11, 121-126.

Peck, V.L., Yu, J., Kender, S., Riesselman, C.R., 2010. Shifting ocean carbonate chemistry during the Eocene-Oligocene climate transition: Implications for deep-ocean Mg/Ca paleothermometry. Paleoceanography 25.

Peck, V.L., Allen, C.S., Kender, S., McClymont, E.L., Hodgson, D.A., 2015. Oceanographic variability on the West Antarctic Peninsula during the Holocene and the influence of upper circumpolar deep water. Quaternary Science Reviews 119, 54-65.

Pedro, J.B., Bostock, H.C., Bitz, C.M., He, F., Vandergoes, M.J., Steig, E.J., Chase, B.M., Krause, C.E., Rasmussen, S.O., Markle, B.R., Cortese, G., 2016. The spatial extent and dynamics of the Antarctic Cold Reversal. Nature Geoscience 9, 51-55.

Pike, J., Crosta, X., Maddison, E.J., Stickley, C.E., Denis, D., Barbara, L., Renssen, H., 2009. Observations on the relationship between the Antarctic coastal diatoms Thalassiosira antarctica Comber and Porosira glacialis (Grunow) Jørgensen and sea ice concentrations during the late Quaternary. Marine Micropaleontology 73, 14-25.

Pike, J., Swann, G.E.A., Leng, M.J., Snelling, A.M., 2013. Glacial discharge along the west Antarctic Peninsula during the Holocene. Nature Geoscience 6, 199-202.

Pirrung, M., Fütterer, D., Grobe, H., Matthiessen, J., Niessen, F., 2002. Magnetic susceptibility and ice-rafted debris in surface sediments of the Nordic Seas: implications for Isotope Stage 3 oscillations. Geo-Marine Letters 22, 1-11.

Pollard, D., DeConto, R.M., Alley, R.B., 2015. Potential Antarctic Ice Sheet retreat driven by hydrofracturing and ice cliff failure. Earth and Planetary Science Letters 412, 112-121.

Pope, P. G., Anderson, J. B., 1992. Late Quaternary Glacial History of the Northern Antarctic Peninsula's Western Continental Shelf: Evidence from the Marine Record. In: Elliot, D.H. (Eds.), Contributions to Antarctic Research III.

Post, A.L., Galton-Fenzi, B.K., Riddle, M.J., Herraiz-Borreguero, L., O'Brien, P.E., Hemer, M.A., McMinn, A., Rasch, D., Craven, M., 2014. Modern sedimentation, circulation and life beneath the Amery Ice Shelf, East Antarctica. Continental Shelf Research 74, 77-87.

Powell, R.D., 1984. Glacimarine processes and inductive lithofacies modelling of ice shelf and tidewater glacier sediments based on Quaternary examples. Marine Geology 57, 1-52.

Powell, R.D., Dawber, M., McInnes, J.N., Pyne, A.R., 1996. Observations of the Grounding-line Area at a Floating Glacier Terminus. Annals of Glaciology 22, 217-223.

Powell R.D., Alley R.B., 1997. Grounding-line systems: processes, glaciological inferences and the stratigraphic record. In: Barker P.F., Cooper A.K. (Eds.), Geology and Seismic Stratigraphy of the Antarctic Margin, Part 2. Antarctic Research Series, American Geophysical Union 71, 169–187.

Prézelin, B.B., Hofmann, E.E., Mengelt, C., Klinck, J.M., 2000. The linkage between Upper Circumpolar Deep Water (UCDW) and phytoplankton assemblages on the west Antarctic Peninsula continental shelf. Journal of Marine Research 58, 165-202.

Pritchard, H.D., Ligtenberg, S.R.M., Fricker, H.A., Vaughan, D.G., van den Broeke, M.R., Padman, L., 2012. Antarctic ice-sheet loss driven by basal melting of ice shelves. Nature 484, 502-505.

Prothro, L.O., Simkins, L.M., Majewski, W., Anderson, J.B., 2018. Glacial retreat patterns and processes determined from integrated sedimentology and geomorphology records. Marine Geology 395, 104-119.

Pudsey, C.J., Barker, P.F., Larter, R.D., 1994. Ice sheet retreat from the Antarctic Peninsula shelf. Continental Shelf Research 14, 1647-1675.

Pudsey, C.J., 2002. Neogene record of Antarctic Peninsula glaciation in continental rise sediments: ODP Leg 178, Site 1095., In: Barker, P.F., Camerlenghi, A., Acton, G.D., Ramsay, A.T.S (Eds.), Proceedings of the Ocean Drilling Program Scientific Results, Vol. 178. Ocean Drilling Program, Texas A&M University, College Station, TX, 1-25.

RAISED Consortium, 2014. A community-based geological reconstruction of Antarctic Ice Sheet deglaciation since the Last Glacial Maximum. Quaternary Science Reviews 100, 1–9.

Raphael, M.N., Marshall, G.J., Turner, J., Fogt, R.L., Schneider, D., Dixon, D.A., Hosking, J.S., Jones, J.M., Hobbs, W.R., 2016. The Amundsen Sea Low: Variability, Change, and Impact on Antarctic Climate. Bulletin of the American Meteorological Society 97, 111-121.

Rebesco, M., Domack, E., Zgur, F., Lavoie, C., Leventer, A., Brachfeld, S., Willmott, V., Halverson, G., Truffer, M., Scambos, T., Smith, J., Pettit, E., 2014. Boundary condition of grounding lines prior to collapse, Larsen-B Ice Shelf, Antarctica. Science 345, 1354-1358.

Reinardy, B.T.I., Hiemstra, J.F., Murray, T., Hillenbrand, C.-D., Larter, R.D., 2011. Till genesis at the bed of an Antarctic Peninsula palaeo-ice stream as indicated by micromorphological analysis. Boreas 40, 498-517.

Rignot, E., Casassa, G., Gogineni, P., Krabill, W., Rivera, A., Thomas, R., 2004. Accelerated ice discharge from the Antarctic Peninsula following the collapse of Larsen B ice shelf. Geophysical Research Letters 31.

Rignot, E., Mouginot, J., Scheuchl, B., van den Broeke, M., van Wessem, M.J., Morlighem, M., 2019. Four decades of Antarctic Ice Sheet mass balance from 1979–2017. Proceedings of the National Academy of Sciences 116, 1095.

Rollinson, H.R, 1993. Using Geochemical Data: Evaluation, Presentation, Interpretation. Pearson Education, Upper Saddle River, New Jersey.

Rosenheim, B.E., Day, M.B., Domack, E., Schrum, H., Benthien, A., Hayes, J.M., 2008. Antarctic sediment chronology by programmed-temperature pyrolysis: Methodology and data treatment. Geochemistry, Geophysics, Geosystems 9.

Saba, G.K., Fraser, W.R., Saba, V.S., Iannuzzi, R.A., Coleman, K.E., Doney, S.C., Ducklow, H.W., Martinson, D.G., Miles, T.N., Patterson-Fraser, D.L., Stammerjohn, S.E., Steinberg, D.K., Schofield, O.M., 2014. Winter and spring controls on the summer food web of the coastal West Antarctic Peninsula. Nature Communications 5, 4318.

Sambrotto, R.N., Matsuda, A., Vaillancourt, R., Brown, M., Langdon, C., Jacobs, S.S., Measures, C., 2003. Summer plankton production and nutrient consumption patterns in the Mertz Glacier Region of East Antarctica. Deep Sea Research Part II: Topical Studies in Oceanography 50, 1393-1414.

Sañé, E., Isla, E., Pruski, A.M., Bárcena, M.A., Vétion, G., DeMaster, D., 2011. Diatom valve distribution and sedimentary fatty acid composition in Larsen Bay, Eastern Antarctica Peninsula. Continental Shelf Research 31, 1161-1168.

Scambos, T.A., Bohlander, J.A., Shuman, C.A., Skvarca, P., 2004. Glacier acceleration and thinning after ice shelf collapse in the Larsen B embayment, Antarctica. Geophysical Research Letters 31.

Scherer, R.P., 1994. A new method for the determination of absolute abundance of diatoms and other silt-sized sedimentary particles. Journal of Paleolimnology 12, 171-179.

Schloss, I.R., Ferreyra, G.A., Ruiz-Pino, D., 2002. Phytoplankton biomass in Antarctic shelf zones: a conceptual model based on Potter Cove, King George Island. Journal of Marine Systems 36, 129-143.

Schloss, I.R., Abele, D., Moreau, S., Demers, S., Bers, A.V., González, O., Ferreyra, G.A., 2012. Response of phytoplankton dynamics to 19-year (1991–2009) climate trends in Potter Cove (Antarctica). Journal of Marine Systems 92, 53-66.

Schmidtko, S., Heywood, K.J., Thompson, A.F., Aoki, S., 2014. Multidecadal warming of Antarctic waters. Science 346, 1227.

Schneider, T., Bischoff, T., Haug, G.H., 2014. Migrations and dynamics of the intertropical convergence zone. Nature 513, 45.

Schoof, C., 2007. Ice sheet grounding line dynamics: Steady states, stability, and hysteresis. Journal of Geophysical Research: Earth Surface 112.

Sedwick, P.N., DiTullio, G.R., 1997. Regulation of algal blooms in Antarctic Shelf Waters by the release of iron from melting sea ice. Geophysical Research Letters 24, 2515-2518.

Shemesh, A., Mortlock, R.A., Froelich, P.N., 1989. Late Cenozoic Ge/Si record of marine biogenic opal: Implications for variations of riverine fluxes to the ocean. Paleoceanography 4, 221-234.

Shevenell, A.E., Domack, E.W., Kernan, G.M., 1996. Record of Holocene palaeoclimate change along the Antarctic Peninsula: evidence from glacial marine sediments, Lallemand Fjord. Papers and Proceedings of the Royal Society of Tasmania 130, 55-64.

Shevenell, A.E., Kennett, J.P., 2002. Antarctic Holocene climate change: A benthic foraminiferal stable isotope record from Palmer Deep. Paleoceanography 17.

Shevenell, A.E., Ingalls, A.E., Domack, E.W., Kelly, C., 2011. Holocene Southern Ocean surface temperature variability west of the Antarctic Peninsula. Nature 470, 250-254.

Shukla, S.K., Crosta, X., 2016. Fragilariopsis kerguelensis size variability from the Indian subtropical Southern Ocean over the last 42 000 years. Antarctic Science 29, 139-146.

Simkins, L.M., Greenwood, S.L., Anderson, J.B., 2018. Diagnosing ice sheet grounding line stability from landform morphology. The Cryosphere 12, 2707-2726.

Sjunneskog, C., Taylor, F., 2002. Postglacial marine diatom record of the Palmer Deep, Antarctic Peninsula (ODP Leg 178, Site 1098) 1. Total diatom abundance. Paleoceanography 17, 4-8.

Skvarca, P., 1993. Fast recession of the Northern Larsen Ice Shelf monitored by space images. Annals of Glaciology 17, 317-321.

Smetacek, V.S., 1985. Role of sinking in diatom life-history cycles: ecological, evolutionary and geological significance. Marine Biology 84, 239-251.

Smith, D.A., Hofmann, E.E., Klinck, J.M., Lascara, C.M., 1999. Hydrography and circulation of the West Antarctic Peninsula Continental Shelf. Deep Sea Research Part I: Oceanographic Research Papers 46, 925-949.

Smith, J.A., Bentley, M.J., Hodgson, D.A., Roberts, S.J., Leng, M.J., Lloyd, J.M., Barrett, M.S., Bryant, C., Sugden, D.E., 2007. Oceanic and atmospheric forcing of early Holocene ice shelf retreat, George VI Ice Shelf, Antarctica Peninsula. Quaternary Science Reviews 26, 500-516.

Smith, J.A., Hillenbrand, C.-D., Larter, R.D., Graham, A.G.C., Kuhn, G., 2009. The sediment infill of subglacial meltwater channels on the West Antarctic continental shelf. Quaternary Research 71, 190-200.

Smith, J.A., Hillenbrand, C.-D., Kuhn, G., Larter, R.D., Graham, A.G.C., Ehrmann, W., Moreton, S.G., Forwick, M., 2011. Deglacial history of the West Antarctic Ice Sheet in the western Amundsen Sea Embayment. Quaternary Science Reviews 30, 488-505.

Smith, J.A., Hillenbrand, C.-D., Kuhn, G., Klages, J.P., Graham, A.G.C., Larter, R.D., Ehrmann, W., Moreton, S.G., Wiers, S., Frederichs, T., 2014. New constraints on the timing of West Antarctic Ice Sheet retreat in the eastern Amundsen Sea since the Last Glacial Maximum. Global and Planetary Change 122, 224-237.

Smith, J.A., Andersen, T.J., Shortt, M., Gaffney, A.M., Truffer, M., Stanton, T.P., Bindschadler, R., Dutrieux, P., Jenkins, A., Hillenbrand, C.D., Ehrmann, W., Corr, H.F.J., Farley, N., Crowhurst, S., Vaughan, D.G., 2017. Sub-ice-shelf sediments record history of twentieth-century retreat of Pine Island Glacier. Nature 541, 77-80.

Smith, J.A., Graham, A.G.C., Post, A.L., Hillenbrand, C.-D., Bart, P.J., Powell, R.D. The marine geological imprint of Antarctic ice shelves. In prep.

Stammerjohn, S., Massom, R., Rind, D., Martinson, D., 2012. Regions of rapid sea ice change: An inter-hemispheric seasonal comparison. Geophysical Research Letters 39.

Steig, E.J., Alley, R.B., 2002. Phase relationships between Antarctic and Greenland climate records. Annals of Glaciology 35, 451-456.

Steig, E.J., Ding, Q., Battisti, D.S., Jenkins, A., 2012. Tropical forcing of Circumpolar Deep Water Inflow and outlet glacier thinning in the Amundsen Sea Embayment, West Antarctica. Annals of Glaciology 53, 19-28.

Stickley, C.E., Pike, J., Leventer, A., Dunbar, R., Domack, E.W., Brachfeld, S., Manley, P., McClennan, C., 2005. Deglacial ocean and climate seasonality in laminated diatom sediments, Mac.Robertson Shelf, Antarctica. Palaeogeography, Palaeoclimatology, Palaeoecology 227, 290-310.

Stone, J.O., Balco, G.A., Sugden, D.E., Caffee, M.W., Sass, L.C., Cowdery, S.G., Siddoway, C., 2003. Holocene Deglaciation of Marie Byrd Land, West Antarctica. Science 299, 99-102.

Subt, C., Fangman, K.A., Wellner, J.S., Rosenheim, B.E., 2016. Sediment chronology in Antarctic deglacial sediments: Reconciling organic carbon 14C ages to carbonate 14C ages using Ramped PyrOx. The Holocene 26, 265-273.

Subt, C., I. Yoon, H., Yoo, K.-C., Lee, J.I., Leventer, A., Domack, E., Rosenheim, B., 2017. Sub-ice shelf sediment geochronology utilizing novel radiocarbon methodology for detrital-rich sediments. Geochemistry, Geophysics, Geosystems 18, 1404–1418.

Tanimura, Y., 1992. Distribution of diatom species in the surface sediments of Lützow-Holm Bay, Antarctica. K. Ishizaki, T. Saito (Eds.), Centenary of Japan. Micropalaeontology, 399-411.

Taylor, F., McMinn, A., Franklin, D., 1997. Distribution of diatoms in surface sediments of Prydz Bay, Antarctica. Marine Micropaleontology 32, 209-229.

Taylor, F., Whitehead, J., Domack, E., 2001. Holocene paleoclimate change in the Antarctic Peninsula: evidence from the diatom, sedimentary and geochemical record. Marine Micropaleontology 41, 25-43.

Taylor, F., Sjunneskog, C., 2002. Postglacial marine diatom record of the Palmer Deep, Antarctic Peninsula (ODP Leg 178, Site 1098) 2. Diatom assemblages. Paleoceanography 17.

The IMBIE team, 2018. Mass balance of the Antarctic Ice Sheet from 1992 to 2017. Nature 558, 219-222.

Thoma, M., Jenkins, A., Holland, D., Jacobs, S., 2008. Modelling Circumpolar Deep Water intrusions on the Amundsen Sea continental shelf, Antarctica. Geophysical Research Letters 35.

Thompson, D.W., J., Solomon, S., 2002. Interpretation of Recent Southern Hemisphere Climate Change. Science 296, 895

Turner, J., Lachlan-Cope, T.A., Thomas, J.P., Colwell, S.R., 1995. The synoptic origins of precipitation over the Antarctic Peninsula. Antarctic Science 7, 327-337.

Turner, J., 2004. The El Niño–southern oscillation and Antarctica. International Journal of Climatology 24, 1-31.

Turner, J., Maksym, T., Phillips, T., Marshall, G.J., Meredith, M.P., 2013. The impact of changes in sea ice advance on the large winter warming on the western Antarctic Peninsula. International Journal of Climatology 33, 852-861.

Turner, J., Lu, H., White, I., King, J.C., Phillips, T., Hosking, J.S., Bracegirdle, T.J., Marshall, G.J., Mulvaney, R., Deb, P., 2016. Absence of 21st century warming on Antarctic Peninsula consistent with natural variability. Nature 535, 411.

Turner, J., Phillips, T., Marshall, G.J., Hosking, J.S., Pope, J.O., Bracegirdle, T.J., Deb, P., 2017. Unprecedented springtime retreat of Antarctic sea ice in 2016. Geophysical Research Letters 44, 6868-6875.

Ullermann, J., Lamy, F., Ninnemann, U., Lembke-Jene, L., Gersonde, R., Tiedemann, R., 2016. Pacific-Atlantic Circumpolar Deep Water coupling during the last 500 ka. Paleoceanography, 31, 639-650.

Vaughan, D.G., Marshall, G.J., Connolley, W.M., Parkinson, C., Mulvaney, R., Hodgson, D.A., King, J.C., Pudsey, C.J., Turner, J., 2003. Recent Rapid Regional Climate Warming on the Antarctic Peninsula. Climatic Change 60, 243-274.

Villareal, T.A., Fryxell, G.A., 1983. Temperature effects on the valve structure of the bipolar diatoms Thalassiosira antarctica and Porosira glacialis. Polar Biology 2, 163-169.

WAIS Divide Project Members, 2013. Onset of deglacial warming in West Antarctica driven by local orbital forcing. Nature 500, 440.

WAIS Divide Project Members, 2015. Precise interpolar phasing of abrupt climate change during the last ice age. Nature 520, 661.

Walker, D.P., Brandon, M.A., Jenkins, A., Allen, J.T., Dowdeswell, J.A., Evans, J., 2007. Oceanic heat transport onto the Amundsen Sea shelf through a submarine glacial trough. Geophysical Research Letters 34.

Warnock, J.P., Scherer, R.P., 2015. A revised method for determining the absolute abundance of diatoms. Journal of Paleolimnology 53, 157-163.

Weber, M.E., Clark, P.U., Ricken, W., Mitrovica, J.X., Hostetler, S.W., Kuhn, G., 2011. Interhemispheric Ice-Sheet Synchronicity During the Last Glacial Maximum. Science 334, 1265-1269.

Weber, M.E., Clark, P.U., Kuhn, G., Timmermann, A., Sprenk, D., Gladstone, R., Zhang, X., Lohmann, G., Menviel, L., Chikamoto, M.O., Friedrich, T., Ohlwein, C., 2014. Millennial-scale variability in Antarctic ice-sheet discharge during the last deglaciation. Nature 510, 134.

Weijden van der, C.H., 2002. Pitfalls of normalization of marine geochemical data using a common divisor. Marine Geology 184, 167-187.

Whitehouse, P.L., Bentley, M.J., Le Brocq, A.M., 2012. A deglacial model for Antarctica: geological constraints and glaciological modelling as a basis for a new model of Antarctic glacial isostatic adjustment. Quaternary Science Reviews 32, 1-24.

Wise, M.G., Dowdeswell, J.A., Jakobsson, M., Larter, R.D., 2017. Evidence of marine ice-cliff instability in Pine Island Bay from iceberg-keel plough marks. Nature 550, 506.

Witus, A.E., Branecky, C.M., Anderson, J.B., Szczuciński, W., Schroeder, D.M., Blankenship, D.D., Jakobsson, M., 2014. Meltwater intensive glacial retreat in polar environments and investigation of associated sediments: example from Pine Island Bay, West Antarctica. Quaternary Science Reviews 85, 99-118.

Yoon, H.I., Park, B.-K., Kim, Y., Kang, C.Y., 2002. Glaciomarine sedimentation and its paleoclimatic implications on the Antarctic Peninsula shelf over the last 15 000 years. Palaeogeography, Palaeoclimatology, Palaeoecology 185, 235-254.

Yokoyama, Y., Lambeck, K., De Deckker, P., Johnston, P., Fifield, L.K., 2000. Timing of the Last Glacial Maximum from observed sea-level minima. Nature 406, 713-716.

Yokoyama, Y., Anderson, J.B., Yamane, M., Simkins, L.M., Miyairi, Y., Yamazaki, T., Koizumi, M., Suga, H., Kusahara, K., Prothro, L., Hasumi, H., Southon, J.R., Ohkouchi, N., 2016. Widespread collapse of the Ross Ice Shelf during the late Holocene. Proceedings of the National Academy of Sciences 113, 2354.

Zielinski, U., Gersonde, R., 1997. Diatom distribution in Southern Ocean surface sediments (Atlantic sector): Implications for paleoenvironmental reconstructions. Palaeogeography, Palaeoclimatology, Palaeoecology 129, 213-250.